Machine Learning Assisted Design of Biomedical High Entropy Alloys with Low Elastic Modulus for Orthopedic Applications

by

Hüseyin Can Özdemir

A Dissertation Submitted to the
Graduate School of Sciences and Engineering
in Partial Fulfillment of the Requirements for
the Degree of

Doctor of Philosophy

in

Mechanical Engineering

June 5, 2024

Machine Learning Assisted Design of Biomedical High Entropy Alloys with Low Elastic Modulus for Orthopedic Applications

Koç University

Graduate School of Sciences and Engineering

This is to certify that I have examined this copy of a doctoral dissertation by

Hüseyin Can Özdemir

and have found that it is complete and satisfactory in all respects,
and that any and all revisions required by the final
examining committee have been made.

Committee Members:

_____

Prof. Demircan Canadinç

_____

Prof. Murat Sözer

_____

Assoc. Uğur Ünal

_____

Prof. Ozan Kocadağlı

_____

Prof. Haluk Çabuk

Date: _____

To my mother and father!

ABSTRACT

Machine Learning Assisted Design of Biomedical High Entropy Alloys with Low Elastic Modulus for Orthopedic Applications

Hüseyin Can Özdemir

Doctor of Philosophy in Mechanical Engineering

June 5, 2024

High entropy alloys (HEAs) have received considerable attention from the scientific community since the 2000s due to their excellent properties and potential to be used in various structural and functional applications. HEAs consist of multi-principal elements governing their final properties in addition to manufacturing methods and heat-treatment processes compared to traditional alloys, whose properties are governed by one main principal element. Therefore, understanding the effect of each element on the properties of HEAs is a complex process. Due to the "cocktail effect", one of the core four effects of HEAs, HEAs can attain unpredictable and outstanding performance superior to the performance of all constituent elements. Because HEAs consist of multiple elements, thousands of possible compositions can be developed, giving rise to different properties for the same family of HEAs. Hence, conventional trial-and-error methods become costly and inefficient in discovering new HEAs. A solution to this issue is using computational methods, such as density functional theory (DFT), molecular dynamics (MD), or machine learning (ML). However, DFT and MD are computationally expensive and time-consuming. On the contrary, ML is an efficient tool for establishing complex and non-linear relations between inputs and target property, making the new HEA discovery process faster and cheaper. In this thesis, three new biomedical HEAs, namely, $Hf_{27}Nb_{12}Ta_{10}Ti_{23}Zr_{28}$, $Hf_{30}Nb_{14}Ta_{10}Ti_{28}Zr_{18}$, and $Hf_{12}Nb_{16}Ta_{35}Ti_{29}Zr_{8}$ were designed and developed utilizing ML. In the first chapter, $Hf_{27}Nb_{12}Ta_{10}Ti_{23}Zr_{28}$ and $Hf_{30}Nb_{14}Ta_{10}Ti_{28}Zr_{18}$ HEAs with low elastic modulus, closer to that of the bone, were predicted to reduce the "*stress shielding*" effect between the bone and implant material. Predictions were validated through experimental methods. In the second chapter, in order to enhance the antibacterial properties of HEAs developed in the previous chapter, they were coated with Ag via Physical Vapor Deposition (PVD). Specifically, the effect of PVD process parameters on Ag coatings' mechanical and ion release behavior was investigated. In the following chapter, the microstructure, surface oxide layer properties, and corrosion behavior of $Hf_{27}Nb_{12}Ta_{10}Ti_{23}Zr_{28}$ and $Hf_{30}Nb_{14}Ta_{10}Ti_{28}Zr_{18}$ HEAs were studied, revealing that they exposed superior corrosion behavior in simulated body fluid (SBF) and artificial saliva (AS) compared to conventional implant material, CoCrMo. Lastly, a new corrosion-resistant biomedical $Hf_{12}Nb_{16}Ta_{35}Ti_{29}Zr_{8}$ HEA was developed utilizing ML in the fourth chapter. It was found that the produced ingot had a dendritic microstructure in the center and a homogeneous microstructure around the circumference. Samples cut from the homogenous part of the ingot showed outstanding corrosion resistance as opposed to the samples with dendritic microstructure and conventional implant material, CoCrMo. Overall, the findings of the thesis prove that ML methods can be utilized to discover new HEAs with desired properties.

ÖZETÇE

Ortopedik Uygulamalar için Düşük Elastik Modüle Sahip Biyomedikal Yüksek Entropili Alaşımların Makine Öğrenimi Destekli Tasarımı

Hüseyin Can Özdemir

Makina Mühendisliği, Doktora

5 Haziran 2024

Yüksek entropili alaşımlar (HEA'lar), mükemmel özellikleri ve çeşitli yapısal ve fonksiyonel uygulamalarda kullanılma potansiyelleri nedeniyle 2000'li yıllardan beri bilim camiasından büyük ilgisini görmektedir. HEA'lar, özellikleri tek bir element tarafından yönetilen geleneksel alaşımlarla karşılaştırıldığında, üretim yöntemleri ve ısıl işlem süreçlerine ek olarak nihai özelliklerini belirleyen birden çok elementten oluşur. Bu nedenle, her bir elementin HEA 'ların özellikleri üzerindeki etkisini anlamak karmaşık bir süreçtir. HEA'ların dört temel etkisinden biri olan "kokteyl etkisi" nedeniyle, HEA'lar, tüm bileşen elemanlarının performansından daha üstün, öngörülemeyen ve olağanüstü performans gösterebilir. HEA'lar birden fazla elementten oluştuğundan, aynı HEA ailesi için farklı özelliklere yol açacak şekilde binlerce olası bileşim geliştirilebilir. Bu nedenle, geleneksel deneme-yanılma yöntemleri, yeni HEA'ların keşfedilmesinde maliyetli ve verimsiz hale gelmektedir. Bu soruna bir çözüm, yoğunluk fonksiyonel teorisi (DFT), moleküler dinamik (MD) veya makine öğrenimi (ML) gibi hesaplamalı yöntemlerin kullanılmasıdır. Ancak DFT ve MD hesaplama açısından pahalı ve zaman alıcıdır. Aksine, ML, girdiler ve hedef özellik arasında karmaşık ve doğrusal olmayan ilişkiler kurmak için etkili bir araçtır ve yeni HEA keşif sürecini daha hızlı ve daha ucuz hale getirir. Bu tezde, ML kullanılarak $Hf_{27}Nb_{12}Ta_{10}Ti_{23}Zr_{28}$, $Hf_{30}Nb_{14}Ta_{10}Ti_{28}Zr_{18}$, ve $Hf_{12}Nb_{16}Ta_{35}Ti_{29}Zr_{8}$ olmak üzere üç yeni biyomedikal HEA tasarlanmış ve geliştirildi. İlk bölümde, kemik ile implant malzemesi arasındaki "stres kalkanı" etkisini azaltmak için; kemiğe yakın, düşük elastik modüle sahip $Hf_{27}Nb_{12}Ta_{10}Ti_{23}Zr_{28}$ ve $Hf_{30}Nb_{14}Ta_{10}Ti_{28}Zr_{18}$ HEA'lar tahmin edildi. Tahminler ayrıca deneysel yöntemlerle doğrulandı. İkinci bölümde, bir önceki bölümde geliştirilen HEA'ların anti bakteriyel özelliklerini iyileştirmek amacıyla Fiziksel Buhar Biriktirme (PVD) yöntemiyle Ag ile kaplandı. Spesifik olarak, PVD proses parametrelerinin Ag kaplamaların mekanik ve iyon salınım davranışı üzerindeki etkisi araştırıldı. Bir sonraki bölümde, $Hf_{30}Nb_{14}Ta_{10}Ti_{28}Zr_{18}$, ve $Hf_{12}Nb_{16}Ta_{35}Ti_{29}Zr_{8}$ HEA'ların mikro yapısı, yüzey oksit tabakası özellikleri ve korozyon davranışları incelendi ve geleneksel implant malzemesine CoCrMo'a kıyasla simüle edilmiş vücut sıvısı (SBF) ve yapay tükürükte (AS) üstün korozyon davranışı sergiledikleri ortaya çıkarıldı. Son olarak dördüncü bölümde ML kullanılarak korozyona dayanıklı yeni bir biyomedikal $Hf_{12}Nb_{16}Ta_{35}Ti_{29}Zr_{8}$ HEA geliştirildi. Üretilen külçenin merkezinde dendritik bir mikro yapıya, çevresinde ise homojen bir mikro yapıya sahip olduğu tespit edildi. Külçenin homojen kısmından kesilen numuneler, dendritik mikro yapıya sahip numunelerin ve geleneksel implant malzemesi CoCrMo'un aksine olağanüstü korozyon direnci gösterdi. Genel olarak bu tezin bulguları, istenilen özelliklere sahip yeni HEA'ların keşfedilmesinde ML yöntemlerinin kullanılabileceğini kanıtlamaktadır.

ACKNOWLEDGMENTS

First of all, I would like to express my sincere gratitude to my Ph.D. advisor Prof. Dr. Demircan Canadinç for his support both in my academic and personal life. His constant guidance and mentorship were invaluable. The opportunities that he provided have contributed to and will shape my career in academia. There is no doubt that he as my advisor opened the way for me that would not have been possible without him.

My sincere appreciation also goes to my thesis committee members, Prof. Dr. Murat Sözer and Assoc. Dr. Uğur Ünal. Their suggestions and guidance contributed significantly to this thesis. Specifically, I would like to thank Dr. Ünal for his constant support when I needed help and guidance with XPS. He shared his knowledge with me patiently and thought me a lot. I would like to also thank to Prof. Dr. Hans Jürgen Maier for his support during my visit at the Institute für Werkstoffkunde (IW) in Leibniz Universitat Hannover in Germany.

Additionally, I would like to thank my colleague and friend Dr. Alireza Nazarahari for his help and support all the time both scientifically and in life. The things we went through together contributed to me personally and to this thesis in a great amount. Furthermore, my sincere appreciation goes to my colleagues and friends, Mr. Christian Hinte and Ms. Tatiana Blank, both of whom helped me in every way during my time at IW in Leibniz Universitat Hannover. I also would like to thank to my colleague and friend Dr. Bengisu Yılmaz for her support and guidance in electrochemistry, which is an important part of this thesis. Also, my dear friend Ms. Ezgi Demiröz was always there for me whenever I need, thus, she deserves a special thanks.

I also would like to thank Ms. Katharina Reimann for her constant help and support during my visit at Leibniz Universitat Hannover. Also, I want to present my special thanks to Ms. Anja Krabbenhöft and my friend Ms. Ece Kesme for their support in SEM characterization and surface preparation, respectively. Furthermore, I would like to thank Anja Schumann for her help in cutting my samples and her great work ethics.

Finally, I would like to thank to my family who have support me always in every way possible during my whole life and made me the person who I am today.

TABLE OF CONTENTS

LIST OF TABLES

LIST OF FIGURES

ABBREVIATIONS

AFM	Atomic Force Microscope
AS	Artificial Saliva
at%	Atomic Percent
BCC	Body-Centered Cubic
CV	Cross-validation
DFT	Density Functional Theory
E	Elastic Modulus
EDM	Electro-discharge Machining
EDX	Energy-dispersive X-ray Spectroscopy Detector
EI	Expected Improvement
FESEM	Field Emission Scanning Electron Microscope
GIXRD	Grazing Incidence X-ray Diffraction
H	Hardness
HCP	Hexagonal Close-packed
HEA	High Entropy Alloy
ICP-MS	Inductively Coupled Plasma-mass Spectrometer
KNN	K-nearest Neighbors Regression
LIN	Linear Regression
MAE	Mean absolute error
MD	Molecular Dynamics
ML	Machine Learning
MLFFNN	Multilayer Feed Forward Neural Network
MPEA	Multi Principal Element Alloy
NPs	Nanoparticles
PBS	Phosphate Buffer Saline
PVD	Physical Vapor Deposition
R^2	Coefficient of Determination
RF	Random Forest
RMSE	Root Mean Squared Error
SBF	Simulated Body Fluid
SCE	Saturated Calomel Electrode
SEM	Scanning Electron Microscope
SMAs	Shape Memory Alloys
SVR.L	Support Vector Regression with a Linear Kernel
SVR.P	Support Vector Regression with a Polynomial Kernel
SVR.R	Support Vector Regression with a Radial Basis Kernel
VAM	Vacuum Arc-melting
VAM	Vacuum Arc-melting
wt%	Weight Precent
XPS	X-ray Photo Spectrometry
XRD	X-ray Diffraction

Chapter 1:
INTRODUCTION

1.1 High Entropy Alloys (HEAs)

High Entropy Alloys (HEA), also known as multi-principal element alloys (MPEA), started to become popular and get an immense amount of attention from the scientific community within the last two decades. The original idea suggests that these alloys have outstanding mechanical, physical, and chemical properties along with high thermal stability at elevated temperatures due to the high configurational entropy they possess, leading to a single solid solution phase [1,2]. The initial work on MPEAs was done in the late 1970s by an undergraduate student, which led to the first published paper on the subject by Cantor et al. in 2004 [1].

There are two different explanations in the literature regarding the definition of HEAs, but the most famous is the concept of high configurational entropy. Basically, it divides HEAs into low, medium, and high entropy categories based on the total configurational molar entropy in an ideal solid solution. An entropy lower than 0.69R, between 0.69R and 1.61R, and higher than 1.61R means Low Entropy Alloy, Medium Entropy Alloy, and HEA, respectively, where R is the gas constant. The other definition is the composition-based definition, where HEAs are defined as alloys containing five or more principal elements with near equimolar ratios. Though the equimolar ratios maximize the high entropy effect, the composition-based definition states that these alloys have multi-principal elements, with each element's composition being between 5-35 at.% [3]. However, HEAs containing minor alloying elements, which do not comply with the composition-based definition, have also been studied in the literature over the years in order to optimize the properties of HEAs [4], expanding the possible number of HEAs that can be designed and manufactured.

1.1.1 Four core effects for HEAs

In order to explain and rationalize the excellent properties of HEAs, four core effects were proposed:

The high entropy effect:

As mentioned above, the high entropy effect is the key concept of HEAs, which basically claims that the high configurational entropy, caused by mixing more than five or more elements in equimolar ratios, favors the formation of solid solution phases over intermetallic compounds. As a result, the Gibbs free energy of a single solid solution is minimized, i.e., its Gibbs free energy becomes smaller compared to the Gibbs free energy of an intermetallic compound. More specifically, the Gibbs free energy of a system is defined by the following formula:

$$G = H - TS \tag{1.1}$$

where G is the Gibbs free energy, H is the enthalpy, T is temperature, and S is the entropy. Therefore, $G_{solid\ solution} < G_{intermetallic}$ is obtained due to a high $S_{configurational}$, which favors the solid solution formation in HEAs. Nevertheless, it should be noted that the configurational term is assumed to dominate during entropy calculations in HEAs, ignoring the vibrational, electronic, and magnetic terms [2,3]. Actually, a big portion of HEAs produced until now have been shown to form intermetallic phases, although they had a high configurational entropy [5].

The lattice distortion effect:

The introduction of substitutional atoms into a solvent matrix results in the movement of neighboring atoms from their ideal positions, generating a strain field and changing the bulk properties of the materials. Actually, severe lattice distortion in HEAs stems from the different atomic radii of atoms, causing a high mismatch of radii among the constituent elements [3,6]. The severe lattice distortion concept suggests that the lattice mismatch in HEAs is higher than conventional alloys, as shown with a schematic in Figure 1.1, resulting in proposed excellent mechanical properties. It has been claimed that the local increase in the lattice straining due to lattice distortion effect causes a decrease in the peak intensity of X-ray diffraction (XRD) peaks of HEAs [7,8]. This is expected as increased local lattice straining decreases diffraction peak intensity while more homogenous lattice strains do not cause XRD peak broadening as in the case of HEAs [9,10]. Moreover, severe lattice distortion is claimed to reduce electrical and thermal conductivity and increase hardness. However, there is still no clear and enough investigation to understand and distinguish the degree of the effect of each four core on these properties [3]. For instance, Stepanov et al. reported that single FCC phase

$Fe_{40}Mn_{28}Ni_{32-x}Cr_x$ (x=4, 12, 18, 24 at.%) HEAs showed low yield strengths between 200 and 350 MPa, proving that these results cannot be explained by the lattice distortion effect [11].

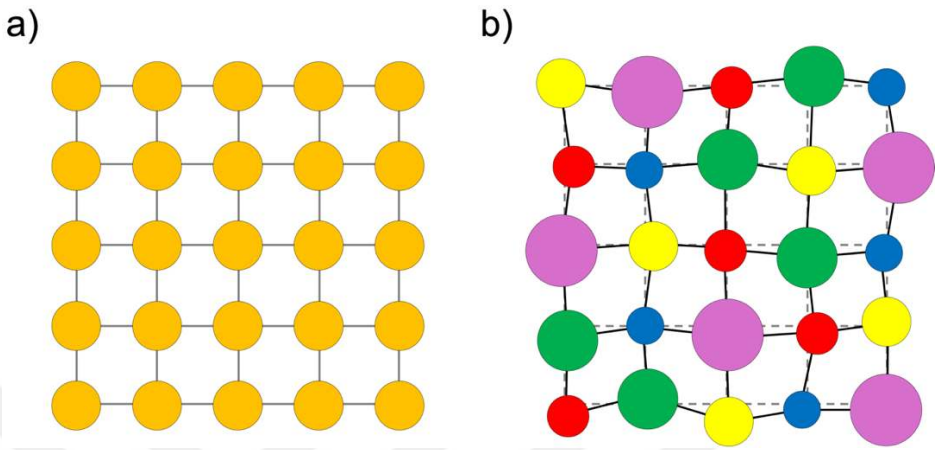

Figure 1-1: An example of lattice structure of (a) ideal single element alloy and (b) HEAs. The different colors in (b) designate different elements with different sizes.

The sluggish diffusion effect:

The diffusion in HEAs is acknowledged as sluggish compared to conventional alloys such as steel. The reason for such a definition comes from the observation of nanoprecipitations in the microstructure the investigated HEAs, alluding that formation of these precipitations are easy, but they grow slowly. Thus, slow diffusion contributes to the high temperature stability in these alloys based on the qualitative observations. Yeh et al. claimed that sluggish diffusion in HEAs stems from the different potential energies of lattice sites, whereas in pure element or dilute solid solution, the potential energy does not fluctuate as drastically as it does in the case of HEAs. As a result, there are lattice sites in HEAs where only the bonding for specific diffusing species is preferable compared to other constituent elements. Thus, lattice sites with varying potential energy in HEAs act as traps, slowing down diffusion [12].

The cocktail effect:

The cocktail effect proposes that unexpected and remarkable properties can be obtained as a result of the mixing of multi-principal elements, where the resulting properties are unpredictable and better than the properties of constituent elements. This effect suggests that properties of HEAs can be modified by changing the composition of

an alloy family, i.e., the different synergy among the elements in various contents can lead to obtaining varying properties in an alloy family [13]. For example, Kao et al. showed that the hardness of $Al_xCoCrFeNi$ ($0 \leq x \leq 2$) changed between 110 and 510 HV with altered Al content. Specifically, the increasing Al content brought about a transition of the microstructure from face-centered cubic (FCC) to body-centered cubic (BCC) + FCC and then BCC structure, leading to an increase in both lattice parameters and hardness of the designed alloys [14].

1.2 Potential applications of HEAs

There are numerous industries in which HEAs can be utilized, such as automotive, aerospace, nuclear reactors, machine tools, biomedical, electronics, and marine applications. Considering all of these applications, multiple structural and functional properties of HEAs should be tuned simultaneously, such as strength, toughness, wear resistance, oxidation, microstructural stability, corrosion resistance, radiation damage resistance, soft and hard magnetic properties, creep resistance, catalytic reactivity, and stability. In this section of the introduction, some of the most popular application areas of HEAs will be discussed.

1.2.1 Nuclear applications

Advanced power energy systems are required for sustainable clean energy production and reduction in the emission of greenhouse gases. Especially, fusion reactors, being an advanced power energy system, operate under very harsh conditions; thus, they require materials that can withstand extreme operating conditions, such as high temperature, radiation, and stress [15]. The conventional materials used in nuclear applications are austenitic stainless steels (304L), V-based, or W-based. The materials being used in nuclear applications are being exposed to harsh operating conditions, causing failures, including irradiation hardening, swelling, irradiation-induced segregation and phase transformation, irradiation creep, and helium bubble formation [16,17]. Therefore, new materials are needed to increase the efficiency of reactors and achieve sustainable clean energy production.

It has been proposed that HEAs exhibit very promising irradiation resistance. The reason for this is attributed to their sluggish diffusion mechanism restricts the movement

of atoms implanted by irradiation. The term ‘self-healing’ mechanism is used to account for the improved radiation of HEAs. To elaborate, the electrical and thermal conductivity are reduced due to the decrease in the mean free path of the electrons because of the increase in the number of components in HEAs. Actually, the short-range movement of interstitial clusters increments the recombination rate of vacancy and interstitials, hindering pore swelling in concentrated solid-solution alloys [18–20]. In short, while chemical disorder increases the chance of the recombination of vacancies and interstitial atoms, both chemical disorder and lattice distortion elevates the energy levels for formation of vacancies, and also obstructs their migration. Hence, general irradiation resistance is enhanced in HEAs as opposed to conventional nuclear materials [20].

In general, it has been acknowledged that BCC HEAs are better at resisting irradiation induced defects as opposed to FCC ones [20]. However, an FCC HEA ($Al_xCrFeCoNi$) demonstrated less swelling compared to its BCC counterparts; though, it had more ordered structures and lower configurational entropy [21]. Although, BCC or multi-phase HEAs are more resistant to irradiation induced hardening, due to larger stacking fault energy and higher lattice distortion, than FCC HEAs, their high intrinsic hardness makes them even more vulnerable to brittle fracture after irradiation [17,22]. On the other hand, some HEAs, such as the FCC CrFeCoNiPd and FCC CrMnFeCoNi demonstrated 0.31% volume swelling at 38 dpa at a temperature of 580 °C and 0.10% volume swelling at 60 dpa at a temperature of 500 °C, respectively, which is a decrease of two orders of magnitude as opposed to the pure nickel irradiated under similar conditions [23]. Most of the work about the investigation of irradiation hardening have been performed on CrFeMnNi, $Al_xCrFeCoNi$, as well as Cantor-based alloys. Though, various refractory HEAs containing W, Ta, Ti, V, Cr, Hf, and Zr were also investigated [20]. For instance, HfTaTiVZr HEA demonstrated superior irradiation hardening resistance compared to 304 stainless steel [18,24].

1.2.2 High-temperature applications

Reducing fuel consumption and increasing working efficiency of an engine requires engines operating at higher temperatures than the current conventional materials have been operating. Therefore, there is a need for developing new novel materials that can withstand high temperatures with an excellent microstructure stability and mechanical

properties [25,26]. One of the alloy family being used in high temperature applications is Ni-based superalloys, the operating temperature range of which is restricted due to their melting temperatures being around 1300 °C [27].

The common Ni-based and Co-based superalloys consist of ɣ and ɣ′ phases, where FCC ɣ phase forms a continuous matrix with ɣ′ precipitates with L12 structure residing in the matrix [28]. Microstructural stability is one of the important characteristics required for high temperature materials. Ni-based super alloys are generally not stable at high temperatures, where high Fe content initiates the formation of Fe-Cr rich phases at 900 °C. Moreover, Ni-based superalloys with no Fe and low Cr content experience β phase formation suddenly at 900 °C. On the other hand, HEAs have higher microstructural stabilities at higher temperatures because of high entropy and sluggish diffusion effects, as opposed to conventional superalloys [29]. For example, precipitation or other kind of phase formations were not observed in $Al_{0.7}Co_{20.6}Cr_{12.2}Fe_{11.5}Ni_{40.7}Ti_{7.2}$ after isothermal aging at 1050 °C for 500h [30]. These Ni containing alloys are also being called as high entropy superalloys in the literature. Therefore, phase stability at higher temperatures should be investigated more in depth to understand the maximum temperatures that these new materials can operate safely [29].

In addition to good microstructural stability at high temperatures, some refractory HEAs exhibited outstanding mechanical properties at elevated temperatures. The refractory HEAs, namely, NbMoTaW and VNbMoTaW, proposed by Senkov et al. have an exceptional yield strength over 400 MPa at 1600 °C [31,32]. On the contrary, Inconel 718 softens above 600 °C, which is a drive for motivation to investigate these refractory HEAs in depth. Furthermore, grain boundary sliding and driving force for the recrystallization at high temperature are suppressed in especially refractory HEAs due to sluggish diffusion and lattice distortion effects [29]. On the other hand, one issue with the refractory HEAs is the very poor ductility. For instance, NbMoTaW and VNbMoTaW demonstrated a compressive plasticity of 2.6% and 1.7% at room temperature respectively [31,32]. Other refractory HEAs, such as $Hf_{0.5}Nb_{0.5}Ta_{0.5}Ti_{1.5}Zr$ [33], HfNbTiZr [34], and HfNbTaTiZr [35] showed 18.8%, 14.9%, and 7% tensile elongation, respectively.

Another problem at elevated temperature is oxidation, which degrades the material properties [26,29]. Some of the elements, such as V, Mo, and W, that are present in the composition of the materials being used at elevated temperatures have very volatile

oxides that deteriorates the general oxidation resistance of the refractory alloys. V_2O_5 has a melting point of 690 °C, which is very low and, therefore volatilizes at high temperatures very easily. Mo forms gaseous oxides above 800 °C, which evaporates quickly. Lastly, the evaporation of WO_3 occurs above 1150 °C. The evaporation of the oxides creates pores in the oxide scales which promotes the diffusion of oxygen inside the bulk metal. Compared to conventional refractory alloys, it is suggested that refractory HEAs have better oxidation resistance due to formation of complex oxides and slow diffusion of oxygen because of highly alloying [29]. Moreover, when there is Cr and Al in the composition, Cr2O3 and Al2O3 can prevent the oxides of refractory elements from evaporating [36].

1.2.3 Hydrogen storage

Hydrogen can be used as a clean sustainable fuel instead of fossil fuels, which are the main reason for environmental pollution. The main issue with using hydrogen to produce clean energy is to store it. The efficient hydrogen storage problem is an ongoing challenge that scientists and engineers are trying to solve [37]. Hydrogen can be stored in form of gas, liquid, and/or metal-based hydrides. Storing hydrogen in gaseous form required high pressure and volume, which makes in efficient and dangerous for non-stationary applications as hydrogen is highly flammable gas. The safest way to store hydrogen is in the form of metal hydride, but metal hydrides are inefficient one way or another, opening the way for discovery of new novel hydrogen storage materials [38].

The desirable characteristics for hydrogen storage materials are high gravimetric, high-volume capacity, fast absorption/desorption rate, and good hydrogen absorption/desorption temperature and pressure [38]. The most promising material for hydrogen storage is Mg because of its low cost and high hydrogen storage capacity. Tough, the dehydrogenation of MgH_2 requires high temperatures as MgH_2 is very stable thermodynamically. Amorphous alloys with rare earth elements, such as MgLaNi or MgCeNi were also proposed as candidate hydrogen storage materials. Mg-based nano glasses and titanium-based quasicrystals also were studied in the literature. Recently, HEAs have received a lot of attention due to their good mechanical and functional properties, one of which is their ability to efficiently store hydrogen making them a new category of materials that can be used in future hydrogen storage applications [37].

The first work regarding the hydrogen storage properties of HEAs was done on $CoFeMnTi_{0.5\text{-}2.5}VZr$, $CoFeMnTiV_{0.4\text{-}3}Zr$, and $CoFeMnTiVZr_{0.4\text{-}3}$ [39]. Kao et al. showed that the materials manufactured by arc-melting had C14 Laves phase in the microstructure, and the absorption and desorption of hydrogen did not affect the microstructure and the stability of the phases. By varying the Ti, V, and Zr content, the hydrogen storage properties of the HEAs changed drastically without a change in the microstructure. Higher storage capability of the alloys was enhanced with lower Ti and Zr content. The reduction in the hydrogen storage ability of the HEA with higher Ti and Zr content was because of the phase segregation occurred in the microstructure due to higher Ti and Zr [38,39]. There are three categories of HEAs in the literature for hydrogen storage: BCC, lightweight, and intermetallic HEAs; among which BCC ones are the most promising ones. It has been reported that equimolar BCC HfNbTiVZr has a H/M ratio of 2.5, which is very high compared to conventional BCC alloys [38,40].

1.2.4 Catalysis applications

Electrocatalysis is another field where HEAs have attracted great interest due to their microstructural stabilities and outstanding catalytic activities for different catalytic reactions [41]. The vastness of the compositional space of HEAs gives scientists/engineers a chance to tune the surface microstructure and chemistry by altering and controlling the constituent elements, which broadens the possibilities to design and discover new materials for catalysis [42,43]. There are several advantages that supports the use of HEAs in catalytic reactions.

First, by carefully choosing constituent elements and altering their compositions, the binding energy of the surface of any HEAs can be adjusted as desired for any electrochemical reaction. Second, HEA surface provides multifunctionality because the active sites with different binding energies behave as an independent catalytic site, allowing catalyzing multiple reactions on the same surface, making it very attractive for cascade reactions. The flexibility in selecting and adjusting elements also provides additional benefits in terms of economic, environmental, and ethical concerns. On the other hand, there are some negative aspects of utilizing HEAs in catalysis applications. Though multifunctionality is advantages for cascade reactions, total active sites for each functionality exists in lower amounts in the surface. Moreover, some HEAs can be

unstable in operating temperatures for some catalytic reactions. Therefore, specific routes or process should be developed in order to adjust and control the surface and microstructure of catalyst HEAs [44].

In spite of some disadvantages, HEAs still stand as new potential material family for electrocatalysis because of their improved catalytic activities, which is possible once the composition and surface morphology are optimized. In addition to enhance catalytic activity, improvement of catalytic selectivity is also possible because electronic structures, i.e., the d-band center, of HEAs can be modified. The d-band center is the electronic property controlling/governing metal-molecule interactions. To elaborate, while an upshift of the d-band center results in a stronger metal-molecule interaction, a downshift of the d-band center results otherwise. In HEAs, the position of d-band center can be modified based on the selection of constituent elements and their compositions. Furthermore, it was reported that the lattice distortion in HEAs can also be an effective factor altering the d-band center [45].

Recently, RuRhCoNiIr HEA nanoparticles were developed for NH_3 decomposition. In this design, Rh, Co, and Ir were added into the Ru-Ni system, which has a large immiscibility gap, in order to increase configurational entropy and obtain a single solid solution. RuRhCoNiIr HEA nanoparticles exhibit excellent stability compared to previously reported Ru-based catalysts [46]. The oxidation of NH_3 is another catalytic process necessary for industrial synthesis. PtPdRh-based catalysts are mostly utilized alloys in the industry in spite of their high cost and immiscibility. Yao et al. introduced Ru and Ce elements into the PtPdRh system, which resulted in a homogeneous microstructure as well as enhanced catalytic activity with reduced cost as opposed to PtPdRh system [47]. CO oxidation, hydrogen evolution, oxygen evolution, oxygen reduction, methanol oxidation, and CO2 reduction reactions are the processes where HEAs can be candidates to remedy the problems that the current catalysts result in [45].

1.2.5 Biomedical applications

To increase patients' comfort and reduce the revision surgeries, new biomedical materials are needed. Biomaterials have been utilized in biomedical applications, such as orthopedic and dental implants and stents [48]. It is important that these materials are safe and biocompatible with the human body. For instance, the most commonly used metallic

materials for orthopedic implants are CoCr-based alloys, stainless steel, and Ti alloys. Among these materials, Ti alloys stand out because of their low elastic modulus, good strength, and biocompatibility, which is why they have been widely used in the human body [49]. Though, Ti-based alloys have lower elastic modulus, closer to that of the bone, as opposed to previously mentioned other metallic biomaterials, there is still a biomechanical mismatch issue between the conventional implant materials and the bone, because of higher elastic moduli the conventional biomaterials possess [50].

When the implant material has higher elastic modulus compared to the surrounding issue, most of the stress exerted is accommodated by the stiff metallic material, which in turn results in inhomogeneous allocation of the stresses. In the case of inhomogeneous stress distribution, bone has the capability to adapt itself by growing or remodeling itself against changing mechanical conditions [50]. To elaborate, bone can become denser in the presence of high mechanical loading or reduce its density in case of lack of necessary force, which is called bone resorption [49,51]. The inhomogeneous stress distribution as a result of the elastic modulus mismatch between the implant material and the bone is known as stress shielding effect, which is the case in which bone gets thinner and implant loosening occurs. Besides the concerns regarding the mechanical aspects, the toxic elements, such as Al and V can cause toxicity, which has adverse effects on living tissue and organs [52]. There new novel biomedical metallic materials should be designed and developed in order to address aforementioned problems.

Recently, the HEAs have also been studies in terms of their usage in biomedical applications. Their high strengths and good biocompatibilities have made them possible candidates for the future biomaterials [48,50,53]. Wang et al. studied investigated microstructure, mechanical properties, corrosion, and wear resistance of TiZrHfNbFe family of HEAs [54]. Especially, $TiZrHfNbFe_{0.5}$ HEA exhibited good compressive mechanical properties in addition to a better corrosion resistance in phosphate buffer saline (PBS) solution compared to conventional Ti6Al4V alloy [54]. In another study, it was reported that equimolar TiZrNbTa HEA displayed excellent corrosion resistance as opposed to CoCrMo, Ti6Al4V, and stainless steel (316L), suggesting that the surface oxide layer is not vulnerable against pitting, which reduces the ion release from the bulk material into the blood stream [55]. Iijima et al. analyzed osteoblast cell densities cultivated on stainless steel (316L), CoCrMo, CP-Ti, and $Ti_{28.33}Zr_{28.33}Hf_{28.33}Nb_{6.74}Ta_{0.80}Mo_{1.55}$. It was shown that the cell densities on stainless steel

(316L) and CoCrMo samples were significantly lower than the one acquired on CP-Ti, and $Ti_{28.33}Zr_{28.33}Hf_{28.33}Nb_{6.74}Ta_{0.80}Mo_{1.55}$. Furthermore, the cells cultivated on CP-Ti, and $Ti_{28.33}Zr_{28.33}Hf_{28.33}Nb_{6.74}Ta_{0.80}Mo_{1.55}$ were found to be spreading widely with a dense network of fibers [56]. Therefore, it can be concluded that biomedical HEAs have the potential to be the new generation metallic biomaterials with the desired properties for biomedical applications.

1.3 HEA compositional space and method for HEA discovery

1.3.1 Vastness of HEA compositional space

Although the official definition of HEAs states that the composition should be either equimolar or near equimolar in order to maximize the configurational entropy, composition-based definition establishes that the composition can vary between 5-35 at.%. Thus, composition-based definition opens the way for development of thousands of different HEAs for different applications. Senkov et al. reported that it is possible to manufacture 435,897 5-element combinations considering one specific alloy family only. Therefore, there are thousands of alloys families and millions of possible HEA compositions that can be designed and developed considering the whole periodic table. When carbides, borides, and nitrides included, the possibilities grow further [3]. Composition is only one of the factors that affect the final desired property. The effect of composition in HEAs might not reflect the expected outcome though. For example, adding aluminum resulted in formation of AlNi-rich BCC phases in AlCoCrFeNi alloy system, which made the surface to more vulnerable against the chloride ions [57]. Therefore, it can be concluded that the design of HEAs is complicated and since multiple elements govern final properties, it is hard to understand and control influence of each element compared to conventional alloys [58].

As mentioned earlier, there are thousands of possible combinations of elements in one HEA alloy family. However, even when one composition is selected among all the possible combinations, the final property can be still modified via microstructural engineering. Especially, manufacturing technique might be a very important factor to determine/guess whether the final microstructure will be dendritic or amorphous. Moreover, heat-treatment might be implemented based on the final desired microstructural features, such as phases, spacing, or size of precipitates. Hence, elements,

processing, and microstructure determines the final properties of HEAs altogether, allowing engineers and materials scientist to obtain desired properties [3,58].

1.3.2 Methods for HEA discovery

Since there exists a high degree of freedom due to multi-principal element concept in HEAs, the informed-design process is cumbersome. Considering all possible combination of compositional, processing, and heat-treatment effects, the discovery and design process of HEAs is costly and time consuming as opposed to conventional trial-and-error methods [59]. Computational tools, such as density functional theory (DFT), molecular dynamics (MD), and machine learning (ML) are the methods that can be helpful to increase the efficiency of alloy design process and avoid expensive trial-and-error methods.

Yuan et al. investigated structural stability of BCC Ti-Zr-Hf-Nb refractory HEAs using DFT method. To elaborate, the formation and free energies of [Ti-Hf_{14}]Nb_3, [Ti-Zr_8Hf_6]Nb_3, and [Ti-$Zr_8Hf_4Ti_2$]Nb_3 alloys were estimated by using DFT calculations. Based on the DFT results, it was concluded that [Ti-$Zr_8Hf_4Ti_2$]Nb_3 alloy had the lowest formation and free energy, suggesting the highest BCC structural stability among the three HEAs studied in the work. In addition to DFT calculations, the authors also confirmed the results experimentally, showing that small number of precipitations were observed in [Ti-Hf_{14}]Nb_3 and [Ti-Zr_8Hf_6]Nb_3, while [Ti-$Zr_8Hf_4Ti_2$]Nb_3 possessed a single BCC phase [60]. In another work, hydrogen storage properties of TiZrHfScMo HEA were studied by DFT. The calculations indicated that the hydrogenation process was exothermic, and the hydrides were stable. Moreover, the behavior of individual constituent elements was shown to be different from each other during hydrogenation process [61]. Although, DFT is very useful when it is not possible to gather some information experimentally, it requires an immense amount of computational power, which slows down the discovery process.

Another computational tool for alloy design and discovery is MD. For instance, Chen et al. tried to understand the effect of element content, short-range ordering and precipitation on melting temperature of AlCoFeNiCu HEA family via MD simulations. The results can be summarized as: decreasing Cu concentration increases the melting temperature; and increasing Cu content promotes short-range ordering and precipitation

which reduced the melting temperature of the alloys [62]. In another study, the relation between tensile mechanical properties and deformation mechanisms in CoCrFeMnNi family of alloys were examined using MD simulations [63]. Compared to DFT, MD requires less compositional power. However, the lack of interatomic potential representing different compositional spaces for various HEA families limits the capability of MD simulations in HEA design and development.

On the other hand, ML is an efficient tool to establish the relationship and unearth the implicit connections between the features and target property, making the design process much faster than DFT and MD methods [64,65]. Thus, the number of ML-related publications on discovering new materials with desired properties to address complex problems in materials science has increased [66]. For instance, ML techniques have been utilized in a wide range of optimization problems for HEAs to predict properties such as high-temperature yield strength [67], hardness [68,69], ultimate tensile strength, electric conductivity [70], Young's modulus [71,72], fatigue life [73]. In addition, a vast amount of work focused on phase prediction in HEAs [64,74,75]. Huang et al. utilized a dataset based on ab-initio calculations to predict the lattice distortion and phase stability for the Co-Ni-Cr-Mo-V system [76]. In another work, MD simulations and ML were combined to optimize the yield strength of the V-Cr-Fe-Co-Ni system [77].

Chapter 2:

MACHINE LEARNING ASSISTED DESIGN OF BIOMEDICAL HIGH ENTROPY ALLOYS WITH LOW ELASTIC MODULUS FOR ORTHOPEDIC IMPLANTS

2.1 Introduction

Metallic materials, being utilized in the manufacturing of more than 70% of medical implants, have a substantial standing in biomedical applications since they are substituted for failed hard tissue in human body to enhance the quality of life of the patients [78–80]. Compared to other metallic biomaterials such as Co-based alloys or stainless steels, Ti and its alloys have gained popularity in medical and dental applications owing to their excellent biocompatibility and corrosion resistance [49,81,82]. Recently, Ti-based high entropy alloys (HEAs), comprising biocompatible elements such as Ta, Hf, Nb, Zr and Mo, have been studied by researchers as potential alternative implant materials [83–86]. As opposed to conventional metallic implant materials comprised of one or two principal elements along with minor additional elements, the HEAs are composed of 4 or more principal elements with concentrations varying between 5 at% and 35 at% in equimolar or near-equimolar proportions [87,88]. Due to the high configurational entropy brought about mixing of multiple principal elements promoting the formation of a single stable solid solution phase [3,84], HEAs exhibit superior mechanical properties such as excellent corrosion resistance [89,90], high hardness and wear resistance [34,91,92], high strength and toughness [84,90] and high thermal stability at elevated temperatures [90,93]. For the last ten years, promising novel biocompatible HEAs have been synthesized and it has been confirmed that these alloys have a favorable combination of physical and mechanical properties in comparison to other biomaterials. Even though some biocompatible HEAs possess lower elastic moduli than currently implemented biomedical alloys such as 316L, CoCrMo, and Ti6Al4V [85], they are still far from the elastic modulus of bone, which varies between 4 and 30 GPa [80,94]. Therefore, the long-term functionality of these implants decreases due to structural dissimilarities.

The stiffness mismatch between the implant and the bone promotes possible implant loosening, failure of the implant, and tissue loss [49,84,95]. Namely, the implant material whose elastic modulus is much higher than that of the bone starts to carry the majority of the applied stresses, leading to inhomogeneous allocation of the exerted load between the implant and the surrounding tissue. As a result of this phenomenon also known as stress shielding, the bone adapts itself by either reducing its mass (bone absorption) or becoming thinner (bone remodeling) [49,51,78,79,82]. The aforementioned challenges bring about a need for the search for new implant materials with a desirable combination of biological and biomechanical compatibilities [49,79,82]. In particular, it is essential for the implant to be strong and durable with a structural stiffness matching to that of the bone in order for it to properly function in the long term without failing or requiring revision surgery [78–80]. Hence, the investigation and optimization of biocompatibility of HEAs as potential implant materials from both biological and mechanical aspects is crucial for their safe utility as implant materials. For instance, an equimolar TiZrNbTaMo HEA designed for orthopedic implants possessing an elastic modulus of 153 GPa displayed excellent corrosion resistance and high stability against pitting. However, multiple dendritic body-centered cubic (BCC) phases having severe Mo segregation were observed, leading to an inhomogeneous microstructure, which may be due to the higher melting temperature of Mo as compared to other constituent elements [96]. Other biocompatible HEAs were also reported in the literature such as equimolar TiZrTaHfNb and $Ti_{1.5}ZrTa_{0.5}Hf_{0.5}Nb_{0.5}$ with excellent corrosion resistance, good wettability and wear resistance, possessing elastic moduli of 112.74 GPa and 98.57 GPa, respectively [85]. The variations in the elastic moduli of the HEAs with the same constituent elements [85] evidence that alloying elements in different quantities alter the properties of HEAs substantially, making new alloy design more attractive and broadening their utility for different applications [79,97].

Alloy design with preferred intrinsic properties can be accomplished through controlled chemical alloying which modifies microstructure and phases present in the matrix [3,33,79]. Sakaguchi et al. explored ternary and quaternary TiNbTaZr system with varying Nb (0-40 wt.%), Ta (0-20 wt.%) and Zr (0-10 wt.%) contents. It was demonstrated that Nb and Ta concentrations affect the stress-strain behavior; therefore, the deformation mechanisms and the mechanical properties. For instance, elastic modulus of the system first decreases and then increases as Ta concentration changes from 0 to 20

wt.%, validating high sensitivity of the system's intrinsic properties to Ta content. Furthermore, varying Nb concentration results in a more complicated modification in elastic modulus as compared to the effects of Ta and Zr concentrations [98–100]. Additionally, based on the investigations on TiV and TiNbSn alloys [101], and Ti35Nb4Sn6MoxZr (x varying from 0 to 15 wt.%) system [82], it was shown that the elastic modulus depends on chemical composition in an inexplicit way. Thus, considering the design of an alloy with more than 4 principal elements such as HEAs, determining the interactions and resulting properties by trial-and-error or intuition remains an inefficient approach as there exists a very large search space for HEAs with a high number of possible combinations of the constituent elements [3,89,102].

An effective and very efficient remedy for this problem is the implementation of machine learning (ML), which has recently become popular in materials science community. For the last couple of years, increase in the availability of data and the ML methods' ability to identify underlying trends from data have expedited materials research and discovery by significantly decreasing computational and experimental costs as compared to traditional methods [103–108]. Specifically, the ML algorithms are trained using a training dataset, validated, and then utilized to make predictions on the test dataset which the algorithms do not have access during training and validations processes [109,110]. Employment of the ML methods in material discovery processes enables detecting complex and nonlinear connections among the physical and chemical features in a dataset, which makes prediction of previously unknown yet existing information and/or relationships possible. These capabilities are very advantageous in materials discovery where the compositional search space is very large and the relations among parameters are unknown [107,108].

In recent years, ML methods have been put into use in various fields of materials science, including phase selection in HEAs [111–117], hardness prediction [90,118], corrosion resistance optimization [119,120], improvement of properties of shape memory alloys (SMAs) [121–123], and molecular dynamics simulation integrated property predictions [124,125]. There exist numerous studies in the literature which used ML based approach for designing new alloy compositions for specific alloy systems with desired properties. For instance, the safest NiTi SMA composition releasing the least amount of Ni ions into oral cavity for dental applications was successfully predicted using a multilayer feed forward neural network (MLFFNN) trained on the experimental data

available in literature on the Ni ion release into artificial saliva solutions for different NiTi compositions [120]. In another example, utility functions were utilized to iteratively increase ML methods' capability which resulted in prediction of 17 new alloy compositions in AlCoCrCuFeNi HEA system, the hardness values of which are 10% higher than those in the training dataset [90]. These promising examples clearly demonstrate how ML can assist and transform the approach to materials design and discovery problems compared to costly and time-consuming conventional methods.

The aim of the current work is to obtain the optimum composition for $Ti_xTa_yHf_zNb_mZr_n$ biomedical HEAs with elastic moduli close to the stiffness of the bone by employing ML algorithms with the specific purpose of providing a better structural match between the implant and the bone in orthopedic applications. To reach this target, first a new dataset was curated from existing literature on Ti-containing HEAs and medium entropy alloys (MEAs) along with their measured elastic moduli. Then, the dataset was used to train several ML algorithms which were employed to construct a model to predict the elastic modulus of new compositions. In the final step, two of the predicted biomedical HEAs with optimum compositions were subjected to validation experiments to confirm the accuracy of the predictions. As a result, two novel biomedical HEAs, namely $Ti_{23}Ta_{10}Hf_{27}Nb_{12}Zr_{28}$ and $Ti_{28}Ta_{10}Hf_{30}Nb_{14}Zr_{18}$, were obtained with elastic moduli of 83.5 ± 2.9 GPa and 87.4 ± 2.2 GPa, respectively. The work presented herein, thus, illustrates that the ML methods were successfully implemented to optimize $Ti_xTa_yHf_zNb_mZr_n$ biomedical HEA compositions with the aim of minimizing elastic modulus in order to ensure mechanical compatibility between the implant and bone.

2.2 Computational methods

2.2.1 Data Mining

To construct the dataset required for training of the ML algorithms, first a detailed literature search was conducted within the HEA literature published since 2000s. Then, all the articles on quaternary, quinary, and senary as-cast HEAs synthesized by arc melting process and including the experimentally measured elastic moduli information were scanned and put together to form the preliminary dataset. The dataset consisted of 53 datapoints shared in Supplementary Information of [71] (each datapoint, i.e., each row in the dataset, has alloy composition, calculated empirical parameters and corresponding

elastic modulus as target variable) after the elastic moduli of datapoints with the same compositions were averaged and treated as a single datapoint. In order to increase the number of datapoints in the training dataset and enhance the generalization capability of the ML models [118], HEAs containing toxic elements such as V and Al were also considered. The dataset utilized in this work possesses a limited number of datapoints for the following reasons: the occurrence of the published articles in literature on biomedical HEAs hasn't been very frequent until recent years, and not all the published literature have the relevant experimental data. In fact, acquisition of large numbers of datapoints is one of the main struggles in materials informatics where obtaining materials and corresponding target variables are experimentally challenging and costly [107], leading to datasets with limited amount of datapoints.

Each datapoint in the dataset is composed of nine elements (Ti, Ta, Hf, Nb, Zr, Mo, W, V, Al), eleven empirical features, and one target variable, i.e., the elastic modulus. The eleven calculated empirical features are valance electron concentration (VEC), atomic size difference (δr), difference of electronegativity ($\Delta\chi$), mixing enthalpy (ΔH), configurational entropy (ΔS) [126], Ω parameter proposed by Yang et al. [127], Λ parameter defined by Singh et al. [128], ɣ parameter suggested by Wang et al. [129], number of itinerant electrons (e/a) [130], difference of shear modulus (δG), and difference of melting temperature (δTm). The latter two empirical features are proposed based on the analogy to δr. Most of the aforementioned empirical features are related to crystal structure, phase type and formation or stability of single-phase solid solution of HEAs, which are the governing factors for controlling mechanical properties in HEAs [3,13]. All the empirical features utilized herein are listed in Table 2-1.

In Table 2-1, the features C_i, VEC_i, r_i, χ_i, $(e/a)_i$, G_i, and T_i refer to the atomic concentration, VEC, atomic radius, Pauling electronegativity, e/a, shear modulus, and melting temperature of each element in an alloy, respectively. The averages of atomic radius $\overline{r}$, Pauling electronegativity $\overline{\chi}$, shear modulus $\overline{G}$, and melting temperature $\overline{T}$ are calculated as $\overline{r} = \sum_{i=1}^{n} C_i r_i$, $\overline{\chi} = \sum_{i=1}^{n} C_i \chi_i$, $\overline{G} = \sum_{i=1}^{n} C_i G_i$, and $\overline{T} = \sum_{i=1}^{n} C_i T_i$, respectively. R, n, r_{min}, and r_{max} are universal gas constant, the number of constituent elements, and the atomic radii for the smallest and largest atoms, respectively. ΔH_{ij}^{mix} is the mixing enthalpy of atomic pairs in a binary system estimated by Takeuchi and Inoue utilizing Miedema method [131].

Table 2-1: List of empirical features and the corresponding mathematical formulae.

Description of empirical features	**Formulae**
Valance electron concentration (VEC)	$VEC = \sum_{i=1}^{n} C_i * VEC_i$
Atomic size difference (δr)	$\delta r = \sqrt{\sum_{i=1}^{n} C_i * (1 - \frac{r_i}{\overline{r}})^2}$
Difference of electronegativity ($\Delta\chi$)	$\Delta\chi = \sqrt{\sum_{i=1}^{n} C_i * (\overline{\chi} - \chi_i)^2}$
Mixing enthalpy (ΔH)	$\Delta H = \sum_{i=1,j>1}^{n} 4 * C_i * C_j * \Delta H_{ij}^{mix}$
Configurational entropy (ΔS)	$\Delta S = -R\sum_{i=1}^{n} C_i * \ln(C_i)$
Ω parameter	$\Omega = \frac{\overline{T} * \Delta S}{\Delta H}$
Λ parameter	$\Lambda = \frac{\Delta S}{\delta r * \delta r}$
ɣ parameter	$\gamma = (1 - \sqrt{\frac{(\overline{r}+r_{min})^2 - \overline{r}^2}{(\overline{r}+r_{min})^2}}) \Big/ (1 - \sqrt{\frac{(\overline{r}+r_{max})^2 - \overline{r}^2}{(\overline{r}+r_{max})^2}})$
Number of itinerant electrons (e/a)	$e/a = \sum_{i=1}^{n} C_i * (e/a)_i$
Difference of shear modulus (δG)	$\delta G = \sqrt{\sum_{i=1}^{n} C_i * (1 - \frac{G_i}{\overline{G}})^2}$
Difference of melting temperature (δT_m)	$\delta T_m = \sqrt{\sum_{i=1}^{n} C_i * (1 - \frac{T_i}{\overline{T}})^2}$

In ML applications, due to the nature of the predictors within the dataset, a preprocessing of the variables may be required to improve the performance of the whole ML process. Specifically, the variables in a dataset might have a non-normal distribution, can be highly skewed or in different scales, all of which deteriorate the general performance of the ML algorithms. Therefore, an analysis of the dataset should be carried out before training to understand the data and implement the appropriate data transformation process. With data transformation, the variables are normalized and scaled so that all of them are treated equally by the ML algorithms [111,120]. In this study, a min-max normalization method was applied to scale and normalize the features between 0 and 1 by using the following methodology:

$$X_i' = \frac{X_i - X_{min}}{X_{max} - X_{min}} \tag{2.1}$$

where X_i', X_i, X_{min}, and X_{max} are normalized data, the sample data, the minimum and maximum values in the X sample space, respectively.

2.2.2 Feature selection

One of the major obstacles in ML implementations with a high dimensional dataset is how to select the most relevant features to train the ML algorithms. Too many input features result in overfitting, especially in datasets containing small number of instances, due to high degrees of freedom they introduce into the algorithms, leading to a decrease in the generalization capability of the ML models. Hence, a careful selection of features which explain most of the variance in a target variable is required to discard the redundant information from a dataset, and thus, have a critical impact on the prediction accuracy and performance of a model [119]. Choosing the best set of features becomes an even more difficult task in the presence of high correlation among the features. Highly correlated features affect model performance and prediction accuracy due to the fact that they have the same information about the target variable, i.e., the essence of the correlated features is so similar, such that the ML algorithms cannot differentiate among them [107,132]. One of the frequently used parameters for the correlation analysis is the Pearson correlation coefficient (PCC).

$$r_{xy} = \frac{\sum_{i=1}^{n}(x_i - \overline{x})(y_i - \overline{y})}{\sqrt{\sum_{i=1}^{n}(x_i - \overline{x})^2}\sqrt{\sum_{i=1}^{n}(y_i - \overline{y})^2}} \tag{2.2}$$

where x_i and $\overline{x}$ are the sample value and mean of x variable, y_i and $\overline{y}$ are the sample value and mean of y variable, respectively. The coefficient r_{xy}, which takes values from -1 to 1, is a representation of the strength of the linear relationship between x and y variables. The positive and negative sign of the coefficient demonstrate the positive and inverse relationship between x and y, respectively. The closer $|r_{xy}|$ is to 1, the stronger the correlation between x and y is [109]. The PCC provides a metric for linear relationship among the features and target variables, but it fails to capture the nonlinearity between

the features. To overcome this issue, Random Forest (RF) method which is a very attractive choice for classification and regression problem was also employed for feature selection in this work. Compared to other feature selection methods, the RF method provides a measure of importance of variables by ranking them based on their performances during the optimization of the model [132,133]. Thus, by combining the two methods, the most relevant features were selected to train the ML algorithms.

2.2.3 Machine learning algorithms and synthetic dataset

In this study, different ML algorithms, namely linear regression (LIN), k-nearest neighbors regression (KNN), RF, support vector regression with a linear kernel (SVR.L), support vector regression with a polynomial kernel (SVR.P), support vector regression with a radial basis kernel (SVR.R), and MLFFNN, were evaluated based on their performance in predicting the target variable. Prior to training the models, the initial dataset was divided into a training (used for optimization of the models) and test dataset (used at the end to obtain the models' performance accuracy predicting the unseen data). While optimizing the models using hyperparameters found with grid search strategy, which is a method in which various combinations of hyperparameters are tried out to select the best batch, repeated cross validation and bootstrapping with replacement were utilized to improve training process to avoid overfitting as much as possible with a small training dataset. The ML models were evaluated based on their prediction errors on the test dataset. The error metrics utilized are root mean squared error (RMSE) and mean absolute error (MAE), and calculated as:

$$RMSE = \sqrt{\frac{1}{n}\sum_{i=1}^{n}(y_i - \hat{y})^2} \tag{2.3}$$

$$MAE = \frac{1}{n}\sum_{i=1}^{n}|y_i - \hat{y}| \tag{2.4}$$

where y_i and $\hat{y}$ are true value and predicted value, respectively. All computations were performed using scikit-learn library with python programming language [134]. To find

the optimum composition leading to the smallest possible elastic modulus, a synthetic dataset was constructed with more than 500000 different compositions, where Ti, Ta, Hf, Nb, and Zr contents ranged from 5 to 35 at% with 1 at% intervals, complying with the widely accepted HEA definition. Then, the synthetic dataset was fed into the best ML model to make new predictions in the aforementioned composition range.

2.3 Computational results

2.3.1 The effect of training and test set split proportions

The general notion in any ML algorithm is that the larger the dataset, the better the model performance will be, because a large dataset contains an extensive amount of information about the target variable. Therefore, both training and test datasets randomly taken from this large dataset will have a normal distribution representing the whole sample space for both sets, making any model better at generalizing and reducing variance due to a reduced outlier effect. Overfitting due to outliers can be alleviated with data transformation such as normalizing and scaling of the data [119]. However, when the dataset is small, normalization and scaling of the data might not be as effective as it is in the case of a large dataset. In addition to a transformation, a careful split of data creating a bell-shaped distribution of both training and test datasets should be taken into consideration to avoid any overfitting. Therefore, the ratio of split of a small dataset similar to the one employed in this study is very critical so as to make sure that datapoints in both sets follow the same distribution. As illustrated in Figure 2-1a, the prediction error for KNN, SVR.R, SVR.P, SVR.L, and RF decreases as the proportion of training dataset increased from 30% to 90%. The RMSE values shown in Figure 2-1a is the mean value of RMSE estimated 200 times on randomly selected testing set for different algorithms by using only the compositions as input variables. In Figure 2-1b, bootstrapping with replacement is also implemented as another evaluation method for RMSE using 70% of the training dataset. A split ratio of 70% training dataset is considered in this work because of the very limited amount of datapoints present in the dataset. Decreasing the proportion of the datapoints in the testing set may be misleading in the evaluation of the models as only few datapoints in the testing set will contribute to calculation of RMSE. Based on Figure 2-1, KNN algorithm outperforms others and can be selected as the main model.

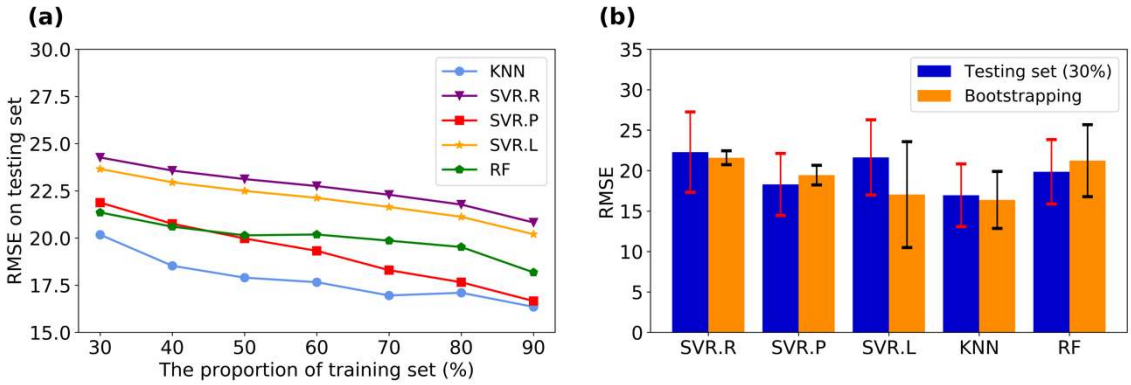

Figure 2-1: (a) the evolution of RMSE on test dataset with changing training dataset proportions for KNN, SVR.R, SVR.P, SVR.L, and RF to evaluate and select the best performing model (b) the estimation of RMSE with repeated holdout validation approach and bootstrapping methods, pointing out KNN is the best performing model.

2.3.2 Feature selection

The aim of selecting the right features is to eliminate any redundant or duplicate information present in the dataset and decrease degrees of freedom of the models so as to reduce complexity and prevent overfitting [132]. The correlation of each input feature to the target, i.e., elastic modulus, is presented in Appendix A. Solely based on Appendix A, δr, Al, and δT_m features seem to be very uncorrelated with elastic modulus, indicating that they don't contain relevant information about the target. The PCC values for the empirical features δG, $\Delta\chi$, and VEC, on the other hand, are larger than 0.5, indicating a strong correlation between these three empirical features and the target. While understanding the relationship between input and output variables is helpful in conceptualizing a preliminary plan for feature selection, the investigation of the correlation among input features is also crucial as the correlation between them deteriorates efficiency and accuracy of ML algorithms [135].

The heatmap for PCCs among input variables is presented in Figure 2-2. Accordingly, Mo and $\Delta\chi$ have a PCC of 0.95, which is the highest correlation among all features. The second highest correlated features are Mo and δG, and Al and ΔH. In an ideal scenario, all input variables should be uncorrelated [107]. Therefore, only one feature is selected in the presence of strong correlation between features to prevent duplicate information in the dataset [90,119]. There are two main drawbacks of PCC:

first, it neglects any existing nonlinearity in the dataset; second, the performance of ML algorithms is not included in the process of estimating PCCs [116,132].

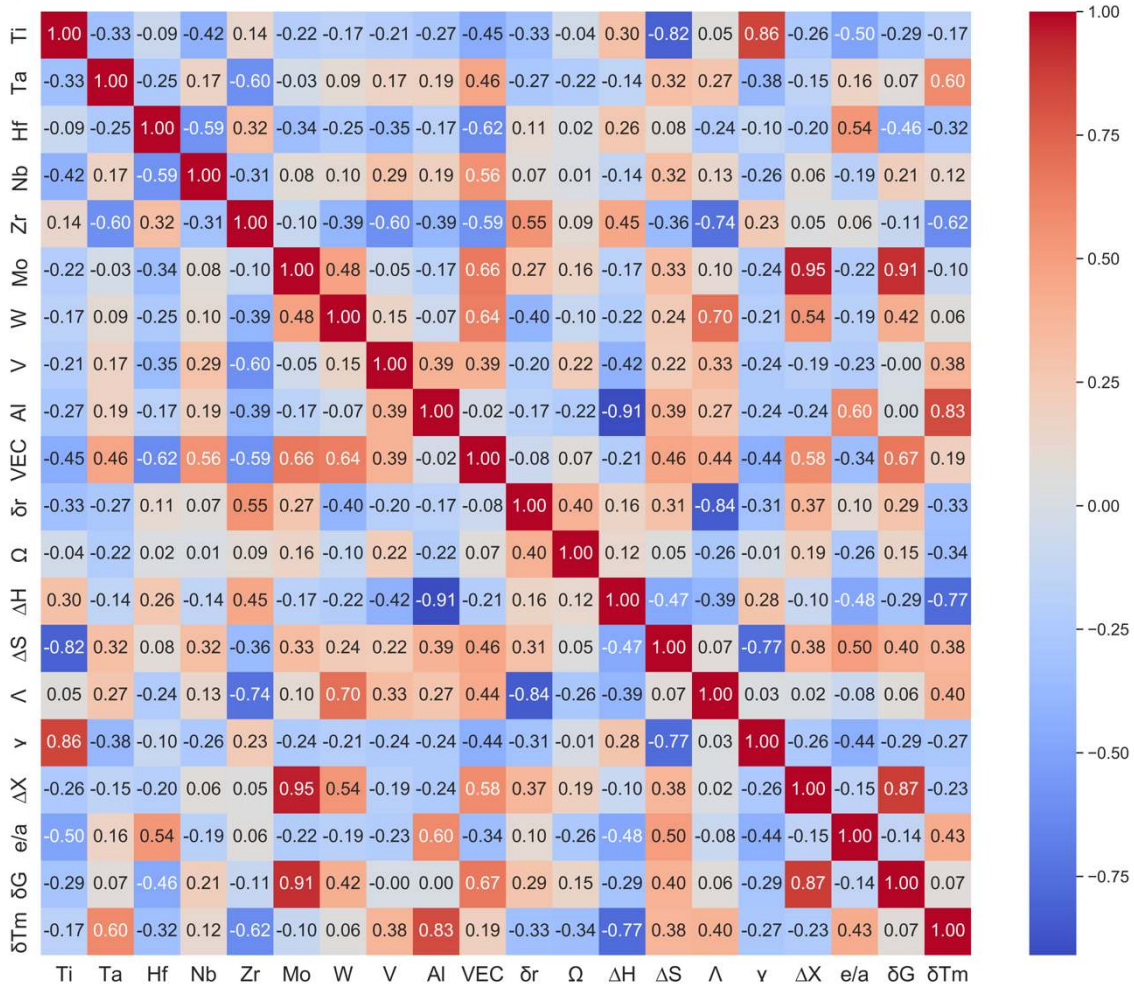

Figure 2-2: The heatmap of PCCs for chemical composition and empirical features. The higher the color intensities are, the more the correlation between the two features is. Red and blue colors indicate positive and negative correlation, respectively.

To decrease the effect of high correlation in the dataset, the RF method was employed in the process of feature selection in addition to PCC. RF consists of a forest with many decision trees, each of which is created by only considering a subset of features resulting in uncorrelated trees as compared to basic decision trees. One advantage of RF is that it provides the user with the feature importance making it an attractive tool for feature selection. By restricting each tree to consider only a subset of all available features, it calculates each feature's performance/importance in increasing the accuracy when splitting a node while growing a tree [136]. The corresponding feature importance results

obtained from the RF algorithm utilized in this work are demonstrated in Figure 2-3. Accordingly, VEC stands out as the best predictor, leaving all other compositional and empirical features behind. The next three most important features are $\Delta\chi$, δG, and ΔH, suggesting that empirical features contain relevant information related to intrinsic properties of the alloys within the dataset. Compared to Appendix A, W does not seem to be of importance when the model performance is included in the selection process. Based on Appendix A, ΔH is not highly correlated with the target. On the other hand, when its performance is evaluated considering its importance as a feature in RF method as shown in Figure 2-3, it can be inferred that elastic modulus is nonlinearly dependent on ΔH. Since Mo and $\Delta\chi$ are highly correlated and Mo is one of the elements representing alloys in the dataset, $\Delta\chi$ was not considered in the following feature selection process.

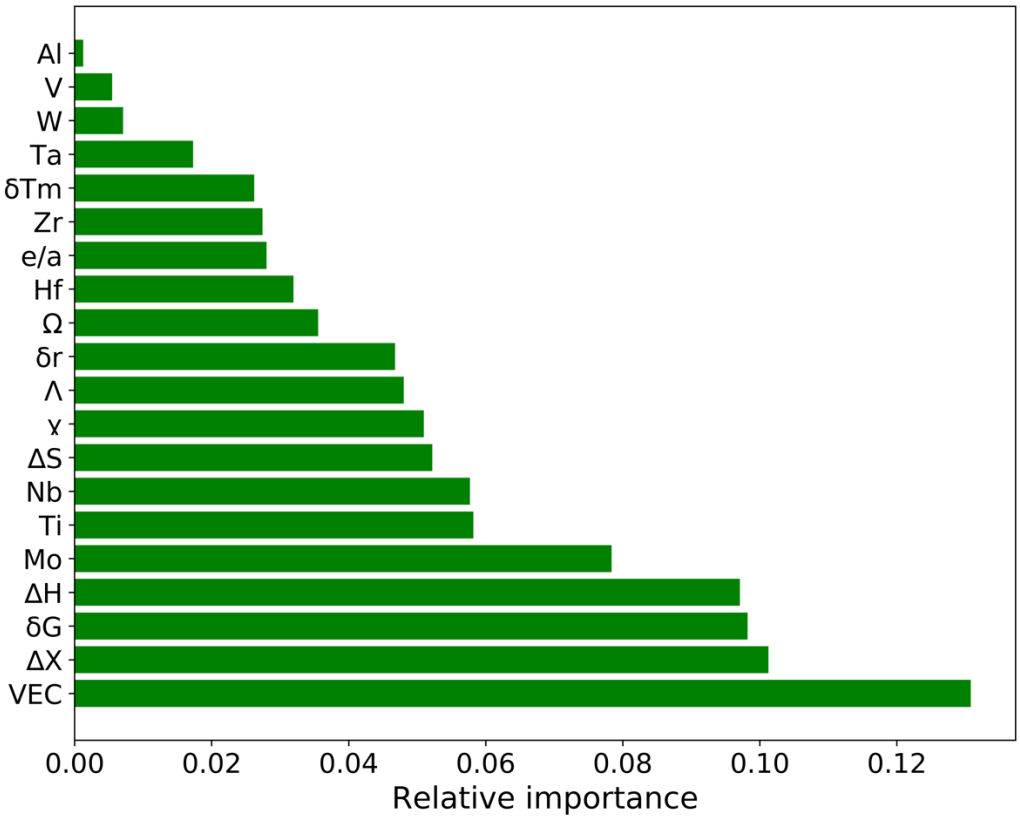

Figure 2-3: The relative feature importance for input variables based on their performance in reducing error while splitting a node when constructing trees in RF method.

The total number of empirical features to be included in ML algorithms leading to minimum prediction error was investigated iteratively using recursive feature elimination

method based on RF algorithm [132]. Figure 2-4 presents the evolution of RMSE of the RF method on the test dataset by adding one feature at a time on top of each other iteratively and greedily selecting the best performing feature and eliminating the rest at each iteration. In Figure 2-4, the green circle which represents the subset consisting of three features; namely, ΔH, VEC, and δG, was selected although the minimum RMSE was obtained with the addition of the 5th empirical feature. As demonstrated in Figure 2-4, there is no substantial improvement in RMSE after the addition of the fourth feature. Therefore, the final set of features included the chemical compositions and the three empirical features, namely ΔH, VEC, and δG in order for the models not to lose their generalization capabilities. Shaikh et al. reported that increase in VEC enhances average bond strength leading to a higher elastic modulus, as well as melting temperature and density of HEAs, which indicates a positive correlation between VEC and elastic modulus [137]. Furthermore, VEC was also utilized as a parameter for designing ductile HEAs where it was reduced through controlled alloying [33,138]. Furthermore, it was reported that ΔH_{ij}^{mix} is related to bond strength, and as the number of bonds with high ΔH_{ij}^{mix}rises, elastic modulus increases [139]. Therefore, ΔH represents the information inherently at the atomistic level. Finally, Figure 4 indicates that utilizing composition with empirical features associated with HEAs in ML framework augments the learning process by extracting more information from the training dataset [90].

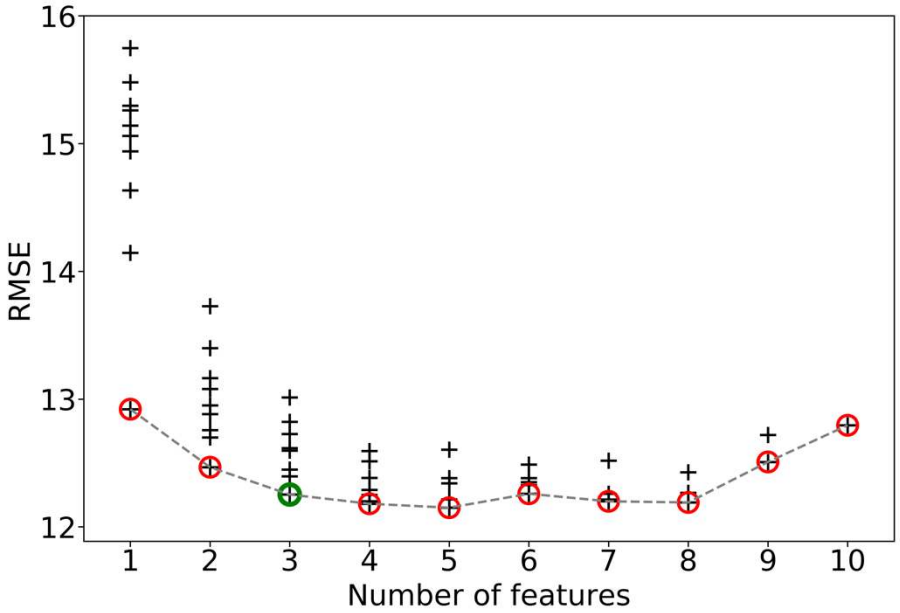

Figure 2-4: Variation of RMSE with the addition of each empirical parameter on composition utilizing recursive feature elimination method using RF model. The red circles show the best performing subset of features resulting in the least prediction error for each combination of features. The green circle indicates the selected subset of features as a result of feature elimination which are ΔH, VEC, and δG.

2.3.3 Machine learning results

Various ML algorithms were trained using composition and three selected features and employed to predict novel biomedical HEAs with low elastic modulus. RMSE and MAE values on the test dataset for seven different ML methods, namely LIN, KNN, RF, SVR.L, SVR.P, SVR.R, and MLFFNN, are presented in Figure 2-5. Accordingly, the worst performing ML algorithm was LIN as compared to others. The underlying reason of this relatively poor performance might be the fact that the relationship between input and output variables is highly complex and nonlinear so that a linear model is not an appropriate choice to extract information from the dataset. On the other hand, RF, SVR.L, SVR.P, SVR.R, and MLFFNN showed almost the same performance in terms of their prediction capabilities, although RMSE and MAE values for RF were the highest among the five models. Ultimately, the best performing model was the KNN method with the least RMSE and MAE values. Comparing to Figure 2-1, Figure 2-5 reveals that utilization of the three chosen feature in addition to composition in the training of the ML algorithms results in an improvement of more than 50% in RMSE for RF, SVR.L, SVR.P, SVR.R,

and KNN models. This shows the importance of using additional empirical features along with compositions in accelerating the optimization process of new HEAs.

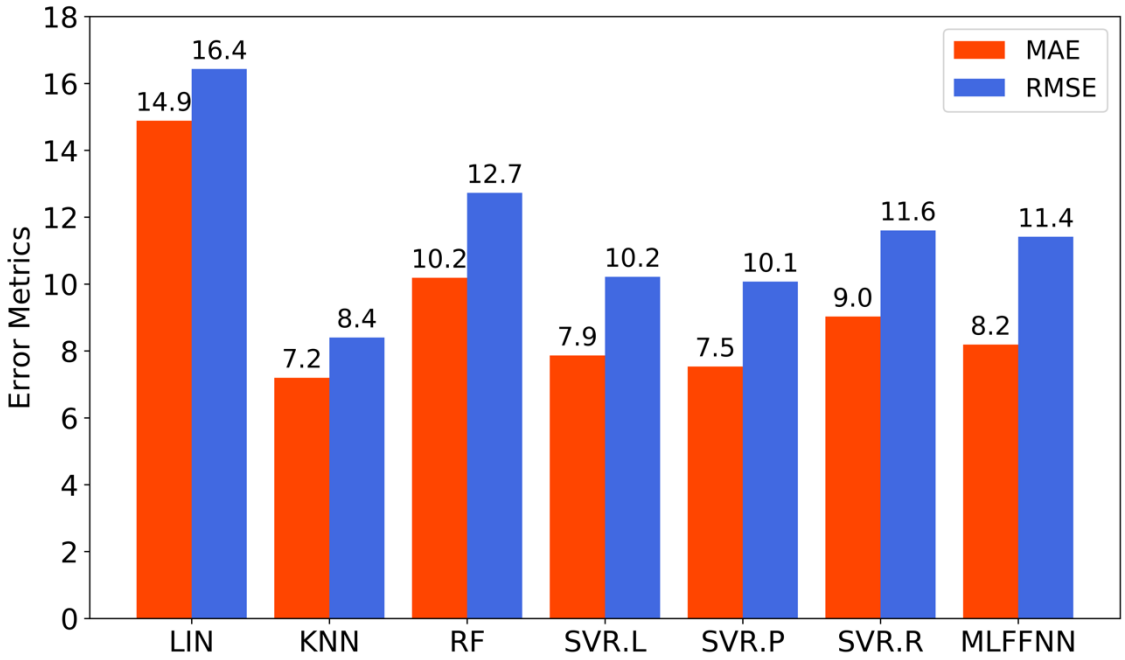

Figure 2-5: RMSE and MAE on test errors for various ML algorithms employed in this study by using composition and three selected features as input.

The KNN algorithm can be utilized for both classification and regression problems. This method utilizes the training dataset as a guide to make new predictions based on resemblance of datapoints. Predictions for datapoints are made considering how close they are to a number of datapoints in training dataset using a distance metric. In the KNN method, the k parameter defines the number of the closest neighbors in training dataset when a new datapoint is predicted. When k is equal to 1, the method is highly flexible closely following any pattern in training dataset. As the k parameter increases, the model grows to be less flexible with some generalization capabilities. The algorithm can assign weights equally or using a distance function between neighbors and datapoints. In this study, the hyperparameters implemented for training the KNN algorithm were as follows: *k*, *weights*, and *metric* which were set as '2', 'uniform', and 'manhattan', respectively. The variation in RMSE value with respect to growing k hyperparameter and the true vs predicted elastic modulus values for the datapoints in the test dataset are demonstrated in Figure 2-6a. Figure 2-6b, c, and d illustrate the actual and predicted elastic moduli values for KNN, SVR.P, and SVR.L, respectively. Figure 2-6b clearly demonstrates that the

prediction performance of KNN algorithm was better as opposed to other SVR.P, and SVR.L. Next, the synthetic dataset with more than 500000 different compositions with Ti, Ta, Hf, Nb, and Zr contents ranging from 5 to 35 at% with 0.1% intervals, complying with the widely accepted HEA definition, was imported to the KNN model to make new predictions in the aforementioned composition space for each datapoint. The two optimum compositions having the smallest elastic modulus predictions, namely 72.5 and 72.9 GPa, were selected for validation experiments. The compositions, the predicted elastic moduli and the empirical features for selected alloys are presented in Table 2-2.

Table 2-2: Composition and empirical feature values for selected alloys.

Selected alloys	**Bio-HEA1**	**Bio-HEA2**
Ti (at%)	23	28
Ta (at%)	10	10
Hf (at%)	27	30
Nb (at%)	12	14
Zr (at%)	28	18
VEC	4.22	4.24
δr (%)	4.81	4.73
$\Delta\chi$	0.12	0.12
ΔH (kJ/mol)	2.03	2.08
ΔS (kJ/mol*K)	12.74	12.74
Ω	14.94	14.67
Λ	0.55	0.57
ɣ	1.63	1.69
e/a	1.47	1.46
δG (%)	22.52	21.20
δT_m (%)	17.11	17.33
Predicted Elastic Modulus	72.5	72.9

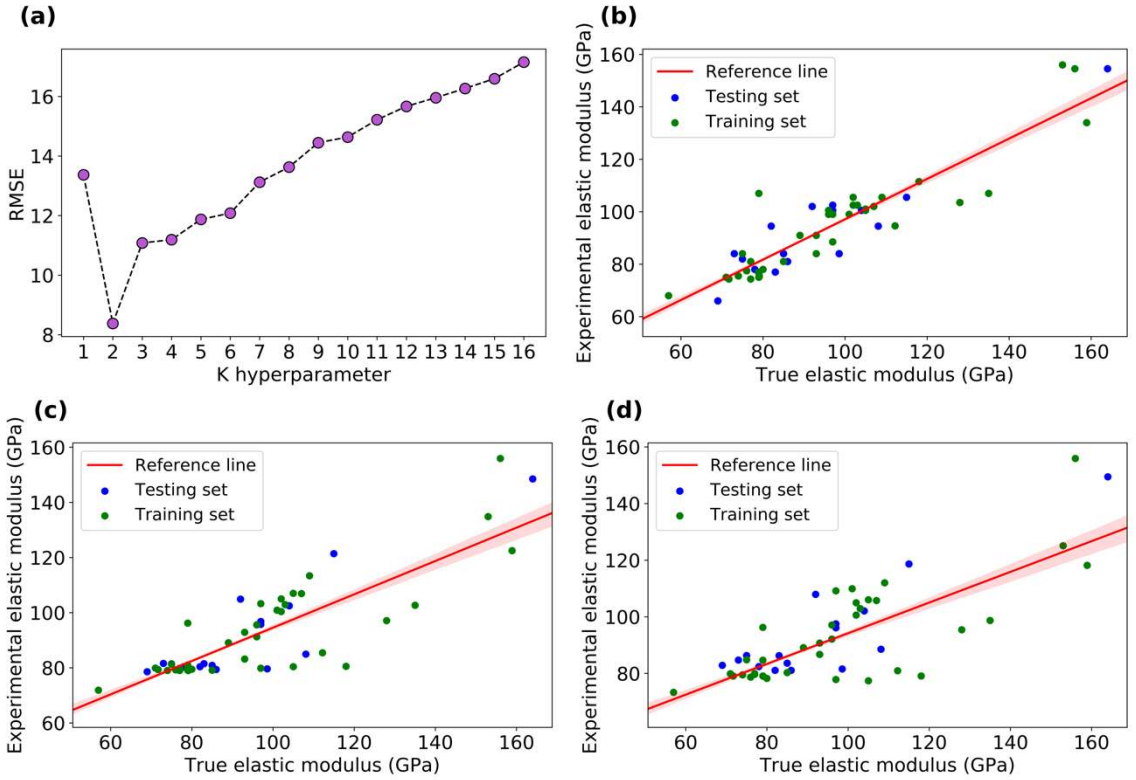

Figure 2-6: (a) the change in RMSE with increasing k hyperparameter for KNN algorithm, performance of (b) KNN (c) SVR.P (d) SVR.L algorithms in predicting elastic modulus values as a function of measured elastic moduli of the alloys available in the testing set.

2.4 Validation experiments

The predicted compositions for Bio-HEA1 and Bio-HEA2 tabulated in Table 2-2 were prepared by vacuum arc melting under a Ti-gettered argon atmosphere on a water-cooled copper crucible. Raw metals of Ti, Ta, Hf, Nb with purity of 99.9% and Zr with purity of 99.2% were used in the production of Bio-HEA1 and Bio-HEA2. The produced alloys had a button shape with an intended mass of 20 grams. To increase mixing and ensure chemical homogeneity, the button-shaped samples were flipped and re-melted at least 5 times. The button-shaped samples were then cut with wire electro-discharge machining (EDM) to obtain ten slices of each alloy with 2 mm thickness. Two slices from each sample were heat-treated at 1000 °C for 12 hours and then cooled down to room temperature in the furnace (the heat-treated samples were named as Bio-HEA1-HT and Bio-HEA2-HT in the remainder of the paper). To eliminate any contamination and surface residue, the samples were ground using SiC emery papers and polished with a 0.30 µm alumina slurry to obtain a mirror-like surface. To clean the bulk-samples,

samples were immersed in and rinsed with de-ionized water. Then, the samples were exposed to immersion experiments in simulated body fluid (SBF) for 28 days. The samples were kept in SBF, whose composition is presented in Table 2-3 [140], at a constant temperature of 37 °C throughout the whole experiment in an electronically controlled water bath. All HEA samples were held in separate sealed tubes, where the volume of the solution in each tube was calculated in accord with the G31 ASTM standards [141]. To measure the amount of mass gain or loss, the weights of the samples were recorded before and after immersion experiments.

Table 2-3: Composition for preparing 1000 mL of SBF solution utilized in the immersion experiments.

Solution	**Reagents**	**Amount (g/L)**
SBF	NaCl	8.036
	NaHCO3	0.352
	KCl	0.225
	$K_2HPO4 \cdot 3H_2O$	0.23
	$MgCl_2 \cdot 6H_2O$	0.311
	1 M HCl	40 mL
	$CaCl_2 \cdot 2H_2O$	0.293
	Na_2SO_4	0.072
	TRIS	6.063
	1 M HCl	2 mL

The phase structures present in the samples were determined by X-ray diffraction (XRD) method utilizing a Bruker D2 Advanced X-ray diffractometer with Cu-Kα radiation source operated at 30 kV and 10mA. The acquisition angle ranged from 20° to 100° with incremental steps of 0.02°, and the incidence angle was 5°. A scanning electron microscope (SEM), which was equipped with an energy-dispersive X-ray spectroscopy detector (EDX), was employed to investigate the surface morphology of the samples. A depth-sensing nanoindentation device (Agilent G200) equipped with a Berkovich diamond indenter tip was employed to obtain the elastic modulus values of the samples from the loading and unloading curves by using the Oliver-Pharr method [142]. During

the indentation experiments, a maximum load of 400 mN was applied at a constant loading rate of 40 mN/s in addition to a holding time of 5 s at maximum load. For each sample, a total of 15 measurements were performed and the average values were presented with respective standard deviation. Furthermore, in order to quantify the quantity of ions released into the SBF solution during the immersion experiments, the remaining fluids of each static immersion tests were inspected employing an inductively coupled plasma-mass spectrometer (ICP-MS, Agilent 7700x).

2.5 Discussion of the results

The XRD patterns of the untested Bio-HEA1, Bio-HEA1-HT, Bio-HEA2, and Bio-HEA2-HT are presented in Figure 2-7. The results point out that all HEAs other than the Bio-HEA1-HT sample exhibited a single BCC phase with the lattice parameters determined as 3.463 Å, 3.439 Å and 3.424 Å for Bio-HEA1, Bio-HEA2 and Bio-HEA2-HT, respectively, where the peak values were estimated utilizing Bragg's Law. The lattice parameter for the BCC phase of the Bio-HEA1-HT, on the other hand, was determined to be 3.452 Å. Although HEAs have a single crystal structure in as-cast condition, phase transformation and precipitation of intermetallic phases can be observed following heat treatment [143,144]. For example, TiTaHfNbZr HEAs were shown to possess a single BCC crystal structure in as-cast condition and after heat treatments between 1000 °C and 1400 °C for one hour [145]. Yet, they can produce different intermetallic phases (BCC Ta-Nb and/or HCP Zr-Hf rich precipitates) when heat treated between 500 °C and 900 °C for one hour in addition to the main BCC matrix [145]. In Figure 2-7c, the star sign (☆) corresponds to $Hf_{0.43}Zr_{0.57}$ compound with hexagonal close-packed (HCP) structure detected in the matrix of the Bio-HEA1-HT [146]. Even though Bio-HEA1-HT and Bio-HEA2-HT were exposed to the same heat treatment, the Bio-HEA2-HT features a single BCC structure, which is attributed to its smaller lattice parameter as opposed to other Bio HEAs. Specifically, this might prevent Zr atoms, having the largest atomic radius in comparison to the other four elements, from diffusing within the matrix. In other words, the thermodynamic stability of Bio-HEA2-HT might be a consequence of high local lattice distortions resulting in sluggish atom diffusion [6].

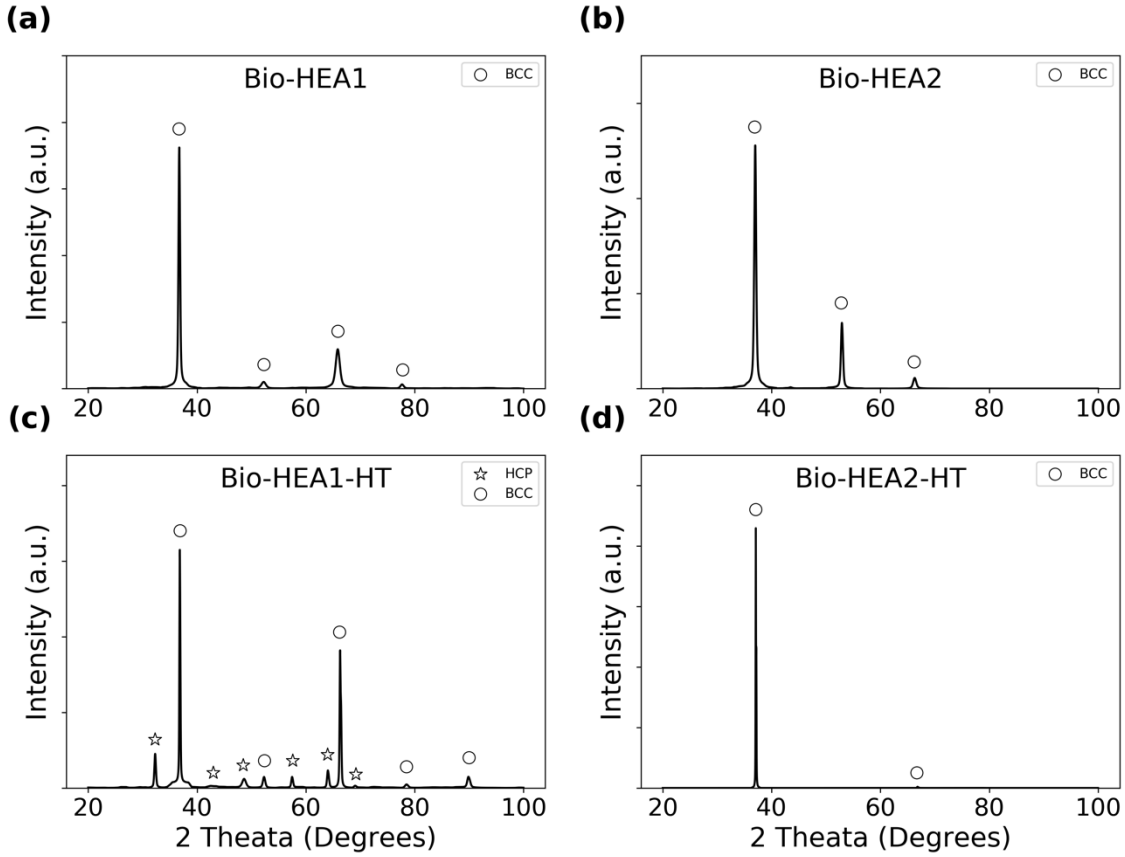

Figure 2-7: XRD results for (a) Bio-HEA1, (b) Bio-HEA2, (c) Bio-HEA1-HT, and (d) Bio-HEA2-HT. The star sign (☆) corresponds to $Hf_{0.43}Zr_{0.57}$ compound with hexagonal close-packed (HCP) structure [146].

The surface morphology of Bio-HEA1 (Figure 2-8) and Bio-HEA2 (Figure 2-9) were investigated by SEM prior to and following the static immersion experiments, revealing that both samples had a smooth surface prior to immersion experiments. However, following the immersion experiments, as opposed to Bio-HEA2, Bio-HEA1 had a highly corroded surface after immersion in SBF for 28 days, and a more locally intense corrosion behavior was prevalent as evidenced by the darker regions in Figure 2-8f. This; however, may lead to severe pitting corrosion for long term applications. On the other hand, based on Figures 2-9b, d, and f which show a few visible locally corroded regions, it can be argued that Bio-HEA2 is more resistant to SBF environment as compared to Bio-HEA1. The reason for Bio-HEA1 to have more visible locally intense corrosion behavior than Bio-HEA2 might be its higher Zr content exceeding the solid solubility level of Zr with other elements in the matrix [147]. It was reported that corrosion resistance of compositionally complex alloys first increased and then decreased with the increasing Zr

content [147,148]. The main cause of the decrease of corrosion resistance is that the excessive Zr enriching on the surface facilitates pitting corrosion, which, in turn, accelerates the corrosion [147]. In Figures 2-10 a and c, and Figures 2-10 b and d, the SEM micrographs of Bio-HEA1-HT and Bio-HEA2-HT samples prior to and following immersion in SBF for 28 days are presented, respectively. For both Bio-HEA1-HT and Bio-HEA2-HT, SBF environment was more deteriorating than it was for Bio-HEA1 and Bio-HEA2. This could be attributed to the formation of new phases in Bio-HEA1-HT and Bio-HEA2-HT as a result of heat treatment, which brings about a decrease in corrosion resistance due to chemical homogeneity in the matrix [149]. However, a detailed investigation of the passive oxide layer formation on the surface of the samples should be conducted by X-ray photoelectron spectroscopy (XPS) analysis to gain further insight and information about the surface layer properties of the samples immersed in SBF for 28 days.

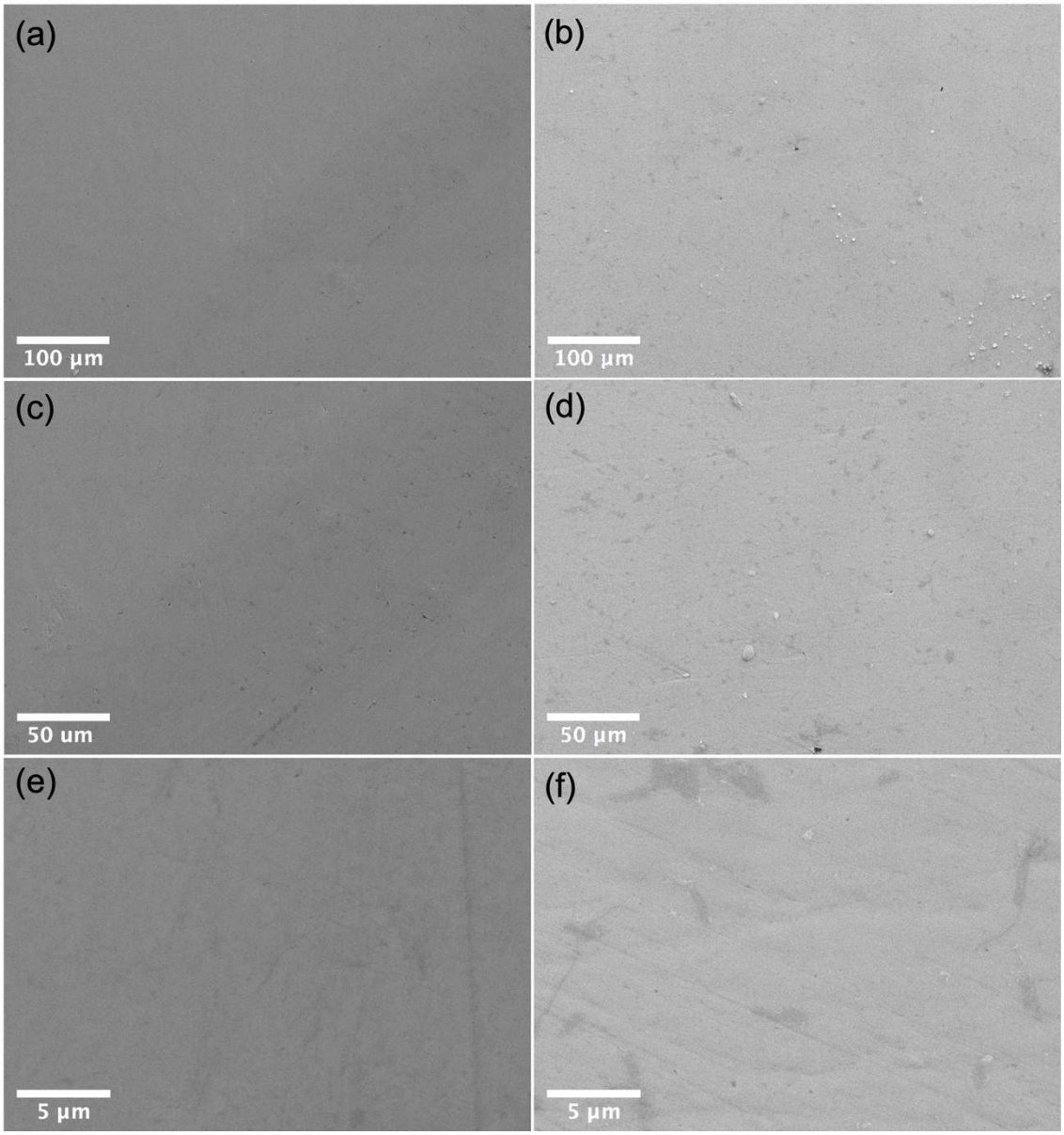

Figure 2-8: SEM images of the as-cast Bio-HEA1. (a), (c), (e): prior to static immersion, with different magnifications showing a smooth surface. (b), (d), (f): the micrographs for Bio-HEA1 following 28 days immersion in SBF demonstrating the locally intense corrosion behavior (darker regions).

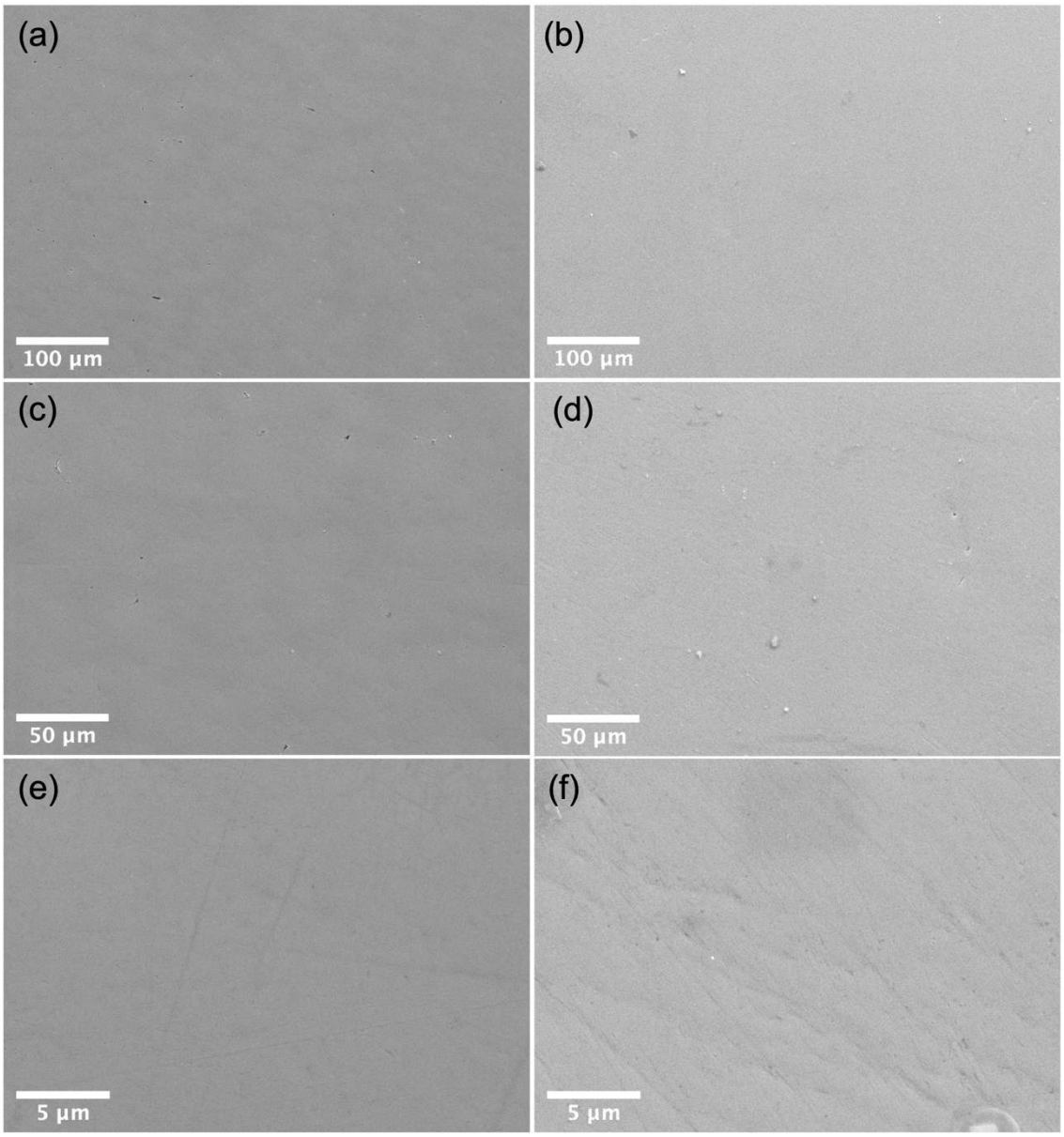

Figure 2-9: SEM micrographs of the as-cast Bio-HEA2. (a), (c), (e): prior to immersion experiments, and (b), (d), (f): following immersion in SBF for 28 days with different magnifications.

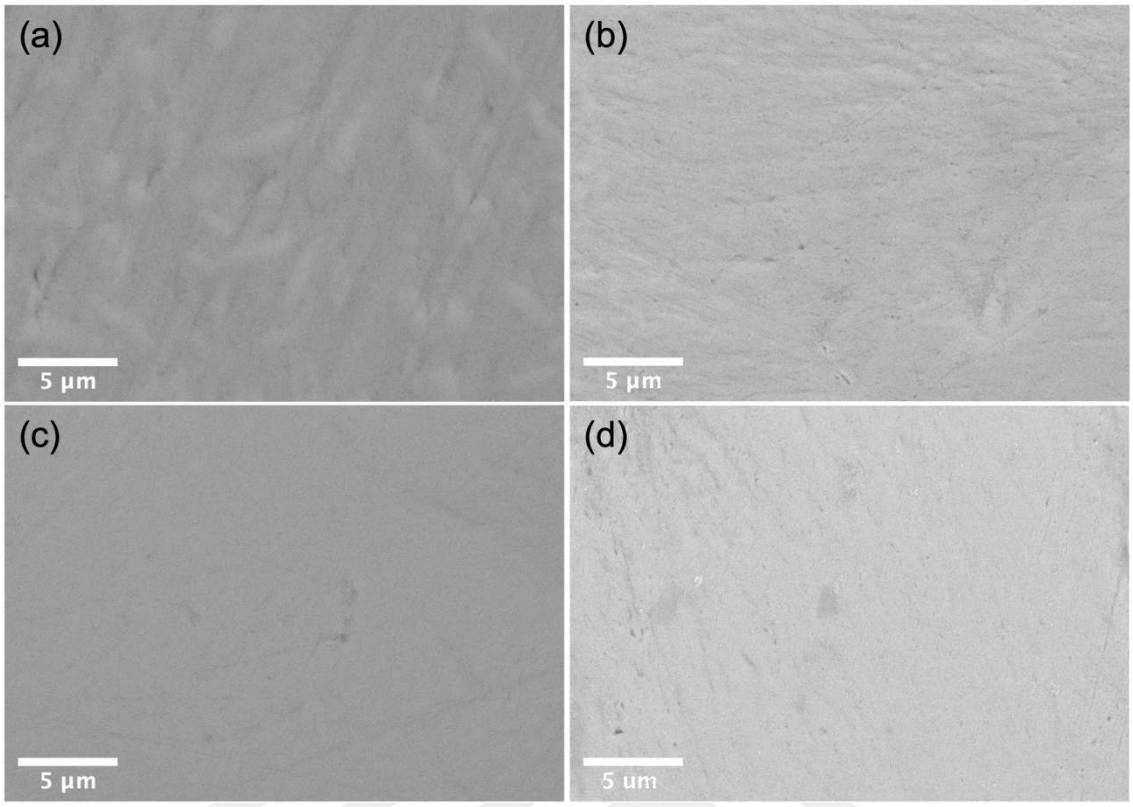

Figure 2-10: SEM images of Bio-HEA1-HT (a) before immersion and (b) after immersion in SBF for 28 days. SEM micrographs of Bio-HEA2-HT (c) before immersion and (d) after immersion in SBF for 28 days.

As tabulated in Table 2-4, the quantity of total ion release from Bio-HEA1, Bio-HEA1-HT, Bio-HEA2, and Bio-HEA2-HT were very similar to each other following 28 days of immersion in SBF. However, it should be noted that only Ti ion concentrations released from all samples were demonstrated in Table 2-4 because of insignificant concentration of other elements. The main advantage of the HEAs studied in this work is that they do not include any toxic elements such as Al, Cr or V [150]. Especially Ti is not a poisonous metallic element, and when present in human body in large doses, it passes through the intestines without being absorbed [150]. Based on a study conducted on the effect of Ti on osteoblast in rat calvaria cultures, it was reported that a Ti concentration higher than 10 ppm inhibits cell proliferation [151]. The concentrations of Ti ion released following a 28-day immersion in SBF from Bio-HEA1, Bio-HEA1-HT, Bio-HEA2, and Bio-HEA2-HT, as shown in Table 2-4, are well below the amounts that a human body can take in a day which is 800 µg/day [150].

Table 2-4: Total ion concentrations released from Bio-HEA1, Bio-HEA1-HT, Bio-HEA2, and Bio-HEA2-HT following 28 days of immersion in SBF. Note that only the amount of Ti released into SBF is presented due to insignificant concentrations of Ta, Hf, Nb, and Zr.

Alloys	Quantity of total ion release in SBF (ppb)
Bio-HEA1	176.48 ± 2.50
Bio-HEA1-HT	183.45 ± 4.46
Bio-HEA2	181.20 ± 3.46
Bio-HEA2-HT	183.27 ± 3.36

Nanoindentation was utilized to measure the elastic modulus of each sample. Nanoindentation is a practical tool to assess the mechanical properties of materials. However, hardness and elastic modulus measurements calculated from loading and unloading curves by using the Oliver-Pharr method may be overestimated because of ignorance of pile-ups forming around the indent [152]. Therefore, extra pile-up area forming around the indenter were considered in this study to adjust the elastic modulus values measured by the nanoindentation experiments taking the pile-up effect into account. The method for correcting the measured elastic modulus values were described by Saha and Nix [153]. The method assumes that pile-ups form arcs around the edge of the indenter and the additional area due to pile-up effect is calculated utilizing geometry of the indenter [153]. In Table 2-5, the predicted and experimental elastic moduli values (after geometric correction) are presented for Bio-HEA1, Bio-HEA1-HT, Bio-HEA2 and Bio-HEA2-HT samples. The lowest elastic modulus measured is 83.5 ± 2.9 GPa, which belongs to Bio-HEA1 whose predicted elastic modulus was 72.46 GPa. The predicted and experimental elastic modulus results of Bio-HEA1 and Bio-HEA2 are close to each other verifying the effectiveness of ML methods employed in this work. The reason that the elastic modulus is higher for Bio-HEA1-HT and Bio-HEA2-HT as opposed to Bio-HEA1 and Bio-HEA2, respectively, is associated with the change in size, total volume and distribution of intermetallic phases in the matrix upon heat treatment, leading to alterations in the mechanical properties. For instance, the microhardness of CoCrFeNiMnVx HEAs were shown to first increase and then decrease with increasing and then decreasing amount of harder intermetallic phases concomitant with annealing temperature [154].

Table 2-5: Predicted and experimental elastic modulus values of Bio-HEA1, Bio-HEA1-HT, Bio-HEA2, and Bio-HEA2-HT obtained from nanoindentation experiments (Since heat-treatment parameters were not included in the dataset, predictions were made for compositions in as-cast condition).

	Predicted Elastic Modulus (GPa)	Experimental Elastic Modulus (GPa)
Bio-HEA1	72.5	83.5 ± 2.9
Bio-HEA1-HT	-	88.2 ± 2.6
Bio-HEA2	72.9	87.4 ± 2.2
Bio-HEA2-HT	-	90.5 ± 3.4

2.6 Conclusion

The results of the work presented herein demonstrate the capability of machine learning (ML) methods trained with a limited amount of experimental data to predict novel biomedical high entropy alloy (HEA) compositions with optimum elastic moduli for utility in orthopedic applications. During the training process of the ML algorithms, estimated empirical features were utilized in addition to compositions of the alloys in the dataset, revealing the importance of using intrinsic properties of the elements to increase the soundness of the model. The ML algorithm utilized in this work predicted two novel biomedical HEA compositions, namely $Ti_{23}Ta_{10}Hf_{27}Nb_{12}Zr_{28}$ and $Ti_{28}Ta_{10}Hf_{30}Nb_{14}Zr_{18}$, with elastic moduli of 83.5 ± 2.9 GPa and 87.4 ± 2.2 GPa, respectively. The predicted elastic moduli of the new alloys were validated by nano-indentation experiments once the materials were manufactured. The samples were then subjected to immersion experiments in simulated body fluid (SBF) for 28 days to assess their biocompatibility and ion release behavior. The predicted alloys were also annealed in 1000 °C for 12 hours to examine the changes in microstructure, and corresponding elastic moduli and ion release behavior. As a result, it was shown that heat treatment brought about formation of additional phases in the microstructure which showed that these alloys with a single BCC phase in the as-cast state can be used without heat treatment. Overall, the findings presented herein demonstrate that these materials have promising properties to be utilized as implant

materials, but further investigation of their biocompatibility is necessary prior to their utility as orthopedic implant materials.

Chapter 3:

OPTIMIZING MECHANICAL PROPERTIES AND AG ION RELEASE RATE OF SILVER COATINGS DEPOSITED ON TI-BASED HIGH ENTROPY ALLOYS

3.1 Introduction

The reliable and long-term utility of metallic implant materials necessitates some fundamental characteristics such as excellent biocompatibility, high corrosion resistance, good mechanical properties, and high wear resistance [155]. For instance, Ti and its alloys, such as Ti6Al4V, have been in commercial use for decades as they possess a satisfactory combination of mechanical and physical properties. However, in spite of being one of the most popular metallic implant materials, Ti6Al4V still possesses some disadvantages, such as low wear resistance and a high coefficient of friction, which result in debris formation around the surrounding tissue, leading to inflammatory reactions [156,157]. Furthermore, the release of toxic V and Al ions to the adjacent tissue has been associated with health problems, including peripheral neuropathy, osteomalacia, and Alzheimer's disease, undermining its utility in long-term biomedical applications [78,156,158,159]. A conventional alternative to Ti6Al4V alloy for biomedical applications is 316L stainless steel which has good wear and mechanical properties. Nevertheless, it exhibits insufficient antibacterial properties [160], leading to an increased chance of infection while in use [161,162]. Recently, high entropy alloys (HEAs) comprising non-toxic elements such as Hf, Nb, Ta, Ti, and Zr have come into consideration to replace the Ti6Al4V alloy in biomedical applications, mainly owing to their superior mechanical properties, excellent biocompatibility, and corrosion resistance [83–86], in addition to exhibiting better mechanical compatibility with human bone [85]. However, they also suffer from the lack of antibacterial defense mechanisms against the bacterial biofilms forming between the implant and surrounding tissue during and following implantation [163,164].

Infections due to the adhesion of bacteria to the implant surface are one of the major complications that can come about during surgery, affecting the long-term performance

of the implants, which may sometimes lead to a complete failure of the implant [165]. In order to reduce the risk of infection around the implants, antibiotics are generally utilized. However, the distribution of the antibiotics to the surroundings of the infected hard tissue is ineffective owing to reduced blood circulation around the damaged tissue. To increase the effectiveness of antibiotics, it is required to attain higher concentration levels which may be harmful and induce toxicity [166]. Additionally, side effects regarding excessive and misuse of antibiotics include increased resistance of bacteria against antibiotics, which, in turn, impairs the efficacy of antibiotics [167,168]. Hence, it is of utmost importance to redesign the implant surface, which can be achieved by applying a coating onto the implant surface to release antibacterial agents [169,170] and serve as an effective barrier against toxic ion release from the bulk material into the bloodstream [171,172].

For this purpose, metallic ions, such as Cu^{2+} [173], Zn^{2+} [174], and Ag^{+} [161,164,175,176], have been studied as antibacterial agents. Silver ions are mostly preferred owing to their capability to annihilate antibiotic-resistant bacteria [162] and the low levels of local toxicity they cause to human cells [161,177,178] without deteriorating the metabolic activity and proliferation of osteoblast and epithelial cells [161]. For instance, it was shown that increased silver ion release resulted in a decrease in the E.coli and Staphylococcus aureus adhesion to the surface of the Ag-TiO_2 coatings [179]. In another study, a 13-fold reduction in the number of colonies formed by P. aeruginosa and total inactivation of E.coli and Staphylococcus bacteria after 48 hours due to Ag^{+} was reported [164]. The mechanism by which Ag^{+} hinders bacterial activity has not been clearly identified yet, but there are three possible mechanisms proposed in the literature [164,180–184], all of which indicate that the rate and amount of the Ag ion release constitute the key factors determining the effectiveness of the antibacterial defense mechanism of the coatings. In fact, if released in high amounts, Ag ions can be toxic to human cells. Thus, controlling the Ag ion release is essential for obtaining a coating with good antimicrobial properties and improved cytocompatibility.

The antimicrobial properties of pure silver or silver-containing coatings depend on the amount of silver present in the system, which changes with the size, morphology, and surface-to-volume ratio of nanoparticles (NPs) and silver clusters [185]. The crystal structures and mechanical properties of the coatings, as well as NPs and agglomerates forming on the coatings, are factors which can be modified by controlling the sputtering parameters. Additional parameters dictating the final properties are the substrate itself, as

well as the temperature and pressure in the deposition chamber. Specifically, owing to its impact on the mobility and interactions of deposited atoms on the surface, the substrate temperature was shown to result in variations in the microstructure and growth dynamics of the coatings. In general, an increase in crystallite size and a decrease in compressive internal macro stresses leading to lower hardness values were observed with rising substrate temperature due to enhanced atom mobility on the surface [186]. The type or the ratio of different gases fed into the deposition chamber is another parameter influencing the final properties of the coatings. For example, an increase in N_2/Ar fraction can reduce the film's crystallinity, leading to a transformation of the microstructure to an amorphous phase [186,187]. Furthermore, it was demonstrated that the microstructure, thermal stresses, and residual stresses in metallic films were affected by the substrate on which they were deposited, namely by their crystal structure, surface roughness, and thermal expansion coefficients [188]. The working pressure during sputtering is another important parameter, such that it can change the residual stresses from compressive to tensile when increased [189]. Overall, the number of involved deposition parameters increases the difficulty of controlling the final coating properties. Yet, optimizing the deposition parameters also provides an opportunity to tailor the microstructure and mechanical properties of the coatings.

The current work aims at applying Ag coatings on two novel biomedical HEAs, recently designed by the authors implementing machine learning techniques, to be utilized in orthopedic implants [71], namely the $Ti_{23}Ta_{10}Hf_{27}Nb_{12}Zr_{28}$ (HEA-Ti23) and $Ti_{28}Ta_{10}Hf_{30}Nb_{14}Zr_{18}$ (HEA-Ti28) alloys, in order to increase their antibacterial properties by tuning the amount of ion release from the Ag films sputtered on them. The focus was placed on the evolution of microstructure, texture, mechanical properties, and ion release behavior of Ag thin films sputtered under different conditions. As a result, both deposition time and Ar flow rate were demonstrated to significantly affect the texture evolution, mechanical properties, and ion release behavior of the thin Ag films coated on Ti-based novel HEAs. For instance, a decrease in Ar flow rate resulted in the evolution of small silver NPs, leading to a severe increase in ion release, suggesting that ion release can be altered by controlling texture and NP size together via deposition time and Ar flow rate. The experimental outcomes of the work presented herein demonstrate that there exists a complicated relationship between the final properties of the antibacterial Ag films and the RF magnetron sputtering process parameters, yet also indicate that the delicate

balance among these parameters could also be beneficial in enhancing the biocompatibility of the Ti-based HEAs to be utilized in orthopedic implants.

3.2 Materials and methods

The silver coatings were deposited on the HEA-Ti23 and HEA-Ti28 substrates, fabricated by arc melting of Ti, Ta, Hf, and Nb with 99.9 % purity and Zr with a purity of 99.2% under a Ti-gettered argon atmosphere on a water-cooled copper crucible. To ensure chemical homogeneity, the button-shaped samples were flipped and re-melted at least five times. Then, the samples were cut with wire electro-discharge machining (EDM) to obtain samples with 2 mm thickness. For all the experiments, the surfaces of substrates were prepared using a series of SiC emery papers up to 2500 grit size, followed by polishing with 0.25 μm alumina suspension to acquire a mirror-like surface. The polished substrates were then ultrasonically cleaned with acetone, ethanol, and de-ionized water for fifteen minutes, respectively.

Table 3-1: Sample names, varied deposition parameters, and thickness measurements based on a cross-sectional analysis of the films deposited on silicon wafers.

Sample	Substrate	Ar flow rate (sccm)	Deposition time (min)	Thickness (nm)
H23-20min	HEA-Ti23	10	20	350
H28-20min	HEA-Ti28			
H23-40min	HEA-Ti23	10	40	720
H28-40min	HEA-Ti28			
H23-60min	HEA-Ti23	10	60	1025
H28-60min	HEA-Ti28			
H23-5sccm	HEA-Ti23	5	40	890
H28-5sccm	HEA-Ti28			
H23-20sccm	HEA-Ti23	20	40	380
H28-20sccm	HEA-Ti28			

Ag coatings with thicknesses ranging from 300 to 1025 nm were deposited on HEA-Ti23, HEA-Ti28, and silicon wafers by radio frequency magnetron sputtering (Nanovak

NVTS-400) operating in Ar atmosphere without substrate bias. The silicon wafer was chosen for cross-sectional investigations because of its convenient preparation procedure. The system was maintained at a base pressure of $1x10^{-7}$ Torr by a turbo pump backed by a mechanical pump, and the power was set to 100 W for all experiments. Five different sets of coating samples deposited on HEA-Ti23 and HEA-Ti28 were produced by varying deposition time and Ar flow rate. To eliminate any impurities residing on the Ag target (99.9 % purity) surface, the target was pre-sputtered for 15 minutes, where the substrates were isolated from plasma by a movable shutter. The experimental details related to varied sputtering parameters (Ar flow rate and deposition time) and measured thickness values from the cross-sectional analysis are summarized in Table 3-1. For H23-20min, H23-40min, H23-60min, H28-20min, H28-40min, and H28-60min samples, the Ar flow rate was kept constant, and the deposition time was varied. On the other hand, the deposition time was maintained, and the Ar flow rate was altered for H23-5sccm, H23-20sccm, H28-5sccm, and H28-20sccm samples.

The phase structure of each substrate was characterized by the X-ray diffraction (XRD) method utilizing a Bruker D2 Advanced X-ray diffractometer with Cu-Kα radiation, where the acquisition angle ranged from 20° to 80° with incremental steps of 0.02°. For identifying the crystal structure of the coatings, the XRD device was set to grazing incidence X-ray diffraction (GIXRD) mode, and the data were collected at an incidence angle of 1°. The surface morphology and cross-section investigations of the coatings were performed using a field emission scanning electron microscope (FESEM, Zeiss, Ultra Plus). To examine the surface topography of the substrates and the coatings, an atomic force microscope (AFM) operated in tapping mode was employed.

To investigate the amount of ion release from the coatings, the coated substrates were exposed to immersion experiments in SBF (Table 3-2) for 28 days in an electronically controlled water bath at a constant temperature of 37 °C. Since only one surface of each thin substrate was coated, the uncoated surfaces of the substrates were covered with epoxy in order to prevent contact of the uncoated HEA surfaces with the SBF medium. All coated samples were held in separate sealed tubes, where the necessary amount of SBF volume for each sample in each tube was calculated in accord with the G31 ASTM standards [141]. Following 28 days of immersion in SBF, the quantity of ions released into the SBF medium was investigated employing an inductively coupled plasma-mass spectrometer (ICP-MS, Agilent 7700x).

Table 3-2: Composition for preparing 1000 mL of SBF solution utilized in the static immersion experiments.

Solution	**Reagents**	**Amount (g/L)**
SBF	NaCl	8.036
	NaHCO3	0.352
	KCl	0.225
	$K_2HPO4 \cdot 3H_2O$	0.23
	$MgCl_2 \cdot 6H_2O$	0.311
	1 M HCl	40 mL
	$CaCl_2 \cdot 2H_2O$	0.293
	Na_2SO_4	0.072
	TRIS	6.063
	1 M HCl	2 mL

A depth-sensing nanoindentation device (Agilent G200) equipped with a Berkovich diamond indenter tip was employed to acquire elastic modulus (E) and hardness values (H) of the coated samples from the loading and unloading curves by using the Oliver-Pharr method. The effect of substrate on the E and H measurements of coatings was avoided by controlling the indenter's penetration depth at 1/10th of coatings with different thicknesses during the measurements. Fifteen measurements were performed on each coating, and the average values for E and H were reported along with the standard deviation.

3.3 Results and discussion

The substrates HEA-Ti23 and HEA-Ti28 used in this study have a body-centered cubic (BCC) crystal structure with lattice parameters of 3.486 Å and 3.458 Å, respectively [71]. In Figure 3-1, the GIXRD results of the coatings deposited on HEA-Ti23 and HEA-Ti28 are presented. It can be inferred that the coatings revealed a face-centered cubic (FCC) crystal structure with a (111) preferred orientation regardless of the varying deposition time and gas flow rate, which is consistent with the literature [190,191]. The (111) plane is the most close-packed orientation in FCC crystal structure favored in terms

of thermodynamics [192,193]. To elaborate, as small islands start to form, random texture begins to emerge on the substrate surface at the onset of deposition, and these islands join as they grow, which is called island coalescence. Coarsening during coalescence is the determinant phenomenon in the evolution of preferred orientation in thin films. Namely, the surface adatoms diffusing by surface diffusion and incoming atoms deposited near grain boundaries have a high tendency to diffuse towards the grains with orientation providing a more stable and low potential energy sites [194,195]. Therefore, the (111) oriented grains grow faster in thin films with FCC crystal structure, consuming other grains with high diffusivity planes [194].

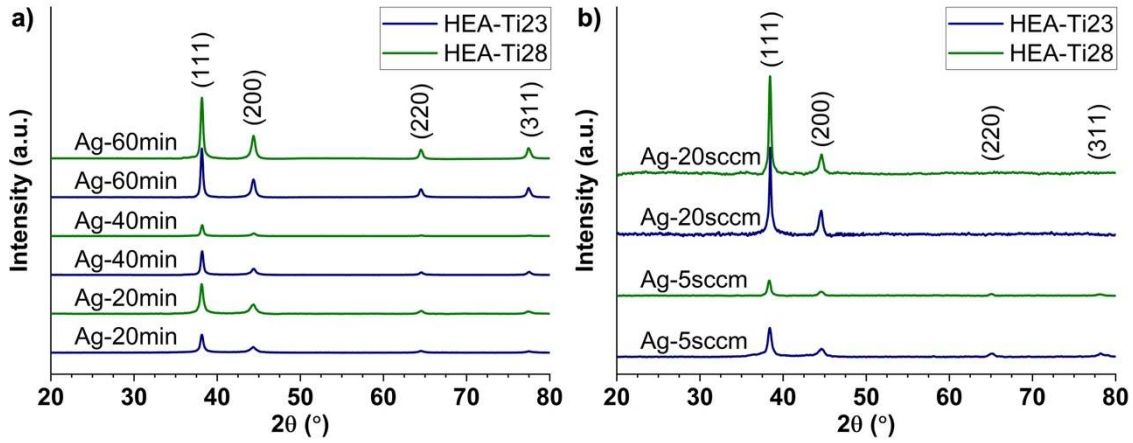

Figure 3-1: GIXRD patterns of the coatings deposited on HEA-Ti23 and HEA-Ti28 substrates: (a) the case of constant Ar flow rate of 10 sccm with varied deposition time of 20, 40, and 60 min, and (b) for constant deposition time of 40 min with Ar flow rates of 5, and 20 sccm.

The crystallite sizes for the coatings were calculated based on the full width at half maximum (FWHM) of the (111) peaks of each coating utilizing the Scherrer equation:

$$D = \frac{K\lambda}{\beta cos\theta} \tag{3.1}$$

where D is the crystallite size, K is a dimensionless shape factor which is taken as 0.9 following a general assumption that the crystals are spherical in shape [193], λ is the wavelength of Cu Kα1, β is the FWHM, and θ is the Bragg angle of the (111) peak. The estimated crystallite size of the coatings with varying deposition time and Ar flow rate is

shown in Figure 3-2a and b, respectively. Based on Figure 3-2, it can be concluded that the crystallite size increases concomitant with the deposition time and gas flow rate. The impact of gas flow rate on the crystallite size can be better understood by keeping the thickness constant: when the H23-20min and H28-20min (350 nm) samples are compared to H23-20sccm and H28-20sccm (380 nm) samples because their thicknesses are similar (Table 3-1), it becomes evident that an increase in the Ar flow rate resulted in enlarged crystallites. Similarly, a decrease in the Ar flow rate resulted in a shrinkage in crystallite size owing to defects created on the surface due to incoming atoms with high kinetic energy, hence increasing the number of available potential nucleation sites leading to a decrease in crystallite size [192]. It should be noted that, as the gas flow rate decreased, the deposition rate increased, and therefore the thickness of the coatings deposited in 5 sccm was larger than the ones deposited in 20 sccm (Table 3-1). Accordingly, one can deduce that as the Ar flow rate decreases (i.e., the thickness increases), the crystallite size decreases. However, this trend observed in Figure 3-2b contradicts the one demonstrated in Figure 3-2a and what was previously observed for Ag thin films [193] and NbMoTaW refractory HEA thin films [194]: the increment in thickness brings about an enlargement in the crystallite size. To elaborate more, the results obtained in the aforementioned studies [193,194] employed a constant gas flow rate in the experiments and showed that crystallite growth occurred as the film thickness increased. On the contrary, our results demonstrated that, although the film thickness increased (due to a higher deposition rate obtained at a low Ar flow rate), a decrease in the crystallite size was observed owing to the high magnitude of coalescence stress caused by adatoms with high momentum [196,197] and an increasing number of available potential nucleation sites brought about by the decrease in gas flow rate [192]. Thus, this contradiction implies that thickness and Ar flow rate are both significant parameters affecting crystallite size and can be used interchangeably to adjust the crystallite size.

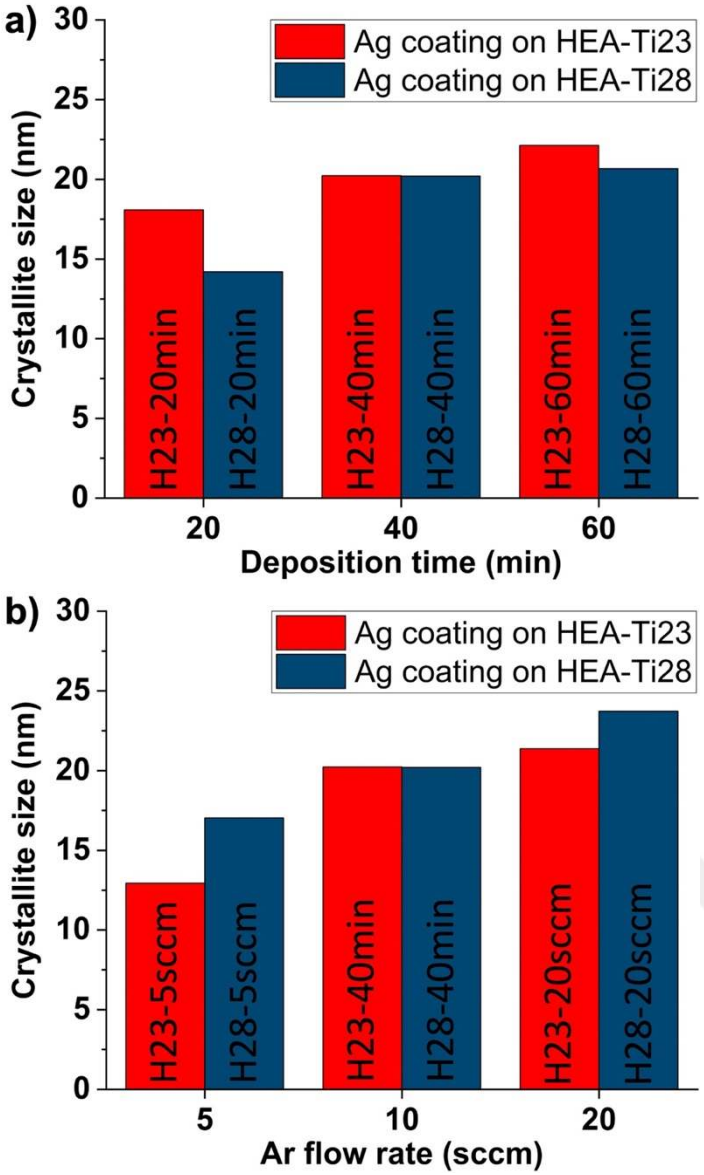

Figure 3-2: Crystallite sizes of the coatings deposited on HEA-Ti23 and HEA-Ti28 substrates: (a) the case of constant Ar flow rate of 10 sccm with varied deposition time of 20, 40, and 60 min, and (b) for constant deposition time of 40 min with Ar flow rates of 5, 10, and 20 sccm.

Figure 3-3 demonstrates the ratio of the two prevalent crystal orientations detected on the coating surfaces (Figure 3-1), namely the ratio of the (200) orientation to (111) orientation (I_{200}/I_{111}), for the silver coatings deposited on HEA-Ti23 and HEA-Ti28 substrates. In fact, there are two active mechanisms competing during thin film deposition to minimize the system's total energy: surface and strain energy minimization [198]. The (111) plane minimizes the surface energy, whereas the (200) plane minimizes the strain energy of the system during deposition for FCC crystal structure [199,200]. As

demonstrated in Figure 3-3a, the I_{200}/I_{111} ratio first decreases, then increments as the deposition time increases from 20 min to 60 min while the Ar flow rate is kept constant at 10 sccm. It appears that 40 min is the transition point (i.e., the critical thickness, 720 nm) where a transformation from minimization of surface energy to minimization of strain energy took place as deposition time increased further. In other words, below a critical thickness level of 720 nm, the surface energy minimization is the dominating mechanism; on the other hand, the leading active mechanism is the strain energy minimization above the critical thickness. The strong (111) texture in H23-40min and H28-40min samples also indicates that the intrinsic stresses at 720 nm thickness level are very high (Figure 3-3a). This increase in the intrinsic stresses is brought about by the high density of (111) orientation restricting the mobility/diffusion of the surface atoms due to incoming high energetic atoms, which, in turn, hinders the release of accumulated strain energy [198]. Once the deposition time increased from 40 to 60 min, the I200/I111 ratio surged, indicating that the intensity of the initially less prominent (200) orientation became higher, leading to relaxation of the accumulated strain energy [198]. This observed trend for Ag films investigated in this study contradicts the previous observation on TiN coatings deposited by RF magnetron sputtering, where the governing mechanism for texture evolution was the minimization of the strain energy with increasing thin film thickness [201]. This difference stems from Ag being a soft, low melting material and having low activation energy for self-diffusion, which can accommodate the accumulating intrinsic stresses (relaxation by stress-driven diffusion) during deposition, as opposed to a harder and higher melting point material such as TiN [189].

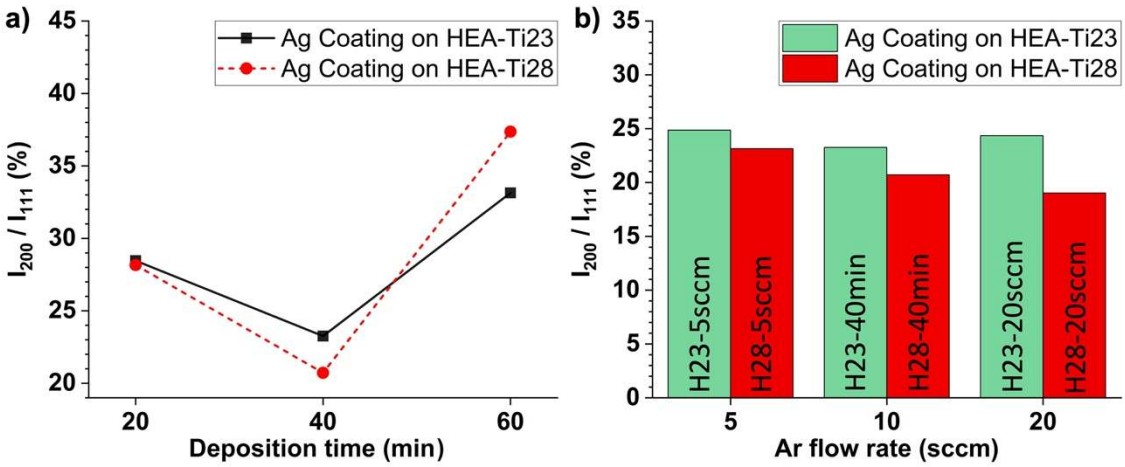

Figure 3-3: The ratio of the (200) orientation to (111) orientation of the coatings deposited on HEA-Ti23 and HEA-Ti28 substrates: (a) the case of constant Ar flow rate of 10 sccm with varied deposition time of 20, 40, and 60 min, and (b) for constant deposition time of 40 min with Ar flow rates of 5, 10, and 20 sccm.

To elucidate the effect of changing Ar flow rate on the I_{200}/I_{111} ratio, a comparison among the samples should be made based on the data presented in Figure 3-3b. When H23-20sccm and H28-20sccm are compared to H23-20min and H28-20min, respectively, the effect of increasing Ar flow rate from 10 to 20 sccm can be made below the critical thickness (720 nm), where surface energy minimization is the dominating mechanism for the coatings. Below the critical thickness (720 nm), the values of I_{200}/I_{111} ratio for H23-20min and H28-20min (350 nm) decreased compared to H23-20sccm and H28-20sccm (380 nm), respectively. The main conclusion that can be drawn from these results is that the surface energy minimization becomes stronger for the coatings deposited at a higher Ar flow rate as opposed to the coatings sputtered at a lower Ar flow rate with the same thickness values below critical thickness (720 nm). The reason why the surface energy minimization became more dominant for the coatings (Figure 3-4c) deposited in a high Ar flow rate might also be explained by the higher surface roughness obtained for these coatings as opposed to the coatings (Figure 3-4b) deposited at a lower Ar flow rate. When H23-5sccm and H28-5sccm (890 nm) are compared to H23-60min and H28-60min (1025 nm) above critical thickness where strain energy minimization is the dominating mechanism, the values of I_{200}/I_{111} ratio for H23-5sccm and H28-5sccm decreased compared to H23-60min and H28-60min, respectively. This suggests that the portion of strain energy minimization in the total system energy minimization dropped for the coatings deposited in 5 sccm Ar flow rate as opposed to the coatings deposited in 10 sccm

above critical thickness (720 nm). These findings imply that high Ar flow rate results in an increase in the portion of surface energy minimization below critical thickness and strain energy minimization above critical thickness in the total energy minimization process.

Table 3-3: The (111) peak positions and the ratio of (220) orientation intensity to that of the (111) orientation calculated from GIXRD data (* indicates that no (220) peaks were observed).

Sample	**(111) peak position (2θ)**	**I_{220} / I_{111} (%)**
H23-20min	38.14	8.53
H28-20min	38.13	8.90
H23-40min	38.19	10.31
H28-40min	38.23	5.51
H23-60min	38.14	14.66
H28-60min	38.12	15.24
H23-5sccm	38.15	12.98
H28-5sccm	38.25	8.47
H23-20sccm	38.44	*
H28-20sccm	38.41	*

To understand the microstructure and texture evolution in more detail, the angular positions of (111) peaks are compared, as presented in Table 3-3. At a constant Ar flow rate, when the deposition time increased from 20 to 60 min, a shift to higher 2θ angles and then lower angles was observed for the (111) orientation. The increase in the (111) peak 2θ angle when the deposition time was 40 min points out that the compressive intrinsic stresses were accumulating within the coatings. This also complies with the increase in the intensity of the (111) peak as compared to that of the (200) peak, as demonstrated in Figure 3-3a, suggesting an increase in strain energy in the system while surface energy minimization was in progress prior to reaching the critical thickness. When the Ar flow rate increased from 5 to 20 sccm, a shift to very high angles, i.e., extreme lattice shrinkage, was observed: from 38.15 to 38.44 and from 38.25 to 38.41 for the thin films deposited on HEA-Ti23 and HEA-Ti28, respectively. Lower angles observed for

(111) peak positions for the coatings deposited at the Ar flow rate of 5 sccm as compared to the ones deposited in 20 sccm can be explained by the atomic peening effect due to high energy atoms coming from the target [189,202,203]. Specifically, these incoming atoms with high momentum bombard the surface of the growing films enhancing the diffusion and displacement of the surface atoms towards deeper positions, leading to vacancy filling and planes providing lower potential energy sites. On the other hand, higher angles detected for (111) peak position for the coatings deposited at the Ar flow rate of 20 sccm can be attributed to the incorporation of Ar atoms into the lattice due to a high number of Ar present in the plasma, resulting in high compressive stresses [192].

The ratio of the (220) orientation intensity to that of the (111) orientation is demonstrated in Table 3-3, which can be used as an indicator of the yielding state of the grains. In particular, when all the grains in FCC metallic coatings reach their yield stress, another strain energy minimizing orientation, namely the (220) orientation possessing lower yield strength as compared to (111) and (200) orientations, might start to evolve [195]. Furthermore, the (220) orientation has a higher surface energy as compared to the (111) and (200) orientations. In the current experiments, a steady increase in the I_{220}/I_{111} ratio for H23-20min, H23-40min, and H23-60min, i.e., while the deposition time or the thickness was increasing, the (220) indexed orientation was evolving to compensate for the grains yielding. Accordingly, in the coatings deposited on the HEA-Ti23 substrate, the growth of grains with the (220) orientation served as an active mechanism of strain energy release. However, as for the coatings on the HEA-Ti28, first, a decrease and then a steep rise in the I_{220}/I_{111} ratio was observed. The sharp increase from 5.51 to 15.24 % in the I_{220}/I_{111} ratio as deposition time increased from 40 to 60 min for the films deposited on the HEA-Ti28 substrates illustrates that the crystallites reached their elastic limits, which favored further/faster growth/evolution of the (220) oriented grains. These results suggest that the strain energy release behavior of the coatings deposited in the same conditions on different substrates might differ. Additionally, based on the results tabulated in Table 3-3, (220) peaks were not observed for the coatings sputtered at the Ar flow rate of 20 sccm. This is associated with the thicknesses of H23-20sccm and H28-20sccm samples being below the critical limit, where surface energy minimization is the dominating factor.

The 3D AFM images of the uncoated HEA-Ti23 substrate and the H23-5sccm, H23-20sccm, H23-20min, H23-40min, and H23-60min samples obtained from an area of 10

µm x 10 µm are provided in Figure 3-4. The mean surface roughness value, Ra, was measured as 3.45 nm, 8.36 nm, 9.48 nm, 5.95 nm, 7.33 nm, and 12.9 nm for the HEA-Ti23 substrate, and the H23-5sccm, H23-20sccm, H23-20min, H23-40min and H23-60min samples, respectively. While the substrate exhibited a smooth surface morphology, the coatings revealed a relatively rougher surface appearance. Based on Figure 3-4d, e, and f, it can be inferred that with increasing deposition time and thickness, the average roughness of the coating increases [193,204]. Furthermore, a comparison of the surface morphologies of the H23-20sccm (Figure 3-4c) and the H23-20min (Figure 3-4d) samples, where the latter sample experienced an Ar flow rate of 10 sccm, reveals that the increasing Ar flow rate results in an increase in surface roughness.

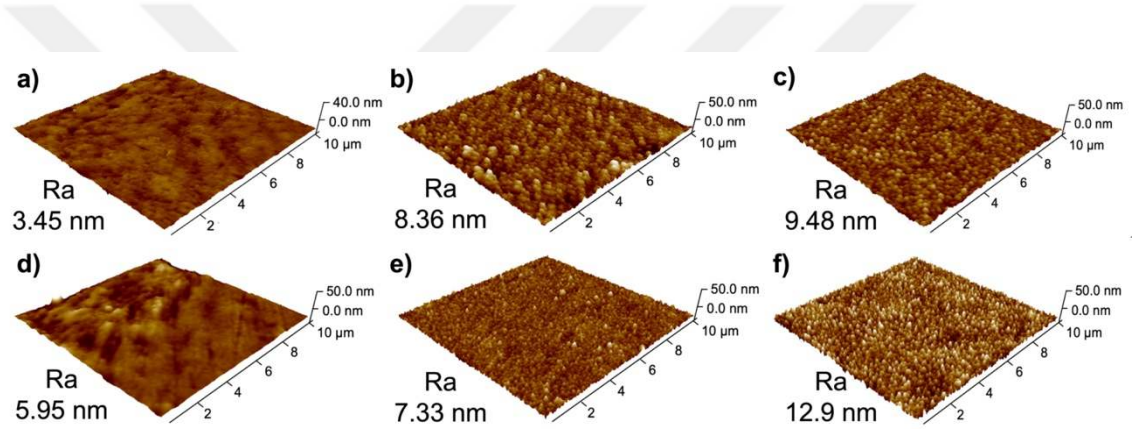

Figure 3-4: AFM images and surface roughness values of the (a) uncoated HEA-Ti23 substrate, and the (b) H23-5sccm, (c) H23-20sccm, (d) H23-20min, (e) H23-40min, and (f) H23-60min samples.

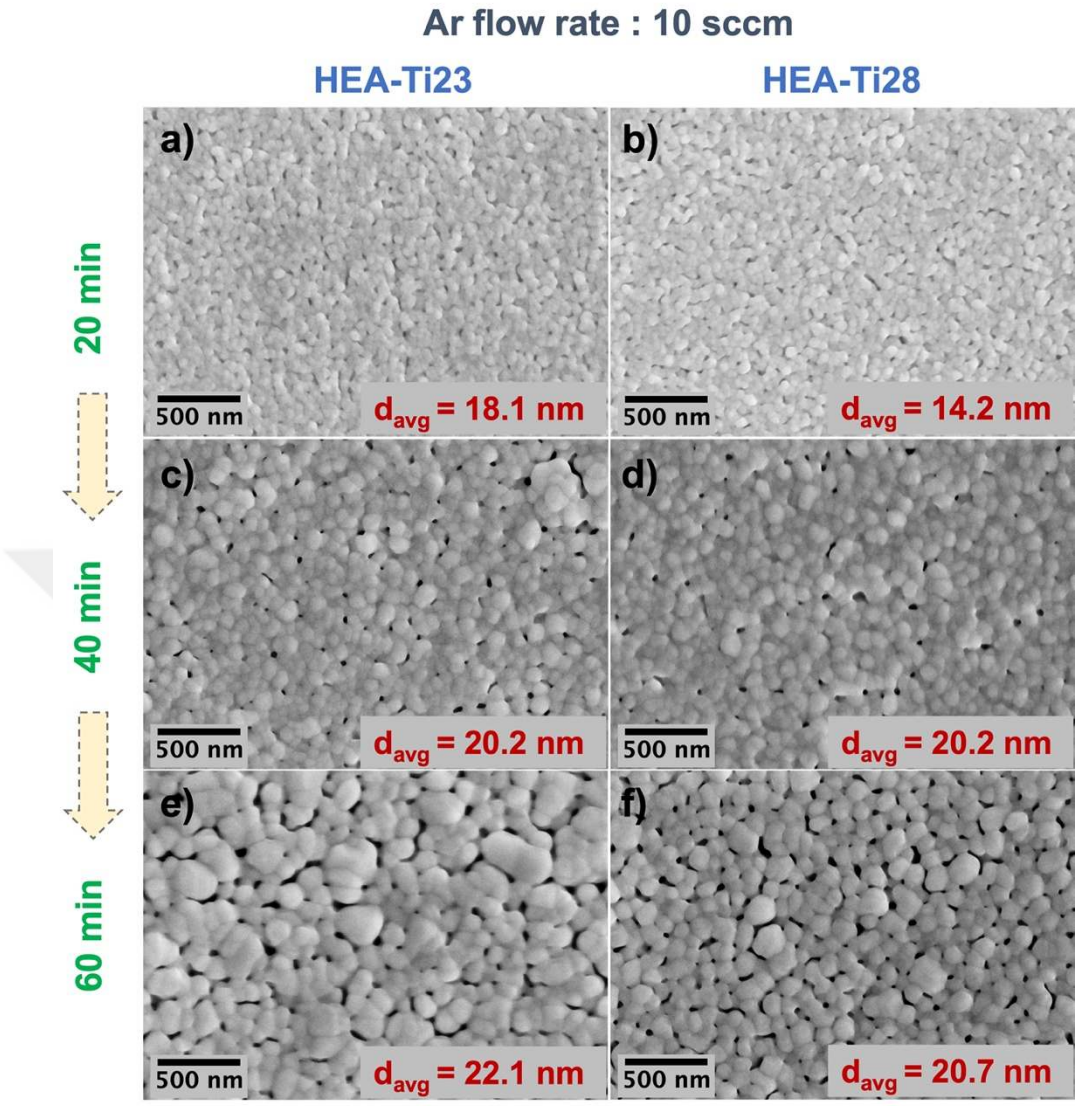

Figure 3-5: FESEM micrographs of (a) H23-20min, (b) H28-20min, (c) H23-40min, (d) H28-40min, (e) H23-60min, and (f) H28-60min samples prior to immersion experiments (davg represents the crystallite size).

The FESEM micrographs of the H23-20min, H23-40min, H23-60min, H28-20min, H28-40min, and H28-60min samples prior to static immersion in SBF are presented in Figure 3-5. Accordingly, the average grain size increased concomitant with deposition time in coatings sputtered on both HEA-Ti23 and HEA-Ti28. For the HEA-Ti23 sample, the grain growth becomes significant when the deposition time increases from 40 min (Figure 5c) to 60 min (Figure 5e), where the strain energy minimization is the governing mechanism promoting strain energy relief by grain growth [200]. This notable grain growth in the HEA-Ti23 samples when the deposition time increased from 40 min to 60 min was not present in the HEA-Ti28 samples (Figure 5d and f), where only a slight

increase of the average grain size was evident. This indicates the existence of another strain relief mechanism for the coatings deposited on HEA-Ti28 substrates, which can be associated with the lattice mismatch between the substrates and coatings, i.e., texture and the surface energies of the substrates [205]. Specifically, when the deposition time raised from 40 min to 60 min, new grains on the surface started to evolve in a different orientation [200], possibly the (220) orientation, which would explain the abrupt increase in the I_{220}/I_{111} ratio reported in Table 3-3. Consequently, the new grains forming along the (220) orientation might be the primary mechanism to release the strain energy for the coatings deposited on the HEA-Ti28 substrates.

The influence of the Ar flow rate during deposition on the grain size was not as dramatic as that of the deposition time: the FESEM images of H23-5sccm, H23-20sccm, H28-5sccm, and H28-20sccm samples are demonstrated in Figure 3-6, and comparing the 5 sccm samples (Figure 6a and b) and 20 sccm samples (Figure 6c and d) with the 10 sccm samples (Figure 3-5), the 5 sccm samples (Figure 6a and b) reveal a more visible NP formation on the surface prior to static immersion experiments. Similarly, when Ar pressure decreased to low sccm values, very small and fine Ag NPs were also observed on the surface for TiN coatings. The formation of fine NPs when the Ar flow rate decreased can be explained by the high number of preferential nucleation sites generated and lower adatom mobility resulting from the re-sputtering of adatoms due to increased high-energy atom bombardment [192]. These findings suggest that for either pure Ag or Ag-doped biomedical coatings, very fine Ag NPs can be acquired based on the application area since the toxicity of these Ag NPs is size-dependent [206].

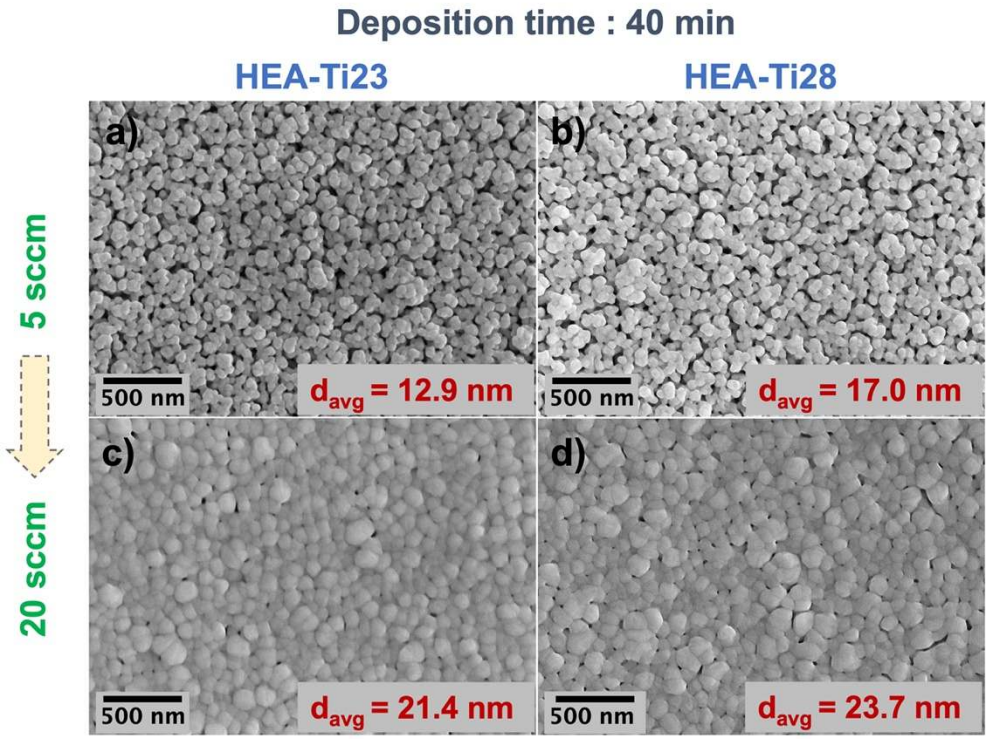

Figure 3-6: FESEM micrographs of (a) H23-5sccm, (b) H28-5sccm, (c) H23-20sccm, and (d) H28-20sccm samples prior to immersion experiments (davg represents the crystallite size).

It is well known that in silver thin films, there exist regions of inhomogeneous nucleation that are energetically favorable, such that a mass flow of silver atoms diffuses into these relaxed areas due to the chemical potential gradient generated between the relieved zone and the surrounding region [207]. As a result of this mass flow of silver atoms, a cluster or agglomerate of silver atoms is created on the surface. The agglomeration detected on H23-20min, H23-40min, H23-60min, H28-20min, H28-40min, and H28-60min samples can be seen in FESEM micrographs presented in Figure 3-7. The general trend observed herein is the growth in size and number of these agglomerates as the thickness of the coatings increased. The agglomerate formation, which is a stress relief mechanism [208], is an indication of the existence of intrinsic compressive stresses [209], as well as the thermal stresses due to the difference in the thermal expansion coefficient between various substrates and metal films deposited on them [208,210]. The governing mechanism of the formation of these Ag agglomerates is the diffusion creep process involving volume and grain boundary diffusion [207]. A closer inspection of Figure 3-7e and f indicates that the size of Ag agglomerates on coatings deposited on HEA-Ti28 were much larger than the ones forming on the HEA-

Ti23 substrate. The larger grains in the films sputtered on the HEA-Ti23 substrates might be preventing the diffusion of these Ag particles to the energetically favored zones as the grain boundary diffusion is one of the controlling agglomeration mechanisms [210]. Furthermore, the existence of a smaller and larger number of agglomerates on the H23-60min samples might be an indication of more uniform relaxation of strain and thermal stresses, as opposed to the coatings on HEA-Ti28. The larger and severely localized Ag agglomerates developing on the coatings deposited on HEA-Ti28 (H28-60min sample) might be triggered by the higher rate/percentage of increase in the ratio of I_{200}/I_{111} (Figure 3-3a). In other words, stronger gradients, along with higher rate of strain relaxation, might be developing through these localized zones, which may be the driving force for increased surface diffusion of silver atoms found in the H28-60min sample [207,211]. As opposed to the deposition time, the role of the Ar flow rate is relatively indistinguishable, such that a small amount of decrease in both size and number of the agglomerates can be seen with increasing Ar flow rate (Figure 3-8).

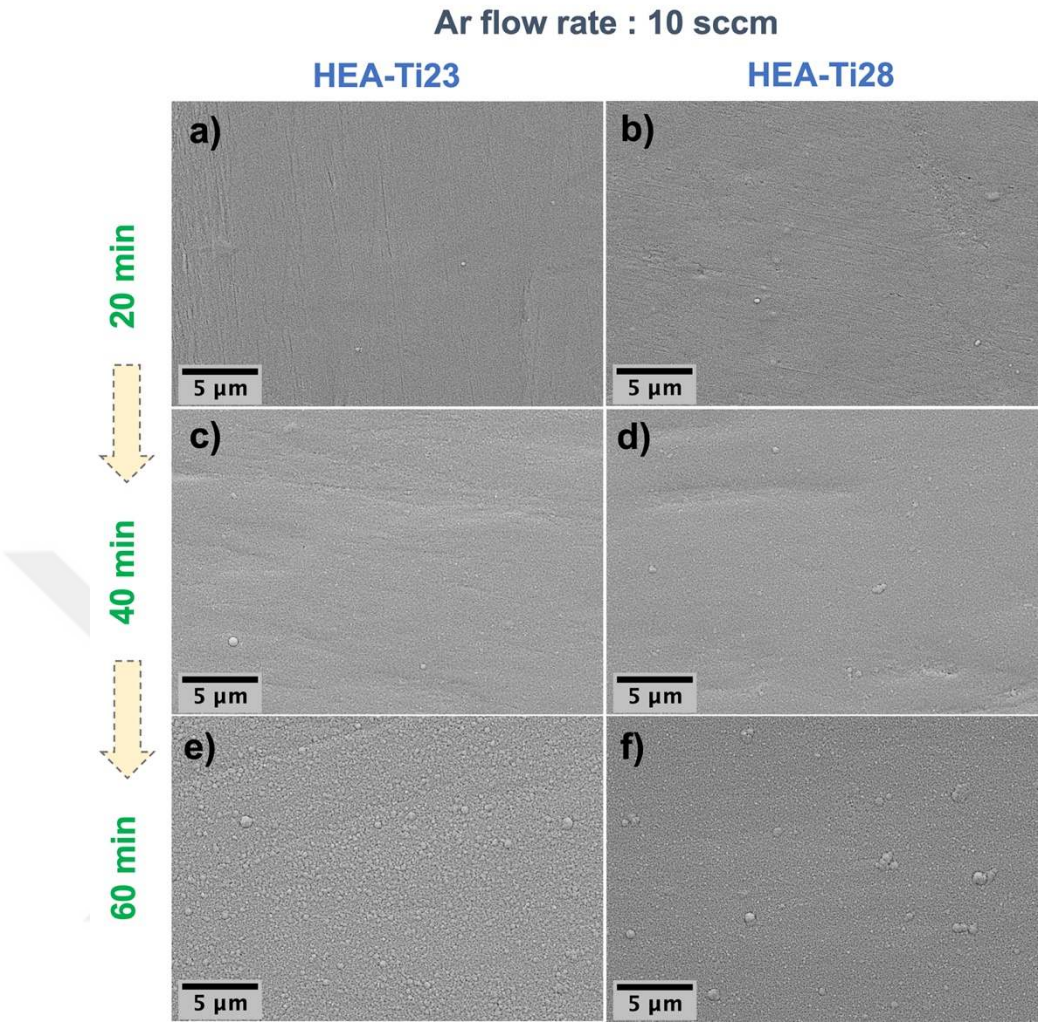

Figure 3-7: FESEM micrographs of agglomerate formation observed on the surface of (a) H23-20min, (b) H28-20min, (c) H23-40min, (d) H28-40min, (e) H23-60min, and (f) H28-60min samples prior to immersion experiments.

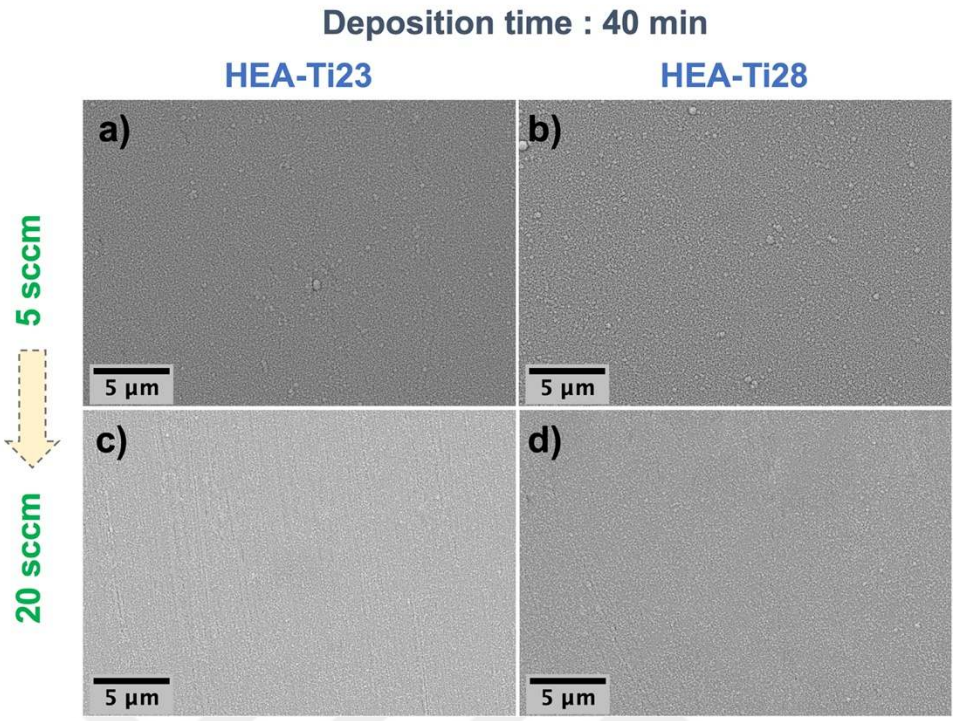

Figure 3-8: FESEM micrographs of agglomerate formation observed on the surface of (a) H23-5sccm, (b) H28-5sccm, (c) H23-20sccm, and (d) H28-20sccm samples prior to immersion experiments.

The nanoindentation results for the coatings are shown in Table 3-4. At a constant Ar flow rate of 10 sccm, both E and H values increased and then decreased with increasing deposition time for the coatings deposited on HEA-Ti23 substrates. The trend seen in the E and H values is similar to the one observed in Figure 3-3a. Specifically, the highest E and H values are associated with a strong (111) texture present in the H23-40min sample. On the other hand, the coatings deposited on the HEA-Ti28 substrates revealed a different trend for H values: as thickness increased, the H values decreased. This might be due to larger agglomerates developed on the surface of coatings deposited on HEA-Ti28, which act as stress concentration points and facilitate crack initiation in edges under applied mechanical stress [169,186,212]. The sudden drop in the H value when the deposition time increased from 20 to 40 min (H28-20min and H28-40min samples, respectively) might be associated with the rapid growth of crystallites, as evident from Figure 3-2a. As for the Ar flow rate, when it decreased to 5 sccm, both E and H values decreased drastically, although the normal expectation would be an increase owing to the smaller crystallite sizes of the H23-5sccm and H28-5sccm samples as compared to other coatings studied herein. The same trend was also reported for (AlCrTaTiZr)N films that did not

follow the Hall-Petch relationship, implying that a reduction in crystallite size does not always enhance the hardness [186]. The decrease might also be stemming from the voids present in the microstructure, as can be seen in Figure 3-6a and b. The very complex behavior of H values uncovers that there are multiple parameters, such as crystallite size, texture, intrinsic stresses, and agglomeration, dictating the measured mechanical properties of the coatings all at once [186,213].

Table 3-4: Experimentally measured elastic modulus and hardness values of the coatings.

Sample	**E (GPa)**	**H (GPa)**
H23-20min	88.3 ± 16.0	1.20 ± 0.22
H28-20min	88.8 ± 19.8	1.37 ± 0.30
H23-40min	101.7 ± 12.4	1.33 ± 0.26
H28-40min	96.8 ± 16.0	1.12 ± 0.25
H23-60min	87.3 ± 15.9	1.01 ± 0.26
H28-60min	89.7 ± 10.9	1.11 ± 0.21
H23-5sccm	75.3 ± 15.3	0.57 ± 0.18
H28-5sccm	74.16 ± 12.0	0.68 ± 0.19
H23-20sccm	85.3 ± 20.8	1.28 ± 0.34
H28-20sccm	94.4 ± 16.6	0.82 ± 0.15

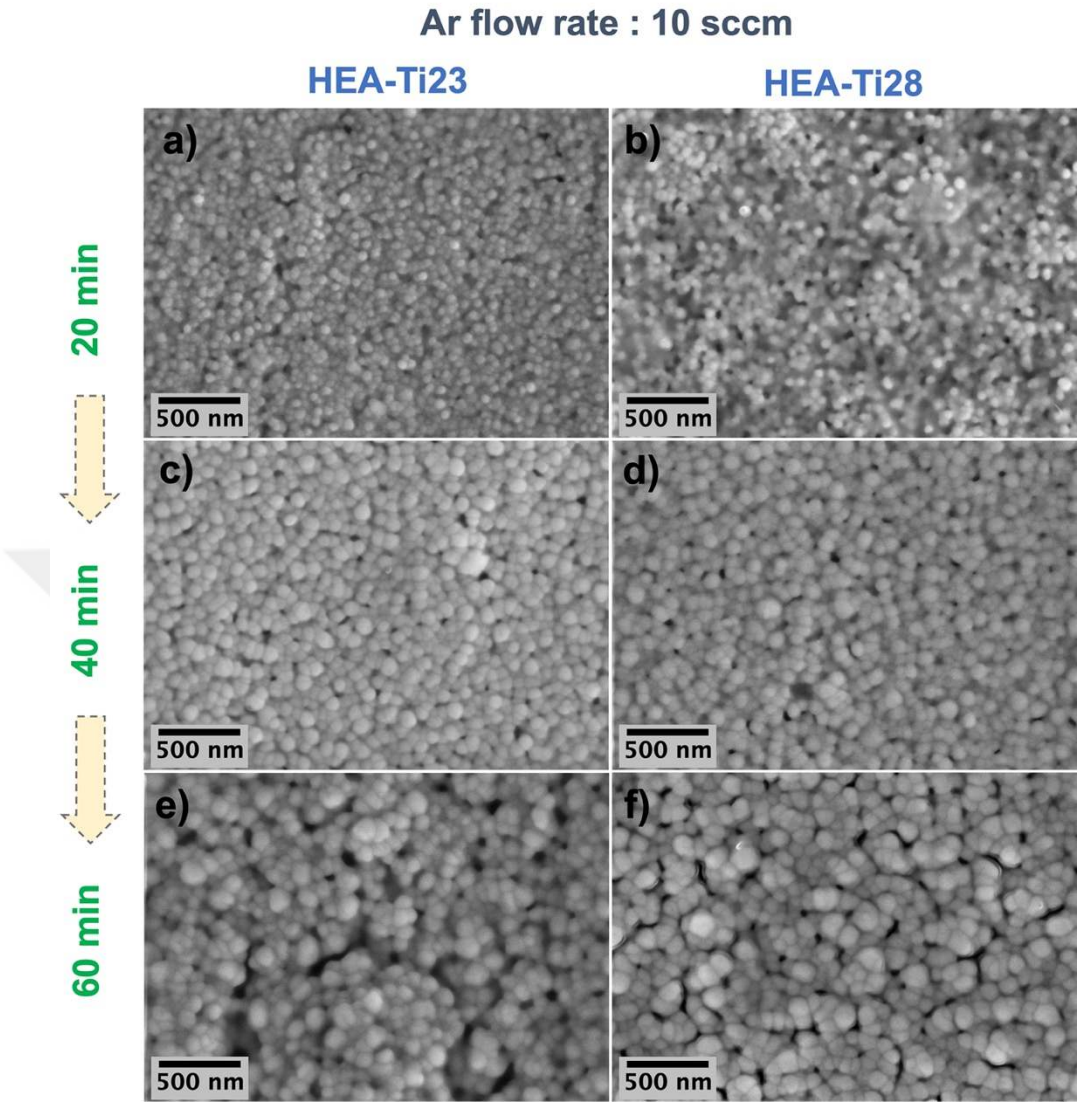

Figure 3-9: FESEM micrographs of (a) H23-20min, (b) H28-20min, (c) H23-40min, (d) H28-40min, (e) H23-60min, and (f) H28-60min samples following immersion in SBF for 28 days.

A detailed FESEM analysis was undertaken to uncover the roles of deposition time (Figure 3-9) and Ar flow rate (Figure 3-10) on the Ag ion release behavior of coated HEA samples when immersed in SBF for 28 days, in addition to the ICP-MS analysis (Figure 3-11). One notable observation is that the surface damage present in H28-20min (Figure 3-9b) was more severe than the damage observed in H23-20min sample (Figure 3-9a), which correlates well with the higher Ag ion concentration detected in the immersion fluid of the H28-20min sample after 28 days (Figure 3-11a). Specifically, the increase in deposition time first resulted in a decrease and then an increase in the Ag ion release, proving that thicker coatings do not necessarily release a higher amount of Ag ion and

implying the presence of other parameters affecting the ion release behavior [214]. To elaborate, the reason behind the low ion release from the H23-40min and H28-40min samples might be the strong (111) texture, which is the orientation with the lowest interfacial energy, abating the dissolution rate of Ag ions in these samples [199]. Figure 3-11a unveils that the texture has an impact on the ion release behavior of the coatings as the ICPMS results follow a similar trend to that of the I_{200}/I_{111} ratio presented in Figure 3-3a.

Another important observation is that the surfaces of the H23-5sccm (Figure 3-10a), H28-5sccm (Figure 3-10b), and H28-20sccm (Figure 3-10d) samples sustained less damage upon immersion in SBF for 28 days as compared to the H23-20sccm sample with a hazy appearance (Figure 3-10c). In addition, the ICP-MS results (Figure 3-11b) point out that the decreasing Ar flow rate brings about a sharp increase in Ag ion release. This can be attributed to the very small Ag NPs present on the surface (Figure 3-6a and b): it was reported that small-sized particles are more toxic owing to higher surface-to-volume ratio, leading to an enhanced interaction with body fluids, thereby facilitating faster dissolution and ion release [206,215,216]. This shows that the dissolution of Ag NPs is size dependent, and the rate of ion release increases exponentially with decreasing particle size [206,216]. Hence, the ion release behavior of coatings does not depend only on texture but also on particle size. Overall, it can be concluded that the Ar flow rate is an important parameter in the control of particle size affecting the ion release of the thin films.

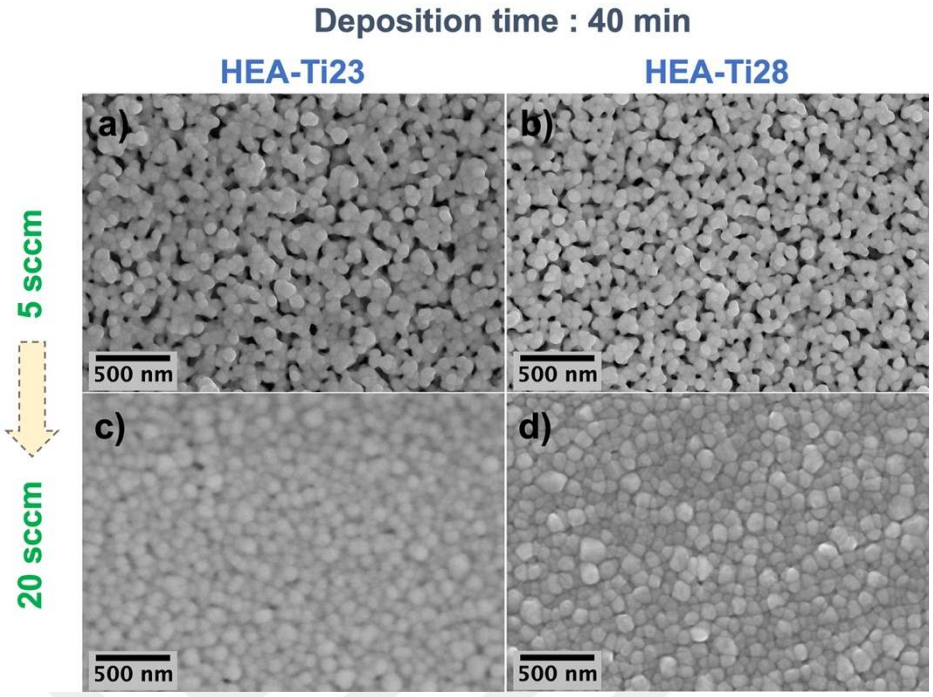

Figure 3-10: FESEM micrographs of (a) H23-5sccm, (b) H28-5sccm, (c) H23-20sccm, and (d) H28-20sccm samples following immersion in SBF for 28 days.

The level of ion-induced toxicity to various human cells might be different from each other. For instance, it was reported that no proof of toxicity was detected for fibroblast cells until a level of Ag ion release of 1200 ppb was reached [178]. In another study, cytotoxicity in monocytes, a type of white blood cell, was observed above an Ag concentration of 1000 ppb. On the other hand, the viability of T-cells and human mesenchymal stem cells was shown to be affected only beyond an Ag ion concentration of 1500 ppb [216]. As illustrated in Figure 3-11, except for the H23-5sccm and H28-5sccm samples, the concentrations measured upon static immersion of HEA-Ti23 and HEA-Ti28 samples in SBF for 28 days remained below 1000 ppb. Considering both ion release behavior and mechanical compatibility, the H23-40min sample stands out with E and H values of 101.7 ± 12.4 and 1.33 ± 0.26 GPa, respectively, and an Ag ion concentration of 404.2 ± 1.6 ppb detected in SBF upon 28 days of static immersion, warranting further elaboration to assess the potential of this Ag coated HEA for utility in orthopedic implants.

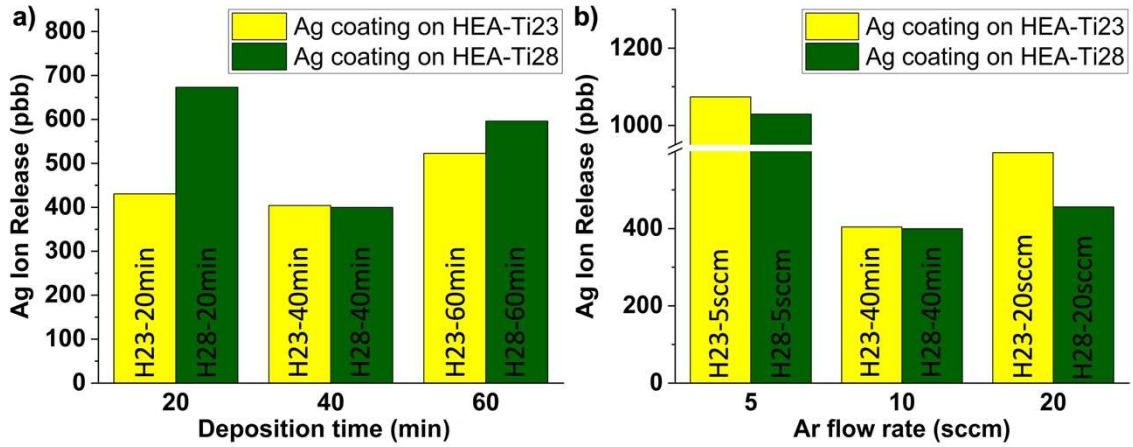

Figure 3-11: Released Ag ion concentrations of the coatings deposited on HEA-Ti23 and HEA-Ti28 substrates (a) with the constant Ar flow rate of 10 sccm for deposition times of 20, 40, and 60 min, and (b) for 40 min at Ar flow rates of 5, 10 and 20 sccm.

3.4 Conclusion

This work aimed at uncovering the evolution of microstructural, mechanical, and ion release behavior of Ag coatings sputtered on biomedical high entropy alloys (HEAs). The study proved that the properties of the coatings deposited on different substrates might be different from each other even though they were prepared under the same conditions. The deposition time was shown to affect the texture, roughness of the coatings, number, and size of agglomerates, and the critical thickness, where the surface energy to strain energy minimization transformation took place. Specifically, above a critical thickness, the evolution of two different strain energy mechanisms was observed for films sputtered on $Ti_{23}Ta_{10}Hf_{27}Nb_{12}Zr_{28}$ and $Ti_{28}Ta_{10}Hf_{30}Nb_{14}Zr_{18}$ HEAs: grain growth and formation of (220) oriented grains, respectively. Furthermore, the Ar flow rate was shown to have an impact on NP size, increasing the amount of ion release drastically due to the increase in the surface-to-volume ratio of these particles. It was affirmed that the ion release rate depends not only on the NP size but also on the texture of the coating, which can be modified by changing the deposition time and the Ar flow rate. More specifically, the (111) texture brought about a decrease in the amount of Ag ion release yet a higher elastic modulus and hardness values for the HEA-Ag film composite. The experimental findings of the study also indicate that the surface energy of the substrate, and the lattice mismatch between the coating and the substrate might be associated with the different properties observed for the coatings deposited on $Ti_{23}Ta_{10}Hf_{27}Nb_{12}Zr_{28}$ and $Ti_{28}Ta_{10}Hf_{30}Nb_{14}Zr_{18}$

HEAs. Overall, the results presented herein suggest that the desired combination of enhanced biocompatibility and mechanical properties can be achieved for the Ag-HEA composites by optimizing the Ag film deposition parameters.

Chapter 4:
UNDERSTANDING THE ENHANCED CORROSION PERFORMANCE OF TWO NOVEL TI-BASED BIOMEDICAL HIGH ENTROPY ALLOYS

4.1 Introduction

Metallic biomaterials have been a prominent choice for replacing failed hard tissue in the human body, such as hip, knee joint, and dental roots [78,81,217]. Among metallic biomaterials, 316L stainless steel (SS), CoCr-based, and Ti-based alloys are among the most utilized implant materials in biomedical applications. Nevertheless, concerns have been raised due to their tendency to fail in long-term usage [218,219]. For instance, with an elastic modulus of about 200 GPa, which is much higher than that of the bone (about 30 GPa), the utility of the 316L SS alloy leads to a modulus mismatch between the implant and the bone, known as "stress shielding," eventually leading to implant loosening or complete failure of the implant [79,82]. Due to their high strength, good wear, and corrosion resistance, CoCr-based alloys have been frequently utilized for hip and total knee joint replacements [217]. The good corrosion resistance of CoCr-based alloys is associated with the spontaneous formation of a thin oxide film of Cr2O3 on its surface in the human body [217,220,221]. However, one major drawback of CoCr-based biomedical alloys is the release of Co and Cr metallic ions. It has been reported that Co and Cr release could cause cytotoxicity, carcinogenic effects, and pseudotumors [96,219]. Similarly, Ti-based alloys, especially the Ti6Al4V alloy, have received considerable attention because of their good biocompatibility and corrosion resistance [49,79,81,220,222]. Notably, the lower elastic modulus of Ti6Al4V reduces the effect of stress shielding; however, the release of Al and V ions has raised serious concerns as they cause cytotoxic effects in the human body [155,217,223,224]. In particular, the toxic Al and V ions inhibit the growth of the bone and can lead to Alzheimer's disease and peripheral neuropathy [156,159].

Recently, high entropy alloys (HEAs) composed of multi-principal elements with concentrations varying between 5 at% and 35 at% have gained much attention due to their high strength, superior high-temperature properties, corrosion resistance, and mechanical

properties, which are attributed to the four-core effect: high entropy, lattice distortion, sluggish diffusion, and cocktail effects [3,225]. Various HEA systems have been manufactured in recent years [31,84,226–228]. Several HEAs containing a combination of Hf, Nb, Ta, Ti, and Zr elements, including Ti-Zr-Nb-Ta [55,229], Ti-Nb-Zr-Sn [224], Ti-Zr-Nb-Mo [230], Ti-Zr-Hf-Nb-Fe [54], Ti-Zr-Nb-Ta-Mo [231,232], and Ti-Zr-Hf-Nb-Ta-Mo [233], have been developed. Previous studies reported that alloying with Mo made the Ti-Zr-Nb-based refractory HEAs brittle, which is inconvenient from a biomedical perspective [84,232]. It was found that human gingival fibroblasts exhibited better adhesion and proliferation behaviors on $Ti_{40}Zr_{20}Hf_{10}Nb_{20}Ta_{10}$ alloy, developed as a potential candidate for dental implants [234]. In another study, good viability and proliferation behaviors of MC3T3-E1 pre-osteoblasts obtained on equimolar TiZrHfNbTa HEA showed its promising in vitro biocompatibility and high bio-corrosion resistance in Hank's solution at 300 K [235]. However, in terms of biomechanical compatibility, these HEAs still possess notably higher elastic moduli than that of the bone, which in turn might result in stress shielding, thereby, bone degradation [96,232].

Despite the theoretical description suggesting that HEAs form single-phase solid solutions over intermetallic compounds owing to the high configurational entropy induced by mixing multiple principal elements [3,102], researchers have demonstrated that phase decomposition may occur in some HEAs [96,236,237], including biomedical ones from the HfNbTaTiZr alloy family [238,239]. From a biomedical point of view, elemental segregation and phases present in the microstructure are significant factors affecting materials' corrosion behavior and resistance. More specifically, phase structure and elemental segregation would alter the passive oxide layer's properties influencing the dissolution kinetics [240]. Therefore, a detailed analysis of oxide layer stability, which depends on the chemical composition of the bulk material and the high and low valence oxides forming on it, should be conducted, especially when in contact with bodily fluids to affirm the durability of the implant [241].

After implantation, conventional biomedical alloys were shown to be vulnerable to different corrosion types, such as localized pitting and crevice corrosion in contact with bodily fluids [85,222]. In the literature, simple electrolytes, such as phosphate-buffered saline (PBS), are commonly used to rank the biomaterials. Nonetheless, PBS electrolyte does not have the diversity of the chemical compounds in human blood and might result in overestimating biomaterials' chemical resistance [242]. Therefore, SBF electrolyte,

possessing a closer chemical composition to that of the blood [140], would be a better choice for replicating the in vivo conditions in the human body by means of in vitro experiments [243]. In assessing the functionality and durability of implant materials for dental applications, the conditions in the human oral cavity should be replicated. The oral cavity, one of the most dynamic environments in the human body with exposure to many acidic foods, can result in accelerated ion release and corrosion [244]. Therefore, to simulate the biological and aggressive conditions in the human body, SBF and artificial saliva (AS) electrolytes would be a better choice to investigate ion release behavior, passive layer formation, and corrosion resistance of metallic implant materials. To sum up, developing novel metallic implant materials and exploring their corrosion resistance in bodily fluids is an essential step that should be taken before conducting in vivo studies, which are financially and time-wise costly [83,86,245,246].

To address the complications emerging due to stiffness mismatch between the hard tissue and the implant, two new biomedical HEAs were recently designed and produced with the aid of machine learning: namely, the $Hf_{27}Nb_{12}Ta_{10}Ti_{23}Zr_{28}$ (HEA-Ti23) and $Hf_{30}Nb_{14}Ta_{10}Ti_{28}Zr_{18}$ (HEA-Ti28) with elastic moduli closer to that of the bone (83.5 GPa and 87.4 GPa, respectively) [71]. The current study aimed to assess the ion release and corrosion resistance of HEA-Ti23 and HEA-Ti28. First, the arc-melted alloys' as-cast microstructures were characterized to investigate the degree of elemental segregation and microstructural evolution during the arc-melting process. Then, the alloys were exposed to static immersion experiments in AS and SBF to monitor the ion release behaviors. The corresponding oxide films that formed on the HEAs upon being immersed in AS and SBF were investigated by X-ray photoelectron spectroscopy (XPS). Finally, the electrochemical behaviors of the two novel HEAs were assessed by performing potentiodynamic polarization tests in SBF and AS electrolytes and compared with the corrosion behavior of the CoCrMo, utilized as control material. The experimental findings presented herein show that both HEA-Ti23 and HEA-Ti28 exhibit a dendritic microstructure in the as-cast condition and allow for the formation of a passive oxide layer consisting of high valence oxides and sub-oxides and have a better corrosion behavior in both AS and SBF as opposed to the conventional CoCrMo alloy, which is widely used as an implant material.

4.2 Experimental details

The $Hf_{27}Nb_{12}Ta_{10}Ti_{23}Zr_{28}$ (HEA-Ti23) and $Hf_{30}Nb_{14}Ta_{10}Ti_{28}Zr_{18}$ (HEA-Ti28) HEAs were prepared by vacuum arc melting on a water-cooled copper crucible, using Ti, Ta, Hf, and Nb with a purity of 99.9 %, and Zr with a purity of 99.2 %, under a Ti-gettered argon atmosphere. Button-shaped ingots with an intended mass of 20 grams were prepared. The arc-melted ingots were flipped and re-melted at least five times between each melting to ensure compositional homogeneity. The as-cast ingots were then cut by wire electro-discharge machining (EDM) to obtain slices with 2 mm thickness. The average density of the alloys was measured following the Archimedes principle (MK 2200 Industrievertretungen GmbH) using water as the immersing medium, as tabulated in Table 4-1. The specimens' surfaces were ground using SiC emery papers up to 2500 grit size for all experiments and polished with 0.3 μm alumina slurry.

Table 4-1: Average densities of the HEA-Ti23 and HEA-Ti28 samples.

	HEA-Ti23	**HEA-Ti28**
Density (g/cm^3)	9.39 ± 0.18	9.22 ± 0.25

The crystal structures of the samples were analyzed by X-ray Diffraction (XRD) utilizing a Bruker D8 Advanced X-ray diffractometer with a Cu-Kα radiation source, where the acquisition angle ranged from 20° to 100° with an incremental step size of 0.02°. The microstructure of the as-cast specimens was examined under a Zeiss SUPRA 55VP scanning electron microscope (SEM). Chemical composition and elemental mapping of the specimens were obtained using an energy dispersive X-ray spectroscopy (EDX) detector (Bruker AXS GmbH), and the data were collected with an acceleration voltage of 20 kV. The final composition of HEA-Ti23 and HEA-Ti28 was confirmed by EDS, as listed in Table 4-2.

Table 4-2: Nominal and actual chemical composition of two HEAs determined using EDS.

Alloy	Composition (at%)	Hf	Nb	Ta	Ti	Zr
HEA-Ti23	Nominal	27	12	10	23	28
	Actual	25.1 ± 1.1	12.7 ± 0.4	8.7 ± 0.4	24.4 ± 0.3	29.1 ± 0.9
HEA-Ti28	Nominal	30	14	10	28	18
	Actual	28.6 ± 1.2	15.1 ± 0.5	8.3 ± 0.4	30.1 ± 0.4	17.9 ± 0.6

The samples were exposed to static immersion experiments in AS and SBF for 1, 7, 14, 28, and 56 days at a constant temperature of 37 ± 0.5 ºC in an electronically controlled water bath. The composition of SBF (pH = 7.4 ± 0.05) [140] and AS (pH = 2.3 ± 0.05) [247] is presented in Table 4-3, where the acidity of AS was adjusted using lactic acid [247]. During the immersion experiments, the samples were kept in separate sealed tubes, where the volume-to-surface area ratio of 20 ml/cm^2 was preserved in each tube, in accord with ASTM standards [141]. Following static immersion tests, the solutions were analyzed employing an inductively coupled plasma-mass spectrometer (ICP-MS, Agilent 7700x) to quantify the ions released into the AS and SBF media.

Following 28 and 56 days of immersion tests in AS and SBF, the oxides films that had formed on the surface of HEA-Ti23 and HEA-Ti28 were investigated by X-ray photoelectron spectroscopy (XPS, Thermo Scientific K-Alpha), employing a monochromatic Al-Kα X-ray source (1486.6 eV), to gain insight regarding the oxidation states of the species. The relative sensitivity factors of the pure elements were considered while calculating the apparent surface composition of the oxide species formed on the surface of the alloys, using integrated intensities (peak area) of deconvoluted peaks. Thermo-Scientific Advantage software (v. 5.949) was utilized for quantitative analysis and peak deconvolution.

The corrosion resistance of HEA-Ti23 and HEA-Ti28 alloys was evaluated in AS (pH=2.3) and SBF (pH=7.4). Once the samples were cut by EDM, they were covered with epoxy, leaving only 1 cm^2 of the surface area exposed to the electrolyte. Then the exposed surface was polished with 0.3 μm alumina slurry. The electrochemical studies were carried out in a three-electrode cell with a platinum spiral wire as a counter electrode and a saturated calomel electrode (SCE) as a reference electrode at a constant temperature

of 37 ± 1 ºC by using an electronically controlled thermostatic bath. The electrochemical measurements were conducted using a Potentiostat (Biologic Science Instruments, VSP) controlled by a computer equipped with the EC Lab software. All potentials were referred to the SCE reference electrode. Prior to each experiment, the working electrode was immersed in the solution for 30 minutes to stabilize the open circuit potential (EOCP). Potentiodynamic polarization curves were recorded from -1 V to 1.2 V with respect to EOCP at a scan rate of 1 mV s^{-1}. The corrosion potential and rate were obtained by extrapolating the Tafel slope.

Table 4-3: Composition of the SBF and AS solutions utilized in the static immersion and potentiodynamic polarization experiments.

Solution	**Ingredients**	**Amount (g/L)**	**pH**
AS	KCl	0.4	2.3
	NaCl	0.4	
	$CaCl_2 \cdot 2H_2O$	0.906	
	$NaH_2PO_4 \cdot 2H_2O$	0.69	
	$Na_2S \cdot 9H_2O$	0.005	
	Urea	1	
SBF	NaCl	8.035	7.4
	NaHCO3	0.355	
	KCl	0.225	
	$K_2HPO_4 \cdot 3H_2O$	0.231	
	$MgCl_2 \cdot 6H_2O$	0.311	
	1 M HCl	39 ml	
	$CaCl_2$	0.292	
	Na_2SO_4	0.072	
	TRIS	6.118	
	1 M HCl	0 – 5 ml	

4.3 Results and discussion

4.3.1 Microstructural characterization

The crystal structures of HEA-Ti23 and HEA-Ti28 were determined to be body-centered cubic (BCC) in previous work [71]. The XRD measurements were taken from the dendritic part of the samples as well as all other experiments we have performed in this work. A closer inspection of the (110) diffraction peak (Figure 4-1), whose line profiles were fitted using a Lorentz function, suggests that two BCC phases, namely, BCC1 and BCC2 exist in the HEAs' microstructure. The very close angular positions of the BCC1 and BCC2 phases show that their lattice parameters slightly deviate from each other, implying that the microstructures are close to a random solid solution in the as-cast state [96]. Such phase separation phenomena have also been observed in various refractory HEAs with similar compositions [248–251]. Additionally, it was reported that interstitial elements, such as Nitrogen [252] and Oxygen [253], might result in the formation of new phases and phase separation in some HEAs. Therefore, such effects should also be further investigated in detail, which is out of the scope of the current work.

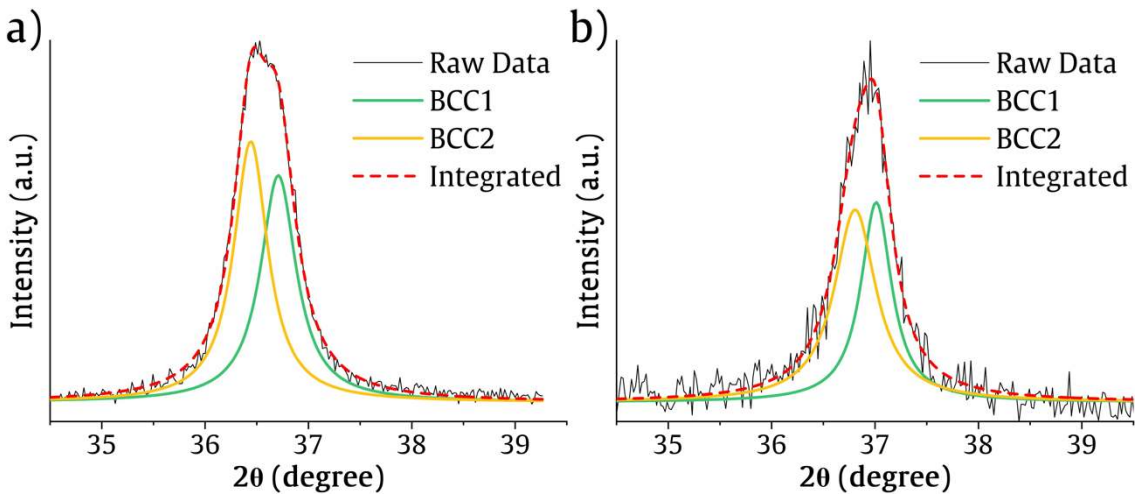

Figure 4-1: XRD patterns of the (110) peak of (a) HEA-Ti23 and (b) HEA-Ti28, utilizing the Lorentz function. The data was recompiled from [71].

To assess the arc-melting process's effect on the HEAs' microstructural evolution, samples were examined under the SEM. Corresponding SEM images of the HEA-Ti23 alloy are presented in Figure 4-2. SEM images taken from the top (Figure 4-2a) and bottom (Figure 4-2c) part of the HEA-Ti23 specimen, which was cut from the middle part

of the arc-melted ingot, are shown in Figure 4-2 (The top part indicates the curvy top and bottom part indicates the flat bottom section of the specimen, where the button-shaped ingot touches the water-cooled copper during arc-melting). The results revealed that, from bottom to top, the arc-melted buttons display distinct microstructural features. While the top region shows a fine dendritic structure (Figure 2a), the bottom part consists of equiaxed grains (Figure 4-2c). Specifically, during arc melting, the top part in contact with the Ar gas cools down very quickly when the arc is cut prior to remelting and at the end of the process, leading to a fine dendritic structure. As for the bottom part, due to a faster heat transfer from the bottom region to the water-cooled copper crucible, this part never really liquifies, hence promoting grain growth and limiting the formation of a dendritic structure [254]. Furthermore, the middle region (below top transition region (T-TR) in Figure 4-2a and above bottom transition region (B-TR) in Figure 4-2c) has coarser dendrites, implying a slower solidification rate as opposed to the top and bottom areas.

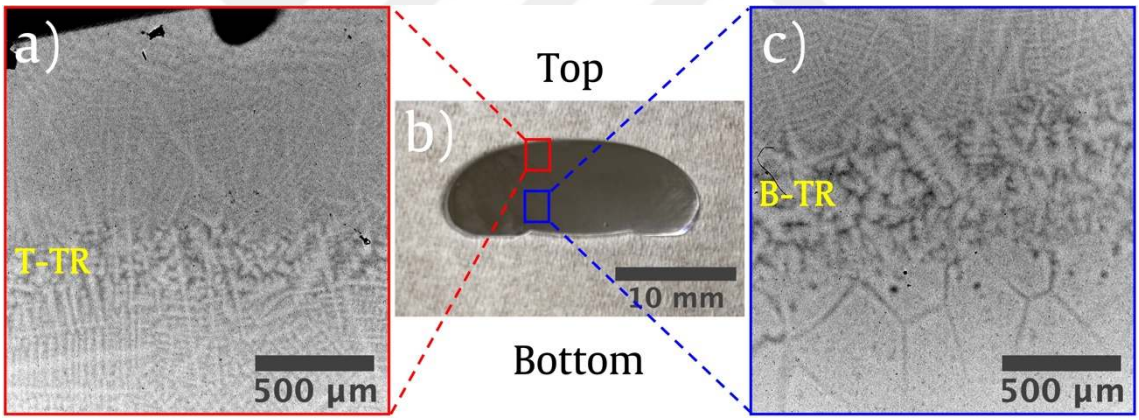

Figure 4-2: SEM images detailing the microstructural features of the (a) top and (c) bottom parts of (b) the HEA-Ti23 specimen cut from the middle part of the button-shaped ingot produced by arc-melting.

Higher magnification backscattered images and corresponding EDS maps of the constituent elements of HEA-Ti23 and HEA-Ti28 are provided in Figure 4-3 and Figure 4-4, respectively. To quantify the elemental segregation, the average concentrations at the center of dendrite arms (C_{da}), inter-dendritic regions (C_{idr}), and the partition coefficient K = C_{da}/C_{idr}, determined based on the EDS data are tabulated in Table 4-4. The partition coefficient K reflects the degree of elemental segregation in the microstructure. While the increase in the deviation of the K value from 1 implies more severe segregation, K being higher than 1 for a designated element indicates that it is segregated in the dendrite arms

[32]. Based on Table 4-4, it can be inferred that Ta segregated into dendrite arms (brighter areas in Figure 4-3a and Figure 4-4a), and Ti and Zr segregated into inter-dendritic regions (darker areas in Figure 4-3a and Figure 4-4a). This behavior has also been reported previously in other refractory HEAs. The formation of dendritic and inter-dendritic regions has been attributed to the tendency of the elements with higher melting temperatures to solidify first, resulting in redistribution of the elements in the microstructure during the solidification [226,231,255,256]. Moreover, the bright Ta-rich dendrites and the dark TiZr-rich inter-dendrites correspond to the BCC1 and BCC2 peaks, respectively, as shown in Figure 4-1. Furthermore, based on the partition coefficient K listed in Table 4-4, Hf and Nb are more inclined to segregate in the dendritic region. However, the degree of segregation is very slight and not as severe as in the case of Ta.

Table 4-4: Average chemical composition (at%) at the center of dendrite arms, C_{da}, and inter-dendritic regions, C_{idr}, along with the partition coefficient $K = C_{da}/C_{idr}$ for each alloy.

Alloy		Hf	Nb	Ta	Ti	Zr
HEA-Ti23	C_{idr}	24.6 ± 0.8	11.4 ± 0.5	7.6 ± 0.3	27.2 ± 0.7	29.2 ± 0.8
	C_{da}	26.9 ± 0.6	11.9 ± 0.6	9.4 ± 0.4	25.1 ± 0.8	26.7 ± 0.6
	K	1.09	1.03	1.24	0.93	0.92
HEA-Ti28	C_{idr}	26.8 ± 0.3	14.5 ± 0.3	7.1 ± 0.5	32.9 ± 0.6	18.7 ± 0.4
	C_{da}	28.5 ± 0.5	15 ± 0.2	8.6 ± 0.3	30.8 ± 0.6	17.1 ± 0.5
	K	1.06	1.04	1.22	0.93	0.91

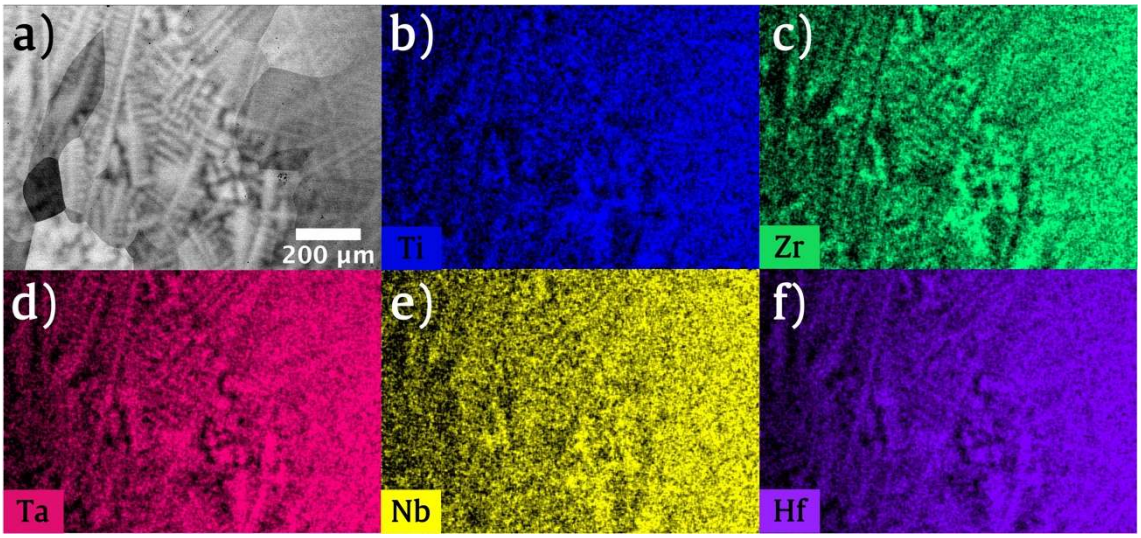

Figure 4-3: High magnification SEM image of HEA-Ti23 (a) and the corresponding elemental maps for (b) Ti, (c) Zr, (d) Ta, (e) Nb, and (f) Hf.

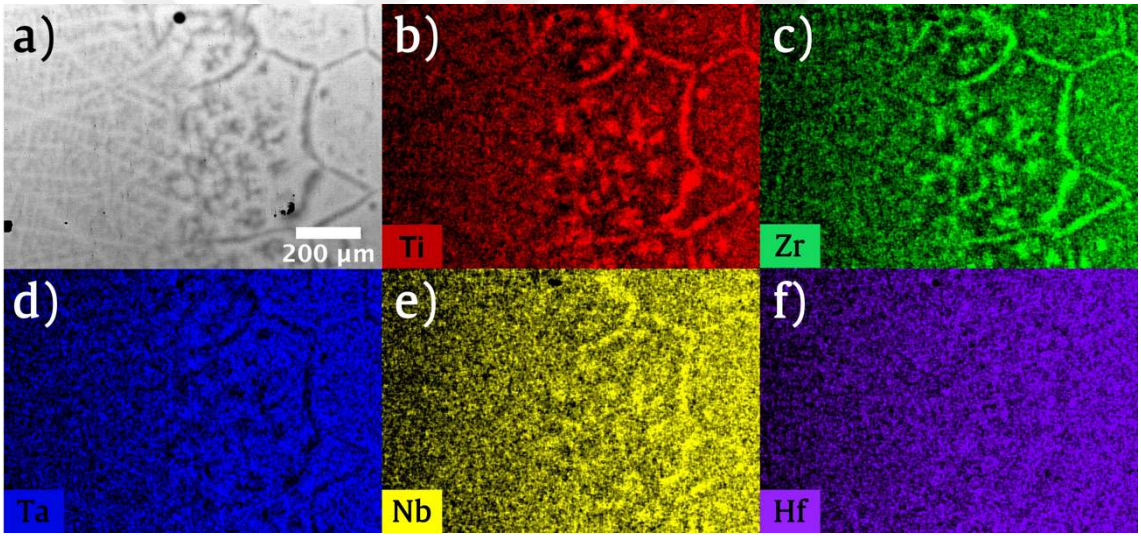

Figure 4-4: High magnification SEM image of HEA-Ti28 (a) and the corresponding elemental maps for (b) Ti, (c) Zr, (d) Ta, (e) Nb, and (f) Hf.

4.3.2 Ion release behavior and surface characterization

The cumulative Ti ion release from HEA-Ti23 and HEA-Ti28 into AS and SBF following 1, 7, 14, 28, and 56 days of immersion at 37 ºC is illustrated in Figure 4-5. Only released Ti amounts are presented in Figure 4-5, owing to the insignificant concentration of other elements in the immersion media. One of the critical parameters affecting the quantity of ion release is the acidity of the immersion fluid in addition to the Cl ion concentration [257]. Based on Figure 4-5a, the amount of Ti ion release in AS medium is higher for all immersion durations than the corresponding amounts released into SBF, as

demonstrated in Figure 4-5b. However, the trends of Ti ion release in AS and SBF differ, yet the amount of ion release after the first day of immersion was the highest in both AS and SBF [258]. After the first day, the cumulative ion release amount increased at a slower rate until the 28th day of immersion in SBF, as demonstrated in Figure 4-5b. In other words, the net Ti ion release after the first day was very low, showing that the dissolution rate was at the minimum, and a more stable oxide film formed on the surface between 1st and 7th days. However, a decrease in the cumulative Ti ion release on the 56th day of immersion in SBF was observed. This can be attributed to a new hydrated Ti oxide formation with hydrated phosphate ions [259] or precipitation of Ti phosphate species in the solution [260,261] after the 28th day in SBF. However, no visible precipitates were observed in the immersion tubes.

On the contrary, cumulative Ti ion release in AS medium constantly decreased after the 1st day of immersion. This may be associated with faster precipitation of Ti phosphate species in AS solution. In vitro experiments showed that Ti concentrations above ten ppm inhibit cell proliferation, and concentrations above five ppm significantly lower Ca uptake, hindering hydroxyapatite formation on the surface [151]. The total amount of ion release for all immersion durations in both AS and SBF was below 310 ppb (Figure 4-5), suggesting that the released quantities of Ti ions are well below the limits that would induce cytotoxicity [151]. Furthermore, the surface morphologies of HEA-Ti23, following 56 days of immersion in AS and SBF, are shown in Figure 4-6. Based on Figure 4-6b, darker regions verify that more locally intense corrosion occurred in the SBF medium as opposed to the one in AS (Figure 4-6a).

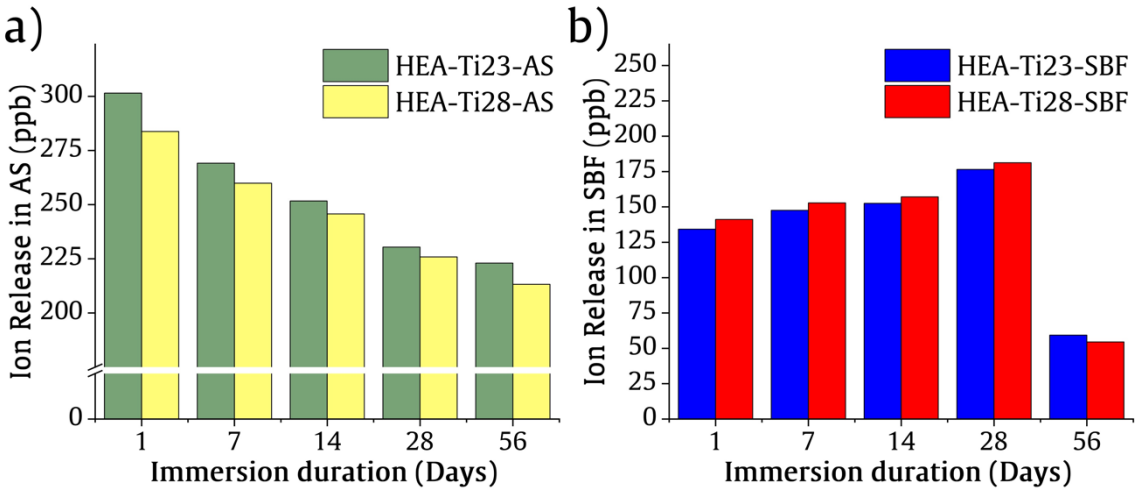

Figure 4-5: Cumulative Ti ion release from HEA-Ti23 and HEA-Ti28 upon immersion in (a) AS and (b) SBF for 1, 7, 14, 28, and 56 days at 37 ºC.

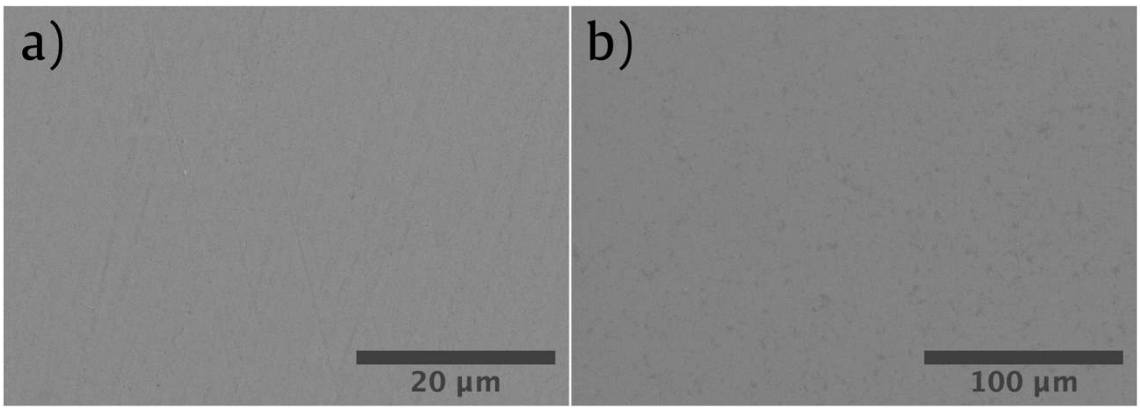

Figure 4-6: SEM micrographs for HEA-Ti23 following 56 days of immersion in (a) AS and (b) SBF at 37 ºC.

XPS was employed to analyze the surface chemistry and composition of the oxide films of HEA-Ti23 and HEA-Ti28 before and after exposure to AS and SBF for 28 and 56 days at 37 ºC. Figure 4-7 and Figure 4-8 present the XPS spectra of the (a) Hf 4f, (b) Nb 3d, (c) Ta 4f, (d) Ti 2p, and (e) Zr 3d of the HEA-Ti23 and HEA-Ti28, respectively (i, ii, and iii denote the XPS results for the air-formed oxide (AIR), and oxides formed after 56 days of immersion in AS (AS56) and SBF (SBF56), respectively). Binding energies associated with Hf, Nb, Ta, Ti, and Zr peaks are listed in Table 4-5 for HEA-Ti23 and Table 4-6 for HEA-Ti28. Moreover, the XPS results for the HEAs after immersion in AS and SBF for 28 days are shared in Figure 4-9 and Figure 4-10 for HEA-Ti23 and HEA-Ti28, respectively. The deconvoluted spectrum in the Hf 4f region for both HEA-Ti23 (Figure 4-7a) and HEA-Ti28 (Figure 4-8a) displayed two doublet peaks corresponding to the metallic state of Hf and the Hf4+ oxidation state (HfO2) [262]. Similarly, the deconvoluted Zr 3d spectrum of the HEA-Ti23 (Figure 4-7e) and HEA-Ti28 (Figure 4-8e) showed two sets of doublet peaks corresponding to metallic Zr and ZrO2 [262,263]. It is worth mentioning that the XPS spectra of air-formed oxides of the HEAs revealed metallic Hf and Zr peaks with visible intensities, as demonstrated in Figure 4-7((a)-(i) and (e)-(i)) and Figure 4-8((a)-(i) and (e)-(i)). On the other hand, the metallic peaks of Hf and Zr with very low intensities were included only to obtain a good fitting during the deconvolution process. Furthermore, no sub-oxide formation was detected on Hf and Zr XPS spectra.

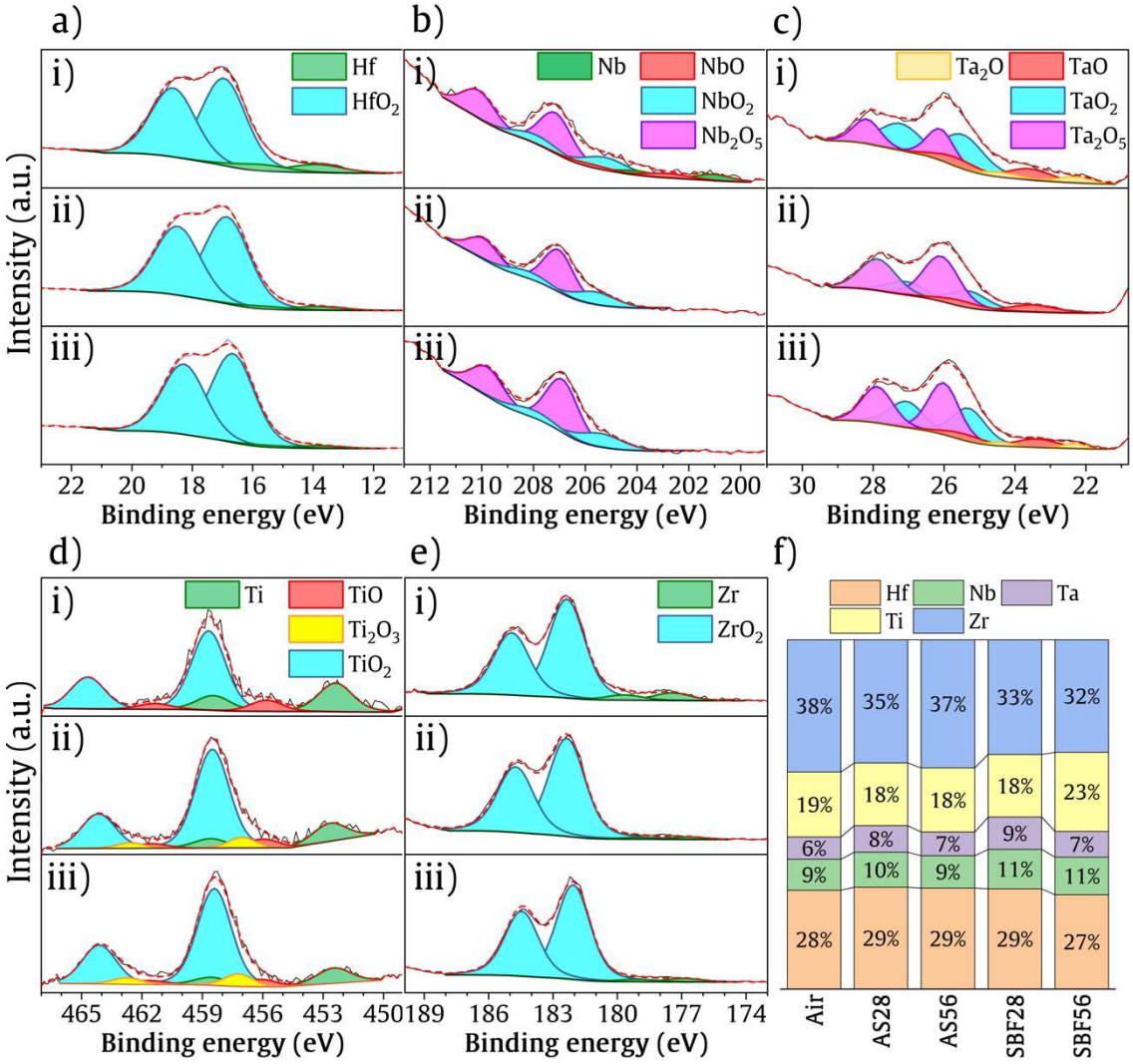

Figure 4-7: High-resolution XPS spectra of HEA-Ti23 after exposure to (i) air, (ii) immersed in AS, and (iii) SBF for 56 days, taken from the outermost surface for (a) Hf, (b) Nb, (c) Ta, (d) Ti, and (e) Zr; (f) total oxide concentrations (at%) for each element (i.e., sub-oxides included) in the passive films of the alloys exposed to air and immersed in AS and SBF for 28 and 56 days.

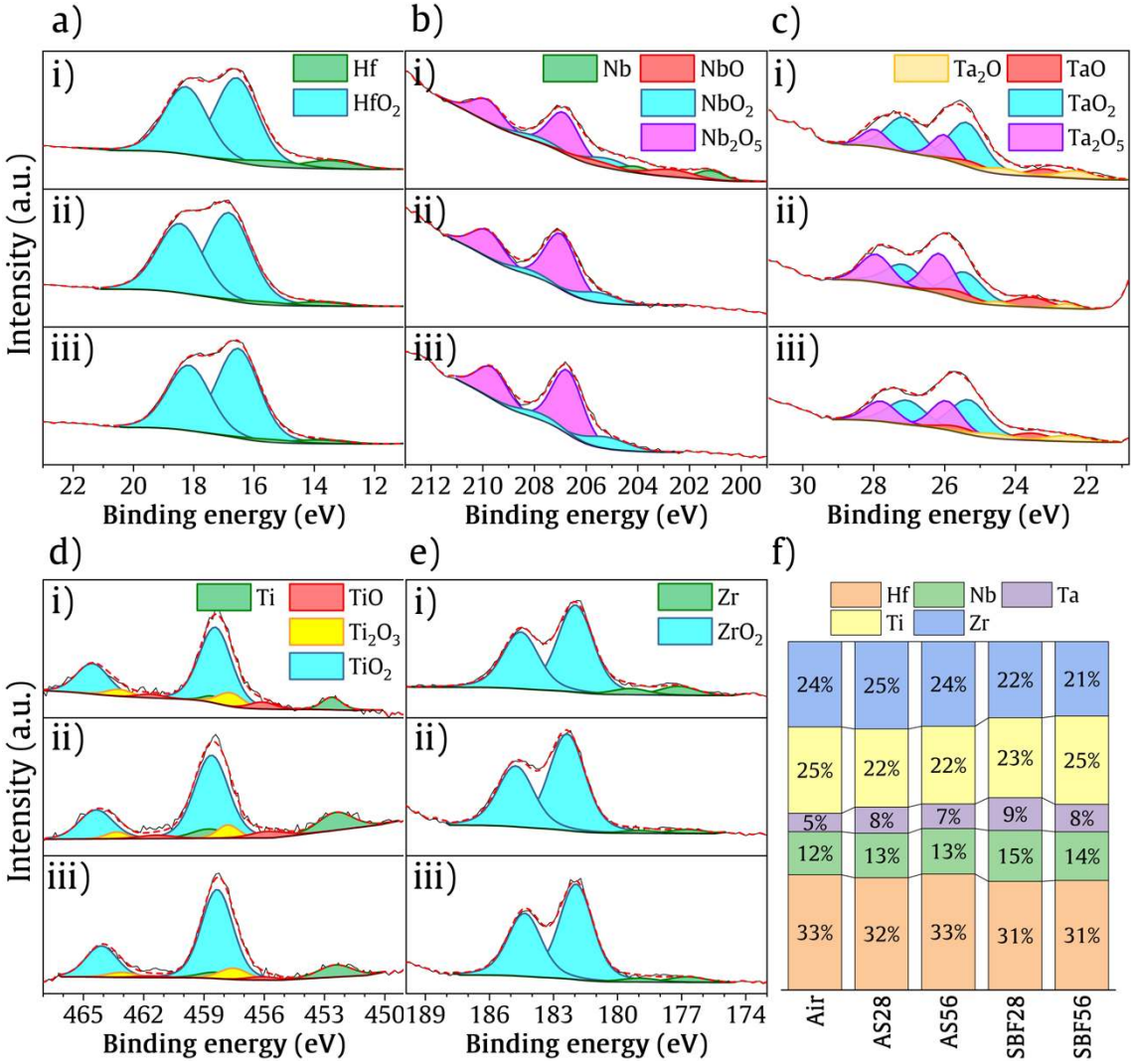

Figure 4-8: High-resolution XPS spectra of HEA-Ti28 after exposure to (i) air, (ii) immersed in AS, and (iii) SBF for 56 days, taken from the outermost surface for (a) Hf, (b) Nb, (c) Ta, (d) Ti, and (e) Zr; (f) total oxide concentrations (at%) for each element (i.e., sub-oxides included) in the passive films of the alloys exposed to air and immersed in AS and SBF for 28 and 56 days.

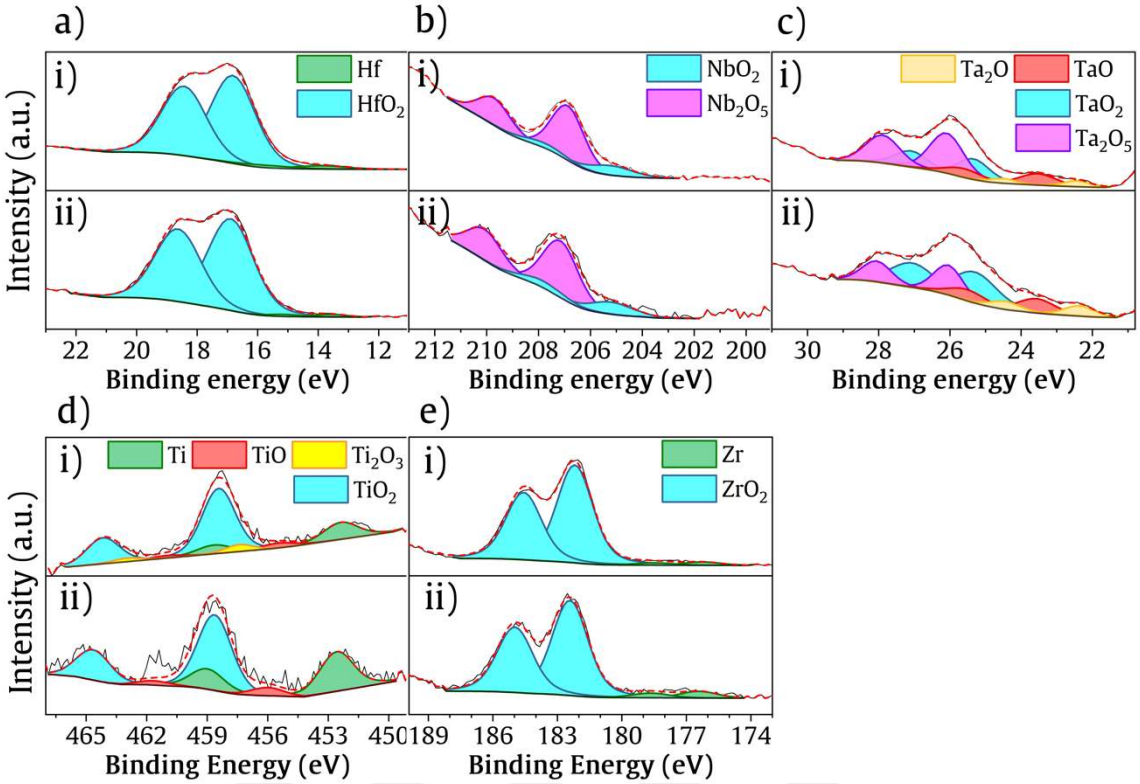

Figure 4-9: High-resolution XPS spectra of HEA-Ti23 after immersed in (i) AS and (ii) SBF for 28 days, taken from the outermost surface for (a) Hf, (b) Nb, (c) Ta, (d) Ti, and (e) Zr.

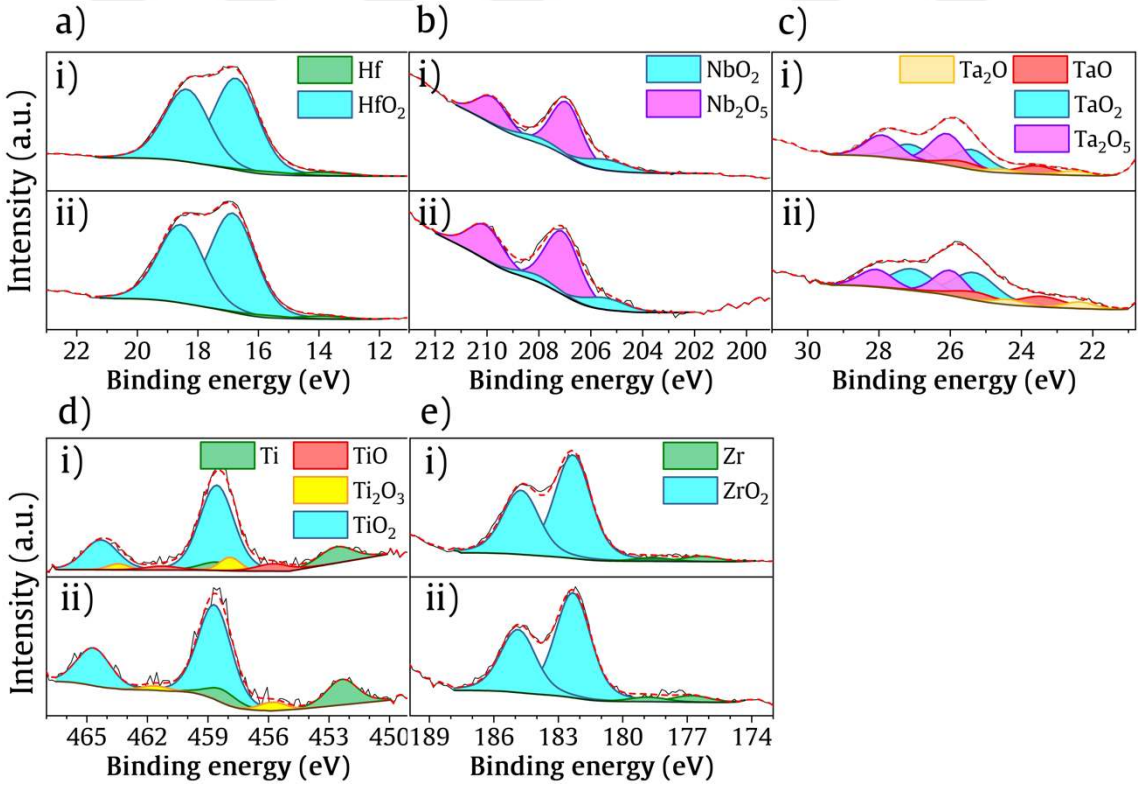

Figure 4-10: High-resolution XPS spectra of HEA-Ti28 after immersed in (i) AS and (ii) SBF for 28 days, taken from the outermost surface for (a) Hf, (b) Nb, (c) Ta, (d) Ti, and (e) Zr.

Nb 3d spectra exhibited peaks corresponding to Nb in the metallic state and different oxidation states, namely Nb^{2+} (NbO), Nb^{4+} (NbO_2), and Nb^{5+} (Nb_2O_5), the binding energies of which are tabulated in Table 4-5 and 4-6 [235,263]. The metallic Nb and NbO sub-oxide were only detected in the oxide films formed in the air (Figure 4-7b-(i) and Figure 4-8b-(i)). In Ta 4f spectra of the HEAs (Figure 4-7c and Figure 4-8c), Ta was detected in the high-valance oxide state Ta^{5+} (Ta_2O_5), as well as low-valence oxide states such as Ta^{4+} (TaO_2), Ta^{2+} (TaO), and Ta^{1+} (Ta_2O). Ta^{1+} (Ta_2O) oxidation state was not observed in the oxide films formed in AS (Figure 4-7b-(ii) and Figure 4-8b-(ii)) [264–266]. The deconvoluted spectrum in the Ti 2p region for both HEA-Ti23 (Figure 4-7d) and HEA-Ti28 (Figure 4-8d) displayed similar peaks with binding energy varying between 452 and 453 eV. These Ti0 peaks detected in the XPS are associated with the metallic Ti peak observed in the XPS spectra of the TiC [267]. Previous TEM investigations reported that some HEAs produced by arc-melting exhibited carbides around the grain boundaries [84]. Additionally, the other peaks displayed in Figure 4-7d and Figure 4-8d correspond to Ti^{4+} (TiO_2), Ti^{3+} (Ti_2O_3), and Ti^{2+} (TiO) oxidation states [266,268].

Table 4-5: Metallic and oxide binding energies of the alloying elements present in air-formed and passive oxide layer formed in AS and SBF after 56 days for HEA-Ti23.

Oxidation/Chemical State	**Binding Energy (eV)**		
	Air	**AS56**	**SBF56**
Hf^{4+} (HfO_2)	16.95: 18.63	16.85: 18.48	16.66: 18.28
Hf^{0}	13.9: 15.76	13.9: 15.6	13.9: 15.44
Nb^{5+} (Nb_2O_5)	207.15: 210.11	207.03: 209.92	206.89: 209.79
Nb^{4+} (NbO_2)	205.25: 207.89	205.59: 208.24	205.4: 208.04
Nb^{2+} (NbO)	202.85: 205.81	-	-
Nb^{0}	201.04: 204:00	-	-
Ta^{5+} (Ta_2O_5)	26.11: 28.18	26.08: 27.87	26.01: 27.88
Ta^{4+} (TaO_2)	25.47: 27.24	25.30: 27.06	25.30: 27.06
Ta^{2+} (TaO)	23.59: 25.66	23.49: 25.57	23.39: 25.46
Ta^{1+} (Ta_2O)	22.30: 24.38	-	22.31: 24.38
Ti^{4+} (TiO_2)	458.69: 464.69	458.50: 464.16	458.4: 464.12
Ti^{3+} (Ti_2O_3)	-	457.03: 462.57	457.21: 462.75
Ti^{2+} (TiO)	455.81: 461.35	455.99: 461.54	456.1: 461.64
Ti^{0}	452.38: 458.44	452.66: 458.6	452.46: 458.52
Zr^{4+} (ZrO_2)	182.36: 184.92	182.36: 184.74	182.06: 184.46
Zr^{0}	177.44: 179.68	176.73: 178.96	176.87: 179.11

Table 4-6: Metallic and oxide binding energies of the alloying elements present in air-formed and passive oxide layer formed in AS and SBF after 56 days for HEA-Ti28.

Oxidation/Chemical State	**Binding Energy (eV)**		
	Air	**AS56**	**SBF56**
Hf^{4+} (HfO_2)	16.57: 18.26	16.85: 18.48	16.52: 18.16
Hf^0	13.50: 15.36	13.90: 15.60	13.90: 15.45
Nb^{5+} (Nb_2O_5)	206.86: 209.82	207.03: 209.92	206.73: 209.64
Nb^{4+} (NbO_2)	205.20: 207.84	205.59: 208.24	205.22: 207.87
Nb^{2+} (NbO)	202.73: 205.69	-	-
Nb^0	201.19: 204.05	-	-
Ta^{5+} (Ta_2O_5)	26.00: 27.98	26.08: 27.87	25.95: 27.8
Ta^{4+} (TaO_2)	25.36: 27.15	25.30: 27.06	25.31: 27.07
Ta^{2+} (TaO)	23.16: 25.24	23.49: 25.57	23.55: 25.63
Ta_2O	22.30: 24.38	22.55: 24.50	22.41: 24.49
Ti^{4+} (TiO_2)	458.48: 464.54	458.50: 464.16	458.34: 464.10
Ti^{3+} (Ti_2O_3)	457.67: 463.21	457.03: 462.57	457.52: 463.07
Ti^{2+} (TiO)	456.1: 461.64	455.99: 461.54	456.08: 461.62
Ti^0	452.63: 458.57	452.66: 458.60	452.45: 458.39
Zr^{4+} ZrO_2	181.97: 184.54	182.36: 184.74	181.94: 184.35
Zr^0	177.15: 179.39	176.73: 178.96	176.73: 178.97

The total oxide concentrations for each element (including the sub-oxides) in the passive films of the alloys exposed to air, immersed in AS and SBF for 28 and 56 days were estimated using the areas under the deconvoluted peaks and presented in Figure 4-7f and Figure 4-8f for HEA-Ti23 and HEA-Ti28, respectively. These results show that the concentrations of Hf and Zr oxides formed on the surface films were higher than those in the bulk alloys (Table 4-2). Theoretical and experimental investigations revealed that the group IV elements (Hf, Zr, and Ti) oxidize preferentially over group V elements (Nb and Ta), and the oxides of Hf, Zr, and Ti are thermodynamically more stable [269,270]. Also, the Ellingham diagrams [271,272] clearly show that the ability of each element in

our alloys to form stable oxides is as follows: Hf > Zr > Ti > Nb > Ta. These thermodynamic observations are consistent with the enrichment of HEA-Ti23 and HEA-Ti28 preferentially with Hf and Zr oxides. Although the fraction of HfO2 on the oxide layer did not change upon exposure to air and immersion in AS and SBF for 28 and 56 days, the fraction of ZrO^2 on the oxide layers of the alloys declined after the alloys were immersed in SBF. This might be due to the increase in the total content of Nb, Ta, and Ti oxides in the passive oxide layers forming when immersed in SBF as opposed to the ones that formed in AS (Figure 4-7f and Figure 4-8f). In particular, the stability and corrosion resistance of the oxide films on Zr and its alloys deteriorate concomitant with increasing Cl^- content, resulting in pitting on the oxide film [263]. The concentration of both Nb and Ta oxides in the oxide layers on HEA-Ti23 and HEA-Ti28 increased following immersion in AS and SBF compared to the air-formed oxide layer. It has been shown that alloying with Nb increases the pitting resistance and stability of the passive film, reducing the dissolution of the oxide layer [263]. Furthermore, the Nb^{5+} and Ta^{5+} ions make the passive film less defective by canceling out the anion vacancies [250]. The atomic percentage of the Ti oxides in the passive film that formed upon immersion in AS (AS28 and AS56 in Figure 4-7(f) and Figure 4-8f) and SBF (SBF28 in Figure 4-7f and Figure 4-8f) decreased relative to the Ti concentration in the air-formed oxide layer. This might be explained by the Nb^{5+} ions being doped into the TiO_2 lattice and preventing the outward diffusion of Ti^{4+}, thus slowing down the formation of the TiO_2 [273]. On the other hand, the atomic percentage of the Ti oxides in the passive film that formed upon immersion in SBF for 56 days (SBF56 in Figure 4-7f and Figure 4-8f) was higher. This might be associated with the formation of a new hydrated phosphate ion incorporated Ti oxide layer [259], which was responsible for the Ti ion release decrease observed for the 56 days of immersion experiments performed in SBF (Figure 4-5b). Previous studies showed that the OH^- species stemming from the hydrated metal oxides could repair the passive film and increase the resistance against the chloride ion attacks [264].

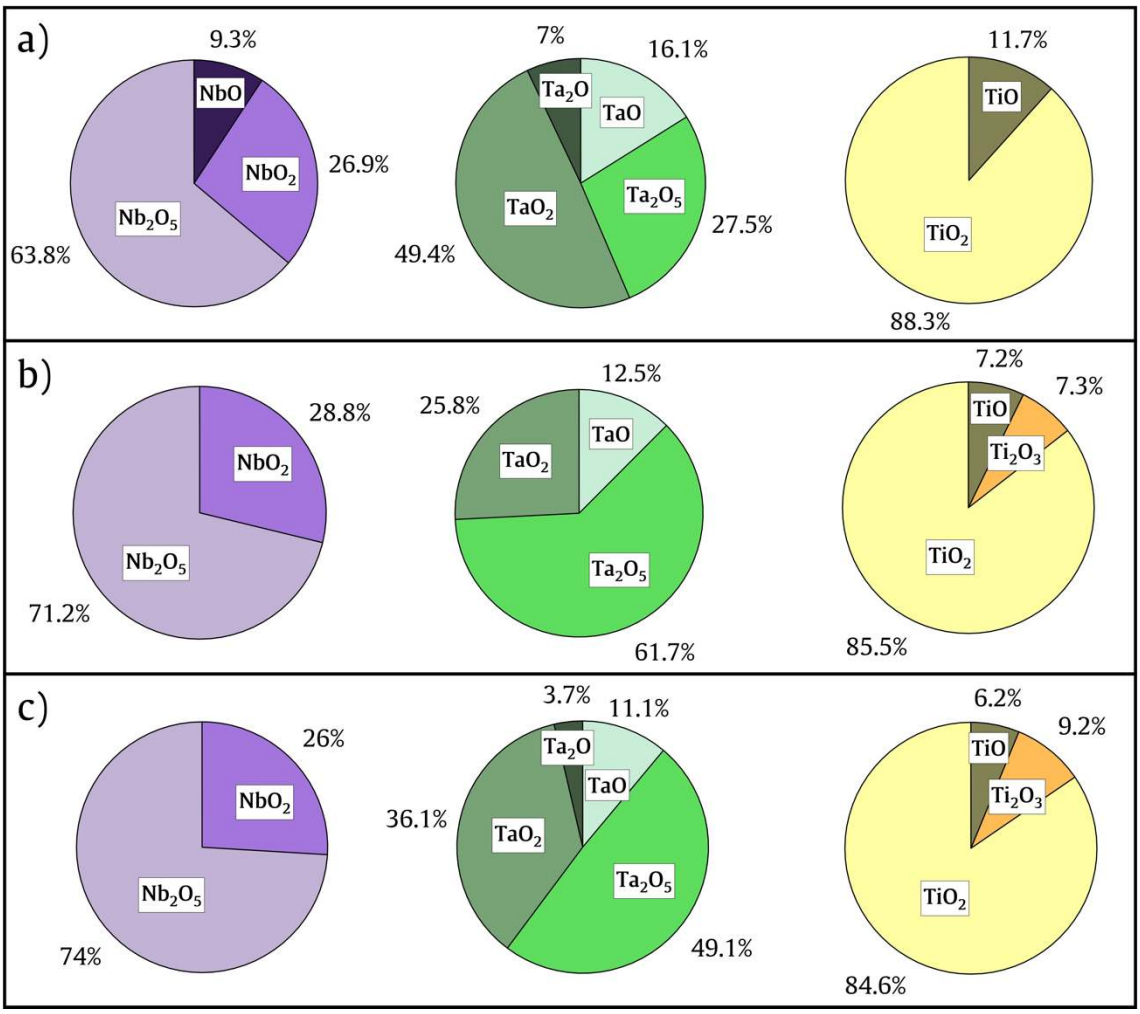

Figure 4-11: Pie charts detailing the sub-oxide fractions (at%) of Nb, Ta, and Ti in the passive films of HEA-Ti23 exposed to (a) air, immersed in (b) AS, and (c) SBF for 56 days.

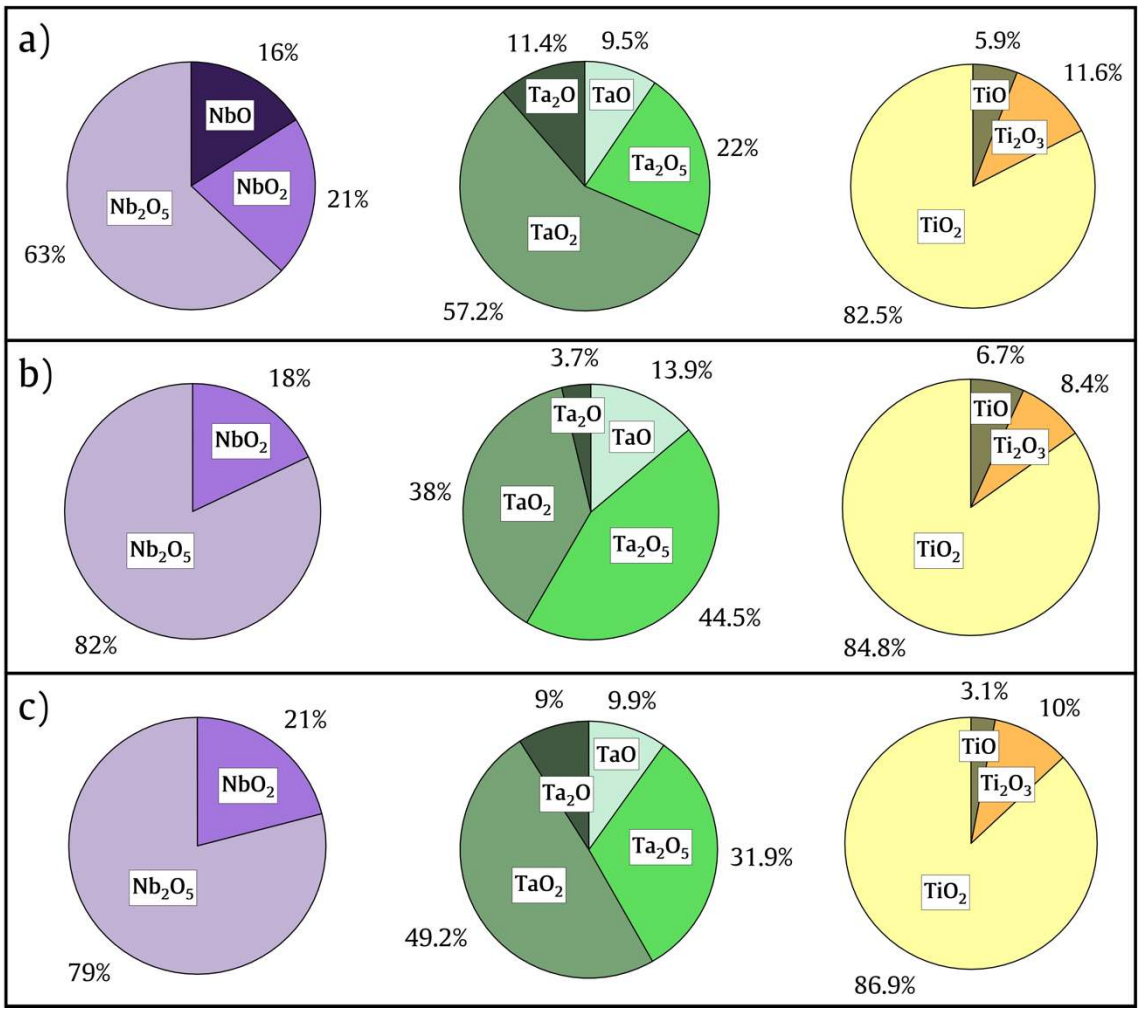

Figure 4-12: Pie charts detailing the sub-oxide fractions (at%) of Nb, Ta, and Ti in the passive films of HEA-Ti28 exposed to (a) air, immersed in (b) AS, and (c) SBF for 56 days.

The total fractions of high valence stable oxides in the oxide layers that formed upon exposure to air, immersion in AS, and SBF for 56 days are tabulated in Table 4-7. It can be deduced that the concentration of stable oxides that formed in the oxide layers of HEA-Ti23 samples was slightly higher than the amounts detected in HEA-Ti28 samples. The stable oxides, such as HfO_2, Nb_2O_5, Ta_2O_5, TiO_2, and ZrO_2, are essential because they are chemically less active and possess low solubility, preventing metal ions' release [263]. Based on Table 4-7, the oxide layers formed on HEA-Ti23 and HEA-Ti28 consist of stable oxides. To see the relative distribution of the oxidation states of Nb, Ta, and Ti elements within themselves, pie charts are presented in Figure 4-11 (HEA-Ti23) and Figure 4-12 (HEA-Ti28): note that no sub-oxides of Hf and Zr formed on either of the alloys. As opposed to the high valence oxides of Nb and Ta, the percentage of stable Ti

oxide TiO_2 compared to its sub-oxides was relatively higher on the surface of HEA-Ti23 and HEA-Ti28 (Figure 4-11 and Figure 4-12).

Table 4-7: Total amount (at%) of high-valence stable oxides present in the passive layer for HEA-Ti23 and HEA-Ti28.

Alloy	**Air**	**AS56**	**SBF56**
HEA-Ti23	89.9	92.1	89.9
HEA-Ti28	86.9	90.4	88.4

On the other hand, the stable oxides of Nb and Ta, namely Nb_2O_5 and Ta_2O_5, were lower in percentage compared to their sub-oxides, Ta being the one with less percentage of high valence oxide. To elaborate, a constant outward migration of Ta ions is required from the bulk to the surface for the initially formed sub-oxide layer to be transformed into a stable stochiometric Ta oxide. For this to happen, a critical concentration of Ta should be present below the surface of the passive film [266]. Therefore, as shown in Figure 4-11 and Figure 4-12, Ta having a higher percentage of sub-oxides might be attributed to the low amount of Ta content in the bulk alloys (Table 4-2). Low-valence oxides are considered unprotective oxides [264]. Additionally, the elemental segregations observed in EDS maps of HEA-Ti23 (Figure 4-3) and HEA-Ti28 (Figure 4-4) might be promoting the formation of less stable oxides [274]. It should also be mentioned that dendritic and inter-dendritic regions with different compositions may create a potential difference, resulting in a galvanic reaction between the two regions in the as-cast HEAs [275].

Adsorbed elemental Ca and P were also detected on the surfaces of HEA-Ti23 (Figure 4-13a-b) and HEA-Ti28 (Figure 4-13c-d) following immersion in AS and SBF for 56 days ((i) and (ii) denote AS56 and SBF56 in Figure 4-13), which was also observed in $(TiZrNbTa)_{90}Mo_{10}$ immersed in Ringer's solution [276]. In the XPS spectra of Ca, a peak corresponding to the Zr^{4+} $3p_{1/2}$ orbital was also detected [277]. Based on Ca 2p spectra of the HEA-Ti23 (Figure 4-13a(ii)) and HEA-Ti28 (Figure 4-13c(ii)) immersed in SBF, Ca 2p doublet was observed, which is associated with the Ca bond characteristics of hydroxyapatite ($Ca_{10}(PO_4)_6(OH)_2$) and Ca bonded to some carbon species, such as carbonate [278]. The presence of hydroxyapatite on the surface favors the osteointegration of the implant, especially in orthopedic applications [244]; thus, it is a

good in vitro indication of the biocompatibility of HEA-Ti23 and HEA-Ti28. On the other hand, based on Ca 2p spectra of HEA-Ti23 (Figure 4-13a(i)) and HEA-Ti28 (Figure 4-13c(i)) immersed in AS, Ca 2p peaks associated with the Ca bonded to OH^- was not observed as expected since AS is highly acidic (i.e., the effect of pH) [262]. In this case, the Ca 2p peaks can be attributed to Ca bonded to oxygen atoms of adsorbed water and some carbon species. The P 2p spectra, as shown in Figure 4-13b and Figure 4-13d can be attributed to the phosphate $(PO_4)^{3-}$ species existing on the surface and the metallic P on the surface of the alloys [278].

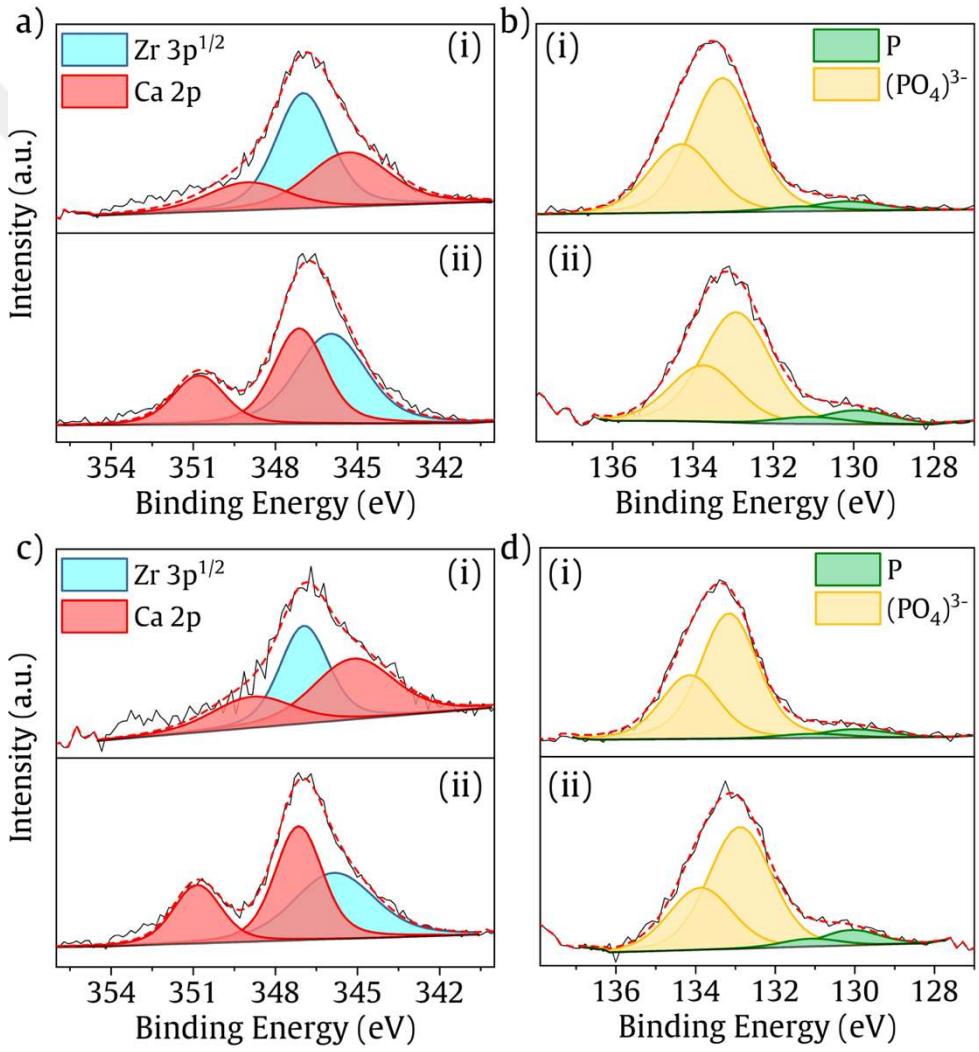

Figure 4-13: High-resolution XPS spectra of HEA-Ti23 for (a) Ca and (b) P, and HEA-Ti28 for (c) Ca and (d) P after immersed in (i) AS and (ii) SBF for 56 days.

4.3.3 Potentiodynamic polarization behavior in AS and SBF

The potentiodynamic polarization curves of HEA-Ti23 and HEA-Ti28 (Note that the dendritic part of the samples was considered during experiments), in comparison with CoCrMo (27 wt% Cr, 6 wt% Mo and balance Co [279]) as the reference material, in AS and SBF are presented in Figure 4-14a and Figure 4-14b, respectively. Figure 4-14a shows that an active-to-passive transition (E_{ap}) occurred for both the HEAs and the reference material CoCrMo. This active-to-passive transition region is where the passive film forms and grows [243]. The active-to-passive transition was more unstable for the CoCrMo alloy compared to the HEAs. In the region between -0.25 V and 0.8 V in Figure 4-14a, current fluctuations indicating the formation and re-passivation of metastable pits were observed for HEA-Ti28. Although the occurrence and rapid annihilation of the metastable pits indicate a substantial film-repairing capability, the current density increases successively up to E_p, where a more stable passive oxide layer is formed for HEA-Ti28. The severe current fluctuations in the region between E_{ap} and E_p for HEA-Ti28 can be attributed to the higher percentage of sub-oxides it contains (Figure 4-12) as opposed to the sub-oxide portion present in the passive layer on HEA-Ti23 (Figure 4-11). It was reported that NbO_2, TaO_2, and especially Ti_2O_3 induce metastable pitting [264]. On the other hand, a stable passive oxide layer formed on HEA-Ti23 in AS medium. The current density increases very slowly for the HEA-Ti23 as the anodic potential rises, indicating that the passive layer is more stable in this case (Figure 4-14a). It should be noted that no apparent breakdown of the passive oxide film occurred on both HEA-Ti23 and HEA-Ti28, while the passive oxide layer of CoCrMo broke down at a potential of about 0.8 V.

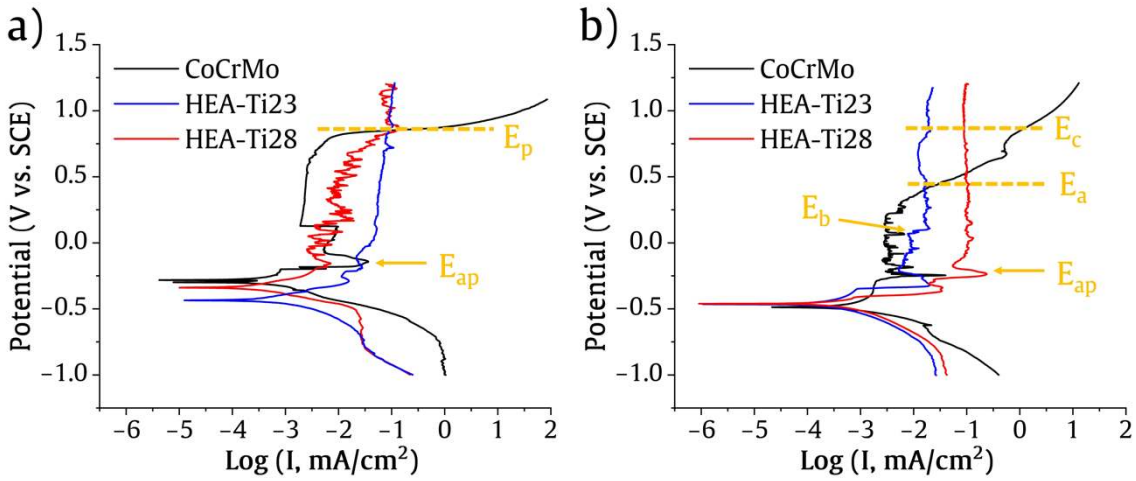

Figure 4-14: Potentiodynamic curves of HEA-Ti23, HEA-Ti28, and CoCrMo in (a) AS and (b) SBF at 37 °C.

Figure 4-14b shows that an active-to-passive transition, i.e., E_{ap}, was also observed for the HEAs and the reference material CoCrMo in the SBF medium. However, the passive oxide layer formed on the conventional CoCrMo implant broke down very early, corresponding to an anodic potential value of about 0.25 V. This behavior and breakdown potential are also consistent with the potentiodynamic experiments previously performed on CoCrMo in SBF [280]. By contrast, for HEA-Ti28, the surface revealed a continuous passive plateau without any pitting and breakdown. Thus, it can be concluded that the passive oxide layer forming on HEA-Ti28 in SBF is more stable than the one forming in AS with a very low pH. On the other hand, the corrosion behavior of HEA-Ti23 in SBF (Figure 4-14b) was different than the one observed in AS (Figure 4-14a). First, pitting occurred at point E_b (Figure 4-14b), but the passive film recovered, and the sample re-passivated quickly. This behavior might be due to the higher Zr content of HEA-Ti23, as shown in Table 4-2, making it more susceptible to pitting in mediums containing excessive amounts of chloride ions, such as SBF [264]. Until point E_a, the surface showed a continuous passive plateau. The drop in current density observed in the E_a to E_c region for HEA-Ti23 might be attributed to a phase change in the passivating oxide film [274,281]. In particular, the sub-oxide formed at the point E_b might have transformed into a more stable oxide in the E_a to E_c region.

The corrosion parameters acquired from the potentiodynamic polarization curves utilizing the Tafel extrapolation method are summarized in Table 4-8. The corrosion potential (E_{corr}) and corrosion current density (i_{corr}) are used to assess the corrosion

resistance of the materials. The current density reflects the corrosion rate of the materials. Both HEA-Ti23 and HEA-Ti28 revealed lower icorr values in both AS and SBF compared to CoCrMo, indicating that the corrosion resistance of HEAs is superior. The E_{corr} values of the HEAs were higher, as shown in Table 4-8, implying that they are more prone to be corroded in an acidic environment, such as AS. On the other hand, they revealed lower E_{corr} values reflecting that they are less likely to be corroded in SBF medium. Additionally, polarization resistance (R_p) was estimated from the Tafel plots utilizing the Stern-Geary [282] equation:

$$R_{\mathrm{p}} = \frac{\beta_{\mathrm{a}}\beta_{\mathrm{c}}}{2.303 i_{\mathrm{corr}}(\beta_{\mathrm{a}} + \beta_{\mathrm{c}})} \tag{4.1}$$

where β_a the anodic Tafel slope, and β_c is the cathodic Tafel slope. The R_p demonstrates the resistance of a material to general corrosion, and the higher value reflects a better corrosion resistance [230]. The R_p values of both HEAs are greater than that of the CoCrMo, indicating a superior corrosion resistance for HEAs in both AS and SBF media. The SEM micrographs of HEA-Ti23, HEA-Ti28, and CoCrMo acquired from their surface after electrochemical experiments in SBF are presented in Figure 4-15. As shown in Figure 4-15a and Figure 4-15b, both HEAs showed localized corrosion zones with small pits on the surface. On the hand, on the CoCrMo surface (Figure 4-15c), larger pits distributed on the whole surface were observed.

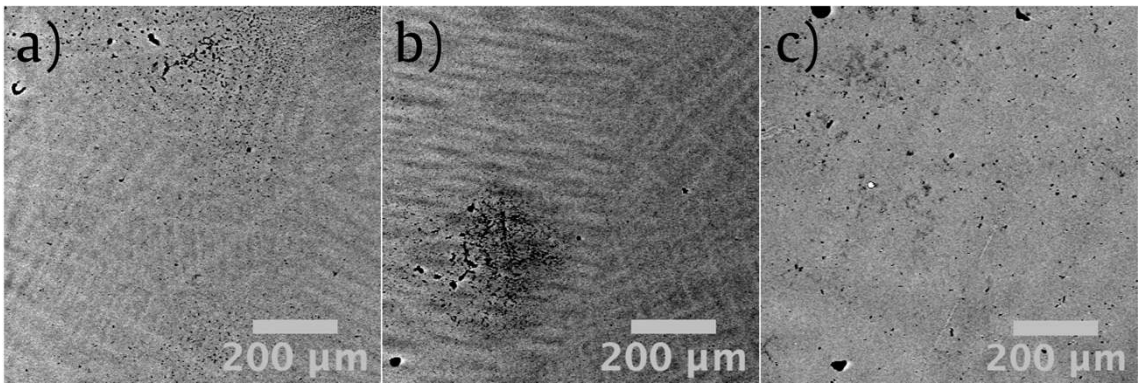

Figure 4-15: Backscattered SEM images of (a) HEA-Ti23, (b) HEA-Ti28, and (c) CoCrMo after electrochemical polarization tests in SBF at 37 °C.

Table 4-8: Electrochemical parameters of HEA-Ti23, HEA-Ti28, and CoCrMo in AS and SBF at 37 °C.

Electrolyte	Alloys	E_{corr} (mV)	i_{corr} (μA/cm^2)	β_a (mV)	β_c (mV)	R_p (kΩ cm^2)
AS	HEA-Ti23	-433	0.19	35.2	28.2	35
	HEA-Ti28	-335	0.21	68.9	71.3	73
	CoCrMo	-299	0.25	31.9	29.9	27
SBF	HEA-Ti23	-463	0.13	65.1	55.6	98
	HEA-Ti28	-459	0.17	45	52.1	61
	CoCrMo	-487	0.27	33.4	25.7	23

4.4 Conclusion

The microstructural features, ion release, and corrosion behavior of two novel biomedical HEAs, namely $Hf_{27}Nb_{12}Ta_{10}Ti_{23}Zr_{28}$ (HEA-Ti23) and $Hf_{30}Nb_{14}Ta_{10}Ti_{28}Zr_{18}$ (HEA-Ti23), were investigated. The following are the primary outcomes:

(1) Both HEAs possess a dendritic structure, with Ta being mostly segregated into dendrite arms during the solidification due to its higher melting point than other elements in bulk. The elemental segregation also depends on the cooling conditions posed by the arc-melting.

(2) While the cumulative Ti ion release increased until the 28th day and decreased afterward in SBF, a successive decrease in the cumulative Ti ion release was detected in AS. This was attributed to the formation of a new hydrated phosphate ion incorporated Ti oxide and possible precipitation of Ti phosphate species during the immersion experiments.

(3) The fraction of ZrO_2 in the oxide layer that formed on the surface of the alloys was found to be lower in the SBF medium, which is attributed to the development of a layer more resistant to chloride attacks, consisting of increased concentration of Nb, Ta, and Ti oxides.

(4) For two reasons, Ta was mainly present in the passive oxide layer in the form of its sub-oxides: the bulk alloys are deficient in Ta content, and severe segregation of Ta in dendrite arms.

(5) Potentiodynamic experiments performed in AS pointed out that HEA-Ti28 had a relatively high passive dissolution which may be associated with the higher concentration of sub-oxides it contains as opposed to HEA-Ti23, especially Ti_2O_3 which is regarded as an inducer for metastable pits.

(6) The corrosion resistance of both HEAs was found to be superior compared to that of the CoCrMo in both AS and SBF.

(7) Overall, the preliminary findings of this work demonstrate that the novel $Hf_{27}Nb_{12}Ta_{10}Ti_{23}Zr_{28}$ and $Hf_{30}Nb_{14}Ta_{10}Ti_{28}Zr_{18}$ HEAs exhibit high potential for utility as orthopedic implant materials, which is yet to be confirmed by in vivo experiments focusing on their biocompatibilities.

Chapter 5:
MACHINE LEARNING-INFORMED DEVELOPMENT OF HIGH ENTROPY ALLOYS WITH ENHANCED CORROSION RESISTANCE

5.1 Introduction

Corrosion jeopardizes the longevity and safety of engineering materials, making it a major concern for automotive, maritime, and aerospace industries, as well as for power plants and biomedical applications. Therefore, new materials with superior corrosion resistance are needed in various industries due to technological advancements pushing the limits of conventional materials currently in use [283]. An emerging class of materials, namely, high entropy alloys (HEAs), consisting of multi-principal elements with elemental concentrations ranging from 5 to 35 at%, have become popular due to their excellent mechanical and other chemical and physical properties, which are attributed to the four core effects that HEAs inherit: high entropy, lattice distortion, sluggish diffusion, and cocktail effects [225]. Shi et al. [240] and Scully et al. [284] further elaborated on HEAs being a potential candidate specifically for applications requiring high corrosion-resistant materials and highlighted that a detailed rationalization of the corrosion mechanism of HEAs is needed. However, investigating and clarifying the underlying mechanisms behind the corrosion behavior of HEAs is a rather complicated endeavor due to the complex interactions among the constituent elements resulting in different microstructural features and surface properties [240].

Composition is a crucial factor affecting the microstructure (i.e., elemental distribution, grain and grain boundaries, precipitation) of HEAs, and comprehending the correlation among the composition, microstructure, and corrosion resistance of HEAs can help researchers find out more about the mechanisms governing the properties of HEAs [58]. Although processing techniques are as critical for the corrosion resistance as the alloy composition, the following discussion will be restricted to the effect of composition on the corrosion behavior of HEAs. For instance, Wang et al. developed $TiZrHfNbFe_x$ (x = 0, 0.25, 0.5, 0.75, 1, 1.5, 2, at%) refractory HEAs for biomedical applications and

concluded that an increasing Fe content first improved and then deteriorated the corrosion resistance of the alloys. More specifically, the deterioration was attributed to the formation of the Laves phase, resulting in galvanic corrosion due to the dual-phase microstructure upon adding the element Fe [54]. In another work, it was shown that increasing Al content degraded the localized corrosion resistance of the AlxCoCrFeNi (x = 0.3, 0.5, 0.7, at.%) system in 3.5 wt.% NaCl solution. With Al content increasing, ordered and disordered AlNi-rich body-centered cubic (BCC) phases started to form along with the CrFe-rich face-centered cubic (FCC) matrix. As a result, the formation of the Cr-depleted BCC phase was favored, making the surface more sensitive to chloride ions [57].

Since multiple elements altogether dictate the final properties of the HEAs (i.e., cocktail effect) as opposed to conventional alloys, it is very challenging to decipher the influence of every element separately [58]. This complicates the informed-design process of HEAs due to a high degree of freedom because of multi-principal elements in the bulk. Considering the design of such alloys with multi-principal elements, even the final properties of the HEAs within the same system might be very different from each other due to numerous possible combinations of constituent elements, which makes the discovery and design process cumbersome by just using conventional trial-and-error methods [59]. As a remedy for this problem, computational tools such as density functional theory (DFT), molecular dynamics (MD) simulations, and machine learning (ML) applications can be helpful. Within these methods, designing alloys using DFT requires a vast amount of computational power, and the lack of inter-atomic potential functions representing different compositional spaces for HEAs restricts the efficient use of MD simulations. On the other hand, ML is an efficient tool to establish the relationship and unearth the implicit connections between the features and target property, making the design process much faster than DFT and MD methods [64,65].

From a corrosion engineering perspective, the earliest works regarding ML applications in corrosion science were mostly on developing corrosion-resistant steels for marine applications in the last decade [119,285]. Though few, ML methods were also recently implemented for developing corrosion-resistant HEAs. Being one of the first, Yuan et al. utilized the extreme gradient-boosting regression algorithm to predict a new HEA composition in the U-Mo-Nb-Ti-Zr system with a high corrosion-resistant lifetime in 343 ºC boiling water, using a dataset consisting of 50 experimental observations [286].

In another work, Sasidhar et al. reported that transition metal HEAs containing large amounts of carbon and nitrogen interstitials indicated improved pitting corrosion resistance, while chloride ion concentration was determined to be the most detrimental environmental parameter for all alloy systems in their datasets [287]. In addition to compositional information and environmental parameters, using additional features (i.e., descriptors representing the chemical and physical properties of the alloys) was also proven to be a practical approach for enhancing the accuracy of the predictions in the materials science [90]. For instance, the pH of the medium, halide molarity, difference in lattice parameters, average reduction potential, and the composition of the element with minimum reduction potential were selected out of 30 features to train a gradient-boosting regression (GBR) algorithm and predict the corrosion rate of medium entropy alloys [288].

In the current study, an ML-based HEA prediction framework (Figure 5-1) consisting of five major steps was developed. These included dataset preparation, feature engineering, model evaluation and feature selection, inverse composition design, and experimental validation showcasing the design of HEAs with desired corrosion properties. After the dataset was constructed from the literature and the calculated features were added, feature selection and model evaluations were performed. The Random Forest (RF) algorithm was selected as the final model to screen the whole compositional space in the HfNbTaTiZr system and find an optimum composition. The dataset consisted of experimental works on as-cast samples produced by arc melting. Thus, the optimized composition was also manufactured with arc melting. The optimized composition was then synthesized, and predictions were validated with potentiodynamic polarization experiments. Additionally, X-ray photoelectron spectroscopy (XPS) analysis was performed to investigate the oxide layer composition on the surface of the new HEA.

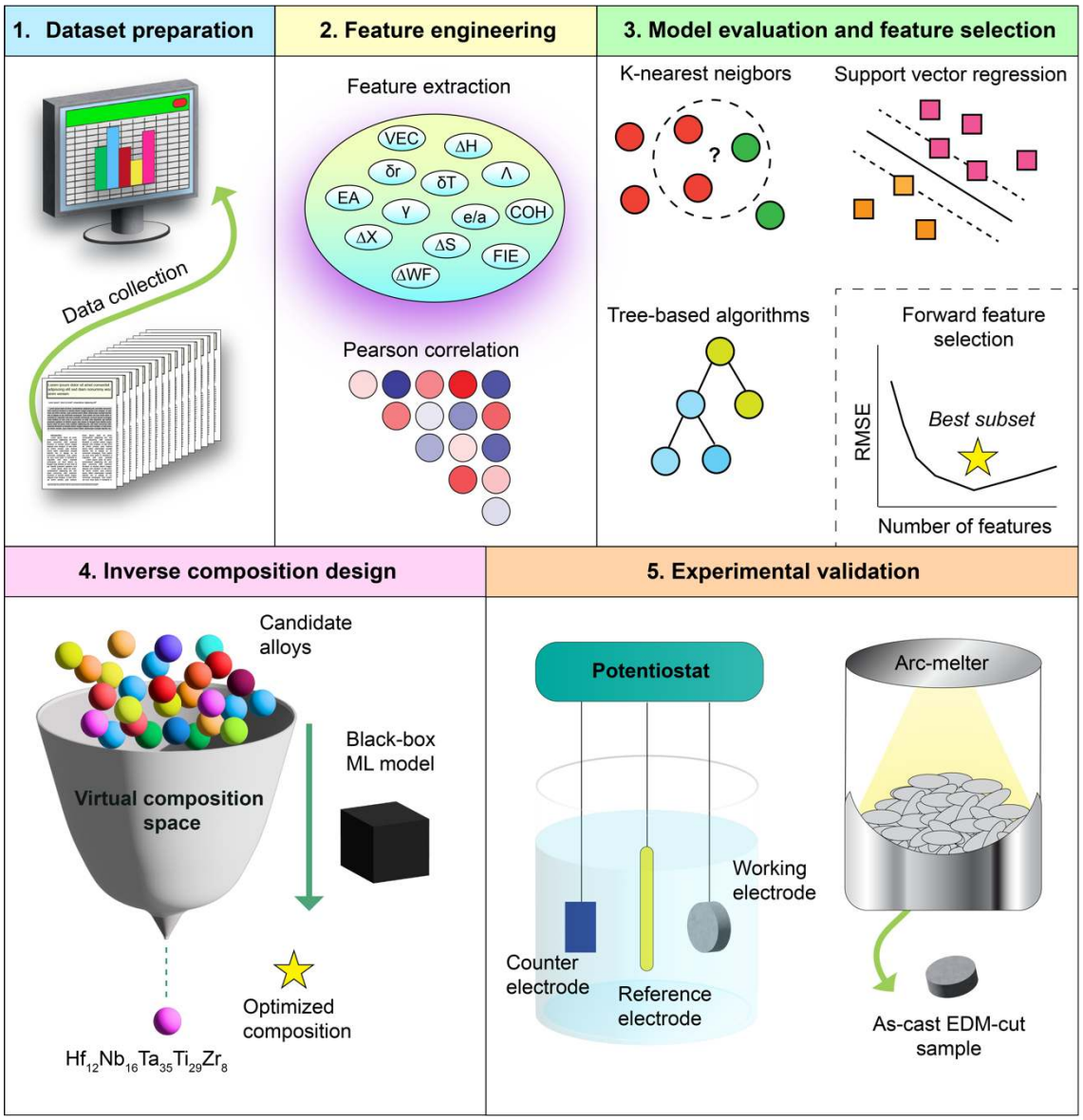

Figure 5-1: Schematic of the machine learning-informed alloy design strategy for predicting the HEA composition with the desired corrosion potential.

The experimental findings detailed herein demonstrated that the optimized composition $Hf_{12}Nb_{16}Ta_{35}Ti_{29}Zr_8$ (HEA-Center), predicted utilizing the RF algorithm, possessed a dendritic microstructure in the center of the ingot. The EDX line scans performed on the HEA-Center sample indicated the formation of Ta-rich dendrites with severe segregation during manufacturing. The corrosion potential (E_{corr}) predicted for HEA-Center was -409 ± 35 mV, which was very close to the predicted value of -404 mV, demonstrating that the ML model can make accurate predictions for the E_{corr}. XPS investigations showed that Ti oxide formation was favored in the potentiodynamic polarization experiments carried out in simulated body fluid (SBF) at 37 ± 1 ºC compared

to the air-formed oxide layer. Although the discussion was mainly restricted to the specimens extracted from the center of the ingot (referred to as HEA-Center) with dendritic microstructure, it was found that some other parts (referred to as HEA-Top) of the ingot had more homogeneous microstructure due to the different solidification conditions experienced during the arc melting process. Polarization experiments performed on the HEA-Top sample with the same elemental composition as that of the HEA-Center revealed superior corrosion properties. These findings indicate that once the composition and microstructure are tuned, HEAs can have superior corrosion resistance, warranting further research to understand the factors governing the corrosion behavior of these alloys.

5.2 Methods

5.2.1 Computational

In the first step, a dataset was constructed gathering binary, ternary, quaternary, quinary, and senary alloys from the literature, having different compositions with diverse combinations containing Ti, Ta, Hf, Nb, Zr, Mo, and Sn elements. In addition to the alloy compositions (designated in at% in the dataset), the corresponding corrosion potential (E_{corr}) and the other experimental details, such as electrolyte type, pH, and temperature at which the polarization experiments were performed, were collected from the corresponding references. To eliminate the effect of processing or heat-treatment conditions on the target property, i.e., E_{corr}, only alloys synthesized by vacuum arc-melting (VAM) and tested in as-cast form were included in the dataset. The final dataset contained 46 alloys, as listed in the Supplementary Information of [289]. The dataset used in this study is limited in the amount of data it contains for three reasons. First, manufacturing materials with varying compositions and obtaining corresponding target variables are experimentally laborious and costly, especially for HEAs. Furthermore, only some of the published literature possesses the relevant experimental data conducted in the same experimental conditions. The ability of ML algorithms to make accurate predictions depends on the credibility of the experimental data collected since the volume of it is already very limited. Hence, the accuracy and quality of the data added to the datasets are crucial for reducing error during training, resulting in robust ML models with better

generalization capabilities [65]. Additionally, it should be noted that E_{corr} was used in this study to show the applicability of ML in corrosion science with small data sets. However, E_{corr} is a parameter that does not directly reflect the corrosion rate. The reason for not using current density (i_{corr}) is that it is measured from Tafel plots manually by the users. The accuracy of the reported results in the literature depends on the Tafel slope drawn, which is often hard to determine accurately. Considering the small dataset gathered from the literature, using a target variable whose accuracy depends on the different users' experiences would not be feasible.

Modeling the underlying trend between the target variable and the constituents' atomic percentages might not be enough when the compositional input fails to explain the patterns hidden in the target variable [71,90]. Therefore, a feature extraction step from the element's chemical and physical properties is necessary to discover new features correlated to the target variable [90]. In the present study, there were 22 calculated features in the final dataset original feature pool in addition to 12 experimental features (the atomic percentage of the Ti, Ta, Hf, Nb, Zr, Mo, and Sn elements and experimental parameters, such as electrolyte type, pH, and temperature). The final dataset contained 46 alloys, as listed in the Supplementary Information of [289]. The calculated features include the valence electron concentration (VEC), the atomic size difference (δr), the difference in electronegativity (Δχ), the mixing enthalpy (ΔH), the configurational entropy (ΔS) [126], the ∧ parameter designed by Singh et al. [128], the γ parameter suggested by Wang et al. [129], the number of itinerant electrons (e/a) [130], and other features calculated from shear modulus (G), melting temperature (T), electron affinity (EA), first ionization energy (FIE), cohesive energy (COH), and work function (WF) of the elements. The feature set with definitions and formulas is given in the Appendix B.

The problem with having a high number of input variables is that the high correlation between some features might cause multicollinearity, resulting in deteriorated model performance and high standard error in the predictions [290]. In other words, ML algorithms recognize these highly correlated features as duplicate information, thus decreasing the model's robustness and leading to inaccurate predictions. Therefore, after completing the feature creation, a correlation screening [76] among all features was performed to identify the highly correlated features. To accomplish this, the Pearson correlation coefficient (PCC) with a 0.95 threshold to remove one of the two highly correlated features was used. If the PCC between two features is higher than 0.95, the one

with the higher importance is preserved in the dataset [77]. The importance of two correlated features was computed utilizing an RF regressor.

The third component of the design framework consists of ML model comparison, forward feature selection (FFS), and final model selection. To construct the predictive model based on the composition and calculated features, k-nearest neighbor (KNN), GBR, RF, support vector regression with a polynomial kernel (SVR-P), and support vector regression with a radial basis kernel (SVR-R) models were utilized. Since deep learning algorithms and neural networks require abundant data for training [291], such algorithms were not employed in the present study. It should be noted that a standard normalization method, which alleviates the skewness problem in the sample points in the data, was applied to the dataset to scale and normalize the data around zero mean with a standard deviation equal to one. During the model evaluation, 5-fold cross-validation (CV) and bootstrapping with replacement were used to evaluate the models' performances. Bootstrapping is highly effective when assessing the performance and generalization ability of the ML algorithms against the variability of the data in the training dataset [292]. The model evaluations and feature selection were made considering two error metrics: coefficient of determination (R^2) and root mean squared error (RMSE) metrics.

Feature elimination is one of the most important parts of designing a predictive ML algorithm. The more feature is retained in the dataset, the more ML models will be prone to overfitting due to high degrees of freedom, leading to a deterioration in the generalization ability of the ML models. Thus, selecting the best feature set is significant to avoid overfitting and have a simple model with good interpretability and better accuracy. In the present study, after performing PCC combined with RF as the first feature elimination step, FFS was used to select the best subset of features describing the target variable (E_{corr}) more efficiently. FFS is a process that first chooses one feature, maximizing a CV score when the model is trained on every feature. Then, it adds the remaining features sequentially one by one, retaining the one maximizing the CV score in each step [293].

In the fourth component, i.e., inverse composition design, a virtual space was first created containing more than 500000 different compositions, where Ti, Ta, Hf, Nb, and Zr contents were varied between 5 and 35 at% with a one at% step size, complying with the official HEA definition. Subsequently, the compositions in the virtual space were fed

into the best-performed ML model to make E_{corr} predictions. Then, the predictions were sorted from the largest to smallest E_{corr} values. The approach maximizing the expected improvement (EI) utilized by Wen et al. [90] and Xue et al. [294] was followed to select the best candidate in the virtual space out of the best predictions obtained. The EI is defined as $EI = E[max(y - \mu^*, 0)] = \int_{\mu^*}^{\infty}(y - \mu^*)P(y|x')dy = \sigma[\varphi(z) + z\phi(z)]$, where $\varphi(z)$ is the standard normal density function, $\phi(z)$ is the cumulative distribution function, $(y - \mu^*)$ is the possible improvement for the predicted values, $P(y|x')$ is the distribution of the predicted *y* values (predicted *y* values, i.e., E_{corr}, are assumed to have a normal distribution), and $z = (\mu - \mu^*) / \sigma$, where μ^* is the maximum value of E_{corr} in the training data, μ and σ are the mean predicted value and standard deviation. Specifically, μ and σ were calculated from 100 training performed on 100 bootstrap training datasets to obtain 100 predictions for each alloy in the virtual space. In other words, μ and σ were estimated from 100 bootstrap predictions to acquire EI for each alloy in the virtual space. Once the alloys were sorted with respect to the EI values, the best candidate was chosen considering ΔS and σ of 100 bootstrap predictions of the alloys in the final candidate list.

5.2.2 Experimental validation

The final and fifth component of the design framework, as illustrated in Figure 5-1, is experimental validation, where the optimized composition was produced, and polarization experiments were performed to validate the accuracy of the ML model. The alloy selected from the candidate pool with the optimum composition, i.e., $Hf_{12}Nb_{16}Ta_{35}Ti_{29}Zr_8$ (HEA-Center), was synthesized by vacuum arc-melting on a water-cooled copper crucible under a Ti-gettered argon atmosphere. The Ti, Ta, Hf, and Nb elements had a purity of 99.9%, and Zr had a purity of 99.2%. The ingots were flipped five times between each melting to assert compositional homogeneity. The as-cast ingots were then cut by wire electro-discharge machining (EDM) to extract specimens with 10 mm diameter and 2 mm thickness. The surfaces of the samples were ground with SiC paper and polished with 0.3 μm alumina slurry. The phases formed in the samples were characterized by X-ray diffraction (XRD) analysis utilizing a Bruker D8 Discovery X-ray diffractometer equipped with a 2D detector and a Cu-Kα radiation source. A Zeiss SUPRA 55VP scanning electron microscope (SEM) was used to investigate the microstructures of the as-cast specimens. Chemical composition and the elemental

mapping of the samples were acquired utilizing an energy-dispersive X-ray spectroscopy (EDS) detector (Bruker AXS GmbH). An acceleration voltage of 20 kV was applied during the EDS measurements. The predicted (i.e., the nominal) and the actual compositions of the HEA-Center are tabulated in Table 5-1.

Table 5-1: Nominal and actual chemical compositions (at%) of HEA-Center analyzed utilizing EDS.

Element	Nominal (predicted)	Actual
Hf	12	14.6 ± 0.6
Nb	16	16.2 ± 0.5
Ta	35	34.4 ± 1.3
Ti	29	27.3 ± 0.3
Zr	8	7.3 ± 0.2

The corrosion resistance of HEA-Center alloy was evaluated in SBF (pH = 7.4 ± 0.05). The preparation methodology of SBF electrolytes described elsewhere, along with the chemical composition [140], was followed. Before the polarization experiments, the EDM cut samples were covered with epoxy, leaving only a 1 cm^2 surface area, followed by polishing with 0.3 µm alumina slurry. The electrochemical polarization experiments were performed in a three-electrode cell with a platinum spiral wire as a counter electrode and a saturated calomel electrode (SCE) as a reference electrode at a constant temperature of 37 ± 1 ºC by using an electronically controlled thermostatic bath. The electrochemical measurements were conducted using a potentiostat (Biologic Science Instruments, VSP) controlled by a computer equipped with the EC Lab software. All potentials were referred to the SCE reference electrode. Before each experiment, the working electrode was immersed in the solution for 30 minutes to stabilize the open circuit potential (EOCP). Potentiodynamic polarization curves were recorded from an initial potential of -1 V up to the final potential of 1.2 V with respect to EOCP at a scan rate of 1 mV s^{-1}. The corrosion potential (E_{corr}) and corrosion current density (i_{corr}) were acquired by extrapolating the Tafel slope.

The oxide films were investigated by XPS (Thermo Scientific K-Alpha), employing a monochromatic Al-Kα X-ray source (1486.6 eV), to find the oxidation states of the

species. The relative sensitivity factors of the pure elements were considered while calculating the apparent surface composition of each oxide species, using integrated intensities (peak area) of deconvoluted peaks. The XPS analyses were conducted using a pass energy of 50 eV.

5.3 Results

5.3.1 Computational

Initial screening with the PCC method was implemented to remove the features with high correlation. The right-top corner of Figure 5-2 illustrates the PCC values between feature pairs, where a PCC higher than 0.95 indicates a high correlation between the two corresponding features. Based on Figure 5-2, it can be concluded that δr and ΔWF, δG and ΔG, and δT and ΔT are highly correlated feature subsets. After identifying highly correlated features, each feature was evaluated based on its importance using the RF algorithm. A 5-fold CV was used to estimate the importance of each feature, and the results are shown in the left-bottom corner of Figure 5-2, where the same color code represents three different highly correlated feature subsets. Accordingly, ΔWF, ΔG, and δT were eliminated from the dataset as they were determined to be redundant features.

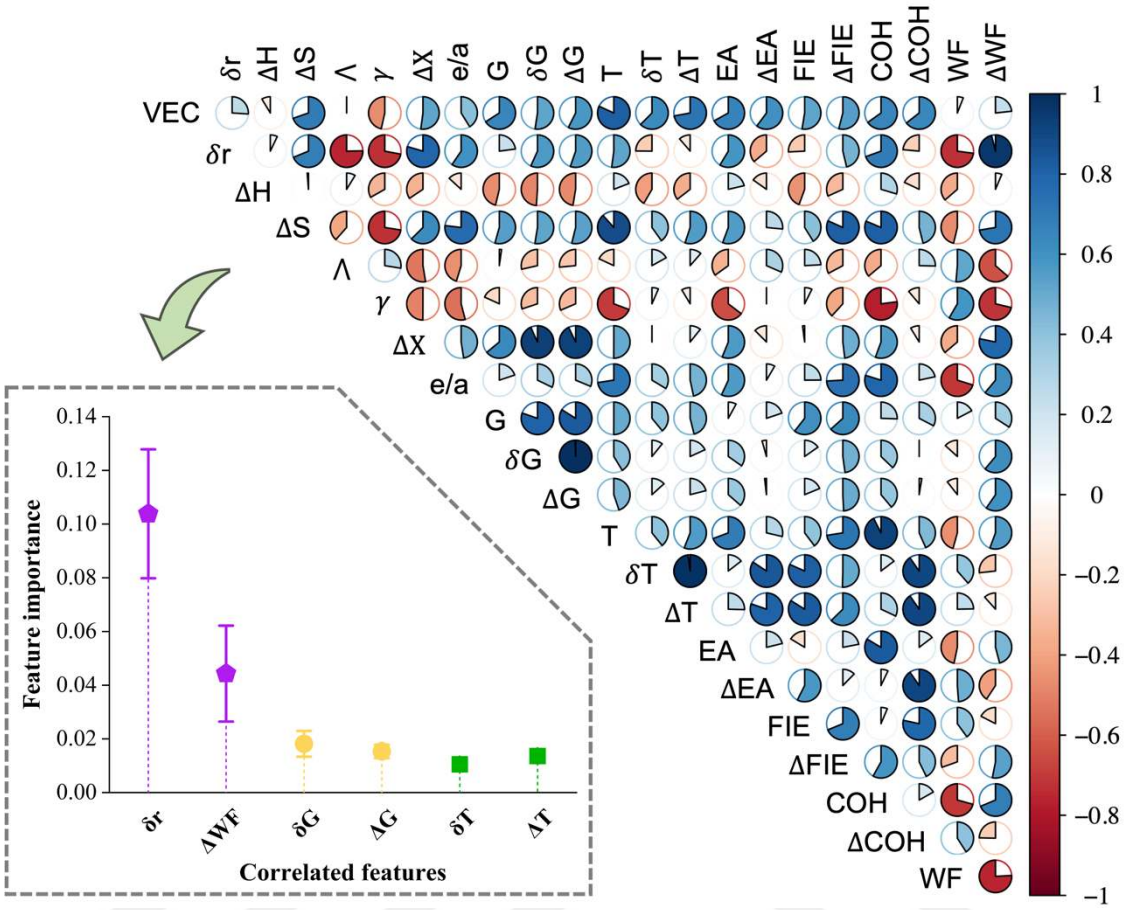

Figure 5-2: Pearson correlation map of the initial twenty-two calculated features, where a circle filled with deeper color indicates a higher level of correlation; in the left-bottom inset, the same-colored features represent the highly correlated features, among which the one with the highest importance was preserved.

Once the redundant features were removed, KNN, GBR, RF, SVR-P, and SVR-R models were used evaluated to construct preliminary predictive models with acceptable accuracy and good generalization ability to predict E_{corr} using elemental compositions, experimental details (compiled from the literature) and calculated feature space. The performance of the models was evaluated based on the R^2 metric estimated by 5-fold CV (Figure 5-3a) and bootstrapping 100 times with replacement (Figure 5-3b). Since the dataset utilized herein contained a limited number of instances due to the aforementioned reasons, using only the CV method to evaluate model performances might give misleading results depending on how the dataset was split. To elaborate with an example, the KNN model provided the best average R^2 value solely based on Figure 5-3a; however, once the model was trained with 100 bootstrapped training datasets, it resulted in a low average R^2 score with a skewed distribution along with the highest number of outliers.

This result indicates that bootstrapping is a powerful method to assess the models' robustness and stability against the uneven data distribution in the training dataset. Based on Figure 5-3, GBR and SVR-P models had a low R^2 score with a wide distribution around the mean. The broader distribution of values around the mean, such as in the case of SVR-P, as shown in Figure 5-3b, demonstrates that the model's generalization capability against variation of data distribution in a dataset is inconsistent. Among all the models trained at this step, the RF algorithm revealed a narrower distribution for the R^2 score around the mean, as demonstrated in Figure 5-3, confirming its robustness. Although the SVR-R model resulted in more variability around the mean for the R^2 score because it had a closer R^2 score to the RF model, it was also selected in addition to the RF model to continue for further evaluation. The reason for choosing the SVR-R model for further evaluation was that SVR-R might perform better and give better accuracy once the feature space is reduced into a smaller one, thus reducing the uncertainty in the predictions.

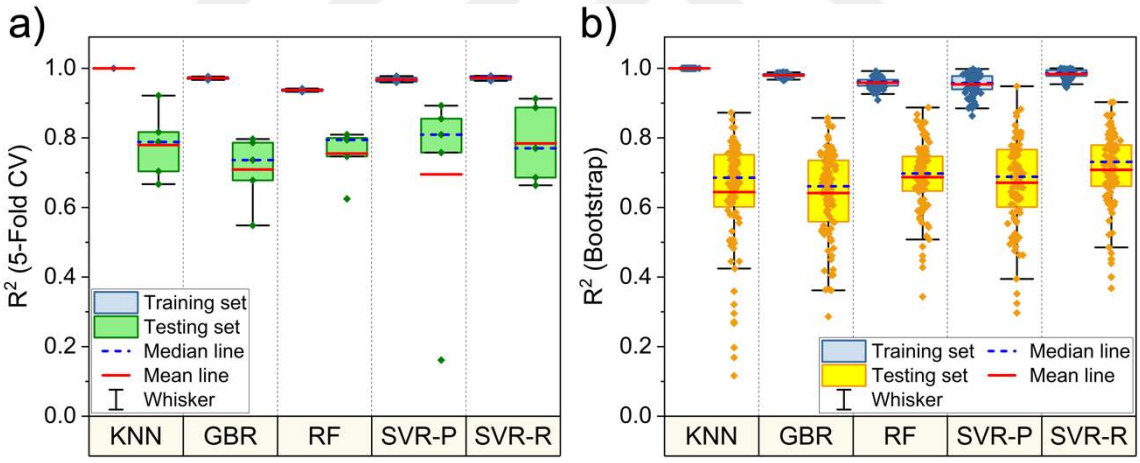

Figure 5-3: Machine learning models and their R2 values estimated utilizing (a) 5-fold CV and (b) bootstrapping 100 times with replacement: The lower and upper limits of the box plots demonstrate the 25th and 75th percentiles, with red and dashed blue lines representing the mean and median of the distribution, respectively; the whiskers extend to the data points within 1.5 times the interquartile range (the points outside the whiskers' caps are outliers); a closer mean and median lines show a distribution with a better bell-like shape around the mean.

Following the evaluation of the models, the FFS process was implemented separately for both RF and SVR-R models. Before starting the feature elimination, the SBF, AS, BF,

pH, and Temp input variables were fixed as a group to be included in the final feature space at the beginning, and the FFS process was carried out by adding every other feature on top of these. In other words, since the current study aimed at making the best E_{corr} predictions considering different electrolyte types, pH, and temperature effects, these features were pre-included in the final feature space to be constructed after forward feature selection. The average RMSE of both models was around 125 mV when the models were trained only with a pre-selected feature set, i.e., SBF, AS, BF, pH, and Temp, indicated by green arrows in Figure 5-4a1 and Figure 5-4a2 for RF and SVR-R, respectively. The decreasing trend followed by an increase in the RMSE was observed for both RF (Figure 5-4a1) and SVR-R (Figure 5-4a2) with an increasing number of features. In other words, as more features are included as input into the models, the error either increases or levels off. The best feature subsets obtained with FFS for RF and SVR-R models are tabulated in Table 5-2 (the yellow triangles in Figure 5-4a1 and Figure 5-4a2). It should be noted that the best feature subsets were selected greedily based on the lowest RMSE. After choosing the best subset of features, a grid search strategy was implemented to optimize the models' hyperparameters.

Table 5-2: The best subset of features selected using the FFS method for RF and SVR-R algorithms.

Algorithm	Best-subset of features
RF	Ti, Ta, Hf, δr, ΔX, ea, G, δG, T, COH, SBF, AS, BF, pH, Temperature
SVR-R	Ta, Hf, Zr, Mo, Sn, δr, ΔH, ΔS, γ, ΔX, G, δG, ΔT, FIE, ΔFIE, ΔCOH, WF, SBF, AS, BF, pH, Temperature

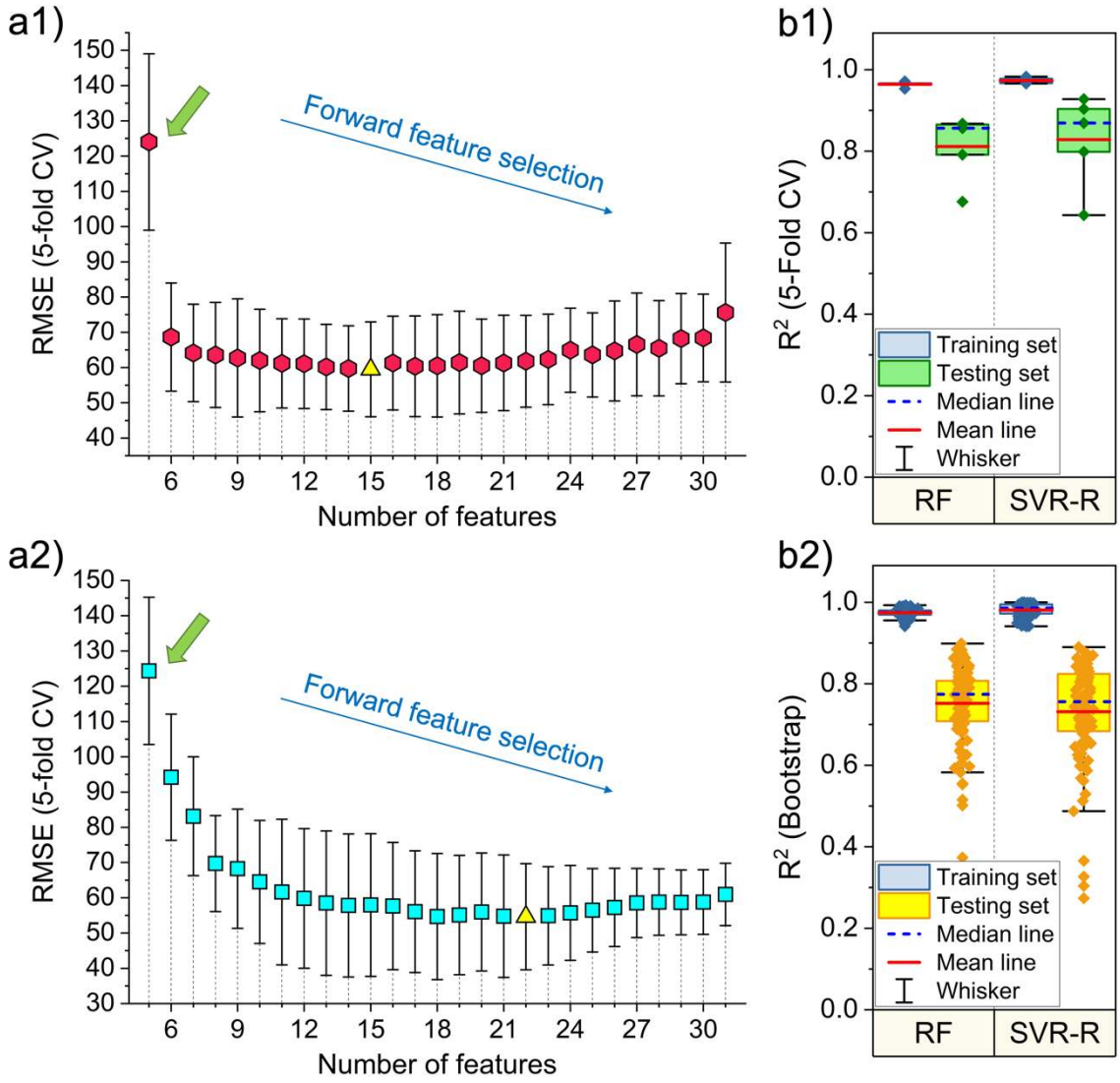

Figure 5-4: The process of FFS for (a1) RF and (a2) SVR-R models (yellow triangles represent the feature subset resulting in the lowest RMSE for both models); the R2 metric, calculated by (b1) 5-fold CV and (b2) bootstrapping, was obtained when the best feature subset was utilized in the training process of RF and SVR-R models.

The distribution of R^2 values, estimated utilizing 5-fold CV and bootstrapping as shown in Figure 5-4b1 and Figure 5-4b2, showcase the performance of the RF and SVR-R models trained with the best subset of features. Although both models performed similarly, the values are more distributed for the SVR-R model, showing its vulnerability to the variations in the dataset due to different splits implemented during CV and bootstrapping. To elaborate, R^2 and RMSE metrics for both RF and SVR-R models are listed in Table 5-3.

Table 5-3: The R^2 and RMSE scores of the final RF and SVR-R algorithms estimated using 5-fold CV and bootstrapping 100 times with replacement.

Method	**Algorithms**	R^2		**RMSE**	
		Training	**Testing**	**Training**	**Testing**
CV	RF	0.96 ± 0.01	0.81 ± 0.07	25.0 ± 1.3	55.2 ± 10.2
	SVR-R	0.98 ± 0.01	0.83 ± 0.10	21.5 ± 2.9	50.5 ± 10.9
Bootstrap	RF	0.97 ± 0.01	0.75 ± 0.09	20.5 ± 3.1	63.9 ± 13.8
	SVR-R	0.98 ± 0.02	0.73 ± 0.12	16.1 ± 7.5	65.9 ± 15.0

Considering the CV results for both R^2 and RMSE, it can be concluded that the SVR-R performed better on the testing dataset, though with a higher deviation than RF around the mean values. Additionally, when bootstrapping was implemented, RF demonstrated better performance on the testing data with a lower variation than SVR-R around the mean values, suggesting that RF was more resistant and influenced less by the scatter in the data during each split of bootstrapping. Thus, the RF algorithm was chosen among all the models used in this study as the final model. It should be noted that the slightly high RMSE values can be attributed to the limited dataset and the possibility of having experimental data with high deviation in the dataset since the data were collected from various sources in the literature [295]. Furthermore, to demonstrate the prediction performance of the RF model, the parity plots are presented in Figure 5-5. In Figure 5-5a, where the dataset was split into two with a training-to-testing ratio of 80:20, and the experimental vs. predicted E_{corr} values are shown. The comparison of the experimental and predicted E_{corr} values for the testing set during CV splits is demonstrated in Figure 5-5b. The prediction results are almost the same, showing similar performances for the testing sets of random split and 5-fold CV.

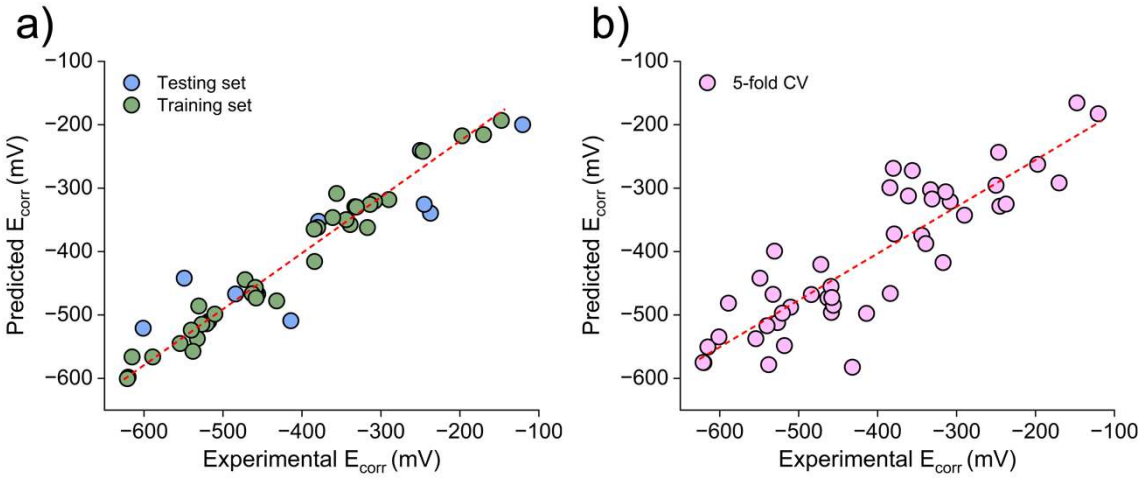

Figure 5-5: The parity plots for (a) randomly split training and testing sets (80:20) and (b) 5-fold CV utilizing the RF model.

5.3.2 Experimental

In Figure 5-6, two specimens, namely, HEA-Top and HEA-Center, were cut from the button-shaped as-cast ingot. The experimental part of this study focuses on the HEA-Center specimen since the dataset employed to predict a new composition consists of alloys produced by VAM, leading to an inhomogeneous microstructure. The middle part of the button-shaped ingot revealed a dendritic microstructure, as shown in Figure 5-6b. However, the microstructure changed from a dendritic to a more homogeneous microstructure from the middle to outer regions of the samples (Figure 5-6b and Figure 5-6d). Furthermore, a thin layer of dendritic structure is observed in the circumference of the as-cast ingot with a thickness of about 0.7 mm, as demonstrated in Figure 5-6c. This variation of the microstructure stems from the nature of the arc-melting process. The ingots are exposed to different solidification rates during the solidification process, affecting the segregation of some species in the dendritic or inter-dendritic arms, thus altering the resulting microstructure.

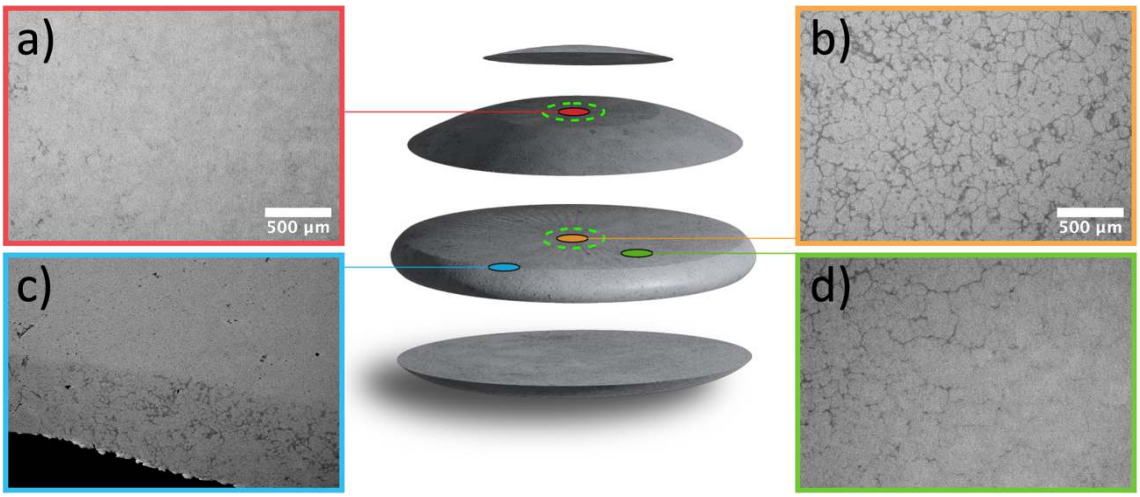

Figure 5-6: Schematic showing how the as-cast ingot was cut by EDM: The red and orange colors represent the specimen cut from (a) the top (HEA-Top) and (b) the center (HEA-Center) parts of the as-cast ingot the change in the microstructure in the disk, from which the HEA-Center sample was cut with EDM, can be seen in the SEM micrographs taken from (b) center, (c) circumference, and (d) a region halfway between the center and circumference. Specifically, the highly dendritic microstructure in the core of the as-cast ingot (b) turns into a more homogenous microstructure closer to the circumference (d), followed by a thin dendritic layer in the circumference (c).

In Figure 5-7a, an elemental map illustrating the severity of the elemental segregation is shown for the sample cut out from the middle, i.e., HEA-Center, of the ingot. Based on the elemental map and the line scans, as illustrated in Figure 5-7a and Figure 5-7b, respectively, Hf, Zr, and Ti segregated into the inter-dendritic regions, whereas Ta segregated into the dendrite arms. However, Nb was more homogeneously distributed throughout the microstructure than the other elements, as demonstrated in the line scan in Figure 5-7b. The formation of dendritic microstructure was also reported in numerous studies related to other refractory HEAs, attributed to the tendencies of the higher melting point elements to solidify first in the dendrite arm, thus affecting diffusion and solidification kinetics [296]. Figure 5-7c demonstrates the XRD pattern acquired from the HEA-Center sample. The crystal structure of the HEA-Center was determined as BCC. Figure 5-7d shows a closer inspection of the (200) peak with BCC1 (brighter Ta-rich dendrites) and BCC2 (darker HfTiZr-rich inter-dendrites) phases coexisting in the microstructure. Additionally, an elemental map for the HEA-Top specimen compared with that of the HEA-Center (Figure 5-7a) is shown in Appendix C.

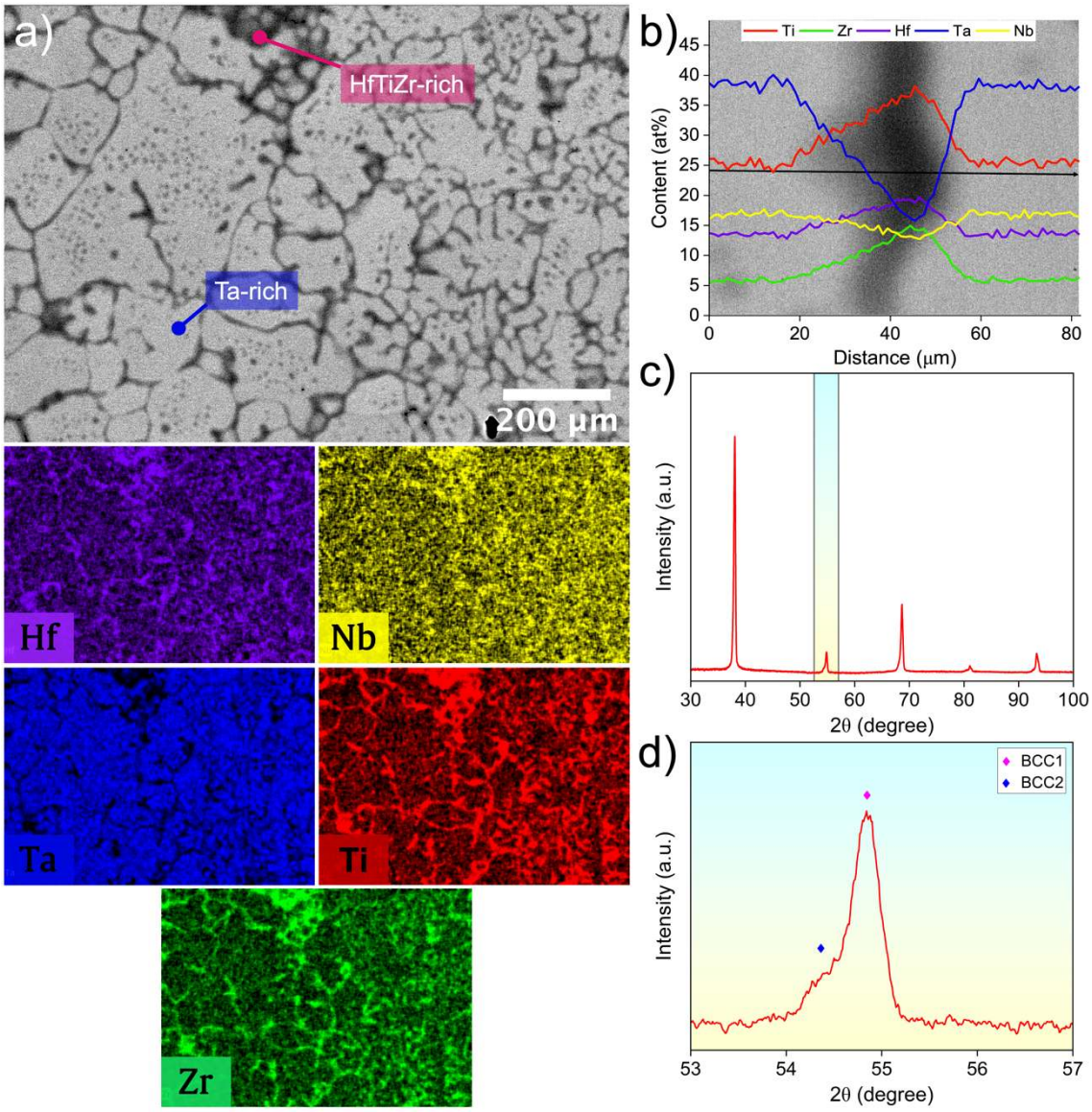

Figure 5-7: (a) High magnification SEM image of HEA-Center with the corresponding elemental maps, (b) EDS line scan of the elements (the black arrow in the middle of the image shows the line that the EDS line scan was performed along), (c) XRD patterns of as-cast HEA-Center sample, and (d) the (200) peak indicating the presence of the BCC1 and BCC2 phases.

To analyze the composition of the oxide film formed on the surface of HEA-Center exposed to air (Figure 5-8a) and during the polarization experiments in SBF at 37 ± 1 ºC (Figure 5-8b), XPS analysis was carried out. Mainly, the XPS spectra of Hf 4f, Nb 3d, Ta 4f, Ti 2p, and Zr 3d were investigated to acquire information related to the oxidation states in the oxide layers. The oxide layer formed upon exposure to air revealed metallic Hf, Nb, Ta, and Zr peaks in their corresponding spectrums, except for Ti, as illustrated in Figure 5-8a. On the contrary, no metallic states were observed after polarization

experiments in SBF based on Figure 5-8b. The deconvoluted spectrum in the Hf 4f region indicated different oxidation states: Hf^{4+} and a low-valance state Hf^{x+} [262]. Similarly, the Zr 3d spectrum displayed different oxidation states: Zr^{4+} and low-valance Zr^{x+} [263]. Ta was detected in the high-valance oxide state Ta^{5+} and low-valance states such as Ta^{4+}, Ta^{3+}, and Ta^{1+} [265]. No Ta^{3+} oxidation state was detected in the oxide layer formed during the polarization experiments in SBF, as shown in Figure 5-8b. The Nb element also revealed peaks corresponding to the high-valance oxide state Nb^{5+} and low-valance states such as Nb^{4+} and Nb^{2+} [296]. The deconvoluted spectrum in the Ti 2p region indicated oxidation states of Ti^{4+} and a low-valance state of Ti^{3+} [266]. Figure 5-8c demonstrates the oxide concentrations (at%) for each element in the passive film of the alloy exposed to air and polarization experiments in SBF at 37 ± 1 ºC. While the high-valance oxidation state Ta^{5+} increased in SBF by about 4.5 at%, the total amount of Ta oxide formed in SBF decreased almost by three at%. Although the concentrations of Hf, Nb, and Zr oxides were in the same range, the total Ti oxide formed in SBF increased by around three at%, compensating for the decrease in the Ta oxide concentration. The increased Ti oxide concentration in the passive film formed in SBF might be associated with Ti being highly resistant to chloride ions [297]. Binding energies associated with Hf, Nb, Ta, Ti, and Zr peaks are listed Appendix D.

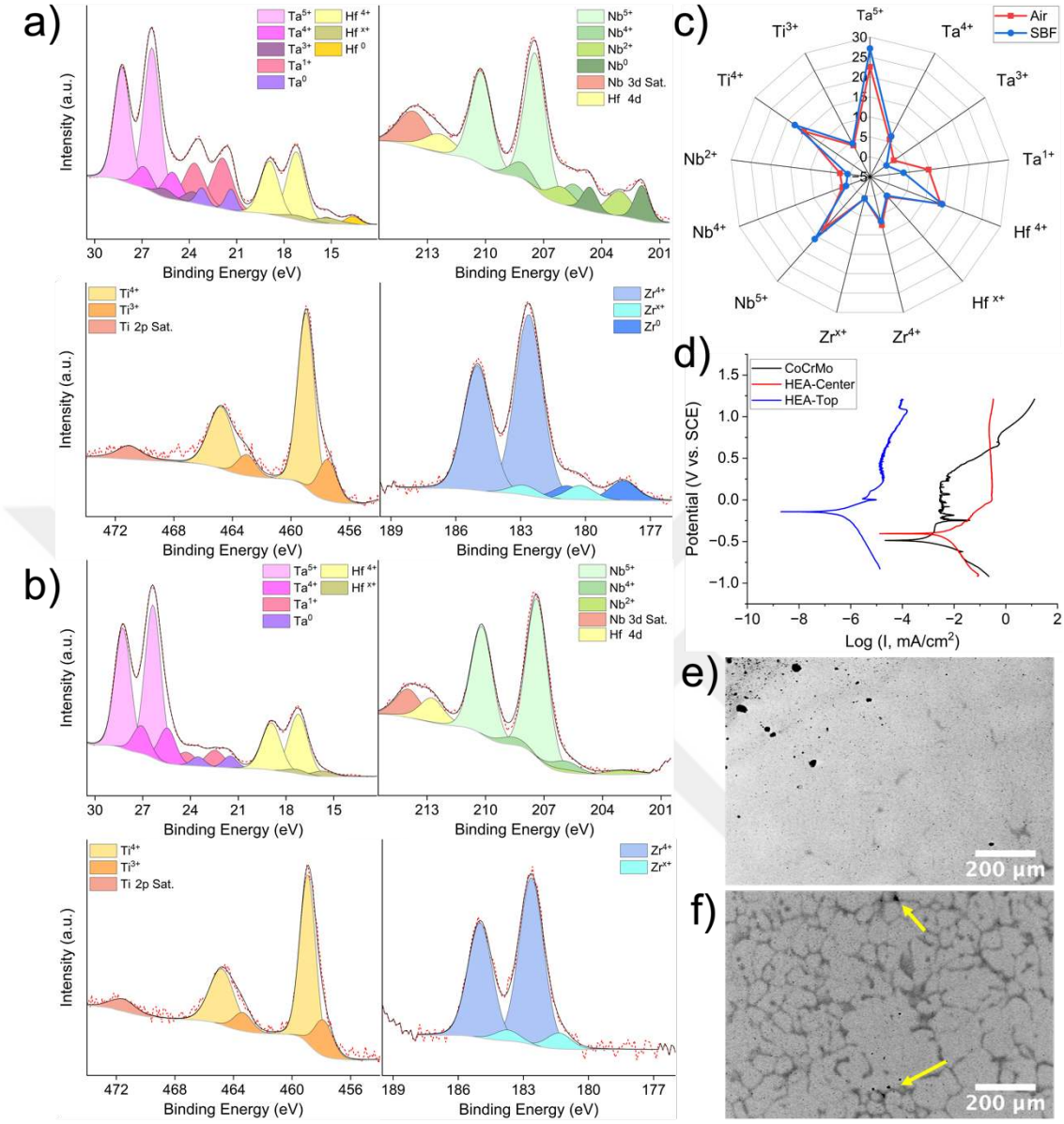

Figure 5-8: High-resolution XPS spectra of the HEA-Center specimen's surface after exposure to (a) air and (b) polarization experiments in SBF at 37 ± 1 ºC; (c) radar plot showcasing oxide concentrations (at%) for each element in the passive film of the alloy exposed to air and polarization experiments in SBF; (d) potentiodynamic curves of HEA-Center, HEA-Top, and CoCrMo (the data were recompiled from [296] for CoCrMo); the SEM images show the microstructure of (e) HEA-Top and (f) HEA-Center following electrochemical polarization tests in SBF.

The potentiodynamic polarization curves of HEA-Top, HEA-Center, and CoCrMo (27 wt% Cr, 6 wt% Mo, and balance Co) as the reference material in SBF are presented in Figure 5-8(d). CoCrMo has been selected as a reference material since it is one of the

most used biomedical alloys for orthopedic applications, in addition to 316L and Ti6Al4V alloys [85,298]. The initial purpose of this study was to investigate the as-cast corrosion properties of the predicted HEA composition, which has a dendritic microstructure. Since it was discovered that a more homogeneous microstructure was also present in the ingot (namely, HEA-Top, as demonstrated in Figure 5-8a), its corrosion behavior was also examined. Based on Figure 5-8d, the passive layer of CoCrMo broke down very early at a potential of about 0.25 V [296]. The HEA-Center specimen showed no sign of metastable pitting or breakdown of the oxide layer, suggesting that the passive oxide layer forming on it was stable and resistant against chloride attacks. The passive oxide layer breakdown around 0.5 V anodic potential and trans-passive dissolution commenced afterward for the HEA-Top specimen.

As for the surface morphology after polarization experiments, HEA-Top exhibited noticeable pits with smaller-sized pits around them, as demonstrated in Figure 5-8e. These large pits might explain the trans-passive dissolution observed in Figure 5-8d for HEA-Top, where the oxide layer could not be completely re-passivated, making it a source for releasing metallic ions. On the contrary, the HEA-Center sample had tiny pits distributed more homogeneously. However, some pits are concentrated severely in the inter-dendritic zones, indicated by yellow arrows in Figure 5-8f.

5.4 Discussion

Table 5-4 illustrates the electrochemical parameters obtained utilizing the Tafel extrapolation method. E_{corr} and i_{corr} values are used to assess the corrosion resistance of the materials. In addition to E_{corr} and i_{corr}, polarization resistance (R_p) was calculated using the Stern-Geary [282] equation:

$$R_{\mathrm{p}} = \frac{\beta_{\mathrm{a}}\beta_{\mathrm{c}}}{2.303 i_{\mathrm{corr}}(\beta_{\mathrm{a}} + \beta_{\mathrm{c}})} \tag{5.1}$$

where β_{a} is the anodic Tafel slope, and β_{c} is the cathodic Tafel slope. R_p indicates the resistance of a material to general corrosion, and higher values reflect a superior corrosion resistance [230]. The results for the designed composition (referred to as HEA-Center (nominal) in Table 5-4) and the actual composition (HEA-Center (actual) in Table 5-4) manufactured using VAM are shown in Table 5-4 in addition to the data for HEA-Top

and CoCrMo samples. The nominal and actual compositions are given in Table 5-1. For the designed composition (HEA-Center (nominal)), an E_{corr} value of -352 ± 55 mV was predicted, as shown in Table 5-4. Because the designed (nominal) and manufactured (actual) compositions are slightly different, especially for Hf, as seen in Table 5-1, the prediction that results for the actual composition is also given. As a result, the E_{corr} predicted for HEA-Center (actual) is -409 ± 35 mV, as shown in Table 5-4. The experimental E_{corr} obtained from the polarization experiments was -404 mV, which is very close to the predicted value for this composition. This indicates that the model can make accurate predictions for the target property. Furthermore, although the final model has a moderate deviation around the mean predicted value, it has good generalization ability since the experimental and predicted results for the HEA-Center (actual) alloy are very close.

Table 5-4: Electrochemical parameters of HEA-Center, HEA-Top, and CoCrMo in SBF at 37 °C ± 1 ºC.

Alloy/Sample	**Predicted E_{corr} (mV)**	**Experimental E_{corr} (mV)**	**i_{corr} (µA/cm²)**	**β_a (mV)**	**β_c (mV)**	**R_p (kΩ cm²)**
HEA-Center (nominal)	-352 ± 55	-	-	-	-	-
HEA-Center (actual)	-409 ± 38	-404	1.03	32.4	57.9	9
HEA-Top	-	-133	$0.27x10^3$	68.1	153.2	$75x10^3$
CoCrMo		-487	0.27	33.4	25.7	23

Based on Table 5-4, although HEA-Center (actual) has higher E_{corr} than the conventional implant material CoCrMo, its i_{corr} and R_p values are lower than for CoCrMo, reflecting a relatively lower general corrosion resistance in SBF. However, its passive oxide layer is more resistant to pitting in a chloride environment without any passive film breakdown, as demonstrated in Figure 5-8d. Interestingly, the HEA-Top specimen, having a more homogenous microstructure in the as-cast form, exhibited noticeably good E_{corr}, i_{corr}, and R_p values warranting further study of this composition with homogenous

microstructure, which was initially beyond the scope of this study. These results verify that HEAs can exhibit good corrosion properties once the appropriate heat treatment is implemented to obtain a homogenous microstructure. Since the predictions were made using the experimental findings of as-cast microstructures in the literature, the discussion is restricted to the HEA-Center specimen with the dendritic microstructure.

The current results show the importance of microstructure on the corrosion properties of the materials, which should be included in the design process of new HEAs using ML. For instance, a novel approach was implemented by Ji et al. where they calculated work function and chloride adsorption energies of the secondary phases present in Al alloys using ab initio calculations to integrate the phase information into the corrosion rate predictions, which resulted in improved prediction accuracy of 17.3% [299]. However, constructing an experimental dataset for corrosion of HEAs, including production methods, heat treatment, and detailed phase information, is financially and timewise very expensive. Moreover, most of the new literature on the effect of heat treatment on HEAs focuses on mechanical properties [229]. Therefore, more work should be done on heat-treated HEAs reporting their corrosion properties to have adequate data to construct a dataset that will aid the prediction of optimized HEA compositions along with process conditions leading to the best corrosion resistance [300].

One of the primary obstacles encountered in the design of HEAs is the need to understand the parameters governing these multi-component systems' mechanical and chemical behavior. While ML has been utilized in HEA design, it does not explain the complex prediction mechanism as the ML algorithm constitutes a black-box model, constraining the understanding of underlying relationships between the inputs and the target. Lundberg and Lee introduced Shapley additive explanations (SHAP) for interpreting model predictions [301] to further elucidate the relationships between the inputs and the target. SHAP is based on the idea of cooperative game theory, which aims to clarify the impact of each feature in each sample on its predicted target. The interpretability of the models is essential for the scientific community to comprehend and decipher some hidden mechanisms behind the factors affecting the properties of HEAs.

The features determined using SHAP analysis are shown in Figure 5-9a, suggesting that Ti and $\Delta\chi$ are the essential features, with $\Delta\chi$ being on top. It can be seen that composition and calculated features played a more crucial role in predicting E_{corr} than electrolyte type, pH, and temperature. The electrolyte types might have also been more

critical if their contents were included as input variables in the dataset; however, this would have increased the degrees of freedom drastically, considering the small volume of corrosion data available. In Figure 5-9b, the distribution of SHAP values of the five most important features is demonstrated.

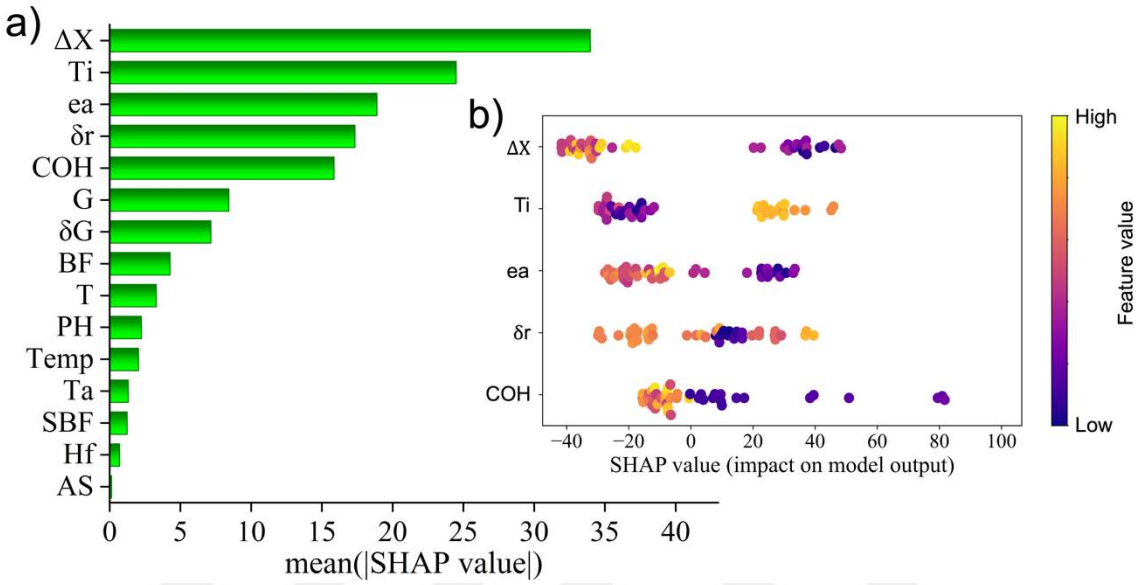

Figure 5-9: (a) Results of the SHAP analysis conducted to determine relative feature importance: since SHAP can be negative, absolute values were utilized to estimate the average feature importance; (b) the five most important features identified with the SHAP analysis; each data point denotes individual alloy data points in the dataset, where the colors were assigned according to the magnitude (high or low) of the feature under question; a positive SHAP value signifies that Ecorr is increased based on the feature value.

To begin with, higher $\Delta\chi$ values posed a negative influence on E_{corr}. Forming a single solid solution requires small values of $\Delta\chi$, whereas higher values promote compound formation [59], deteriorating the corrosion properties of the alloys. Thus, it can be inferred that $\Delta\chi$ might implicitly comprise the model's phase information. Conversely, the greater the Ti content is, the higher the E_{corr} is. However, this effect should be constrained to this system and dataset as it might differ in another family of alloys. For example, Zhao et al. reported that increasing the Ti content resulted in a multi-phase microstructure, leading to lower corrosion resistance in the $Al_{(2-x)}CoCrFeNiTi_x$ system. However, Ti-containing alloys exhibit higher pitting potentials and wider passive regions [302]. For the COH and ea feature, the higher the value is, the lower the E_{corr} is. However, COH and ea features

were calculated using a simple weighted average of COH and ea values of each element in the alloys. Therefore, a proper conclusion should not be drawn from the effects of those features on E_{corr}. The δr effect on E_{corr} is more complicated: the intermediate values of δr improve E_{corr}. In contrast, higher values negatively affect it, as demonstrated in Figure 5-9b. This complicated effect was also reported in the literature before; larger δr results in larger strain in the lattice, hindering the diffusion of chloride ions or oxygen atoms into the lattice, thus increasing corrosion resistance. However, higher δr might also promote secondary phase formation, affecting corrosion properties negatively [288].

Overall, the present findings show that in addition to modifying the composition, fine-tuning the microstructure of the HEAs may result in exceptional properties, opening a venue for their utilization in various applications demanding high corrosion resistance and exceptional mechanical properties.

5.5 Conclusion

This study introduced a machine learning (ML) - based computational framework to predict corrosion potential (E_{corr}) of HEAs in the HfNbTaTiZr alloy family for biomedical applications, followed by experimental validation. The results have shown that E_{corr}, an electrochemical parameter, can be successfully modeled with computational methods. The use and the limitation of the ML method as a potential tool to explore a vast compositional space of HEAs for improved corrosion properties were discussed. The following conclusions can be drawn based on the findings presented herein:

(1) The experimental results matched the predicted values of $E_{corr,}$ demonstrating the success of the RF model trained with a small volume of corrosion data.
(2) Among all the ML models used initially, RF performed the best after the FFS method was implemented to retain the most essential features in the dataset.
(3) Severe element segregation was observed in the microstructure of the as-cast alloy with Ta-rich dendrites.
(4) Though the passive oxide layer consisted mainly of Ta oxides in air an SBF, the total Ti oxide concentration increased in the passive oxide formed in SBF.

(5) The sample cut from the top part of the arc-melted ingot with homogenous microstructure revealed excellent corrosion properties, considering its electrochemical parameters compared to the sample with the dendritic microstructure.

Chapter 6:
CONCLUSION AND FUTURE WORK

The results of the thesis presented herein demonstrate the capability of machine learning (ML) methods trained with a limited amount of experimental data to predict novel biomedical high entropy alloy (HEA) compositions with desired properties. In this thesis, three new biomedical HEAs, namely, $Hf_{27}Nb_{12}Ta_{10}Ti_{23}Zr_{28}$, $Hf_{30}Nb_{14}Ta_{10}Ti_{28}Zr_{18}$, and $Hf_{12}Nb_{16}Ta_{35}Ti_{29}Zr_{8}$ were designed and developed. The first two HEA were developed with an aim to find the lowest possible elastic modulus in the HfNbTaTiZr family of HEAs while the last one ($Hf_{12}Nb_{16}Ta_{35}Ti_{29}Zr_{8}$) was specifically designed to achieve a better corrosion resistance in simulated body fluid (SBF). The predicted compositions of HEAs were produced using vacuum arc-melting (VAM) technique and analysed with various methods, such as X-ray diffraction (XRD), X-ray photon spectroscopy (XPS), field emission scanning electron microscopy (FESEM), and inductively coupled plasma-mass spectrometer (IC-PMS). Moreover, a chapter, in which the effect of PVD process parameters on mechanical properties and ion release behavior of Ag coatings was investigated, was dedicated to Ag coatings sputtered on $Hf_{27}Nb_{12}Ta_{10}Ti_{23}Zr_{28}$ and $Hf_{30}Nb_{14}Ta_{10}Ti_{28}Zr_{18}$ HEAs in order to enhance their antibacterial properties.

In the first chapter, two novel biomedical HEA compositions were predicted, namely $Ti_{23}Ta_{10}Hf_{27}Nb_{12}Zr_{28}$ and $Ti_{28}Ta_{10}Hf_{30}Nb_{14}Zr_{18}$, with elastic moduli of 83.5 ± 2.9 GPa and 87.4 ± 2.2 GPa, respectively. The predicted elastic moduli of the new alloys were validated by nano-indentation experiments. The samples were then subjected to immersion experiments in simulated body fluid (SBF) for 28 days to assess their biocompatibility and ion release behavior. The predicted alloys were also annealed in 1000 °C for 12 hours to examine the changes in microstructure, and corresponding elastic moduli and ion release behavior. As a result, it was shown that heat treatment brought about formation of additional phases in the microstructure which showed that these alloys with a single BCC phase in the as-cast state can be used without heat treatment.

In the second chapter, the evolution of microstructural, mechanical, and ion release behavior of Ag coatings sputtered on biomedical high entropy alloys (HEAs) was studied. The deposition time was shown to affect the texture, roughness of the coatings, number, and size of agglomerates, and the critical thickness, where the surface energy to strain

energy minimization transformation took place. Specifically, above a critical thickness, the evolution of two different strain energy mechanisms was observed for films sputtered on $Ti_{23}Ta_{10}Hf_{27}Nb_{12}Zr_{28}$ and $Ti_{28}Ta_{10}Hf_{30}Nb_{14}Zr_{18}$ HEAs: grain growth and formation of (220) oriented grains, respectively. Furthermore, the Ar flow rate was shown to have an impact on NP size, increasing the amount of ion release drastically due to the increase in the surface-to-volume ratio of these particles. It was affirmed that the ion release rate depends not only on the NP size but also on the texture of the coating, which can be modified by changing the deposition time and the Ar flow rate.

In the third chapter, the microstructural features, ion release, and corrosion behavior of two novel biomedical HEAs developed in the first chapter were investigated. It was found out that both HEAs possess a dendritic structure, with Ta being mostly segregated into dendrite arms during the solidification due to its higher melting point than other elements in bulk. While the cumulative Ti ion release increased until the 28^{th} day and decreased afterward in SBF, a successive decrease in the cumulative Ti ion release was detected in AS. For two reasons, Ta was mainly present in the passive oxide layer in the form of its sub-oxides: the bulk alloys are deficient in Ta content, and severe segregation of Ta in dendrite arms. Potentiodynamic experiments performed in AS pointed out that $Ti_{28}Ta_{10}Hf_{30}Nb_{14}Zr_{18}$ had a relatively high passive dissolution which may be associated with the higher concentration of sub-oxides it contains as opposed to $Ti_{23}Ta_{10}Hf_{27}Nb_{12}Zr_{28}$, especially Ti_2O_3 which is regarded as an inducer for metastable pits. Furthermore, the corrosion resistance of both HEAs was found to be superior compared to that of the CoCrMo in both AS and SBF.

In the last chapter, a new HEA composition with the best corrosion resistance in the HfNbTaTiZr alloy family for biomedical applications was predicted, followed by experimental validation. The results have shown that E_{corr}, an electrochemical parameter, can be successfully modeled with computational methods. The experimental results matched the predicted values of $E_{corr,}$ demonstrating the success of the random forest (RF) model trained with a small volume of corrosion data. Severe element segregation was observed in the microstructure of the as-cast alloy with Ta-rich dendrites. The sample cut from the top part of the arc-melted ingot with homogenous microstructure revealed excellent corrosion properties, considering its electrochemical parameters compared to the sample with the dendritic microstructure.

As discussed in this thesis, the biomedical HEAs that were investigated herein comprise of refractory elements which make them also attractive alternative materials in other applications, especially high temperature applications. Therefore, these materials should be tested at elevated temperatures in order to measure their strength and ductility at high temperature. Besides high temperature, room temperature and cryogenic tests should also be conducted in order to have an understanding of mechanical behavior of the HEAs in a broad temperature range. They can be used in applications such as gas turbines, rockets, and nuclear industries. Additionally, the HEAs can be tested in other electrolytes to reveal their corrosion behavior in harsher environments compared to AS and SBF. The HEAs discussed in this thesis were manufactured with arc-melting technique. However, other methods, such as additive manufacturing, powder metallurgy or ball milling, might result in different microstructure affecting the final properties. Therefore, these HEAs might be manufactured with these manufacturing techniques in order to understand the effect of manufacturing technique on final properties of the alloys.

The alloys investigated in the study were as-cast. Hence, additional heat-treatment and pre-deformation can be applied to the alloys, in order to understand their properties with the corresponding microstructure as a result of the changing production methodology. Once the microstructure and phases formed through heat-treatment are understood, final properties can be tuned through controlling microstructure. Especially, manufacturing HEAs with additive manufacturing have drawn increasing attention lately because of easiness of ability to produce complex shapes and materials savings. Additionally, when HEAs are produced with magnetron sputtering, amorphous phases can be obtained which results in different mechanical response, corrosion behavior and wear resistance as opposed to their bulk counterparts. Therefore, the HEAs investigated herein can be used in other applications other than biomedical. The phases formed and their volumes, and precipitates can be controlled with a well-designed heat-treatment recipe. Molecular dynamics can be a helpful tool in order to investigate the corresponding temperature ranges, where some phases forms and stays stable.

BIBLIOGRAPHY

[1] B. Cantor, I.T.H. Chang, P. Knight, A.J.B. Vincent, Microstructural development in equiatomic multicomponent alloys, Materials Science and Engineering: A 375–377 (2004) 213–218. https://doi.org/10.1016/j.msea.2003.10.257.

[2] J.W. Yeh, S.K. Chen, S.J. Lin, J.Y. Gan, T.S. Chin, T.T. Shun, C.H. Tsau, S.Y. Chang, Nanostructured high-entropy alloys with multiple principal elements: Novel alloy design concepts and outcomes, Adv Eng Mater 6 (2004) 299–303. https://doi.org/10.1002/adem.200300567.

[3] D.B. Miracle, O.N. Senkov, A critical review of high entropy alloys and related concepts, Acta Mater 122 (2017) 448–511. https://doi.org/10.1016/j.actamat.2016.08.081.

[4] S. Zhu, K. Gan, D. Yan, L. Han, P. Wu, Z. Li, Multiple minor elements improve strength-ductility synergy of a high-entropy alloy, Materials Science and Engineering: A 840 (2022) 142901. https://doi.org/10.1016/j.msea.2022.142901.

[5] O.N. Senkov, D.B. Miracle, A new thermodynamic parameter to predict formation of solid solution or intermetallic phases in high entropy alloys, J Alloys Compd 658 (2016) 603–607. https://doi.org/10.1016/j.jallcom.2015.10.279.

[6] E.J. Pickering, N.G. Jones, High-entropy alloys: a critical assessment of their founding principles and future prospects, International Materials Reviews 61 (2016) 183–202. https://doi.org/10.1080/09506608.2016.1180020.

[7] L.R. Owen, N.G. Jones, Lattice distortions in high-entropy alloys, J Mater Res 33 (2018) 2954–2969. https://doi.org/10.1557/jmr.2018.322.

[8] J.W. Yeh, S.Y. Chang, Y. Der Hong, S.K. Chen, S.J. Lin, Anomalous decrease in X-ray diffraction intensities of Cu-Ni-Al-Co-Cr-Fe-Si alloy systems with multi-principal elements, Mater Chem Phys 103 (2007) 41–46. https://doi.org/10.1016/j.matchemphys.2007.01.003.

[9] F.H. Herbstein, B.S. Borie, B.L. Averbach, Local atomic displacements in solid solutions, Acta Crystallogr 9 (1956) 466–471. https://doi.org/10.1107/s0365110x56001261.

[10] B. Borie, X-ray diffraction effects of atomic size in alloys, Acta Crystallogr 10 (1957) 89–96. https://doi.org/10.1107/s0365110x57000274.

[11] N.D. Stepanov, D.G. Shaysultanov, M.A. Tikhonovsky, G.A. Salishchev, Tensile properties of the Cr-Fe-Ni-Mn non-equiatomic multicomponent alloys with different Cr contents, Mater Des 87 (2015) 60–65. https://doi.org/10.1016/j.matdes.2015.08.007.

[12] V. Verma, C.H. Belcher, D. Apelian, E.J. Lavernia, Diffusion in High Entropy Alloy Systems – A Review, Prog Mater Sci 142 (2024) 101245. https://doi.org/10.1016/j.pmatsci.2024.101245.

[13] Y. Zhang, T.T. Zuo, Z. Tang, M.C. Gao, K.A. Dahmen, P.K. Liaw, Z.P. Lu, Microstructures and properties of high-entropy alloys, Prog Mater Sci 61 (2014) 1–93. https://doi.org/10.1016/j.pmatsci.2013.10.001.

[14] Y.F. Kao, T.J. Chen, S.K. Chen, J.W. Yeh, Microstructure and mechanical property of as-cast, -homogenized, and -deformed AlxCoCrFeNi ($0 \leq x \leq 2$) high-entropy alloys, J Alloys Compd 488 (2009) 57–64. https://doi.org/10.1016/j.jallcom.2009.08.090.

[15] O. El Atwani, H.T. Vo, M.A. Tunes, C. Lee, A. Alvarado, N. Krienke, J.D. Poplawsky, A.A. Kohnert, J. Gigax, W.Y. Chen, M. Li, Y.Q. Wang, J.S. Wróbel, D. Nguyen-Manh, J.K.S. Baldwin, O.U. Tukac, E. Aydogan, S. Fensin, E. Martinez, A quinary WTaCrVHf nanocrystalline refractory high-entropy alloy withholding extreme irradiation environments, Nat Commun 14 (2023) 1–12. https://doi.org/10.1038/s41467-023-38000-y.

[16] A. Hussain, R.S. Dhaka, H.J. Ryu, S.K. Sharma, P.K. Kulriya, A critical review on temperature dependent irradiation response of high entropy alloys, J Alloys Compd 948 (2023) 169624. https://doi.org/10.1016/J.JALLCOM.2023.169624.

[17] Z. Cheng, J. Sun, X. Gao, Y. Wang, J. Cui, T. Wang, H. Chang, Irradiation effects in high-entropy alloys and their applications, J Alloys Compd 930 (2023) 166768. https://doi.org/10.1016/j.jallcom.2022.166768.

[18] M. Moschetti, P. Burr, E. Obbard, J.J. Kruzic, P. Hosemann, B. Gludovatz, Design considerations for high entropy alloys in advanced nuclear applications, Journal of Nuclear Materials 567 (2022) 153814. https://doi.org/10.1016/j.jnucmat.2022.153814.

[19] Y. Zhang, L. Wang, W.J. Weber, Charged particles: Unique tools to study irradiation resistance of concentrated solid solution alloys, J Mater Sci Technol 140 (2023) 260–276. https://doi.org/10.1016/j.jmst.2022.08.034.

[20] M. Slobodyan, E. Pesterev, A. Markov, Recent advances and outstanding challenges for implementation of high entropy alloys as structural materials, Mater Today Commun 36 (2023) 106422. https://doi.org/10.1016/j.mtcomm.2023.106422.

[21] S.Q. Xia, X. Yang, T.F. Yang, S. Liu, Y. Zhang, Irradiation Resistance in AlxCoCrFeNi High Entropy Alloys, JOM 67 (2015) 2340–2344. https://doi.org/10.1007/s11837-015-1568-4.

[22] W. Li, D. Xie, D. Li, Y. Zhang, Y. Gao, P.K. Liaw, Mechanical behavior of high-entropy alloys, Prog Mater Sci 118 (2021) 100777. https://doi.org/10.1016/j.pmatsci.2021.100777.

[23] C. Lu, T. Yang, K. Jin, G. Velisa, P. Xiu, M. Song, Q. Peng, F. Gao, Y. Zhang, H. Bei, W.J. Weber, L. Wang, Enhanced void swelling in NiCoFeCrPd high-entropy alloy by indentation-induced dislocations, Mater Res Lett 6 (2018) 584–591. https://doi.org/10.1080/21663831.2018.1504136.

[24] M. Sadeghilaridjani, A. Ayyagari, S. Muskeri, V. Hasannaeimi, R. Salloom, W.Y. Chen, S. Mukherjee, Ion irradiation response and mechanical behavior of reduced activity high entropy alloy, Journal of Nuclear Materials 529 (2020) 151955. https://doi.org/10.1016/j.jnucmat.2019.151955.

[25] S. Praveen, H.S. Kim, High-Entropy Alloys: Potential Candidates for High-Temperature Applications – An Overview, Adv Eng Mater 20 (2018) 1700645. https://doi.org/10.1002/adem.201700645.

[26] S.K. Dewangan, A. Mangish, S. Kumar, A. Sharma, B. Ahn, V. Kumar, A review on High-Temperature Applicability: A milestone for high entropy alloys, Engineering Science and Technology, an International Journal 35 (2022) 101211. https://doi.org/10.1016/j.jestch.2022.101211.

[27] T.M. Pollock, S. Tin, Nickel-based superalloys for advanced turbine engines: Chemistry, microstructure, and properties, J Propuls Power 22 (2006) 361–374. https://doi.org/10.2514/1.18239.

[28] A. Pineau, S.D. Antolovich, High temperature fatigue of nickel-base superalloys - A review with special emphasis on deformation modes and oxidation, Eng Fail Anal 16 (2009) 2668–2697. https://doi.org/10.1016/j.engfailanal.2009.01.010.
[29] J. Chen, X. Zhou, W. Wang, B. Liu, Y. Lv, W. Yang, D. Xu, Y. Liu, A review on fundamental of high entropy alloys with promising high–temperature properties, J Alloys Compd 760 (2018) 15–30. https://doi.org/10.1016/j.jallcom.2018.05.067.
[30] T.K. Tsao, A.C. Yeh, C.M. Kuo, H. Murakami, On The Superior High Temperature Hardness of Precipitation Strengthened High Entropy Ni-Based Alloys, Adv Eng Mater 19 (2017) 1600475. https://doi.org/10.1002/adem.201600475.
[31] O.N. Senkov, G.B. Wilks, J.M. Scott, D.B. Miracle, Mechanical properties of Nb25Mo25Ta 25W25 and V20Nb20Mo 20Ta20W20 refractory high entropy alloys, Intermetallics (Barking) 19 (2011) 698–706. https://doi.org/10.1016/j.intermet.2011.01.004.
[32] O.N. Senkov, G.B. Wilks, D.B. Miracle, C.P. Chuang, P.K. Liaw, Refractory high-entropy alloys, Intermetallics (Barking) 18 (2010) 1758–1765. https://doi.org/10.1016/j.intermet.2010.05.014.
[33] S. Sheikh, S. Shafeie, Q. Hu, J. Ahlström, C. Persson, J. Veselý, J. Zýka, U. Klement, S. Guo, Alloy design for intrinsically ductile refractory high-entropy alloys, J Appl Phys 120 (2016) 164902. https://doi.org/10.1063/1.4966659.
[34] Y.D. Wu, Y.H. Cai, T. Wang, J.J. Si, J. Zhu, Y.D. Wang, X.D. Hui, A refractory Hf25Nb25Ti25Zr25 high-entropy alloy with excellent structural stability and tensile properties, Mater Lett 130 (2014) 277–280. https://doi.org/10.1016/j.matlet.2014.05.134.
[35] G. Dirras, L. Lilensten, P. Djemia, M. Laurent-Brocq, D. Tingaud, J.P. Couzinié, L. Perrière, T. Chauveau, I. Guillot, Elastic and plastic properties of as-cast equimolar TiHfZrTaNb high-entropy alloy, Materials Science and Engineering A 654 (2016) 30–38. https://doi.org/10.1016/j.msea.2015.12.017.
[36] H.M. Daoud, A. Manzoni, R. Völkl, N. Wanderka, U. Glatzel, Microstructure and tensile behavior of Al8Co17Cr 17Cu8Fe17Ni33 (at.%) high-entropy alloy, JOM 65 (2013) 1805–1814. https://doi.org/10.1007/s11837-013-0756-3.
[37] H.J. Lin, Y.S. Lu, L.T. Zhang, H.Z. Liu, K. Edalati, Á. Révész, Recent advances in metastable alloys for hydrogen storage: a review, Rare Metals 41 (2022) 1797–1817. https://doi.org/10.1007/s12598-021-01917-8.
[38] R.R. Shahi, A.K. Gupta, P. Kumari, Perspectives of high entropy alloys as hydrogen storage materials, Int J Hydrogen Energy 48 (2023) 21412–21428. https://doi.org/10.1016/j.ijhydene.2022.02.113.
[39] Y.F. Kao, S.K. Chen, J.H. Sheu, J.T. Lin, W.E. Lin, J.W. Yeh, S.J. Lin, T.H. Liou, C.W. Wang, Hydrogen storage properties of multi-principal-component CoFeMnTixVyZrz alloys, Int J Hydrogen Energy 35 (2010) 9046–9059. https://doi.org/10.1016/j.ijhydene.2010.06.012.
[40] M. Sahlberg, D. Karlsson, C. Zlotea, U. Jansson, Superior hydrogen storage in high entropy alloys, Sci Rep 6 (2016) 1–6. https://doi.org/10.1038/srep36770.
[41] K. Li, W. Chen, Recent progress in high-entropy alloys for catalysts: synthesis, applications, and prospects, Mater Today Energy 20 (2021) 100638. https://doi.org/10.1016/j.mtener.2021.100638.

[42] N. Kumar Katiyar, K. Biswas, J.-W. Yeh, S. Sharma, C. Sekhar Tiwary, A perspective on the catalysis using the high entropy alloys, Nano Energy 88 (2021) 106261. https://doi.org/10.1016/j.nanoen.2021.106261.
[43] L. Yu, K. Zeng, C. Li, X. Lin, H. Liu, W. Shi, H.J. Qiu, Y. Yuan, Y. Yao, High-entropy alloy catalysts: From bulk to nano toward highly efficient carbon and nitrogen catalysis, Carbon Energy 4 (2022) 731–761. https://doi.org/10.1002/cey2.228.
[44] T. Löffler, A. Ludwig, J. Rossmeisl, W. Schuhmann, What Makes High-Entropy Alloys Exceptional Electrocatalysts?, Angewandte Chemie - International Edition 60 (2021) 26894–26903. https://doi.org/10.1002/anie.202109212.
[45] Y. Xin, S. Li, Y. Qian, W. Zhu, H. Yuan, P. Jiang, R. Guo, L. Wang, High-Entropy Alloys as a Platform for Catalysis: Progress, Challenges, and Opportunities, ACS Catal 10 (2020) 11280–11306. https://doi.org/10.1021/acscatal.0c03617.
[46] Y. Yao, Z. Liu, P. Xie, Z. Huang, T. Li, D. Morris, Z. Finfrock, J. Zhou, M. Jiao, J. Gao, Y. Mao, J. Miao, P. Zhang, R. Shahbazian-Yassar, C. Wang, G. Wang, L. Hu, Computationally aided, entropy-driven synthesis of highly efficient and durable multi-elemental alloy catalysts, Sci Adv 6 (2020) 510–523. https://doi.org/10.1126/sciadv.aaz0510.
[47] Y. Yao, Z. Huang, P. Xie, S.D. Lacey, R.J. Jacob, H. Xie, F. Chen, A. Nie, T. Pu, M. Rehwoldt, D. Yu, M.R. Zachariah, C. Wang, R. Shahbazian-Yassar, J. Li, L. Hu, Carbothermal shock synthesis of high-entropy-alloy nanoparticles, Science (1979) 359 (2018) 1489–1494. https://doi.org/10.1126/science.aan5412.
[48] D. Zhu, S. Hu, Y. Fu, N. Zhao, D. Liu, A review of preparation methods, friction and wear, corrosion, and biocompatibility of biomedical high-entropy alloys, J Mater Sci 59 (2024) 1153–1183. https://doi.org/10.1007/s10853-023-09314-5.
[49] P. Nasker, A. Sinha, Titanium based bulk metallic glasses for biomedical applications, Elsevier Ltd, 2018. https://doi.org/10.1016/B978-0-08-102205-4.00012-X.
[50] R. Karre, S.R. Dey, Progress in Development of Beta Titanium Alloys for Biomedical Applications, Elsevier Ltd., 2019. https://doi.org/10.1016/b978-0-12-803581-8.10501-6.
[51] R. Huiskes, H. Weinans, B. Van Rietbergen, The relationship between stress shielding and bone resorption around total hip stems and the effects of flexible materials, Clin Orthop Relat Res (1992) 124–134. https://doi.org/10.1097/00003086-199201000-00014.
[52] S. Attarilar, J. Yang, M. Ebrahimi, Q. Wang, J. Liu, Y. Tang, J. Yang, The Toxicity Phenomenon and the Related Occurrence in Metal and Metal Oxide Nanoparticles: A Brief Review From the Biomedical Perspective, Front Bioeng Biotechnol 8 (2020) 565550. https://doi.org/10.3389/fbioe.2020.00822.
[53] D. Castro, P. Jaeger, A.C. Baptista, J.P. Oliveira, An overview of high-entropy alloys as biomaterials, Metals (Basel) 11 (2021) 648. https://doi.org/10.3390/met11040648.
[54] W. Wang, K. Yang, Q. Wang, P. Dai, H. Fang, F. Wu, Q. Guo, P.K. Liaw, N. Hua, Novel Ti-Zr-Hf-Nb-Fe refractory high-entropy alloys for potential biomedical applications, J Alloys Compd 906 (2022) 164383. https://doi.org/10.1016/j.jallcom.2022.164383.
[55] T. Xiang, P. Du, Z. Cai, K. Li, W. Bao, X. Yang, G. Xie, Phase-tunable equiatomic and non-equiatomic Ti-Zr-Nb-Ta high-entropy alloys with ultrahigh

strength for metallic biomaterials, J Mater Sci Technol 117 (2022) 196–206. https://doi.org/10.1016/j.jmst.2021.12.014.
[56] Y. Iijima, T. Nagase, A. Matsugaki, P. Wang, K. Ameyama, T. Nakano, Design and development of Ti–Zr–Hf–Nb–Ta–Mo high-entropy alloys for metallic biomaterials, Mater Des 202 (2021) 109548. https://doi.org/10.1016/j.matdes.2021.109548.
[57] Y. Shi, B. Yang, X. Xie, J. Brechtl, K.A. Dahmen, P.K. Liaw, Corrosion of Al xCoCrFeNi high-entropy alloys: Al-content and potential scan-rate dependent pitting behavior, Corros Sci 119 (2017) 33–45. https://doi.org/10.1016/j.corsci.2017.02.019.
[58] Y. Fu, J. Li, H. Luo, C. Du, X. Li, Recent advances on environmental corrosion behavior and mechanism of high-entropy alloys, J Mater Sci Technol 80 (2021) 217–233. https://doi.org/10.1016/j.jmst.2020.11.044.
[59] L. Qiao, Y. Liu, J. Zhu, A focused review on machine learning aided high-throughput methods in high entropy alloy, J Alloys Compd 877 (2021) 160295. https://doi.org/10.1016/j.jallcom.2021.160295.
[60] J. Yuan, Y. Liu, Z. Li, M. Wang, Q. Wang, C. Dong, Cluster-Model-Embedded First-Principles Study on Structural Stability of Body-Centered-Cubic-Based Ti-Zr-Hf-Nb Refractory High-Entropy Alloys, Journal of Phase Equilibria and Diffusion 2021 (2021) 1–9. https://doi.org/10.1007/S11669-021-00899-5.
[61] J. Hu, H. Shen, M. Jiang, H. Gong, H. Xiao, Z. Liu, G. Sun, X. Zu, A DFT Study of Hydrogen Storage in High-Entropy Alloy TiZrHfScMo, Nanomaterials 2019, Vol. 9, Page 461 9 (2019) 461. https://doi.org/10.3390/NANO9030461.
[62] S. Chen, T. Wang, X. Li, Y. Cheng, G. Zhang, H. Gao, Short-range ordering and its impact on thermodynamic property of high-entropy alloys, Acta Mater 238 (2022) 118201. https://doi.org/10.1016/j.actamat.2022.118201.
[63] K.-T.T. Chen, T.-J.J. Wei, G.-C.C. Li, M.-Y.Y. Chen, Y.-S.S. Chen, S.-W.W. Chang, H.-W.W. Yen, C.-S.S. Chen, Mechanical properties and deformation mechanisms in CoCrFeMnNi high entropy alloys: A molecular dynamics study, Mater Chem Phys 271 (2021) 124912. https://doi.org/10.1016/j.matchemphys.2021.124912.
[64] S. Singh, N.K. Katiyar, S. Goel, S.N. Joshi, Phase prediction and experimental realisation of a new high entropy alloy using machine learning, Sci Rep 13 (2023) 4811. https://doi.org/10.1038/s41598-023-31461-7.
[65] X. Liu, J. Zhang, Z. Pei, Machine Learning for High-entropy Alloys: Progress, Challenges and Opportunities, Prog Mater Sci 131 (2022) 101018. https://doi.org/10.1016/J.PMATSCI.2022.101018.
[66] Y. Liu, C. Niu, Z. Wang, Y. Gan, Y. Zhu, S. Sun, T. Shen, Machine learning in materials genome initiative: A review, J Mater Sci Technol 57 (2020) 113–122. https://doi.org/10.1016/j.jmst.2020.01.067.
[67] S.A. Giles, D. Sengupta, S.R. Broderick, K. Rajan, Machine-learning-based intelligent framework for discovering refractory high-entropy alloys with improved high-temperature yield strength, NPJ Comput Mater 8 (2022) 1–11. https://doi.org/10.1038/s41524-022-00926-0.
[68] Y.F. Zhang, W. Ren, W.L. Wang, N. Li, Y.X. Zhang, X.M. Li, W.H. Li, Interpretable hardness prediction of high-entropy alloys through ensemble learning, J Alloys Compd 945 (2023) 169329. https://doi.org/10.1016/j.jallcom.2023.169329.

[69] C. Yang, C. Ren, Y. Jia, G. Wang, M. Li, W. Lu, A machine learning-based alloy design system to facilitate the rational design of high entropy alloys with enhanced hardness, Acta Mater 222 (2022) 117431. https://doi.org/10.1016/j.actamat.2021.117431.
[70] H. Zhang, H. Fu, X. He, C. Wang, L. Jiang, L.Q. Chen, J. Xie, Dramatically Enhanced Combination of Ultimate Tensile Strength and Electric Conductivity of Alloys via Machine Learning Screening, Acta Mater 200 (2020) 803–810. https://doi.org/10.1016/j.actamat.2020.09.068.
[71] H.C. Ozdemir, E. Bedir, R. Yilmaz, M.B. Yagci, D. Canadinc, Machine learning-assisted design of biomedical high entropy alloys with low elastic modulus for orthopedic implants, J Mater Sci 57 (2022) 11151–11169. https://doi.org/10.1007/s10853-022-07363-w.
[72] H. Khakurel, M.F.N. Taufique, A. Roy, G. Balasubramanian, G. Ouyang, J. Cui, D.D. Johnson, R. Devanathan, Machine learning assisted prediction of the Young's modulus of compositionally complex alloys, Sci Rep 11 (2021) 1–10. https://doi.org/10.1038/s41598-021-96507-0.
[73] N.J. Sai, P. Rathore, A. Chauhan, Machine learning-based predictions of fatigue life for multi-principal element alloys, Scr Mater 226 (2023) 115214. https://doi.org/10.1016/j.scriptamat.2022.115214.
[74] H. Chang, Y. Tao, P.K. Liaw, J. Ren, Phase prediction and effect of intrinsic residual strain on phase stability in high-entropy alloys with machine learning, J Alloys Compd 921 (2022) 166149. https://doi.org/10.1016/j.jallcom.2022.166149.
[75] K. Lee, M. V. Ayyasamy, P. Delsa, T.Q. Hartnett, P. V. Balachandran, Phase classification of multi-principal element alloys via interpretable machine learning, NPJ Comput Mater 8 (2022) 1–12. https://doi.org/10.1038/s41524-022-00704-y.
[76] J. Huang, W. Fang, C. Xue, T. Peng, H. Yu, J. Li, L. Sun, X. He, B. Liu, Y. Yang, F. Yin, Exploring the relationship between lattice distortion and phase stability in a multi-principal element alloy system based on machine learning method, Comput Mater Sci 221 (2023) 112089. https://doi.org/10.1016/j.commatsci.2023.112089.
[77] L. Chen, A. Jarlöv, H.L. Seet, M.L.S. Nai, Y. Li, K. Zhou, Exploration of V–Cr–Fe–Co–Ni high-entropy alloys with high yield strength: A combination of machine learning and molecular dynamics simulation, Comput Mater Sci 217 (2023) 111888. https://doi.org/10.1016/j.commatsci.2022.111888.
[78] M. Niinomi, M. Nakai, J. Hieda, Development of new metallic alloys for biomedical applications, Acta Biomater 8 (2012) 3888–3903. https://doi.org/10.1016/j.actbio.2012.06.037.
[79] Y. Li, C. Yang, H. Zhao, S. Qu, X. Li, Y. Li, New developments of ti-based alloys for biomedical applications, Materials 7 (2014) 1709–1800. https://doi.org/10.3390/ma7031709.
[80] M. Geetha, A.K. Singh, R. Asokamani, A.K. Gogia, Ti based biomaterials, the ultimate choice for orthopaedic implants - A review, Prog Mater Sci 54 (2009) 397–425. https://doi.org/10.1016/j.pmatsci.2008.06.004.
[81] M. Niinomi, Recent metallic materials for biomedical applications, Metallurgical and Materials Transactions A 33 (2002) 477–486. https://doi.org/10.1007/s11661-002-0109-2.

[82] S.J. Dai, Y. Wang, F. Chen, X.Q. Yu, Y.F. Zhang, Influence of Zr content on microstructure and mechanical properties of implant Ti-35Nb-4Sn-6Mo-xZr alloys, Transactions of Nonferrous Metals Society of China (English Edition) 23 (2013) 1299–1303. https://doi.org/10.1016/S1003-6326(13)62597-2.
[83] S. Gurel, M.B. Yagci, B. Bal, D. Canadinc, Corrosion behavior of novel Titanium-based high entropy alloys designed for medical implants, Mater Chem Phys 254 (2020) 123377.
[84] S. Gurel, M.B. Yagci, D. Canadinc, G. Gerstein, B. Bal, H.J. Maier, Fracture behavior of novel biomedical Ti-based high entropy alloys under impact loading, Materials Science and Engineering A (2020) 140456. https://doi.org/10.1016/j.msea.2020.140456.
[85] A. Motallebzadeh, N.S. Peighambardoust, S. Sheikh, H. Murakami, S. Guo, D. Canadinc, Microstructural, mechanical and electrochemical characterization of TiZrTaHfNb and Ti1.5ZrTa0.5Hf0.5Nb0.5 refractory high-entropy alloys for biomedical applications, Intermetallics (Barking) 113 (2019) 106572. https://doi.org/10.1016/j.intermet.2019.106572.
[86] S. Gurel, A. Nazarahari, D. Canadinc, H. Cabuk, B. Bal, Assessment of biocompatibility of novel TiTaHf-based high entropy alloys for utility in orthopedic implants, Mater Chem Phys 266 (2021) 124573. https://doi.org/10.1016/j.matchemphys.2021.124573.
[87] S. Sheikh, M.K. Bijaksana, A. Motallebzadeh, S. Shafeie, A. Lozinko, L. Gan, T.K. Tsao, U. Klement, D. Canadinc, H. Murakami, S. Guo, Accelerated oxidation in ductile refractory high-entropy alloys, Intermetallics (Barking) 97 (2018) 58–66. https://doi.org/10.1016/j.intermet.2018.04.001.
[88] E.P. George, D. Raabe, R.O. Ritchie, High-entropy alloys, Nat Rev Mater 4 (2019) 515–534. https://doi.org/10.1038/s41578-019-0121-4.
[89] D. Dai, T. Xu, X. Wei, G. Ding, Y. Xu, J. Zhang, H. Zhang, Using machine learning and feature engineering to characterize limited material datasets of high-entropy alloys, Comput Mater Sci 175 (2020) 109618. https://doi.org/10.1016/j.commatsci.2020.109618.
[90] C. Wen, Y. Zhang, C. Wang, D. Xue, Y. Bai, S. Antonov, L. Dai, T. Lookman, Y. Su, Machine learning assisted design of high entropy alloys with desired property, Acta Mater 170 (2019) 109–117. https://doi.org/10.1016/j.actamat.2019.03.010.
[91] Z.S. Nong, J.C. Zhu, Y. Cao, X.W. Yang, Z.H. Lai, Y. Liu, Stability and structure prediction of cubic phase in as cast high entropy alloys, Materials Science and Technology (United Kingdom) 30 (2014) 363–369. https://doi.org/10.1179/1743284713Y.0000000368.
[92] N.N. Guo, L. Wang, L.S. Luo, X.Z. Li, Y.Q. Su, J.J. Guo, H.Z. Fu, Microstructure and mechanical properties of refractory MoNbHfZrTi high-entropy alloy, Mater Des 81 (2015) 87–94. https://doi.org/10.1016/j.matdes.2015.05.019.
[93] X. Yang, Y. Zhang, P.K. Liaw, Microstructure and compressive properties of NbTiVTaAlx high entropy alloys, Procedia Eng 36 (2012) 292–298. https://doi.org/10.1016/j.proeng.2012.03.043.
[94] Y. Song, D.S. Xu, R. Yang, D. Li, W.T. Wu, Z.X. Guo, Theoretical study of the effects of alloying elements on the strength and modulus of β-type bio-titanium alloys, Materials Science and Engineering A 260 (1999) 269–274. https://doi.org/10.1016/s0921-5093(98)00886-7.

[95] Y. Yuan, Y. Wu, Z. Yang, X. Liang, Z. Lei, H. Huang, H. Wang, X. Liu, K. An, W. Wu, Z. Lu, Formation, structure and properties of biocompatible TiZrHfNbTa high-entropy alloys, Mater Res Lett 7 (2019) 225–231. https://doi.org/10.1080/21663831.2019.1584592.
[96] S.P. Wang, J. Xu, TiZrNbTaMo high-entropy alloy designed for orthopedic implants: As-cast microstructure and mechanical properties, Materials Science and Engineering C 73 (2017) 80–89. https://doi.org/10.1016/j.msec.2016.12.057.
[97] S. Jiang, Z. Lin, H. Xu, Y. Sun, Studies on the microstructure and properties of AlxCoCrFeNiTi1-x high entropy alloys, J Alloys Compd 741 (2018) 826–833. https://doi.org/10.1016/j.jallcom.2018.01.247.
[98] N. Sakaguchi, N. Mitsuo, T. Akahori, T. Saito, T. Furuta, Effects of alloying elements on elastic modulus of Ti-Nb-Ta-Zr system alloy for biomedical applications, in: Materials Science Forum, Trans Tech Publications Ltd, 2004: pp. 1269–1272. https://doi.org/10.4028/www.scientific.net/msf.449-452.1269.
[99] N. Sakaguchi, M. Niinomi, T. Akahori, J. Takeda, H. Toda, Effect of Ta content on mechanical properties of Ti-30Nb-XTa-5Zr, in: Materials Science and Engineering C, Elsevier, 2005: pp. 370–376. https://doi.org/10.1016/j.msec.2005.04.003.
[100] N. Sakaguchi, M. Niinomi, T. Akahori, J. Takeda, H. Toda, Relationships between tensile deformation behavior and microstructure in Ti-Nb-Ta-Zr system alloys, in: Materials Science and Engineering C, Elsevier, 2005: pp. 363–369. https://doi.org/10.1016/j.msec.2004.12.014.
[101] T. Ozaki, H. Matsumoto, S. Watanabe, S. Hanada, Beta ti alloys with low young's modulus, in: Mater Trans, Japan Institute of Metals (JIM), 2004: pp. 2776–2779. https://doi.org/10.2320/matertrans.45.2776.
[102] Y.F. Ye, Q. Wang, J. Lu, C.T. Liu, Y. Yang, High-entropy alloy: challenges and prospects, Materials Today 19 (2016) 349–362. https://doi.org/10.1016/j.mattod.2015.11.026.
[103] K. Kaufmann, K.S. Vecchio, Searching for high entropy alloys: A machine learning approach, Acta Mater 198 (2020) 178–222. https://doi.org/10.1016/j.actamat.2020.07.065.
[104] G.R. Schleder, A.C.M. Padilha, C.M. Acosta, M. Costa, A. Fazzio, From DFT to machine learning: recent approaches to materials science–a review, Journal of Physics: Materials 2 (2019) 032001. https://doi.org/10.1088/2515-7639/ab084b.
[105] J. Zhang, X. Liu, S. Bi, J. Yin, G. Zhang, M. Eisenbach, Robust data-driven approach for predicting the configurational energy of high entropy alloys, Mater Des 185 (2020) 108247. https://doi.org/10.1016/j.matdes.2019.108247.
[106] L. Himanen, A. Geurts, A.S. Foster, P. Rinke, Data-Driven Materials Science: Status, Challenges, and Perspectives, Advanced Science 6 (2019) 1900808. https://doi.org/10.1002/advs.201900808.
[107] J. Schmidt, M.A.L.M.R.G. Marques, S. Botti, M.A.L.M.R.G. Marques, Recent advances and applications of machine learning in solid-state materials science, NPJ Comput Mater 5 (2019) 1–36. https://doi.org/10.1038/s41524-019-0221-0.
[108] K.T. Butler, D.W. Davies, H. Cartwright, O. Isayev, A. Walsh, Machine learning for molecular and materials science, Nature 559 (2018) 547–555. https://doi.org/10.1038/s41586-018-0337-2.
[109] J.D. Kelleher, B. Mac Namee, A. D'Arcy, Fundamentals of Machine Learning for Predictive Data Analytics: Algorithms, Worked Examples, and Case Studies, Second, MIT Press, Cambridge, MA, 2020.

[110] E. Alpaydin, Introduction to Machine Learning, MIT Press, 2020.
[111] N. Islam, W. Huang, H.L. Zhuang, Machine learning for phase selection in multi-principal element alloys, Comput Mater Sci 150 (2018) 230–235. https://doi.org/10.1016/j.commatsci.2018.04.003.
[112] W. Huang, P. Martin, H.L. Zhuang, Machine-learning phase prediction of high-entropy alloys, Acta Mater 169 (2019) 225–236. https://doi.org/10.1016/j.actamat.2019.03.012.
[113] Z. Zhou, Y. Zhou, Q. He, Z. Ding, F. Li, Y. Yang, Machine learning guided appraisal and exploration of phase design for high entropy alloys, NPJ Comput Mater 5 (2019) 1–9. https://doi.org/10.1038/s41524-019-0265-1.
[114] R. Machaka, Machine learning-based prediction of phases in high-entropy alloys, Comput Mater Sci 188 (2021) 110244. https://doi.org/10.1016/j.commatsci.2020.110244.
[115] S.Y. Lee, S. Byeon, H.S. Kim, H. Jin, S. Lee, Deep learning-based phase prediction of high-entropy alloys: Optimization, generation, and explanation, Mater Des 197 (2021) 109260. https://doi.org/10.1016/j.matdes.2020.109260.
[116] L. Zhang, H. Chen, X. Tao, H. Cai, J. Liu, Y. Ouyang, Q. Peng, Y. Du, Machine learning reveals the importance of the formation enthalpy and atom-size difference in forming phases of high entropy alloys, Mater Des 193 (2020) 108835. https://doi.org/10.1016/j.matdes.2020.108835.
[117] Z. Pei, J. Yin, J.A. Hawk, D.E. Alman, M.C. Gao, Machine-learning informed prediction of high-entropy solid solution formation: Beyond the Hume-Rothery rules, NPJ Comput Mater 6 (2020). https://doi.org/10.1038/s41524-020-0308-7.
[118] Y.J. Chang, C.Y. Jui, W.J. Lee, A.C. Yeh, Prediction of the Composition and Hardness of High-Entropy Alloys by Machine Learning, Jom 71 (2019) 3433–3442. https://doi.org/10.1007/s11837-019-03704-4.
[119] Y. Diao, L. Yan, K. Gao, Improvement of the machine learning-based corrosion rate prediction model through the optimization of input features, Mater Des 198 (2021) 109326. https://doi.org/10.1016/j.matdes.2020.109326.
[120] A. Nazarahari, D. Canadinc, Prediction of the NiTi shape memory alloy composition with the best corrosion resistance for dental applications utilizing artificial intelligence, Mater Chem Phys 258 (2020) 123974. https://doi.org/10.1016/j.matchemphys.2020.123974.
[121] D. Xue, D. Xue, R. Yuan, Y. Zhou, P. V. Balachandran, X. Ding, J. Sun, T. Lookman, An informatics approach to transformation temperatures of NiTi-based shape memory alloys, Acta Mater 125 (2017) 532–541. https://doi.org/10.1016/j.actamat.2016.12.009.
[122] T. Lookman, P. V. Balachandran, D. Xue, J. Hogden, J. Theiler, Statistical inference and adaptive design for materials discovery, Curr Opin Solid State Mater Sci 21 (2017) 121–128. https://doi.org/10.1016/j.cossms.2016.10.002.
[123] A.A. Catal, E. Bedir, R. Yilmaz, D. Canadinc, Design of a NiTiHf shape memory alloy with an austenite finish temperature beyond 400 °C utilizing artificial intelligence, J Alloys Compd 904 (2022) 164135. https://doi.org/10.1016/j.jallcom.2022.164135.
[124] F.Z. Dai, B. Wen, Y. Sun, H. Xiang, Y. Zhou, Theoretical prediction on thermal and mechanical properties of high entropy (Zr0.2Hf0.2Ti0.2Nb0.2Ta0.2)C by deep learning potential, J Mater Sci Technol 43 (2020) 168–174. https://doi.org/10.1016/j.jmst.2020.01.005.

[125] F.Z. Dai, Y. Sun, B. Wen, H. Xiang, Y. Zhou, Temperature Dependent Thermal and Elastic Properties of High Entropy (Ti0.2Zr0.2Hf0.2Nb0.2Ta0.2)B2: Molecular Dynamics Simulation by Deep Learning Potential, J Mater Sci Technol 72 (2021) 8–15. https://doi.org/10.1016/j.jmst.2020.07.014.
[126] S. Guo, Phase selection rules for cast high entropy alloys: An overview, Materials Science and Technology (United Kingdom) 31 (2015) 1223–1230. https://doi.org/10.1179/1743284715Y.0000000018.
[127] X. Yang, Y. Zhang, Prediction of high-entropy stabilized solid-solution in multi-component alloys, Mater Chem Phys 132 (2012) 233–238. https://doi.org/10.1016/j.matchemphys.2011.11.021.
[128] A.K. Singh, N. Kumar, A. Dwivedi, A. Subramaniam, A geometrical parameter for the formation of disordered solid solutions in multi-component alloys, Intermetallics (Barking) 53 (2014) 112–119. https://doi.org/10.1016/j.intermet.2014.04.019.
[129] Z. Wang, Y. Huang, Y. Yang, J. Wang, C.T. Liu, Atomic-size effect and solid solubility of multicomponent alloys, Scr Mater 94 (2015) 28–31. https://doi.org/10.1016/j.scriptamat.2014.09.010.
[130] U. Mizutani, H. Sato, Determination of electrons per atom ratio for transition metal compounds studied by FLAPW-Fourier calculations, Philosophical Magazine 96 (2016) 3075–3096. https://doi.org/10.1080/14786435.2016.1224946.
[131] A. Takeuchi, A. Inoue, Classification of bulk metallic glasses by atomic size difference, heat of mixing and period of constituent elements and its application to characterization of the main alloying element, Mater Trans 46 (2005) 2817–2829. https://doi.org/10.2320/matertrans.46.2817.
[132] B. Gregorutti, B. Michel, P. Saint-Pierre, Correlation and variable importance in random forests, Stat Comput 27 (2017) 659–678. https://doi.org/10.1007/s11222-016-9646-1.
[133] J. Gómez-Ramírez, M. Ávila-Villanueva, M.Á. Fernández-Blázquez, Selecting the most important self-assessed features for predicting conversion to mild cognitive impairment with random forest and permutation-based methods, Sci Rep 10 (2020) 1–15. https://doi.org/10.1038/s41598-020-77296-4.
[134] D. Cournapeau, F. Pedregosa, V. Michel, O. Grisel, M. Blondel, P. Prettenhofer, R. Weiss, J. Vanderplas, D. Cournapeau, F. Pedregosa, G. Varoquaux, A. Gramfort, B. Thirion, O. Grisel, V. Dubourg, A. Passos, M. Brucher, M. Perrot andÉdouardand, A. Duchesnay, Duchesnay Edouard, Scikit-learn: Machine Learning in Python, Journal of Machine Learning Research 12 (2011) 2825–2830. http://scikit-learn.sourceforge.net. (accessed February 15, 2021).
[135] L. Toloşi, T. Lengauer, Classification with correlated features: Unreliability of feature ranking and solutions, Bioinformatics 27 (2011) 1986–1994. https://doi.org/10.1093/bioinformatics/btr300.
[136] G. James, D. Witten, T. Hastie, R. Tibshiran, An Introduction to Statistical Learning with Applications in R, Springer, New York, 2013.
[137] S.M. Shaikh, V.S. Hariharan, S.K. Yadav, B.S. Murty, CALPHAD and rule-of-mixtures: A comparative study for refractory high entropy alloys, Intermetallics (Barking) 127 (2020) 106926. https://doi.org/10.1016/j.intermet.2020.106926.
[138] T. Yang, Y.L. Zhao, W.H. Liu, J.H. Zhu, J.J. Kai, C.T. Liu, Ductilizing brittle high-entropy alloys via tailoring valence electron concentrations of precipitates

by controlled elemental partitioning, Mater Res Lett 6 (2018) 600–606. https://doi.org/10.1080/21663831.2018.1518276.
[139] W. Zhao, J.L. Cheng, S.D. Feng, G. Li, R.P. Liu, Intrinsic correlation between elastic modulus and atomic bond stiffness in metallic glasses, Mater Lett 175 (2016) 227–230. https://doi.org/10.1016/j.matlet.2016.03.037.
[140] T. Kokubo, H. Takadama, How useful is SBF in predicting in vivo bone bioactivity?, Biomaterials 27 (2006) 2907–2915. https://doi.org/10.1016/j.biomaterials.2006.01.017.
[141] G. Astm, G 31-72: Standard Practice for Laboratory Immersion Corrosion Testing of Metals, Annual Book of Standards (2004).
[142] W.C. Oliver, G.M. Pharr, An improved technique for determining hardness and elastic modulus using load and displacement sensing indentation experiments, J Mater Res 7 (1992) 1564–1583.
[143] M. Wang, Z.L. Ma, Z.Q. Xu, X.W. Cheng, Designing VxNbMoTa refractory high-entropy alloys with improved properties for high-temperature applications, Scr Mater 191 (2021) 131–136. https://doi.org/10.1016/j.scriptamat.2020.09.027.
[144] S.Y. Chen, Y. Tong, K.K. Tseng, J.W. Yeh, J.D. Poplawsky, J.G. Wen, M.C. Gao, G. Kim, W. Chen, Y. Ren, R. Feng, W.D. Li, P.K. Liaw, Phase transformations of HfNbTaTiZr high-entropy alloy at intermediate temperatures, Scr Mater 158 (2019) 50–56. https://doi.org/10.1016/j.scriptamat.2018.08.032.
[145] B. Schuh, B. Völker, J. Todt, N. Schell, L. Perrière, J. Li, J.P. Couzinié, A. Hohenwarter, Thermodynamic instability of a nanocrystalline, single-phase TiZrNbHfTa alloy and its impact on the mechanical properties, Acta Mater 142 (2018) 201–212. https://doi.org/10.1016/j.actamat.2017.09.035.
[146] L.C. Ming, M.H. Manghnani, K.W. Katahara, Investigation of a→w transformation in the Zr-Hf system to 42 GPa, J Appl Phys 52 (1981) 1332–1335. https://doi.org/10.1063/1.329760.
[147] S. Zhou, Y. You, J. Zhang, Y. Cao, Microstructure, Mechanical and Corrosion Properties and Biocompatibility of Mg-Y-Zn-Zr Rolled Alloy for Biomedical Applications, Transactions of the Indian Institute of Metals (2021) 1–10. https://doi.org/10.1007/s12666-021-02401-8.
[148] Y. Yao, Y. Jin, W. Gao, X. Liang, J. Chen, S. Zhu, Corrosion Behavior of AlFeCrCoNiZrx High-Entropy Alloys in 0.5 M Sulfuric Acid Solution, Metals (Basel) 11 (2021) 1471. https://doi.org/10.3390/met11091471.
[149] K. Masemola, P. Popoola, N. Malatji, The effect of annealing temperature on the microstructure, mechanical and electrochemical properties of arc-melted AlCrFeMnNi equi-atomic High entropy alloy, Journal of Materials Research and Technology 9 (2020) 5241–5251. https://doi.org/10.1016/j.jmrt.2020.03.050.
[150] R. Mirea, A.T. Cucuruz, L.C. Ceatra, T. Badea, I. Biris, E. Popescu, A. Paraschiv, R. Ene, G. Sbarcea, M. Cretu, In-depth comparative assessment of different metallic biomaterials in simulated body fluid, Materials 14 (2021) 2774. https://doi.org/10.3390/ma14112774.
[151] H. Liao, T. Wurtz, J. Li, Influence of titanium ion on mineral formation and properties of osteoid nodules in rat calvaria cultures, J Biomed Mater Res 47 (1999) 220–227. https://doi.org/10.1002/(SICI)1097-4636(199911)47:2<220::AID-JBM12>3.0.CO;2-9.
[152] M. Cabibbo, D. Ciccarelli, S. Spigarelli, Nanoindentation Hardness measurement in piling up SiO2 coating, in: Phys Procedia, Elsevier, 2013: pp. 100–112. https://doi.org/10.1016/j.phpro.2012.12.014.

[153] R. Saha, W.D. Nix, Solt films on hard substrates - Nanoindentation of tungsten films on sapphire substrates, Materials Science and Engineering A 319–321 (2001) 898–901. https://doi.org/10.1016/S0921-5093(01)01076-0.
[154] D.G. Shaysultanov, N.D. Stepanov, G.A. Salishchev, M.A. Tikhonovsky, Effect of heat treatment on the structure and hardness of high-entropy alloys CoCrFeNiMnVx (x = 0.25, 0.5, 0.75, 1), Physics of Metals and Metallography 118 (2017) 579–590. https://doi.org/10.1134/S0031918X17060084.
[155] N. Tüten, D. Canadinc, A. Motallebzadeh, B. Bal, Microstructure and tribological properties of TiTaHfNbZr high entropy alloy coatings deposited on Ti–6Al–4V substrates, Intermetallics (Barking) 105 (2019) 99–106. https://doi.org/10.1016/j.intermet.2018.11.015.
[156] C. Wei, L. Luo, Z. Wu, J. Zhang, S. Su, Y. Zhan, New Zr–25Ti–xMo alloys for dental implant application: Properties characterization and surface analysis, J Mech Behav Biomed Mater 111 (2020) 104017. https://doi.org/10.1016/j.jmbbm.2020.104017.
[157] B.D. Beake, T.W. Liskiewicz, Comparison of nano-fretting and nano-scratch tests on biomedical materials, in: Tribol Int, Elsevier, 2013: pp. 123–131. https://doi.org/10.1016/j.triboint.2012.08.007.
[158] J.M. Hernández-López, A. Conde, J. de Damborenea, M.A. Arenas, Correlation of the nanostructure of the anodic layers fabricated on Ti13Nb13Zr with the electrochemical impedance response, Corros Sci 94 (2015) 61–69. https://doi.org/10.1016/j.corsci.2015.01.041.
[159] E.P. Utomo, A. Anawati, F. Rokhmanto, Effect of Sn on corrosion resistance and modulus young of as-cast Ti-Nb-Sn alloys for biocompatible implant, PROCEEDINGS OF THE 3RD INTERNATIONAL SEMINAR ON METALLURGY AND MATERIALS (ISMM2019): Exploring New Innovation in Metallurgy and Materials 2232 (2020) 070007. https://doi.org/10.1063/5.0002699.
[160] R. Alias, R. Mahmoodian, M.H. Abd Shukor, Development and characterization of a multilayer silver/silver-tantalum oxide thin film coating on stainless steel for biomedical applications, Int J Adhes Adhes 92 (2019) 89–98. https://doi.org/10.1016/j.ijadhadh.2019.04.010.
[161] L. Zhao, P.K. Chu, Y. Zhang, Z. Wu, Antibacterial coatings on titanium implants, J Biomed Mater Res B Appl Biomater 91B (2009) 470–480. https://doi.org/10.1002/JBM.B.31463.
[162] R. Xu, X. Yang, J. Jiang, P. Li, X. Zhang, G. Wu, P.K. Chu, Effects of silver plasma immersion ion implantation on the surface characteristics and cytocompatibility of titanium nitride films, Surf Coat Technol 279 (2015) 166–170. https://doi.org/10.1016/j.surfcoat.2015.08.033.
[163] A. Ewald, S.K. Glückermann, R. Thull, U. Gbureck, Antimicrobial titanium/silver PVD coatings on titanium, BioMedical Engineering OnLine 2006 5:1 5 (2006) 1–10. https://doi.org/10.1186/1475-925X-5-22.
[164] K. Koev, N. Donkov, H. Naidenski, R. Nikov, V. Kusovski, T. Nurgaliev, L. Avramov, Antibacterial silver nanolayers for coatings on surgical and microsurgical instruments, J Phys Conf Ser 1492 (2020) 012045. https://doi.org/10.1088/1742-6596/1492/1/012045.
[165] J. Wu, K. Ueda, T. Narushima, Fabrication of Ag and Ta co-doped amorphous calcium phosphate coating films by radiofrequency magnetron sputtering and

their antibacterial activity, Materials Science and Engineering C 109 (2020) 110599. https://doi.org/10.1016/j.msec.2019.110599.
[166] Y. Chen, X. Zheng, Y. Xie, H. Ji, C. Ding, H. Li, K. Dai, Silver release from silver-containing hydroxyapatite coatings, Surf Coat Technol 205 (2010) 1892–1896. https://doi.org/10.1016/j.surfcoat.2010.08.073.
[167] K. Batebi, B. Abbasi Khazaei, A. Afshar, Characterization of sol-gel derived silver/fluor-hydroxyapatite composite coatings on titanium substrate, Surf Coat Technol 352 (2018) 522–528. https://doi.org/10.1016/j.surfcoat.2018.08.021.
[168] E. Zhang, C. Liu, A new antibacterial Co-Cr-Mo-Cu alloy: Preparation, biocorrosion, mechanical and antibacterial property, Materials Science and Engineering C 69 (2016) 134–143. https://doi.org/10.1016/j.msec.2016.05.028.
[169] J.G. Yu, X.H. Sun, H.H. Gong, L. Dong, M.L. Zhao, R.X. Wan, H.Q. Gu, D.J. Li, Influence of Ag concentration on microstructure, mechanical properties and cytocompatibility of nanoscale Ti-Ag-N/Ag multilayers, Surf Coat Technol 312 (2017) 128–133. https://doi.org/10.1016/j.surfcoat.2017.01.104.
[170] A.A. Alamdari, U. Unal, A. Motallebzadeh, Investigation of microstructure, mechanical properties, and biocorrosion behavior of Ti1.5ZrTa0.5Nb0.5W0.5 refractory high-entropy alloy film doped with Ag nanoparticles, Surfaces and Interfaces 28 (2022) 101617. https://doi.org/10.1016/j.surfin.2021.101617.
[171] C. Pierret, L. Maunoury, I. Monnet, S. Bouffard, A. Benyagoub, C. Grygiel, D. Busardo, D. Muller, D. Höche, Friction and wear properties modification of Ti-6Al-4V alloy surfaces by implantation of multi-charged carbon ions, Wear 319 (2014) 19–26. https://doi.org/10.1016/j.wear.2014.07.001.
[172] S.J.L. Sullivan, L.D.T. Topoleski, Surface Modifications for Improved Wear Performance in Artificial Joints: A Review, JOM 67 (2015) 2502–2517. https://doi.org/10.1007/s11837-015-1543-0.
[173] Y. Li, J. Ho, C.P. Ooi, Antibacterial efficacy and cytotoxicity studies of copper (II) and titanium (IV) substituted hydroxyapatite nanoparticles, Materials Science and Engineering C 30 (2010) 1137–1144. https://doi.org/10.1016/j.msec.2010.06.011.
[174] V. Stanić, S. Dimitrijević, J. Antić-Stanković, M. Mitrić, B. Jokić, I.B. Plećaš, S. Raičević, Synthesis, characterization and antimicrobial activity of copper and zinc-doped hydroxyapatite nanopowders, Appl Surf Sci 256 (2010) 6083–6089. https://doi.org/10.1016/j.apsusc.2010.03.124.
[175] X. Song, M. Zhao, D. Li, Effects of Ag/Ta co-implanted TiN coating on medical titanium alloy on biological and antibacterial properties, IOP Conf Ser Mater Sci Eng 1167 (2021) 012011. https://doi.org/10.1088/1757-899x/1167/1/012011.
[176] P.J. Kelly, H. Li, P.S. Benson, K.A. Whitehead, J. Verran, R.D. Arnell, I. Iordanova, Comparison of the tribological and antimicrobial properties of CrN/Ag, ZrN/Ag, TiN/Ag, and TiN/Cu nanocomposite coatings, Surf Coat Technol 205 (2010) 1606–1610. https://doi.org/10.1016/j.surfcoat.2010.07.029.
[177] H.B. Wang, Q.F. Wei, J.Y. Wang, J.H. Hong, X.Y. Zhao, Sputter deposition of nanostructured antibacterial silver on polypropylene non-wovens, Surface Engineering 24 (2008) 70–74. https://doi.org/10.1179/174329408X277493.
[178] G. Gosheger, J. Hardes, H. Ahrens, A. Streitburger, H. Buerger, M. Erren, A. Gunsel, F.H. Kemper, W. Winkelmann, C. Von Eiff, Silver-coated megaendoprostheses in a rabbit model - An analysis of the infection rate and toxicological side effects, Biomaterials 25 (2004) 5547–5556. https://doi.org/10.1016/j.biomaterials.2004.01.008.

[179] C. Liu, L. Geng, Y.F. Yu, Y. Zhang, B. Zhao, Q. Zhao, Mechanisms of the enhanced antibacterial effect of Ag-TiO2 coatings, Biofouling 34 (2018) 190–199. https://doi.org/10.1080/08927014.2017.1423287.
[180] P. Devasconcellos, S. Bose, H. Beyenal, A. Bandyopadhyay, L.G. Zirkle, Antimicrobial particulate silver coatings on stainless steel implants for fracture management, Materials Science and Engineering C 32 (2012) 1112–1120. https://doi.org/10.1016/j.msec.2012.02.020.
[181] Q.L. Feng, J. Wu, G.Q. Chen, F.Z. Cui, T.N. Kim, J.O. Kim, A mechanistic study of the antibacterial effect of silver ions on Escherichia coli and Staphylococcus aureus, J Biomed Mater Res 52 (2000) 662–668. https://doi.org/10.1002/1097-4636(20001215)52:4<662::AID-JBM10>3.0.CO;2-3.
[182] M. Rai, A. Yadav, A. Gade, Silver nanoparticles as a new generation of antimicrobials, Biotechnol Adv 27 (2009) 76–83. https://doi.org/10.1016/j.biotechadv.2008.09.002.
[183] J.R. Morones, J.L. Elechiguerra, A. Camacho, K. Holt, J.B. Kouri, J.T. Ramírez, M.J. Yacaman, The bactericidal effect of silver nanoparticles, Nanotechnology 16 (2005) 2346–2353. https://doi.org/10.1088/0957-4484/16/10/059.
[184] M. Yamanaka, K. Hara, J. Kudo, Bactericidal actions of a silver ion solution on Escherichia coli, studied by energy-filtering transmission electron microscopy and proteomic analysis, Appl Environ Microbiol 71 (2005) 7589–7593. https://doi.org/10.1128/AEM.71.11.7589-7593.2005.
[185] N.K. Manninen, R.E. Galindo, N. Benito, N.M. Figueiredo, A. Cavaleiro, C. Palacio, S. Carvalho, Ag-Ti(C, N)-based coatings for biomedical applications: Influence of silver content on the structural properties, J Phys D Appl Phys 44 (2011) 375501. https://doi.org/10.1088/0022-3727/44/37/375501.
[186] C.H. Lai, M.H. Tsai, S.J. Lin, J.W. Yeh, Influence of substrate temperature on structure and mechanical, properties of multi-element (AlCrTaTiZr)N coatings, Surf Coat Technol 201 (2007) 6993–6998. https://doi.org/10.1016/j.surfcoat.2007.01.001.
[187] T.K. Chen, M.S. Wong, T.T. Shun, J.W. Yeh, Nanostructured nitride films of multi-element high-entropy alloys by reactive DC sputtering, Surf Coat Technol 200 (2005) 1361–1365. https://doi.org/10.1016/j.surfcoat.2005.08.081.
[188] H. Sun, X. Lian, X. Huang, D. Hui, G. Wang, Effects of substrate properties and sputtering methods on self-formation of Ag particles on the Ag-Mo(Zr) alloy films, Nanotechnol Rev 9 (2020) 990–997. https://doi.org/10.1515/ntrev-2020-0077.
[189] J.A. Thornton, D.W. Hoffman, Stress-related effects in thin films, Thin Solid Films 171 (1989) 5–31. https://doi.org/10.1016/0040-6090(89)90030-8.
[190] A. Rizzo, M.A. Tagliente, M. Alvisi, S. Scaglione, Structural and optical properties of silver thin films deposited by RF magnetron sputtering, Thin Solid Films 396 (2001) 29–35. https://doi.org/10.1016/S0040-6090(01)01242-1.
[191] N. Maréchal, E. Quesnel, Y. Pauleau, Silver thin films deposited by magnetron sputtering, Thin Solid Films 241 (1994) 34–38. https://doi.org/10.1016/0040-6090(94)90391-3.
[192] J.E. Sundgren, Structure and properties of TiN coatings, Thin Solid Films 128 (1985) 21–44. https://doi.org/10.1016/0040-6090(85)90333-5.
[193] V. Kapaklis, P. Poulopoulos, V. Karoutsos, T. Manouras, C. Politis, Growth of thin Ag films produced by radio frequency magnetron sputtering, Thin Solid Films 510 (2006) 138–142. https://doi.org/10.1016/J.TSF.2005.12.311.

[194] X.B. Feng, J.Y. Zhang, Y.Q. Wang, Z.Q. Hou, K. Wu, G. Liu, J. Sun, Size effects on the mechanical properties of nanocrystalline NbMoTaW refractory high entropy alloy thin films, Int J Plast 95 (2017) 264–277. https://doi.org/10.1016/j.ijplas.2017.04.013.
[195] R. Carel, Grain growth and texture evolution in thin films, 1995. https://pdfs.semanticscholar.org/fdb5/9c2618a7b8581c94b94eec8792afb1710fef.pdf.
[196] C. V. Thompson, On the grain size and coalescence stress resulting from nucleation and growth processes during formation of polycrystalline thin films, J Mater Res 14 (1999) 3164–3168. https://doi.org/10.1557/JMR.1999.0424.
[197] C. V Thompson, Structure evolution during processing of polycrystalline films, Annu Rev Mater Res 30 (2000).
[198] Y.H. Cheng, B.K. Tay, S.P. Lau, Influence of deposition temperature on the structure and internal stress of TiN films deposited by filtered cathodic vacuum arc, Journal of Vacuum Science & Technology A: Vacuum, Surfaces, and Films 20 (2002) 1270–1274. https://doi.org/10.1116/1.1481043.
[199] N.M. Dang, Z.Y. Wang, C.H. Lin, M.T. Lin, The Effects of Stresses and Interfaces on Texture Transformation in Silver Thin Films, Nanomaterials 12 (2022) 329. https://doi.org/10.3390/nano12030329.
[200] C. V. Thompson, R. Carel, Stress and grain growth in thin films, J Mech Phys Solids 44 (1996) 657–673. https://doi.org/10.1016/0022-5096(96)00022-1.
[201] U.C. Oh, J.H. Je, Effects of strain energy on the preferred orientation of TiN thin films, J Appl Phys 74 (1993) 1692–1696. https://doi.org/10.1063/1.355297.
[202] N. Maréchal, E. Quesnel, Y. Pauleau, Characterization of silver films deposited by radio frequency magnetron sputtering, Journal of Vacuum Science & Technology A: Vacuum, Surfaces, and Films 12 (1998) 707. https://doi.org/10.1116/1.578856.
[203] D.W. Hoffman, J.A. Thornton, Internal stresses in sputtered chromium, Thin Solid Films 40 (1977) 355–363. https://doi.org/10.1016/0040-6090(77)90137-7.
[204] C. Charton, M. Fahland, Growth of Ag films on PET deposited by magnetron sputtering, Vacuum 68 (2002) 65–73. https://doi.org/10.1016/S0042-207X(02)00289-0.
[205] J. He, R.F. Klie, G. Logvenov, I. Bozovic, Y. Zhu, Microstructure of strained La 2 CuO 4+δ thin films on varied substrates, 2006. https://doi.org/10.48550/arxiv.cond-mat/0612129.
[206] J. Xiong, Controlling surface segregation and tuning silver ion release of reactively sputtered Ag / TiO x nanocomposites, 2014.
[207] S.K. Sharma, J. Spitz, Hillock formation, hole growth and agglomeration in thin silver films, Thin Solid Films 65 (1980) 339–350. https://doi.org/10.1016/0040-6090(80)90244-8.
[208] W.B. Pennebaker, Hillock growth and stress relief in sputtered Au films, J Appl Phys 40 (1969) 394–400. https://doi.org/10.1063/1.1657067.
[209] S.K. Lahiri, Stress relief and hillock formation in thin lead films, J Appl Phys 41 (1970) 3172–3176. https://doi.org/10.1063/1.1659383.
[210] S.J. Hwang, J.H. Lee, C.O. Jeong, Y.C. Joo, Effect of film thickness and annealing temperature on hillock distributions in pure Al films, Scr Mater 56 (2007) 17–20. https://doi.org/10.1016/j.scriptamat.2006.09.001.
[211] P. Chaudhari, Hillock growth in thin films, J Appl Phys 45 (1974) 4339–4346. https://doi.org/10.1063/1.1663054.

[212] T. Spalvins, W.A. Brainard, Nodular growth in thick-sputtered metallic coating, J Vac Sci Technol 11 (1974) 1186–1192. https://doi.org/10.1116/1.1318706.
[213] S. Vepřek, The search for novel, superhard materials, Journal of Vacuum Science & Technology A: Vacuum, Surfaces, and Films 17 (1999) 2401–2420. https://doi.org/10.1116/1.581977.
[214] I. Carvalho, M. Curado, C. Palacio, S. Carvalho, A. Cavaleiro, Ag release from sputtered Ag/a:C nanocomposite films after immersion in pure water and NaCl solution, Thin Solid Films 671 (2019) 85–94. https://doi.org/10.1016/j.tsf.2018.12.010.
[215] C. Beer, R. Foldbjerg, Y. Hayashi, D.S. Sutherland, H. Autrup, Toxicity of silver nanoparticles-Nanoparticle or silver ion?, Toxicol Lett 208 (2012) 286–292. https://doi.org/10.1016/j.toxlet.2011.11.002.
[216] C. Greulich, D. Braun, A. Peetsch, J. Diendorf, B. Siebers, M. Epple, M. Köller, The toxic effect of silver ions and silver nanoparticles towards bacteria and human cells occurs in the same concentration range, RSC Adv 2 (2012) 6981–6987. https://doi.org/10.1039/c2ra20684f.
[217] M. Jenko, M. Gorenšek, M. Godec, M. Hodnik, B.Š. Batič, Č. Donik, J.T. Grant, D. Dolinar, Surface chemistry and microstructure of metallic biomaterials for hip and knee endoprostheses, Appl Surf Sci 427 (2018) 584–593. https://doi.org/10.1016/j.apsusc.2017.08.007.
[218] M. Dinu, S. Franchi, V. Pruna, C.M. Cotrut, V. Secchi, M. Santi, I. Titorencu, C. Battocchio, G. Iucci, A. Vladescu, Ti-Nb-Zr system and its surface biofunctionalization for biomedical applications, Elsevier Inc., 2018. https://doi.org/10.1016/B978-0-12-812456-7.00008-1.
[219] M.Z. Ibrahim, A.A.D. Sarhan, F. Yusuf, M. Hamdi, Biomedical materials and techniques to improve the tribological, mechanical and biomedical properties of orthopedic implants – A review article, J Alloys Compd 714 (2017) 636–667. https://doi.org/10.1016/j.jallcom.2017.04.231.
[220] L.C. Zhang, L.Y. Chen, A Review on Biomedical Titanium Alloys: Recent Progress and Prospect, Adv Eng Mater 21 (2019) 1–29. https://doi.org/10.1002/adem.201801215.
[221] S. Mischler, A.I. Muñoz, Wear of CoCrMo alloys used in metal-on-metal hip joints: A tribocorrosion appraisal, Wear 297 (2013) 1081–1094. https://doi.org/10.1016/j.wear.2012.11.061.
[222] H.F. Li, Y.F. Zheng, Recent advances in bulk metallic glasses for biomedical applications, Acta Biomater 36 (2016) 1–20. https://doi.org/10.1016/j.actbio.2016.03.047.
[223] R. Bolmaro, A.C. Parau, V. Pruna, M.A. Surmeneva, L.R. Constantin, M. Avalos, C.M. Cotrut, R. Tutuianu, M. Braic, D. V. Cojocaru, I. Dan, S. Croitoru, R.A. Surmenev, A. Vladescu, Investigation of cast and annealed Ti25Nb10Zr alloy as material for orthopedic devices, Journal of Materials Research and Technology 8 (2019) 3399–3414. https://doi.org/10.1016/j.jmrt.2019.06.006.
[224] L. Salas, J. Chávez, O. Jimenez, M. Flores-Jimenez, F. Alvarado-Hernandez, L. Olmos, J. Pérez-Alvarez, M. Flores, Tribocorrosion and corrosion behavior of quaternary Ti-24Nb-xZr-ySn alloys in SBF, Mater Lett 283 (2021) 128903. https://doi.org/10.1016/j.matlet.2020.128903.
[225] W. Xiong, A.X.Y. Guo, S. Zhan, C.T. Liu, S.C. Cao, Refractory high-entropy alloys: A focused review of preparation methods and properties, J Mater Sci Technol 142 (2023) 196–215. https://doi.org/10.1016/j.jmst.2022.08.046.

[226] O.N. Senkov, J.M. Scott, S. V. Senkova, D.B. Miracle, C.F. Woodward, Microstructure and room temperature properties of a high-entropy TaNbHfZrTi alloy, J Alloys Compd 509 (2011) 6043–6048. https://doi.org/10.1016/j.jallcom.2011.02.171.
[227] Y. Zhang, Z. Chen, D. Cao, J. Zhang, P. Zhang, Q. Tao, X. Yang, Concurrence of spinodal decomposition and nano-phase precipitation in a multi-component AlCoCrCuFeNi high-entropy alloy, Journal of Materials Research and Technology 8 (2019) 726–736. https://doi.org/10.1016/j.jmrt.2018.04.020.
[228] M. Hu, K. Song, W. Song, Dynamic mechanical properties and microstructure evolution of AlCoCrFeNi2.1 eutectic high-entropy alloy at different temperatures, J Alloys Compd 892 (2022) 162097. https://doi.org/10.1016/j.jallcom.2021.162097.
[229] T. Xiang, M. Zhao, P. Du, G. Xie, Heat treatment effects on microstructure and mechanical properties of TiZrNbTa high-entropy alloy, J Alloys Compd 930 (2023) 167408. https://doi.org/10.1016/j.jallcom.2022.167408.
[230] P. Chui, R. Jing, F. Zhang, J. Li, T. Feng, Mechanical properties and corrosion behavior of β-type Ti-Zr-Nb-Mo alloys for biomedical application, J Alloys Compd 842 (2020) 155693. https://doi.org/10.1016/j.jallcom.2020.155693.
[231] N. Hua, W. Wang, Q. Wang, Y. Ye, S. Lin, L. Zhang, Q. Guo, J. Brechtl, P.K. Liaw, Mechanical, corrosion, and wear properties of biomedical Ti–Zr–Nb–Ta–Mo high entropy alloys, J Alloys Compd 861 (2021) 157997. https://doi.org/10.1016/j.jallcom.2020.157997.
[232] M. Akmal, A. Hussain, M. Afzal, Y.I. Lee, H.J. Ryu, Systematic Study of (MoTa)xNbTiZr Medium- and High-Entropy Alloys for Biomedical Implants- In Vivo Biocompatibility Examinations, J Mater Sci Technol 78 (2020) 183–191. https://doi.org/10.1016/j.jmst.2020.10.049.
[233] K. Glowka, M. Zubko, P. Świec, K. Prusik, M. Szklarska, D. Chrobak, J.L. Lábár, D. Stróż, Influence of Molybdenum on the Microstructure, Mechanical Properties and Corrosion Resistance of Ti20Ta20Nb20(ZrHf)20−xMox (Where: x = 0, 5, 10, 15, 20) High Entropy Alloys, Materials 15 (2022) 393. https://doi.org/10.3390/ma15010393.
[234] S. Wang, D. Wu, H. She, M. Wu, D. Shu, A. Dong, H. Lai, B. Sun, Design of high-ductile medium entropy alloys for dental implants, Materials Science and Engineering C 113 (2020) 110959. https://doi.org/10.1016/j.msec.2020.110959.
[235] W. Yang, Y. Liu, S. Pang, P.K. Liaw, T. Zhang, Bio-corrosion behavior and in vitro biocompatibility of equimolar TiZrHfNbTa high-entropy alloy, Intermetallics (Barking) 124 (2020) 106845. https://doi.org/10.1016/j.intermet.2020.106845.
[236] W. Wang, Z. Zhang, J. Niu, H. Wu, S. Zhai, Y. Wang, Effect of Al addition on structural evolution and mechanical properties of the AlxHfNbTiZr high-entropy alloys, Mater Today Commun 16 (2018) 242–249. https://doi.org/10.1016/j.mtcomm.2018.06.004.
[237] X. Pei, Y. Du, X. Hao, H. Wang, Q. Zhou, H. Wu, H. Wang, Microstructure and tribological properties of TiZrV0.5Nb0.5Alx refractory high entropy alloys at elevated temperature, Wear 488–489 (2022) 204166. https://doi.org/10.1016/j.wear.2021.204166.
[238] Y.Y. Tan, Z.J. Chen, M.Y. Su, G. Ding, M.Q. Jiang, Z.C. Xie, Y. Gong, T. Wu, Z.H. Wu, H.Y. Wang, L.H. Dai, Lattice distortion and magnetic property of high

entropy alloys at low temperatures, J Mater Sci Technol 104 (2022) 236–243. https://doi.org/10.1016/j.jmst.2021.07.019.
[239] P.P. Cao, H.L. Huang, S.H. Jiang, X.J. Liu, H. Wang, Y. Wu, Z.P. Lu, Microstructural stability and aging behavior of refractory high entropy alloys at intermediate temperatures, J Mater Sci Technol 122 (2022) 243–254. https://doi.org/10.1016/j.jmst.2021.12.057.
[240] Y. Shi, B. Yang, P.K. Liaw, Corrosion-resistant high-entropy alloys: A review, Metals (Basel) 7 (2017) 1–18. https://doi.org/10.3390/met7020043.
[241] A. Hynowska, A. Blanquer, E. Pellicer, J. Fornell, S. Suriñach, M.D. Baró, S. González, E. Ibáñez, L. Barrios, C. Nogués, J. Sort, Novel Ti-Zr-Hf-Fe nanostructured alloy for biomedical applications, Materials 6 (2013) 4930–4945. https://doi.org/10.3390/ma6114930.
[242] A. Vladescu, A. Pârâu, I. Pana, C.M. Cotrut, L.R. Constantin, V. Braic, D.M. Vrânceanu, In vitro activity assays of sputtered HAp coatings with SiC addition in various simulated biological fluids, Coatings 9 (2019) 389. https://doi.org/10.3390/COATINGS9060389.
[243] N. Eliaz, Corrosion of metallic biomaterials: A review, Materials 12 (2019). https://doi.org/10.3390/ma12030407.
[244] P. Bocchetta, L.Y. Chen, J.D.C. Tardelli, A.C. Dos Reis, F. Almeraya-Calderón, P. Leo, Passive layers and corrosion resistance of biomedical ti-6al-4v and β-ti alloys, Coatings 11 (2021) 487. https://doi.org/10.3390/coatings11050487.
[245] P.F. Ji, B. Li, B.H. Chen, F. Wang, W. Ma, X.Y. Zhang, M.Z. Ma, R.P. Liu, Effect of Nb addition on the stability and biological corrosion resistance of Ti-Zr alloy passivation films, Corros Sci 170 (2020). https://doi.org/10.1016/j.corsci.2020.108696.
[246] C. Te Wu, H.T. Chang, C.Y. Wu, S.W. Chen, S.Y. Huang, M. Huang, Y.T. Pan, P. Bradbury, J. Chou, H.W. Yen, Machine learning recommends affordable new Ti alloy with bone-like modulus, Materials Today 34 (2020) 41–50. https://doi.org/10.1016/j.mattod.2019.08.008.
[247] E. Matykina, R. Arrabal, M. Mohedano, A. Pardo, M.C. Merino, E. Rivero, Stability of plasma electrolytic oxidation coating on titanium in artificial saliva, J Mater Sci Mater Med 24 (2013) 37–51. https://doi.org/10.1007/s10856-012-4787-z.
[248] H. Yao, J. Miao, Y. Liu, E. Guo, H. Huang, Y. Lu, T. Wang, T. Li, Effect of Ti and Nb Contents on Microstructure and Mechanical Properties of HfZrVTaMoWTixNby Refractory High-Entropy Alloys, Adv Eng Mater (2021) 2100225. https://doi.org/10.1002/adem.202100225.
[249] Y.-G. Dong, S. Chen, N.-N. Jia, Q.-H. Zhang, L. Wang, Y.-F. Xue, K. Jin, Microstructures and mechanical properties of Ta–Nb–Zr–Ti–Al refractory high entropy alloys with varying Ta/Ti ratios, Tungsten 1 (2021) 1–9. https://doi.org/10.1007/s42864-021-00111-8.
[250] Z. Wang, Y. Yan, Y. Wu, X. Huang, Y. Zhang, Y. Su, L. Qiao, Corrosion and tribocorrosion behavior of equiatomic refractory medium entropy TiZr(Hf, Ta, Nb) alloys in chloride solutions, Corros Sci 199 (2022) 110166. https://doi.org/10.1016/j.corsci.2022.110166.
[251] T.Y. Liu, J.C. Huang, W.S. Chuang, H.S. Chou, J.Y. Wei, C.Y. Chao, Y.C. Liao, J.S.C. Jang, Spinodal decomposition and mechanical response of a TiZrNbTa high-entropy alloy, Materials 12 (2019) 3508. https://doi.org/10.3390/ma12213508.

[252] S.A.R. Qadri, K.N. Sasidhar, E.A. Jagle, G. Miyamoto, S.R. Meka, Nitrogen-Induced Phase Separation in Equiatomic FeNiCo Medium Entropy Alloy, Metall Mater Trans A Phys Metall Mater Sci 53 (2022) 3216–3223. https://doi.org/10.1007/s11661-022-06746-7.
[253] Y. Wu, Q. Wang, D. Lin, X. Chen, T. Wang, W.Y. Wang, Y. Wang, X. Hui, Phase Stability and Deformation Behavior of TiZrHfNbO High-Entropy Alloys, Front Mater 7 (2020) 394. https://doi.org/10.3389/fmats.2020.589052.
[254] M. Regenberg, G. Hasemann, M. Wilke, T. Halle, M. Krüger, Microstructure evolution and mechanical properties of refractory Mo-Nb-V-W-Ti high-entropy alloys, Metals (Basel) 10 (2020) 1–13. https://doi.org/10.3390/met10111530.
[255] M. Todai, T. Nagase, T. Hori, A. Matsugaki, A. Sekita, T. Nakano, Novel TiNbTaZrMo high-entropy alloys for metallic biomaterials, Scr Mater 129 (2017) 65–68. https://doi.org/10.1016/j.scriptamat.2016.10.028.
[256] C.C. Juan, M.H. Tsai, C.W. Tsai, C.M. Lin, W.R. Wang, C.C. Yang, S.K. Chen, S.J. Lin, J.W. Yeh, Enhanced mechanical properties of HfMoTaTiZr and HfMoNbTaTiZr refractory high-entropy alloys, Intermetallics (Barking) 62 (2015) 76–83. https://doi.org/10.1016/j.intermet.2015.03.013.
[257] Y. Okazaki, E. Gotoh, Metal release from stainless steel, Co-Cr-Mo-Ni-Fe and Ni-Ti alloys in vascular implants, Corros Sci 50 (2008) 3429–3438. https://doi.org/10.1016/j.corsci.2008.09.002.
[258] B. Uzer, O. Birer, D. Canadinc, Investigation of the Dissolution–Reformation Cycle of the Passive Oxide Layer on NiTi Orthodontic Archwires, Shape Memory and Superelasticity 3 (2017) 264–273. https://doi.org/10.1007/s40830-017-0114-3.
[259] T. Hanawa, In vivo metallic biomaterials and surface modification, Materials Science and Engineering A 267 (1999) 260–266. https://doi.org/10.1016/S0921-5093(99)00101-X.
[260] S. Karimi, A.M. Alfantazi, Ion release and surface oxide composition of AISI 316L, Co-28Cr-6Mo, and Ti-6Al-4V alloys immersed in human serum albumin solutions, Materials Science and Engineering C 40 (2014) 435–444. https://doi.org/10.1016/j.msec.2014.04.007.
[261] S. Höhn, S. Virtanen, Effect of inflammatory conditions and H 2 O 2 on bare and coated Ti-6Al-4V surfaces: Corrosion behavior, metal ion release and Ca-P formation under long-term immersion in DMEM, Appl Surf Sci 357 (2015) 101–111. https://doi.org/10.1016/j.apsusc.2015.08.261.
[262] J. Jayaraj, C. Thinaharan, S. Ningshen, C. Mallika, U. Kamachi Mudali, Corrosion behavior and surface film characterization of TaNbHfZrTi high entropy alloy in aggressive nitric acid medium, Intermetallics (Barking) 89 (2017) 123–132. https://doi.org/10.1016/j.intermet.2017.06.002.
[263] F.Y. Zhou, B.L. Wang, K.J. Qiu, W.J. Lin, L. Li, Y.B. Wang, F.L. Nie, Y.F. Zheng, Microstructure, corrosion behavior and cytotoxicity of Zr-Nb alloys for biomedical application, Materials Science and Engineering C 32 (2012) 851–857. https://doi.org/10.1016/j.msec.2012.02.002.
[264] Q. Zhou, S. Sheikh, P. Ou, D. Chen, Q. Hu, S. Guo, Corrosion behavior of Hf0.5Nb0.5Ta0.5Ti1.5Zr refractory high-entropy in aqueous chloride solutions, Electrochem Commun 98 (2019) 63–68. https://doi.org/10.1016/j.elecom.2018.11.009.

[265] R. Simpson, R.G. White, J.F. Watts, M.A. Baker, XPS investigation of monatomic and cluster argon ion sputtering of tantalum pentoxide, Appl Surf Sci 405 (2017) 79–87. https://doi.org/10.1016/j.apsusc.2017.02.006.
[266] S. Mendis, W. Xu, H.P. Tang, L.A. Jones, D. Liang, R. Thompson, P. Choong, M. Brandt, M. Qian, Characteristics of oxide films on Ti-(10–75)Ta alloys and their corrosion performance in an aerated Hank's balanced salt solution, Appl Surf Sci 506 (2020). https://doi.org/10.1016/j.apsusc.2019.145013.
[267] A. Ignaszak, C. Song, W. Zhu, J. Zhang, A. Bauer, R. Baker, V. Neburchilov, S. Ye, S. Campbell, Titanium carbide and its core-shelled derivative TiC@TiO 2 as catalyst supports for proton exchange membrane fuel cells, Electrochim Acta 69 (2012) 397–405. https://doi.org/10.1016/j.electacta.2012.03.039.
[268] E. McCafferty, J.P. Wightman, X-ray photoelectron spectroscopy sputter profile study of the native air-formed oxide film on titanium, Appl Surf Sci 143 (1999) 92–100. https://doi.org/10.1016/S0169-4332(98)00927-1.
[269] L. Backman, J. Gild, J. Luo, E.J. Opila, Part I: Theoretical predictions of preferential oxidation in refractory high entropy materials, Acta Mater 197 (2020) 20–27. https://doi.org/10.1016/j.actamat.2020.07.003.
[270] L. Backman, J. Gild, J. Luo, E.J. Opila, Part II: Experimental verification of computationally predicted preferential oxidation of refractory high entropy ultra-high temperature ceramics, Acta Mater 197 (2020) 81–90. https://doi.org/10.1016/j.actamat.2020.07.004.
[271] W.M. Mellor, K. Kaufmann, O.F. Dippo, S.D. Figueroa, G.D. Schrader, K.S. Vecchio, Development of ultrahigh-entropy ceramics with tailored oxidation behavior, J Eur Ceram Soc 41 (2021) 5791–5800. https://doi.org/10.1016/j.jeurceramsoc.2021.05.010.
[272] S. Osaki, H. Sakai, R.O. Suzuki, Direct Production of Ti–29Nb–13Ta–4.6Zr Biomedical Alloy from Oxide Mixture in Molten CaCl2, J Electrochem Soc 157 (2010) E117. https://doi.org/10.1149/1.3435302.
[273] M. Metikoš-Huković, A. Kwokal, J. Piljac, The influence of niobium and vanadium on passivity of titanium-based implants in physiological solution, Biomaterials 24 (2003) 3765–3775. https://doi.org/10.1016/S0142-9612(03)00252-7.
[274] P.E.L. Moraes, R.J. Contieri, E.S.N. Lopes, A. Robin, R. Caram, Effects of Sn addition on the microstructure, mechanical properties and corrosion behavior of Ti-Nb-Sn alloys, Mater Charact 96 (2014) 273–281. https://doi.org/10.1016/j.matchar.2014.08.014.
[275] A. Ayyagari, V. Hasannaeimi, H.S. Grewal, H. Arora, S. Mukherjee, Corrosion, erosion and wear behavior of complex concentrated alloys: A review, Metals (Basel) 8 (2018) 603. https://doi.org/10.3390/met8080603.
[276] Q.T. Song, J. Xu, (TiZrNbTa)90Mo10 high-entropy alloy: Electrochemical behavior and passive film characterization under exposure to Ringer's solution, Corros Sci 167 (2020) 108513. https://doi.org/10.1016/j.corsci.2020.108513.
[277] D. Shah, S. Bahr, P. Dietrich, M. Meyer, A. Thißen, M.R. Linford, Zirconium oxide particles, by near-ambient pressure XPS, Surface Science Spectra 26 (2019) 024001. https://doi.org/10.1116/1.5086178.
[278] G.C. Gomes, F.F. Borghi, R.O. Ospina, E.O. López, F.O. Borges, A. Mello, Nd:YAG (532 nm) pulsed laser deposition produces crystalline hydroxyapatite thin coatings at room temperature, Surf Coat Technol 329 (2017) 174–183. https://doi.org/10.1016/j.surfcoat.2017.09.008.

[279] S. Gurel, A. Nazarahari, D. Canadinc, G. Gerstein, H.J. Maier, H. Cabuk, T. Bukulmez, M. Cananoglu, M.B. Yagci, S.M. Toker, S. Gunes, M.N. Soykan, From corrosion behavior to radiation response: A comprehensive biocompatibility assessment of a CoCrMo medium entropy alloy for utility in orthopedic and dental implants, Intermetallics (Barking) 149 (2022) 107680. https://doi.org/10.1016/j.intermet.2022.107680.
[280] H. Wang, J. Zheng, X. Sun, Y. Luo, Tribo-corrosion mechanisms and electromechanical behaviours for metal implants materials of CoCrMo, Ti6Al4V and Ti15Mo alloys, Biosurf Biotribol 8 (2022) 44–51. https://doi.org/10.1049/bsb2.12031.
[281] A. Robin, O.A.S. Carvalho, S.G. Schneider, S.G. Schneider, Corrosion behavior of Ti-xNb-13Zr alloys in Ringer's solution, Materials and Corrosion 59 (2008) 929–933. https://doi.org/10.1002/maco.200805014.
[282] M. Stern, A.L. Geaby, Electrochemical polarization. I. A theoretical analysis of the shape of polarization curves, J Electrochem Soc 104 (1957) 56. https://doi.org/10.1149/1.2428496.
[283] N. Birbilis, S. Choudhary, J.R. Scully, M.L. Taheri, A perspective on corrosion of multi-principal element alloys, Npj Mater Degrad 5 (2021) 1–8. https://doi.org/10.1038/s41529-021-00163-8.
[284] J.R. Scully, S.B. Inman, A.Y. Gerard, C.D. Taylor, W. Windl, D.K. Schreiber, P. Lu, J.E. Saal, G.S. Frankel, Controlling the corrosion resistance of multi-principal element alloys, Scr Mater 188 (2020) 96–101. https://doi.org/10.1016/j.scriptamat.2020.06.065.
[285] L. Yan, Y. Diao, Z. Lang, K. Gao, Corrosion rate prediction and influencing factors evaluation of low-alloy steels in marine atmosphere using machine learning approach, Sci Technol Adv Mater 21 (2020) 359–370. https://doi.org/10.1080/14686996.2020.1746196.
[286] J. Yuan, Q. Wang, Z. Li, C. Dong, P. Zhang, X. Ding, Domain-knowledge-oriented data pre-processing and machine learning of corrosion-resistant γ-U alloys with a small database, Comput Mater Sci 194 (2021) 110472. https://doi.org/10.1016/j.commatsci.2021.110472.
[287] K.N. Sasidhar, N.H. Siboni, J.R. Mianroodi, M. Rohwerder, J. Neugebauer, D. Raabe, Deep learning framework for uncovering compositional and environmental contributions to pitting resistance in passivating alloys, Npj Mater Degrad 6 (2022) 1–10. https://doi.org/10.1038/s41529-022-00281-x.
[288] A. Roy, M.F.N. Taufique, H. Khakurel, R. Devanathan, D.D. Johnson, G. Balasubramanian, Machine-learning-guided descriptor selection for predicting corrosion resistance in multi-principal element alloys, Npj Mater Degrad 6 (2022) 1–10. https://doi.org/10.1038/s41529-021-00208-y.
[289] H.C. Ozdemir, A. Nazarahari, B. Yilmaz, D. Canadinc, E. Bedir, R. Yilmaz, U. Unal, H.J. Maier, Machine learning – informed development of high entropy alloys with enhanced corrosion resistance, Electrochim Acta 476 (2024) 143722. https://doi.org/10.1016/j.electacta.2023.143722.
[290] A. Katrutsa, V. Strijov, Comprehensive study of feature selection methods to solve multicollinearity problem according to evaluation criteria, Expert Syst Appl 76 (2017) 1–11. https://doi.org/10.1016/j.eswa.2017.01.048.
[291] X. Liu, P. Xu, J. Zhao, W. Lu, M. Li, G. Wang, Material machine learning for alloys: Applications, challenges and perspectives, J Alloys Compd 921 (2022) 165984. https://doi.org/10.1016/j.jallcom.2022.165984.

[292] Q. Tao, P. Xu, M. Li, W. Lu, Machine learning for perovskite materials design and discovery, NPJ Comput Mater 7 (2021) 1–18. https://doi.org/10.1038/s41524-021-00495-8.
[293] Z. He, L. Li, Z. Huang, H. Situ, Quantum-enhanced feature selection with forward selection and backward elimination, Quantum Inf Process 17 (2018) 1–11. https://doi.org/10.1007/s11128-018-1924-8.
[294] D. Xue, P. V. Balachandran, J. Hogden, J. Theiler, D. Xue, T. Lookman, Accelerated search for materials with targeted properties by adaptive design, Nat Commun 7 (2016) 1–9. https://doi.org/10.1038/ncomms11241.
[295] L.B. Coelho, D. Zhang, Y. Van Ingelgem, D. Steckelmacher, A. Nowé, H. Terryn, Reviewing machine learning of corrosion prediction in a data-oriented perspective, Npj Mater Degrad 6 (2022) 1–16. https://doi.org/10.1038/s41529-022-00218-4.
[296] H.C. Ozdemir, A. Nazarahari, B. Yilmaz, U. Unal, H.J. Maier, D. Canadinc, E. Bedir, R. Yilmaz, Understanding the enhanced corrosion performance of two novel Ti-based biomedical high entropy alloys, J Alloys Compd 956 (2023) 170343. https://doi.org/10.1016/j.jallcom.2023.170343.
[297] X. Gu, Y. Zhuang, D. Huang, Corrosion behaviors related to the microstructural evolutions of as-cast Al0.3CoCrFeNi high entropy alloy with addition of Si and Ti elements, Intermetallics (Barking) 147 (2022) 107600. https://doi.org/10.1016/j.intermet.2022.107600.
[298] Z. Zhou, Q. Wei, Q. Li, B. Jiang, Y. Chen, Y. Sun, Development of Co-based bulk metallic glasses as potential biomaterials, Materials Science and Engineering C 69 (2016) 46–51. https://doi.org/10.1016/j.msec.2016.05.025.
[299] Y. Ji, N. Li, Z. Cheng, X. Fu, M. Ao, M. Li, X. Sun, T. Chowwanonthapunya, D. Zhang, K. Xiao, J. Ren, P. Dey, X. Li, C. Dong, Random forest incorporating ab-initio calculations for corrosion rate prediction with small sample Al alloys data, Npj Mater Degrad 6 (2022) 1–10. https://doi.org/10.1038/s41529-022-00295-5.
[300] E.W. Huang, W.J. Lee, S.S. Singh, P. Kumar, C.Y. Lee, T.N. Lam, H.H. Chin, B.H. Lin, P.K. Liaw, Machine-learning and high-throughput studies for high-entropy materials, Materials Science and Engineering R: Reports 147 (2022) 100645. https://doi.org/10.1016/j.mser.2021.100645.
[301] S.M. Lundberg, S.I. Lee, A unified approach to interpreting model predictions, in: Adv Neural Inf Process Syst, 2017: pp. 4766–4775. https://doi.org/10.5555/3295222.
[302] Y. Zhao, M. Wang, H. Cui, Y. Zhao, X. Song, Y. Zeng, X. Gao, F. Lu, C. Wang, Q. Song, Effects of Ti-to-Al ratios on the phases, microstructures, mechanical properties, and corrosion resistance of Al2-xCoCrFeNiTix high-entropy alloys, J Alloys Compd 805 (2019) 585–596. https://doi.org/10.1016/j.jallcom.2019.07.100.

Appendix A: The correlation of composition and empirical features to elastic modulus – the red bars demonstrate the input features exhibiting close to zero correlation to the target variable.

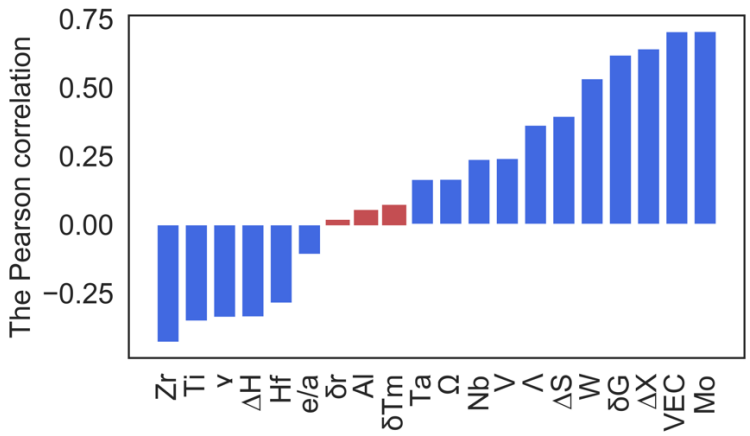

Appendix B: Definition of and explanation for the input features.

Feature Name	Abbreviations	Calculation formula / Description
Elements in the compositions		
Titanium concentration	Ti	-
Tantalum concentration	Ta	-
Hafnium concentration	Hf	-
Niobium concentration	Nb	-
Zirconium concentration	Zr	-
Molybdenum concentration	Mo	-
Tin concentration	Sn	-
Weighted average of some properties*)		
Valence electron concentration	VEC	$k = \sum_{i=1}^{n} c_i * k_i$
Melting temperature	T	
Number of itinerant electrons	e/a	
Shear modulus	G	
Electron affinity	EA	
Cohesive energy	COH	
First ionization energy	FIE	
Work function	WF	
Thermodynamic parameters		
Mixing entropy	ΔS	$\Delta S = -8.314 \sum_{i=1}^{n} c_i * \ln(c_i)$
Mixing enthalpy	ΔH	$\Delta H = 4 \sum_{i=1,\ j>i}^{n} c_i c_j H_{i-j}^{mix}$
Analogues to difference in atomic radii calculation formula		
Difference in shear modulus	δG	$\delta k = \sqrt{\sum_{i=1}^{n} c_i * (1 - \frac{k_i}{k})^2}$
Difference in melting temperature	δT	
Atomic radius related parameters		
Difference in atomic radii	δr	$\delta r = \sqrt{\sum_{i=1}^{n} c_i * (1 - \frac{r_i}{r})^2}$
γ parameter	γ	$\gamma = \frac{1 - \sqrt{\frac{(r + r_{min})^2 - r^2}{(r + r_{min})^2}}}{1 - \sqrt{\frac{(r + r_{max})^2 - r^2}{(r + r_{max})^2}}}$
Electronegativity parameter		
Difference in electronegativity	$\Delta\chi$	$\Delta\chi = \sqrt{\sum_{i=1}^{n} c_i * (\chi - \chi_i)^2}$
Analogues to difference in atomic radii calculation formula		
Shear modulus	ΔG	$\Delta k = \sqrt{\sum_{i=1}^{n} c_i * (k - k_i)^2}$
Electron affinity	ΔEA	
Cohesive energy	ΔCOH	
First ionization energy	ΔFIE	
Work function	ΔWF	
Melting temperature	ΔT	
Other parameters		
Λ parameter	Λ	$\Lambda = \frac{\Delta S}{\delta r}$
Experimental parameters		
Simulated body fluid	SBF	1=yes, 0=no
Artificial saliva	AS	1=yes, 0=no

Bodily fluids	BF	1=yes, 0=no
pH	pH	-
Temperature	Temp	1=37 ºC, 0=25 ºC

Appendix C: High magnification SEM image with the corresponding elemental maps of (a) HEA-Center and (B) HEA-Top.

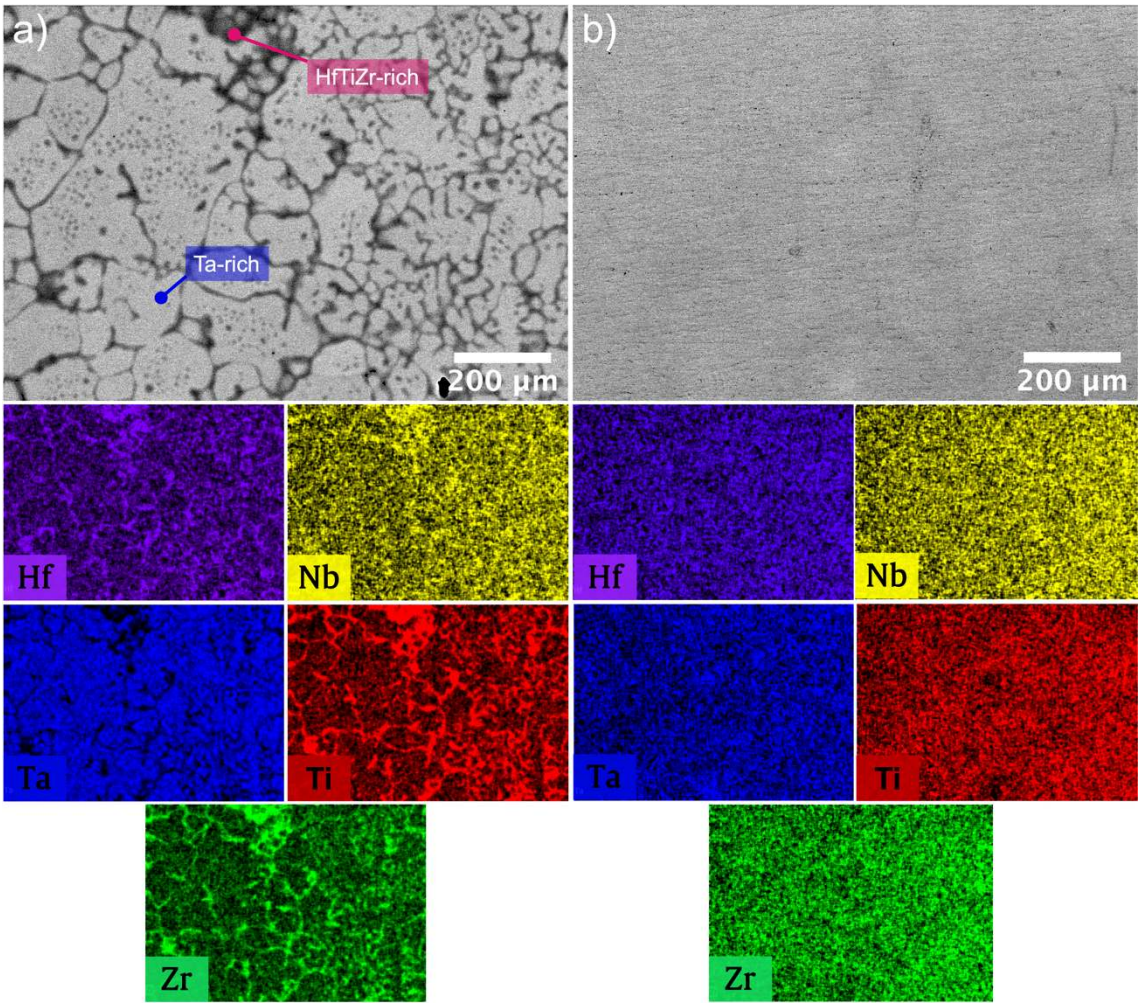

Appendix D: Metallic and oxide binding energies of the alloying elements present in air-formed and passive oxide layer formed in SBF at 37 ± 1 ºC after polarization experiments.

Oxidation/Chemical State	**Photo electron lines**	**Binding Energy (eV)**	
		Air	**SBF**
Hf^{4+}	$4f_{7/2}$: $4f_{5/2}$	17.21: 18.91	17.22: 18.92
Hf^{x+}		15.23: 16.93	15.71: 17.31
Hf^{0}		13.64: 15.30	-
Nb^{5+} (Nb_2O_5)	$3d_{5/2}$: $3d_{3/2}$	207.43: 210.23	207.36: 210.18
Nb^{4+} (NbO_2)		205.51: 208.22	205.92: 208.62
Nb^{2+} (NbO)		203.11: 206.08	203.00: 205.81
Nb^{0}		201.92: 204.62	-
Ta^{5+} (Ta_2O_5)	$4f_{7/2}$: $4f_{5/2}$	26.36: 28.26	26.36: 28.25
Ta^{4+} (TaO_2)		25.07: 26.90	25.45: 27.09
Ta^{3+} (TaO)		23.76: 25.56	-
Ta^{1+} (Ta_2O)		21.90: 23.66	22.47: 24.29
Ta^{0}		21.35: 23.20	21.49: 25.50
Ti^{4+} (TiO_2)	$2p_{3/2}$: $2p_{1/2}$	458.96: 464.77	458.92: 464.79
Ti^{3+} (Ti_2O_3)		457.51: 463.03	457.86: 463.36
Zr^{4+} (ZrO_2)	$3d_{5/2}$: $3d_{3/2}$	182.62: 185.00	182.63: 184.99
Zr^{x+}		180.22: 182.78	181.36: 183.73
Zr^{0}		178.25: 180.85	-